NANOSTRUCTURE MATERIALS FOR RECHARGEABLE LITHIUM-ION AND LITHIUM-OXYGEN BATTERIES

A thesis presented for the award of the degree of

Doctor of Philosophy

from

University of Technology, Sydney

By Bing Sun, B. Eng., M. Eng.

July, 2012

DEDICATION

This thesis is dedicated to my parents.

CERTIFICATION

I, Bing Sun, declare that the work in this thesis has not previously been submitted for a degree nor has it been submitted as part of requirements for a degree except as fully acknowledged within the text.

I also declare that the thesis has been written by me. Any help that I have received in my research work and the preparation of the thesis has been acknowledged. In addition, I declare that all information sources and literature used are indicated in the thesis.

Bing Sun

02-07-2012

ACKNOWLEDGEMENTS

I wash to express my deeply appreciation to my supervisor, Prof. Guoxiu Wang, for his encouragement, understanding, invaluable advice, and constant supporting during my study at University of Technology, Sydney (UTS).

I wish to thank our group members: Dr. Hao Liu, Mr. Bei Wang, Ms. Ying Wang, Mr. Dawei Su, Mr. Kefei Li, Mr. Jinqiang Zhang, Mr. Anjon Kumar Mondal, Mr. Ali Reza Ranjbartoreh and Mr. Shuangqiang Chen. Special thanks will go to Dr. Yueping (Jane) Yao for her support in many ways.

I also wish to thank A/Prof. Alison Ung, Dr. Ronald Shimmon and Dr. Linda Xiao in Chemistry and Forensic Science for their friendly support and kindly discussions during my study.

I am very grateful that Prof. Paul Munroe from University of New South Wales, spending lots of time on the TEM analysis.

I would to give my thanks to Prof. Shixue Dou, Prof. Huakun Liu, Ms. Huimin Wu, Ms. Ruoqi Liu, Mr. Jinsoo Park, Dr. Zhixing Chen and A/Prof. Josip Horvat, in University of Wollongong.

Financial support provided by the Australian Research Council (ARC) through the ARC Linkage project (LP0989134), ARC Discovery Project (DP1093855) and BEZEL New Energy Science and Technology Co., Ltd. is gratefully acknowledged.

Many thanks also got to Dr. Fiona MacIver for the critical reading of this thesis.

Finally, I would like to thank my father, Mr. Huanhai Sun, and my mother, Ms. Lirong Gao, for their love and support during my PhD study.

TABLE OF CONTENTS

LIST OF FIGURES

LIST OF TABLES

LIST OF ABBREVIATIONS

Abbreviation	Full name
a.u.	Arbitrary unit
BET	Brunauer Emmett Teller
CB	Carbon black
cm	Centimeter
CMC	Dimethyl carbonate
C-rate	Current rate
EC	Ethylene carbonate
EIS	Electrochemical impedance spectroscopy
Eq.	Equation
FESEM	Field emission scanning electron microscopy
FTIR	Fourier transform inferior red spectroscopy
EVs	Electric vehicles
HEVs	Hybrid electric vehicles
HF	Hydrofluoric acid
JCPDS	Joint committee on powder diffraction standards
Li	Lithium
nm	Nanometer
NMP	1-methyl-2-pyrrolidinone
OCP	Open circuit potential
PC	Propylene carbonate
PTFE	Polytetrafluoroethylene
PVDF	Polyvinylidene fluoride
SAED	Selected area electron diffraction
SEI	Solid electrolyte interphase
SEM	Scanning electron microscopy
TEM	Transmission electron microscopy
TGA	Thermogravimetric analysis
XRD	X-ray diffraction

LIST OF PUBLICATION

1. **Bing Sun**, Bei Wang, Ying Wang, Paul Munroe and Guoxiu Wang*, "$LiFePO_4$ facet nanoplates/graphene hybrid materials for lithium ion batteries with high rate performance", *Chemistry An-Asian Journal* (Submitted)

2. **Bing Sun**, Hao Liu, Paul Munroe, Hyojun Ahn, Guoxiu Wang*, "Mesoporous CoO/CMK-3 nanocomposite as a high performance cathode catalyst for lithium oxygen batteries", *Nano Research* 5 (2012) 460-469.

3. **Bing Sun***, Ying Wang, Bei Wang, Hyun-Soo Kim, Woo-Seong Kim, Guoxiu Wang*, "Porous $LiFePO_4$/C microspheres as high-power cathode materials for lithium ion batteries", *Journal of nanoscience and nanotechnology* (Accepted)

4. Hao Liu, Dawei Su, Ruifeng Zhou, **Bing Sun**, Guoxiu Wang* and Shizhang Qiao*, "Highly ordered mesoporous MnS_2 with expanded spacing of the (002) crystal plane for ultrafast lithium ion storage", *Advanced Energy Materials* 2 (2012) 970-975.

5. Ying Wang, Jinsoo Park, **Bing Sun**, Hyojun Ahn, Guoxiu Wang*, "Winter sweet flower-like $CoFe_2O_4$/MWCNTs hybrid material for high capacity reversible lithium storage", *Chemistry An-Asian Journal* 7 (2012) 1940-1946.

6. **Bing Sun**, Bei Wang, Dawei Su, Linda Xiao, Hyojun Ahn, Guoxiu Wang*, "Graphene nanosheets as cathode catalysts for lithium-air batteries with an enhanced electrochemical performance", *Carbon* 20 (2012) 727-733.

7. **Bing Sun**, Zhixing Chen, Hyun-Soo Kim, Hyojun Ahn, Guoxiu Wang*, "MnO/C core-shell nanorods as high capacity anode materials for lithium ion batteries", *Journal of Power Sources* 196 (2011) 3346-3349.

8. Ying Wang, **Bing Sun**, Jinsoo Park, Woo-Seong Kim, Hyun-Soo Kim, Guoxiu Wang*, "Morphology control and electrochemical properties of nanosize $LiFePO_4$ cathode material synthesized by co-precipitation combined with in-situ

polymerization", *Journal of Alloys and Compounds* 509 (2011) 1040-1044.

9. **Bing Sun**, Josip Horvat. Hyung-Soo Kim, Woo-Seong Kim, Jung-Ho Ahn, Guoxiu Wang*, "Synthesis of mesoporous α-Fe_2O_3 nanostructures for highly sensitive gas sensors and high capacity anode materials in lithium ion battery", *The Journal of Physical Chemistry C* 114 (2010) 18753-18761.

10. Guoxiu Wang*, Bei Wang, Jinsoo Park, Ying Wang, **Bing Sun**, Jane Yao, "Highly efficient and large-scale synthesis of graphene by electrolytic exfoliation" *Carbon* 47 (2009) 3242-3246.

ABSTRACT

Electrode materials and catalysts are key factors influencing the high power and high efficiency performances of lithium-ion batteries or lithium-oxygen batteries. In this doctoral work, a series of nanostructure materials, such as one-dimensional nanorods, two-dimensional nanoplates and nanosheets, three-dimensional microspheres and mesoporous structures, were successfully synthesized by various methods. Their electrochemical performance in lithium-ion batteries and lithium-oxygen batteries was also measured by galvanostatic charge-discharge, cyclic voltammetry and electrochemical impedance spectra.

$LiFePO_4$ facet nanoplates/graphene hybrid materials and mesoporous nanolayer carbon coated $LiFEPO_4$ microspheres were synthesized by a hydrothermal method combined with high temperature treatment. The as-prepared materials exhibited both high discharge capacities and excellent high-rate performances as cathode materials for lithium-ion batteries.

Mesoporous α-Fe_2O_3 was successfully synthesized by a soft template method for testing as an anode material in lithium-ion batteries. The as-prepared mesoporous α-Fe_2O_3 electrodes showed a high discharge specific capacity and stable cycleability. The excellent electrochemical performance should be attributed to the unique mesostructure, with its high surface area able to provide high surface contact with the electrolyte and decrease the current density per unit area.

One-dimensional MnO/C core-shell nanorods were successfully prepared from the reduction of MnO_2 nanowires. This material exhibited good electrochemical performance as an anode material for lithium-ion batteries, which is higher than that of MnO microparticle and MnO_2 nanowire electrodes. A one-dimensional nanorod structure can greatly shorten the pathways for lithium ion diffusion. The nanoporous carbon coating layer greatly increased the electronic conductivity of the composite.

Graphene nanosheets (GNSs) were prepared by a chemical reduction reaction and directly used as cathode catalysts for lithium-oxygen batteries with an alkyl carbonate electrolyte. The as-prepared GNSs electrode exhibited better cyclability and lower over-potential than that of the Vulcan XC-72 electrode. The reduced over-potential shows the as-prepared GNSs, with many carbon vacancies and defects on their surfaces, were more electrochemically active than Vulcan XC-72 in an alky carbonate electrolyte.

Mesoporous CoO/CMK-3 nanocomposite was synthesised by an impregnation method using the mesoporous carbon CMK-3 as the template. When used as the cathode catalyst in lithium-oxygen batteries, the as-prepared CoO/CMK-3 nanocomposite electrode exhibied better capacity retention than that of bare mesoporous CMK-3 carbon, Super-P or CoO/Super-P nanocomposite. The mesopores inside the CoO/CMK-3 nanocomposite facilitate the diffusion of oxygen during the discharge

process and the release of the charge products during the charging process. The CoO nanoparticles significantly reduce the charge over-potential and increase the round-trip efficiency.

INTRODUCTION

Global warming, limited supplies of fossil-fuel, and increasing city pollution make the urgency for replacing petroleum with clean energy sources (wind, solar, tidal) greater ever before. CO_2 emission, and consequent air pollution, can be reduced by replacement of internal combustion engine (ICE) cars with zero emission electric vehicles (EVs). Energy storage has become more important today than at any time in human history.

Current lithium-ion batteries have proved themselves the most advanced electrochemical power sources for portable electronic devices in the past two decades. However, they cannot meet the stringent requirements for high power in electric vehicles (EVs) and hybrid electric vehicles (HEVs). Intensive research is continuing on all aspects of lithium-ion batteries including, cathode materials, anode materials, binder, electrolytes and the battery production technique. The active materials of the electrode are key to increasing lithium-ion battery energy density and power density above the energy and power densities of current lithium-ion batteries. Commercial lithium-ion battery electrodes are composed of powders containing micro-sized particles which seriously limit lithium ion diffusion. Fortunately, nanotechnology has paved the way for advanced electrode materials to achieve high-power performance. In this doctoral work, nanostructure materials for both cathode and anode electrodes have been developed.

However, even when fully developed, the highest energy storage of current lithium-ion batteries still cannot meet the demands of key markets, such as transport, in the long term. Recently, rechargeable lithium-oxygen batteries have been attracting more and more attention and are considered an option as the power source for electric vehicles. This new configuration of lithium batteries can store 3-4 times higher energy than the state-of-the-art lithium-ion batteries. The development of an efficient air electrode is a huge challenge for lithium-oxygen batteries. The use of nanostructure carbon materials and nanocomposites has shown great potential for improving the electrochemical performance of lithium-oxygen batteries.

The purpose of this doctoral work is to discuss possible ways of improving the electrochemical performance of rechargeable lithium batteries via the use of nanostructure materials and to provide possible opportunities for future research directions. A series of nanostructure materials, such as one-dimensional nanorods, two-dimensional nanoplates and nanosheets, three-dimensional microsphere and mesoporous structures, were successfully synthesized by hydrothermal methods, soft template methods, hard template methods and chemical reduction methods. The morphologies of the as-prepared materials were characterized by scanning electron microscopy and transmission electron microscopy. The electrochemical performance of the as-prepared materials was evaluated by various electrochemical measurements; they were tested for their use as electrode materials for lithium-ion batteries or for their use as as catalysts for lithium-oxygen batteries. The dynamic behavior of lithium ion

diffusion in the electrode was investigated to reveal the mechanisms behind any observed improvement in electrochemical performance. Increased electrocatalivity of the electrochemical reaction in the cathode of lithium-oxygen batteries will be discussed.

An outline of the content is briefly presented as follows:

1. A literature review of lithium-ion batteries and lithium-oxygen batteries is presented in Chapter 1. In this chapter, the basic concepts and principles of lithium-ion batteries are presented. Recent developments in the conventional cathode materials and anode materials for lithium-ion batteries are reviewed. The architectures, electrochemical reactions and the development of cathode catalysts of lithium-oxygen batteries are also introduced.

2. Chapter 2 contains the experimental parts, including the material synthesis methods, physical and structural characterization methods, electrode preparation and electrochemical characterization methods. The synthesis methods include hydrothermal methods, soft template methods, hard template methods and chemical reduction methods. X-ray diffraction and Raman spectroscopy were used to identify the crystal structure of the as-prepared materials. The morphology and particle size distribution were observed by field emission gun scanning electron microscopy and transmission electron microscopy. The carbon content was determined by thermogravimetric analysis. The electrochemical performance was evaluated by

galvanostatic charge-discharge, cyclic voltammetry (CV) and electrochemical impedance spectra.

3. To achieve high-power performance for lithium-ion batteries, $LiFePO_4$ nanostructures were synthesized and used as cathode materials in lithium-ion batteries. As detailed in chapter 3, novel $LiFePO_4$ facet nanoplates/graphene hybrid materials were synthesized by a hydrothermal reaction combined with high temperature treatment. As detailed in Chapter 4, mesoporous nanolayer carbon coated $LiFePO_4$ microspheres were prepared by a hydrothermal method.

4. One-dimensional core-shell MnO nanorods and three-dimensional mesoporous α-Fe_2O_3 were also synthesized and evaluated as high capacity anode materials for lithium-ion batteries. As detailed in Chapter 4, core-shell MnO nanorods were synthesized by reducing MnO_2 nanowires in a reductive atmosphere combined with an in-situ carbon coating technique. As detailed in Chapter 5, mesoporous α-Fe_2O_3 was synthesized by a soft template method using tri-block copolymer F-127 as the template.

5. The effect on the electrochemical performance of lithium-oxygen batteries of using nanostructure materials as cathode catalysts is discussed. As detailed in Chapter 7, graphene nanosheets were used as cathode catalysts and were found to be more active than other forms of carbon towards the electrochemical reaction in lithium-oxygen batteries. As detailed in Chapter 8, a nanocasting technique was used to synthesize mesoporous carbon CMK-3. CoO nanoparticles were loaded on

the CNK-3carbon through an impregnation method. The CoO/CMK-3 nanocomposite was measured as a cathode catalyst for lithium-oxygen batteries.

CHAPTER 1 LITERATURE REVIEW

Lithium-ion batteries have proved themselves the most advanced electrochemical power sources for portable electronic devices in the past two decades because of their high energy density and high power density. Recently, lithium-ion batteries have made a great impact on vehicle electrification, including hybrid electric vehicles (HEVs) and electric vehicles (EVs), in response to the concern to reduce air pollution and global warming.[1-4] However, the current generation of lithium-ion batteries cannot meet the stringent requirements of high power application in terms of energy density, power density, cycle life, cost, safety and environmental concerns.[5] Great efforts have been devoted to increasing the electrochemical performance of lithium-ion battery systems by using nanotechnology with existing materials and by seeking new electrode materials. An alternative response to the limitations of lithium-ion batteries is to explore a new battery system with new chemistry, especially electrochemistry.[6]

Figure 1-1 shows the theoretical and practical energy density of different batteries and gasoline. The theoretical energy density of gasoline is 13,000 Wh kg^{-1} and the usable (practical) energy density is approximately 1,700 Wh kg^{-1} according to the average tank-to-wheel efficiency of the U.S. fleet (12.1%). The energy density of current commercial lithium-ion batteries is between 100 and 200 Wh kg^{-1}. A 10-fold improvement in energy density would be required for these batteries to replace the gasoline as a power sources for vehicles. Notably, the theoretical energy density of

lithium air batteries is 11,680 Wh kg^{-1} based on the weight of lithium metal only. A practical energy density of 1,700 Wh kg^{-1} may be achievable for lithium-air batteries after long-term intensive work, which corresponding to only 14.5 % of the theoretical energy density.[7] For the future EVs/HEVs applications, a possible solution for using rechargeable lithium batteries as the power source is to design a hybrid energy storage system that combines lithium-ion batteries (for high power density) and lithium air batteries (for high energy density).

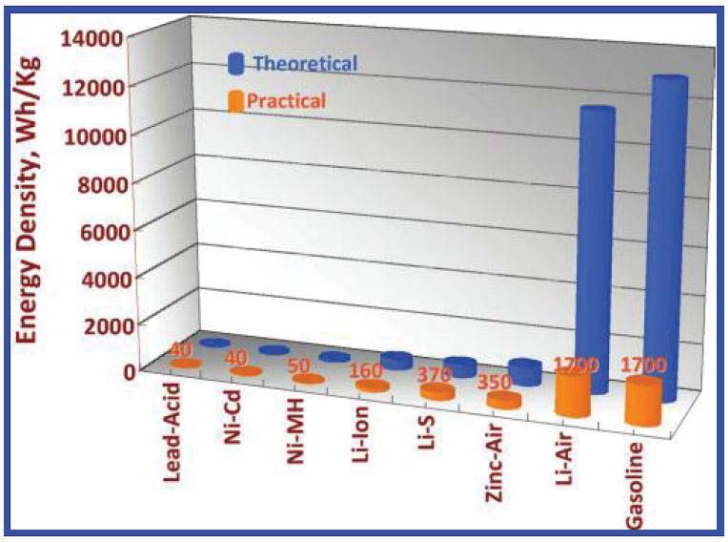

Figure 1-1 The gravimetric energy density (Wh kg^{-1}) for different types of rechargeable batteries and gasoline.[7]

1.1 Lithium-ion Batteries

1.1.1 History of Lithium-Ion Batteries

The lithium-ion battery has dominated the power supply market for portable devices in the past two decades since its commercialization by SONY in 1991. Its energy density is 2-3 times higher than conventional rechargeable batteries, such as nickel-cadmium

batteries and nickel-metal-hydride batteries. The worldwide market for rechargeable lithium-ion batteries is valued at 10 billion US dollars per annum and growing fast. Lithium-ion batteries are also considered the first choice for future EVs and HEVs.

The invention of lithium-ion batteries is not an accident and it took more than two decades to bring lithium-ion batteries from the laboratory to industry. Around 1970 Gamble et al. discovered that a range of electron donating molecules and ions could be intercalated into the layered dichalcogenides.[8] Among all dichalcogenides, titanium disulfide (TiS_2) was considered to be the most promising electrode material for energy storage.[9-11] It is a semimetal with high electronic conductivity and it can form a single phase with lithium ions over the entire composition range of Li_xTiS_2 ($0 \leq x \leq 1$), enabling all the lithium to be removed reversibly.[12,13] However, the low potential and high cost for production limit its commercialization.[14] Later, researchers started to investigate the lithium intercalation behaviour of layered metal oxides, in particular, vanadium pentoxide (V_2O_5). However, the fairly complex phase transition of V_2O_5 during lithium intercalation and poor cycling performance makes this material unsuitable for commercialization of lithium-ion batteries.[15-17] In the 1980s, Goodenough recognized that $LiCoO_2$ had a similar layered structure to the dichalcogenides and the extracted lithium could be intercalated reversibly, making it a very promising electrode material.[18,19] At the same time, Yazami et al. reported the reversible graphite-lithium negative electrode in a solid organic electrolyte.[20] For the carbon anode, the lithium intercalation product is LiC_6. This can reduce the lithium dendritic, avoiding the short

circuit and makes a much safer battery than pure lithium metal. The lithium-ion battery system combining $LiCoO_2$ as the cathode materials and graphite as the anode materials was finally commercialized by SONY after more than 20 years of development.[21]

1.1.2 Basic Concepts and Principles for Lithium-ion Batteries

A rechargeable lithium-ion battery is a lithium-ion device and does not contain lithium metal. It consists of a cathode (positive electrode) and an anode (negative electrode) separated by a porous membrane soaked in a liquid organic electrolyte. Figure 1-2 shows a typical commercial lithium-ion battery configuration. The positive electrode (cathode) is a layered structure lithium metal oxide (e. g. $LiCoO_2$) and the negative electrode (anode) is graphite (e. g. mesocarbon microbeads, MCMB). The electrodes are separated by a porous polymer membrane. The Li^+ conducting electrolyte is a solution of a lithium salt (e.g. $LiPF_6$) in mixed organic solvents (e.g. ethylene carbonate/dimethyl carbonate, EC/DMC). For the charging process, lithium ions extract from the cathode, pass through the electrolyte and intercalate into the anode. The electrons pass through the external circuit from the negative electrode to the positive electrode. The discharge process reverses this process.

The redox reaction is presented below:

$$LiCoO_2 \leftrightarrow Li_{1-x}CoO_2 + xLi^+ + xe^- \ (1<x<0) \qquad \text{cathode} \qquad \text{(Eq. 1-1)}$$

$$6C + xLi^+ + xe^- \leftrightarrow Li_xC_6 \ (1<x<0) \qquad \text{anode} \qquad \text{(Eq. 1-2)}$$

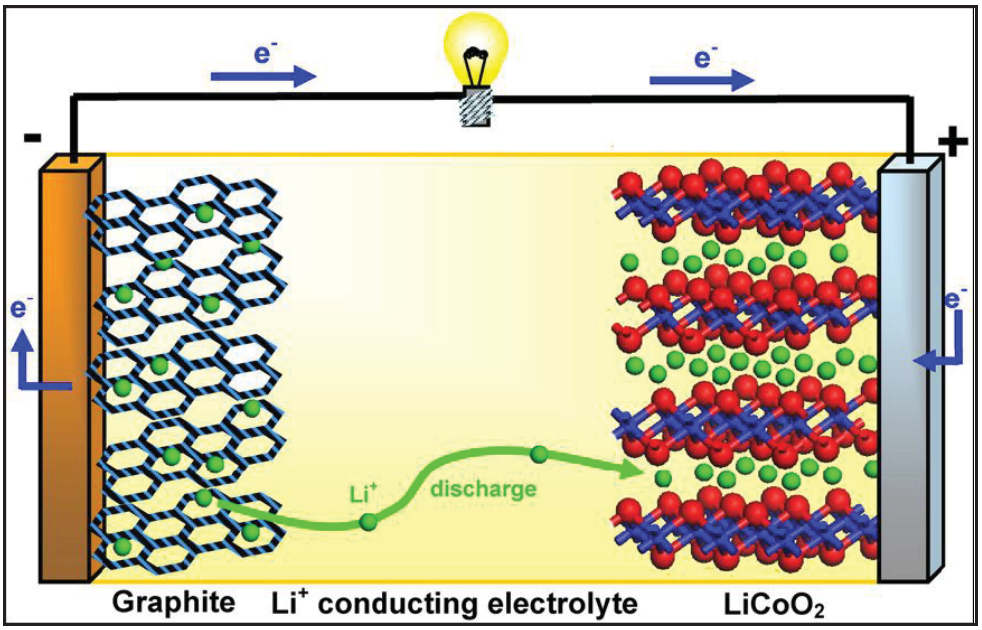

Figure 1-2 Schematic representation of a lithium-ion battery.[22]

Electrode: complex porous composite adhering to the current collector (copper foil for anode and aluminum foil for cathode). It consists of active materials, conductive materials and a binder. Since the electronic conductivity of most active materials is rather low, the addition of materials conductive (e.g. carbon black) is to increase the electronic conductivity of the electrode. The binder is usually a long chain polymer able hold all the electrode materials together on the current collector.

Active materials or active mass: the material that generates electrical current by means of a chemical reaction within the battery.[23] Normally, for rechargeable lithium-metal or lithium-ion batteries, material with a potential higher than 2 V vs Li^+/Li is defined as a cathode material and a material with a potential lower than 2 V vs Li^+/Li is defined as an anode material. The potentials and specific capacities of different electrode materials are summarized in Figure 1-3. The application of nanostructured active materials to

lithium-ion batteries will be reviewed later.

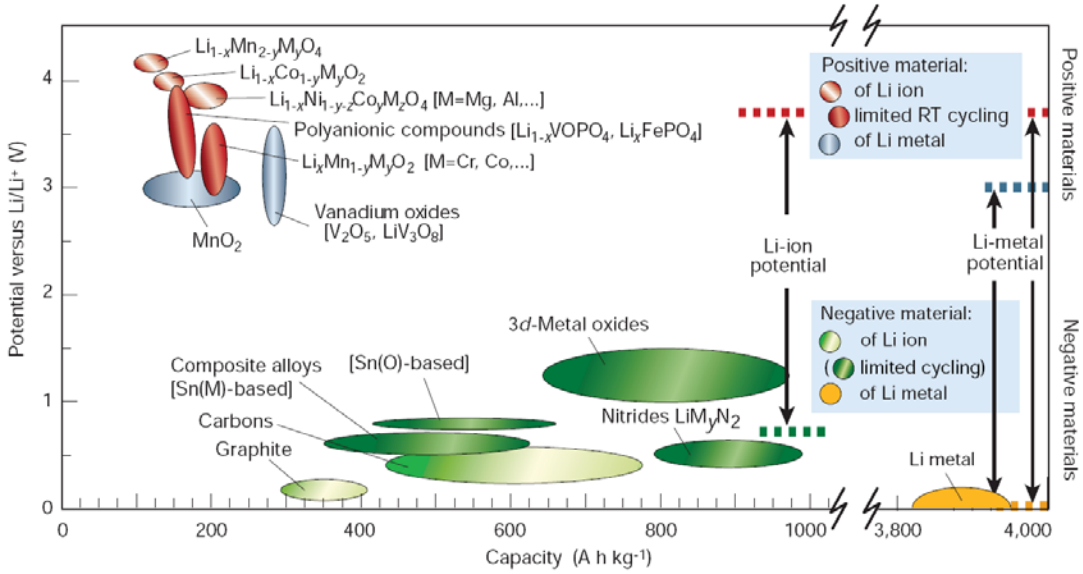

Figure 1-3 Voltage versus capacity for different electrode materials.[4]

Electrolyte: the material that provides pure ionic conductivity between the positive and negative electrodes of a cell.[23] Due to the formation of lithium in anode during the charging process, the electrolyte for lithium-ion batteries should be a nonaqueous electrolyte and must satisfy several requirements as follows:[24,25]

- High Li-ion conductivity $\sigma_{Li} > 10^{-4}$ S cm^{-1} and low electronic conductivity $\sigma_e < 10^{-10}$ S cm^{-1} over the temperature range of battery operation.
- High thermodynamically stable window $V_{oc} \geq 4$ V.
- Good retention of the electrode/electrolyte interface during cycling when the electrode particles are changing their volume.
- A transference number $\sigma_{Li+}/\sigma_{total} \approx 1$, where σ_{total} includes conductivities by other ions in the electrolyte as well as σ_{Li+} and σ_e.
- Good chemical stability over ambient temperature ranges and temperatures in

the battery under high power.

- Chemical stability with respect to the electrodes, including the ability to rapidly form a passivating solid/electrolyte interface (SEI).
- Safety, e.g. preferably nonflammable and non-explosive materials if the cell is short-circuited.
- Low toxicity and low cost.

It is a formidable challenge to meet all these requirements. The electrolyte for lithium-ion batteries basically consists of a lithium salt and solvents. The lithium salts provide the lithium source in the electrolyte for intercalation/de-intercalation between the electrodes, and the solvents provide a medium for lithium ion diffusion. Several types of electrolytes have been developed for particular applications, such as organic liquid electrolytes,[24,26] ionic liquid electrolytes,[27-30] inorganic liquid electrolytes,[31,32] solid polymer electrolytes,[33] inorganic solid electrolytes[34-37] and hybrid electrolytes.[38-46] Table 1-1 lists a series of electrolytes with different compositions.

Separator: a physical barrier between the positive and negative electrodes incorporated into most cell designs to prevent electrical shorting.[23] Separators must be permeable to the ions and inert in the battery environment. Microporous membranes using polyolefins have been developed and used extensively in lithium-ion batteries. The current polyolefin membranes are made of polyethylene (PE), polypropylene (PP), or laminates of polyethylene and polypropylene, which can provide excellent mechanical properties, chemical stability and acceptable cost.[47]

Table 1-1. Nonaqueous electrolytes for lithium-ion batteries.[25]

Electrolytes	Example of classical electrolytes	Ionic conductivity (10^{-3} s/cm) at room temperature	Electrochemical window (V) vs Li^+/Li^0		Remark
			Reduction	Oxidation	
Liquid organic	1M $LiPF_6$ in EC:DEC (1:1)	7	1.3	4.5	Flammable
	1M $LiPF_6$ in EC:DMC (1:1)	10	1.3	>5.0	
Ionic liquids	1M LiTFSI in EMI-TFSI	2.0	1.0	5.3	Non-flammable
	1M $LiBF_4$ in EMI-BF_4	8.0	0.9	5.3	
Polymer	LiTFSI-P(EO/MEEGE)	0.1	<0.0	4.7	Flammable
	$LiClO_4$-PEO_8 +10 wt % TiO_2	0.02	<0.0	5.0	
Inorganic solid	$Li_{4-x}Ge_{1-x}P_xS_4$ (x = 0.75)	2.2	<0.0	>5.0	Non-flammable
	$0.05Li_4SiO_4$+$0.57Li_2S$+$0.38SiS_2$	1.0	<0.0	>8.0	
Inorganic liquid	$LiAlCl_4$+SO_2	70	-	4.4	Non-flammable
Liquid organic + Polymer	$0.04LiPF_6$+0.2EC+0.62DMC +0.14PAN	4.2	-	4.4	Flammable
	$LiClO_4$+EC+PC+PVdF	3.0	-	5.0	
Ionic liquid + Polymer	1M LiTFSI+P_{13}TFSI+ PVdF-HFP	0.18	<0.0	5.8	Less flammable
Ionic liquid + Polymer + Liquid organic	56 wt% LiTFSI-Py_{24}TFSI + 30 wt% PVdF-HFP + 14 wt% EC/PC	0.81	1.5	4.2	Less flammable
Polymer + Inorganic solid	2 vol% $LiClO_4$-TEC-19+ 98 vol% 95 ($0.6Li_2S$ t $0.4Li_2S$)+ $5Li_4SiO_4$	0.03	<0.0	>4.5	Non-flammable

Some basic concepts to evaluate the electrochemical performance of lithium-ion batteries are illustrated as follows:

Cell potential: the potential difference between the cathode and anode materials.

Specific capacity: the amount of electric charge the battery can store per unit mass.

The theoretical specific capacity ($Q_{TSC,}$ mAh g^{-1}) can be calculated from the following

equation:

$$Q_{TSC} = n \times F/M \quad \text{(Eq. 1-3)}$$

where n is the mol number of electron transfer in the electrochemical reaction, F is the Faraday constant (96,485.33 C mol^{-1}), and M is the molecular weight of the active materials.

The specific charge capacity (Q_c, mAh g^{-1}) or specific discharge capacity (Q_d, mAh g^{-1}) can be calculated from the following equation:

$$Q_c \text{ (or } Q_d) = I \times t/m \quad \text{(Eq. 1-4)}$$

where I is the charge or discharge current (mA), t is the charge or discharge time (s), m is the mass of the active materials (g).

Specific energy: defined as the energy per unit mass.

Energy density: a term used for the amount of energy stored in a given system.

The specific energy (*SE*, Wh kg^{-1}) and energy density (*ED*, Wh L^{-1}) can be calculated from the following equations:

$$SE = (E \times Q) / 1000 \quad \text{(Eq. 1-5)}$$

$$ED = (E \times Q \times m) / (1000 \times V) \quad \text{(Eq. 1-6)}$$

Specific power: the ability of the battery to deliver power per unit mass.

Power density: a term used for the ability of the battery to deliver power per unit volume. The specific power (*SP*, Wh kg^{-1}) and power density (*PD*, Wh L^{-1}) can be calculated from the following equations:

$$SP = SE/t \quad \text{(Eq. 1-7)}$$

$$PD = ED/t \quad \text{(Eq. 1-8)}$$

where t (h) is the discharge time.

Irreversible capacity (Q_I): used to define the capacity loss after each cycle.

For cathode materials: $Q_I = {}^{n^{th}}Q_d - {}^{n^{th}}Q_c$ (Eq. 1-9)

For anode materials: $Q_I = {}^{n^{th}}Qc - {}^{n^{th}}Qd$ (Eq. 1-10)

Coulombic efficiency: a term to represent the ratio of discharge capacity to the charge capacity.

$$\mu = {}^{n^{th}}Q_d \ / {}^{n^{th}}Q_c \times 100\% \quad \text{(Eq. 1-11)}$$

1.1.3 Selection Criteria for Lithium-ion Battery Systems

A commercial lithium ion battery system requires the following:[4,23]

- The reactants must have sufficient energy content to provide a useful current and voltage level. The normal energy density for a lithium-ion battery is between 100 Wh L^{-1} and 150 Wh L^{-1}.
- For a general consumer battery, the battery operation temperature should be in the range of 0-40 °C and the storage temperature should be in the range of -20 to 85 °C.
- The materials must maintain their mechanical and chemical stability over time in the operating environment, avoiding, for example, reaction with the

electrolyte or no irreversible phase change.

- A general lithium-ion battery must be capable of complete charge and discharge over 300 cycles with capacity loss less than 20 %. For automotive applications, the cycle life should be more than 2000 cycles.
- The cost of the battery should be affordable for the customer.
- All commercial batteries must be safe in the normal operating environment. Additionally, they should not vent hazardous materials, nor present any hazard under mild abuse conditions (e.g. leaking, explosion, etc).

1.1.4 Nanostructure Electrode Materials for Lithium-ion Batteries

Although the current commercial lithium-ion batteries are successful, especially in small portable devices, they still need to conquer big challenges for high power applications, such as EVs and HEVs. The commercial lithium-ion batteries are based on micro-sized electrode materials. The intrinsic lithium ion diffusion coefficient in the solid state is less than 10^{-8} cm^2 S^{-1}, which significantly limits the rate of lithium ion intercalation/de-intercalation from the solid state, and hence the charge/discharge rate performance. The introduction of nanostructure materials instead of the current micro-sized electrode materials is considered to be the most promising strategy for overcoming the current limits: the reduced dimensions can greatly shorten the lithium ion diffusion path and enable far higher intercalation/deintercalation rates and hence high power.[48] Developments in the use of nanostructure electrode materials for rechargeable lithium-ion batteries are described below. The advantages and

disadvantages of nanostructure electrode materials for rechargeable lithium batteries are summarized first as follows:[49,50]

Advantages

- Reducing the particle size to nanoscale significantly reduces the lithium ion diffusion distance within the particles. The characteristic time constant for diffusion is given by $\tau = L^2/D$, where L is the diffusion length and D is the diffusion constant. The time for lithium ion intercalation/de-intercalation decreases with the square of the particle size, illustrating the remarkable effect of replacing micro-sized with nano-sized particles.
- Electron transport within the particles is also enhanced by nano-sized particles, as described for lithium ions transportation.[48]
- Nanostructure material with a high surface area permits a high contact area between electrode and electrolyte and hence the number of active sites for electrode reactions, which in turn reduces electrode polarization loss and improves the power density.
- Nanostructure materials with new lithium storage mechanisms can achieve much higher capacities than conventional intercalation materials. Recent studies show that excess lithium ions can be stored on the surface, interface,[51-53] and in nanopores.[54-56]
- It has been observed that nano-sized electrode materials become active for lithium ion insertion, an event unable to take place in bulk form.[48,57]
- The redox potentials for lithium ions and electrons may be modified by

nanostructures, resulting in a change of cell voltage.[58,59]

- Nanostructure materials would more easily accommodate the strain associated with lithium intercalation/de-intercalation.[60,61]

Disadvantages

- The synthesis of nanoparticles may be more complex and difficult and their dimensions may be difficult to control.
- High electrolyte/electrode surface area also increases the risk of more significant side reactions with the electrolyte, and, consequently, large irreversible capacity and poor cycle life.
- Nanostructure materials tend to form agglomerations during the electrode fabrication, making it difficult to disperse and mix with carbon black and binder to produce electrodes.
- The tap density of nanostructure material is generally less than the same material formed from micro-sized particles, thus reducing the volumetric energy density.

1.1.4.1 Nanostructure Cathode Materials

In a lithium-ion battery, the cathode material is the active materials in the positive electrode: it is associated with the oxidation reaction and gains electrons from the external circuit during the cell discharge process. A successful cathode material for a lithium-ion battery should meet the following requirements:

- The material should react with lithium ion reversibly and contain a readily ion,

which can participate in the redox reaction.

- The material should have a high free energy to react with lithium to supply a high discharge voltage.
- The material should have high electronic conductivity for electron transportation and high ionic conductivity for lithium ion transportation.
- The material should be stable and safe over the entire operation environment.
- The material should be low cost and friendly to the environment.

A brief review of the development of selected nanostructure cathode materials for lithium-ion batteries follows

Nanostructure Layered Oxides

Since the first report by Goodenough in 1980,[18] layered transition metal oxides, such as $LiCoO_2$, $LiNiO_2$, $LiMnO_2$, $LiNi_{1/2}Mn_{1/2}O_2$ and $LiNi_{1/3}Mn_{1/3}Co_{1/3}$, have received tremendous attention as cathode materials for lithium-ion batteries. In 1991, SONY successfully combined the $LiCoO_2$ cathode with a graphite anode to make the first commercial lithium-ion batteries and this configuration still dominates the lithium battery market. The $LiCoO_2$ cathode had an α-$NaFeO_2$-type structure with the oxygens in a cubic close-packed arrangement and it showed that lithium can be extracted reversibly (Figure 1-4).[62,63] Although the theoretical specific capacity of $LiCoO_2$ is 274 mAh g^{-1}, it can only achieve a practical capacity of about 140 mAh g^{-1}. The electrochemical and in situ X-ray diffraction studies showed that lithium ion ordering occurs at x=0.5, which coupled to a lattice distortion from hexagonal to monoclinic

symmetry.[62] The complete removal of lithium from $LiCoO_2$ will cause the oxygen layers to rearrange giving hexagonal close packing oxygen to CoO_2.[19] The lithium ion diffusion coefficient of $LiCoO_2$ is 5×10^{-9} cm^2 s^{-1}, which is comparable with $LiTiS_2$ (10^{-8} cm^2 s^{-1}).[14] However, the conductivity of Li_xCoO_2 can dramatically change by 2~4 orders of magnitude at ambient temperatures from metal-like material to a typical semiconductor.[64,65]

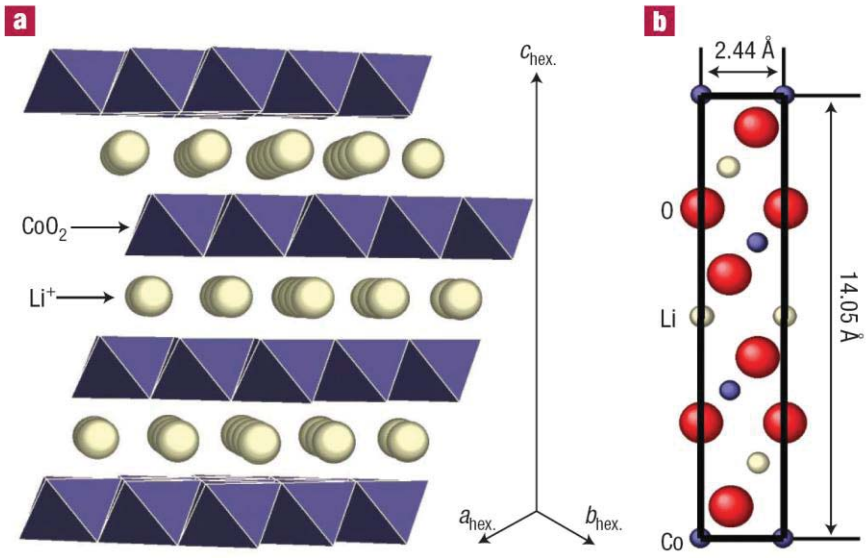

Figure 1-4 Models of the layered $LiCoO_2$ structure with space group $\overline{R}3m$.[63]

To improve the electrochemical performance, nanostructure $LiCoO_2$ has been synthesized and developed. The first strategy was surface modification.[66] Nano-sized carbon coating on $LiCoO_2$ from the decomposition of sucrose showed a higher capacity and lower charge transfer resistance than pristine $LiCoO_2$.[67] Coating a nanolayer metal oxide or phosphate on the surface of the $LiCoO_2$ particles can also significantly improve the capacity. Cho et al. reported that ZrO_2 coated $LiCoO_2$ can deliver a discharge

capacity of 170 mAh g^{-1} when cycled between 2.75 and 4.4 V at room temperature without capacity loss over 70 cycles.[68] Kim et al. reported the $LiCoO_2$ particles coated by $AlPO_4$ can significantly improve the safety for lithium-ion batteries and also exhibited the highest intercalation capacity (230 mAh g^{-1}) in a voltage range of 4.8 and 3 V at a rate of 0.1 C.[69,70] A thin-film coating of metal oxide or metal phosphate on the $LiCoO_2$ particles can suppresses the cobalt dissolution and phase transitions caused by the lattice-constant changes during electrochemical cycling.

The second strategy was to synthesize $LiCoO_2$ with different nanostructure materials to accelerate the lithium intercalation/de-intercalation and thus increase the power density of the battery. $LiCoO_2$ cathode materials with nanowire, or nanotube, or desert rose or ordered mesoporous structures have been synthesized through different methods (Figure 1-5). Zhou et al. first reported the synthesis of $LiCoO_2$ nanowire arrays by a sol–gel template method using porous anodic aluminum oxide (AAO) as the template.[71] Later Li et al. reported that open-ended $LiCoO_2$ nanotubes with uniform size and shape can also be synthesized by a similar method.[72] The nanotubes obtained exhibited higher discharge capacity and better high C-rate performance than those of their nanocrystalline counterparts. Chen et al. reported the synthesis of a new $LiCoO_2$ with desert rose nanostructure by using a molten salt/hydroxide flux method. This $LiCoO_2$ desert rose nanostructure was capable of achieving good electrochemical performance at high rates.[73] Jiao et al. reported the synthesis of nanowire and mesoporous low-temperature $LiCoO_2$ by a hard template route. The mesoporous or nanowire Co_3O_4

was first synthesized using mesoporous silica as the hard templates. Then, after template removal, Co_3O_4 was reacted with a lithium source to get $LiCoO_2$ whilst retaining the nanostructured morphology.[74] However, the major issue is that layered oxides with high surface area increase the risk of secondary reactions with the electrolyte and the associated safety problems. Thus layered oxide nanoparticles may not be particularly useful for practical lithium-ion batteries.[75]

The high cost and the safety problem of $LiCoO_2$ limits its application to large-scale lithium power batteries for EVs and HEVs. Other layered oxides, such as $LiNiO_2$ and $LiMnO_2$, have also been intensively investigated.[76-78] However, unstable structure during the charging state and the complex synthesis method made them difficult to commercialize.[79] Ohzuku et al. reported that the electrochemical performance of $LiCoO_2$ can be improved by multi-substitution to form $LiNi_{1/3}Mn_{1/3}Co_{1/3}$ and that the safety can be improved by further doping with Al, making $LiNi_{1/3}Mn_{1/3}Co_{1/3}$ a potential cathode material for lithium-ion power batteries.[80-84]

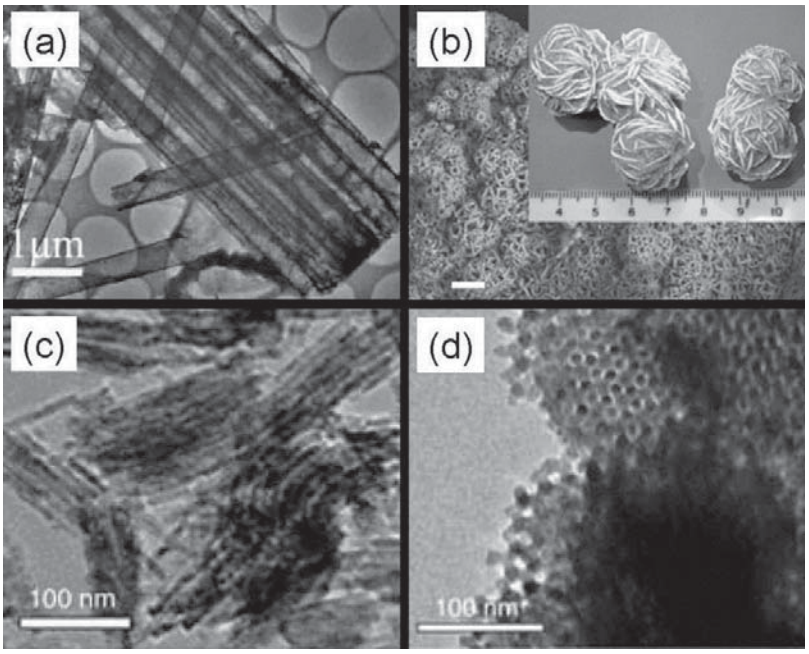

Figure 1-5 (a)TEM images of $LiCoO_2$ nanotubes, (b) SEM image of "desert rose" form of $LiCoO_2$, (c) TEM images of low temperature $LiCoO_2$ nanowires, (d) TEM images of mesoporous low temperature $LiCoO_2$ along the [111] direction.

Nanostructure Spinel Oxides

Spinel $LiMn_2O_4$ is one of the most important intercalation cathode materials for lithium-ion power batteries because manganese is abundant, inexpensive and environmentally benign. Spinel $LiMn_2O_4$ was first reported by Tackeray's group and has been extensively investigated by Bellcore labs.[85-88] The crystal structure again contains cubic close-packed oxygen ions and is closely related to the α-$NaFeO_2$ layer structure, differing only in the distribution of the cations among the available octahedral and tetrahedral sites (Figure 1-6).[14,89] There are two discharge plateaus for spinel $LiMn_2O_4$ during the discharge process: one around 4 V and the other around 3 V. Usually only the 4 V plateau is used, so that the cell is constructed in the discharged state and must be

charged before use, just as for $LiCoO_2$. It has been reported by Tarason et. al that the value of the cubic lattice parameter is critical to obtain effective cycling.[86] Lithium-rich spinel, $Li_{1+x}Mn_{2-x}O_4$, where the average manganese oxidation state is 3.58 or higher, is associated with a lattice parameter $\leq$ 8.23Å, which can minimize dissolution of manganese and also the impact of the Jahn-Teller distortion associated with the Mn^{3+} ion.

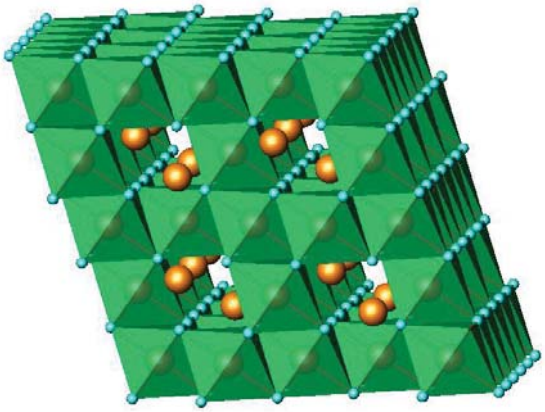

Figure 1-6 Spinel structure of $LiMn_2O_4$.

The major disadvantage of spinel $LiMn_2O_4$ is its slow dissolution of manganese ions in the electrolyte during cycling.[90,91] Nanotechnology has also been applied to improve the electrochemical performance of spinel $LiMn_2O_4$. Coating a nano-layer of metal oxide on the surface of $LiMn_2O_4$ particles is helpful in improving the cycle stability, just as $LiCoO_2$.[92] ZrO_2 coated $LiMn_2O_4$ exhibits tremendously improved cycling stability and high rates performance compared with pristine $LiMn_2O_4$.[93] A ZrO_2 coating layer can act as a highly lithium ion conducting solid electrolyte interface, which reduces the interfacial resistance and protect Mn dissolution by HF from the electrolyte. The rigid

oxide coating layer strongly bonds to $LiMn_2O_4$ particles and tolerates the lattice stress resulting from volume expansion during lithium intercalation.

Spinel $LiMn_2O_4$ also suffers from low electronic conductivity and poor ionic conductivity, which limits its high-rate performance. The strategy to solve this problem is to synthesize $LiMn_2O_4$ with different nanostructure to accelerate the lithium intercalation/deintercalation and the electronic conductivity. Recently, Hosono et al. reported the synthesis of high-quality single crystalline cubic spinel $LiMn_2O_4$ nanowires by using $Na_{0.44}MnO_2$ nanowires as a self-template. The single crystalline $LiMn_2O_4$ nanowires obtained showed high thermal stability and excellent high-rate performance, with both a relative flat charge-discharge plateau and excellent cycle stability at 20 A g^{-1}.[94] Kim et al. reported the synthesis of single-crystalline $LiMn_2O_4$ nanorods from β-MnO_2 nanorods by chemical conversion through a simple solid-state reaction. The $LiMn_2O_4$ nanorods have an average diameter of 130 nm and length of 1.2 μm and exhibit a high charge storage capacity at high power rates compared with commercially available powders. Moreover, more than 85% of the initial charge storage capacity was maintained for over 100 cycles.[95] $LiMn_2O_4$ nanotubes were synthesized by a sol–gel template method using porous anodic aluminum oxide (AAO) as the hard template, similar to the synthesis of $LiCoO_2$ nanotubes.[72] $LiMn_2O_4$ nanotubes can also be synthesized through solid state reaction by sintering the pre-synthesized β-MnO_2 nanotubes with LiOH at high temperature.[96] Jiao et al. reported the synthesis of ordered mesoporous $Li_{1+x}Mn_{2-x}O_4$ spinel for the first time. 3D-ordered mesoporous Mn_2O_3 was

synthesized first by a hard template method followed by transformation to Mn_3O_4 through heating in a reducing atmosphere. The final product was obtained by reacting with LiOH through a solid state reaction as shown in Figure 1-7.[97]

To improve the electronic conductivity of the spinel cathode materials, $LiMn_2O_4$/carbon composites have been synthesized by several groups.[98-100] Bulow et al. reported the synthesis of $LiMn_2O_4$/MWCNTs through low-temperature hydrothermal processing. A $LiMn_2O_4$/MWCNTs nanocomposite incorporating 10 wt% MWCNTs and 5 wt% CB yielded a reversible specific capacity of 120 mAh g^{-1} and an exceptional rate-capability of 96 % and 78 % capacity retention (116 mAh g^{-1} and 94 mAh g^{-1}) at the discharge rates of 10 C and 20 C, respectively.[98] $LiMn_2O_4$ nanoparticles homogeneously anchored on conducting carbon nanotubes and graphene nanosheets have also been fabricated via a self-assembly process combined with solid-state lithiation.[100] The obtained composites showed reversible capacities close to the theoretical value with enhanced power capability and cyclability. The small particle size of $LiMn_2O_4$ significantly improves the lithium ion diffusion kinetics and the conducting carbon matrix supplies an excellent electron transportation pathway. However, nanostructure materials with a high surface area will promote the risk of Mn dissolution into the electrolyte, leading to fading of capacity during cycling.

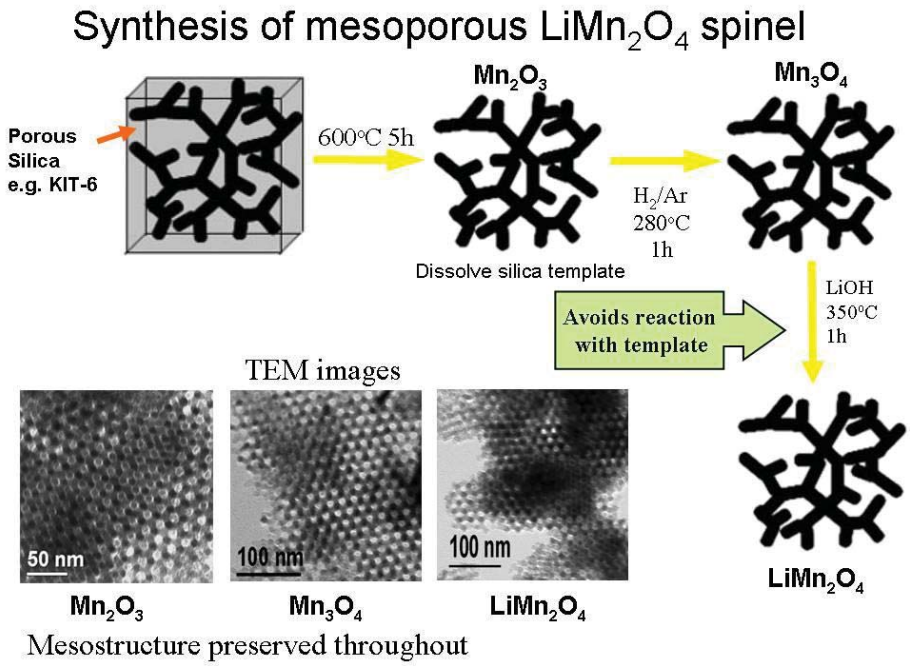

Figure 1-7 Schematic illustration of synthesis process of mesoporous $Li_{1+X}Mn_{2-X}O_4$.

Nanostructure Olivine Cathodes

Since its discovery in 1997, $LiFePO_4$ has been emerging as a new cathode material for lithium-ion batteries, in particular for high power applications.[101,102] It offers several appealing features: a high theoretical capacity of 170 mAh g^{-1}; a flat discharge voltage of 3.4 V vs. lithium that is compatible with a large number of organic electrolytes; a long cycle life with excellent capacity retention (to 1000 cycles); low cost and environmental friendliness.[103-105] $LiFePO_4$ belongs to the orthorhombic olivine structure with space group Pnma (a=10.333 Å, b=6.011 Å, and c=4.696 Å). The oxygen atoms are located in a slightly distorted, hexagonal close-packed arrangement. The phosphorus atoms occupy tetrahedral sites; the iron and lithium atoms occupy octahedral 4a and 4c sites, respectively. Each FeO_6 octahedron is linked with four FeO_6 octahedra through common corners in the b–c plane, forming zigzag planes. The LiO_6 octahedra form

edge-sharing chains along the b-axis. One FeO_6 octahedron has common edges with two LiO_6 octahedra. PO_4 groups share one edge with an FeO_6 octahedron and two edges with LiO_6 octahedra as shown in Figure 1-8.[106,107] The de-lithiation product is $FePO_4$ with the same space group as $LiFePO_4$ (Pnma).

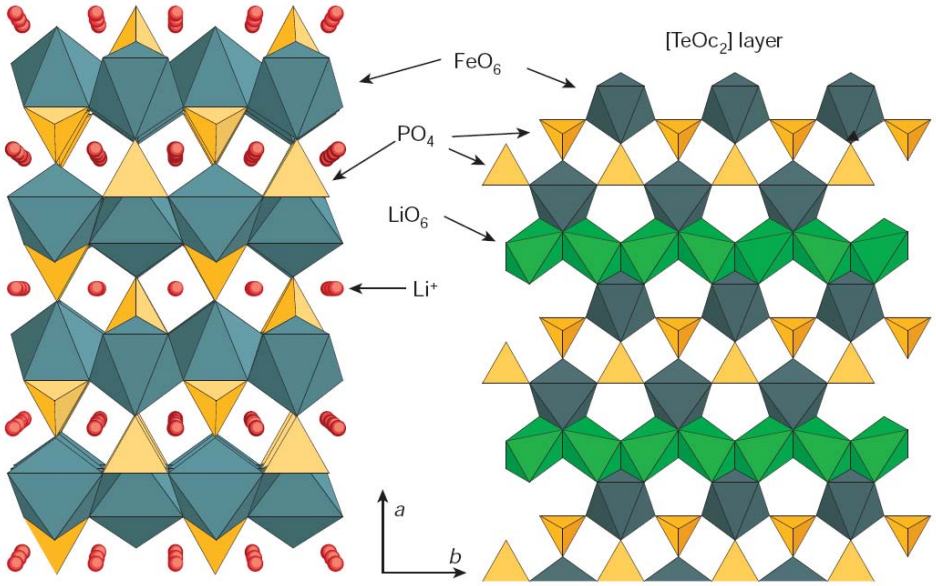

Figure 1-8 The crystal structure of olivine $LiFePO_4$ in projection along [001].[4]

However, $LiFePO_4$ is insulating in nature with a low electronic and ionic conductivity due to the lack of mixed valency and one-dimensional lithium diffusion. This one-dimensional lithium diffusion limits its high C-rate capacity.[108] Many nanotechnologies have been used to improve the electrochemical performance of $LiFePO_4$, including doping with supervalent cations, minimizing the particle size to the nanoscale, and coating the particles with a thin carbon layer or a metal oxide layer.

Chung et al. first reported improved electronic conductivity of $LiFePO_4$ through

alivalent ions doping into the Li 4a site. The electronic conductivity increased by a factor greater than 10^8. They achieved a discharge capacity of about 60 mAh g^{-1} at a high rate of 21.5 C.[108] However, whether the observed increase in electronic conductivity is a true lattice-doping effect or is due to the surface conducting percolation, is still under debate.[103,109]

Reducing the particle size of $LiFePO_4$ is extremely beneficial in overcoming the sluggish lithium ion diffusion rate associated with the olivine structure. The better chemical stability of the lower valent Fe^{2+}/ Fe^{3+} couple together with a lying of the $Fe^{2+/3+}$:3d band well above the top of the O^{2-}:2p band avoiding the side reaction with the electrolyte. Delacourt et al. reported the synthesis of carbon-free nano-sized $LiFePO_4$ crystalline powders by direct precipitation under atmospheric pressure. The particle size distribution is extremely narrow, centered on ca. 140 nm. After a soft thermal treatment under slight reducing conditions, the material obtained can deliver a specific capacity of 147 mAh g^{-1} at 5 C-rate and a good cycle stability with no significant capacity loss after more than 400 cycles at 0.5 C-rate, without the need for carbon coating.[110]

The most common method to improve the electrochemical performance of $LiFePO_4$ is coating a conductive nanolayer on the surface of $LiFePO_4$ particles. In 1999, Armand et al. reported $LiFePO_4$ with 1 wt% carbon coating having achieved almost a full theoretical capacity at 1 C-rate at 80 °C, indicating carbon coating may be a promising way to improve the capacity of $LiFePO_4$.[111] Later, Huang et al. made $LiFePO_4$/C

composites by mixing raw materials with a carbon gel before heating and obtained nano-sized $LiFePO_4$ with particle sizes of 100–200 nm and 15 wt% carbon [112] This composite achieved 90% theoretical capacity at C/2 and excellent rate capability and stability at room temperature with a discharge capacity of about 120 mAh g^{-1} at a 5 C-rate. Huang et al. concluded that both particle size minimization and intimate carbon contact are necessary to optimize the electrochemical performance of $LiFePO_4$. Doeff et al. used Raman microprobe spectroscopic analysis to observe the residual carbon present on the surfaces of the $LiFePO_4$ powders.[113] They found that higher discharge capacities obtained in lithium cells are correlated with the structure and electronic conductivity of residual carbon on particle surfaces. sp^2-coordinated carbon exhibits better electronic properties than disordered or sp^3-coordinated carbonaceous materials. However, these methods based on the thermal decomposition of precursors with a carbon source can only produce partial carbon coated $LiFePO_4$ particles. In 2008, Zhou's group reported the synthesis of a $LiFePO_4$/carbon composite consisting of a highly crystalline $LiFePO_4$ core (20 – 40 nm in size) and a highly graphitic carbon shell (1 – 2 nm in thickness) via in situ polymerization.[114] Their strategy included one in situ polymerization reaction and two typical restriction processes (Figure 1-9). Firstly, Fe^{3+} was added in the solution containing PO_4^{3-} and aniline. Fe^{3+} was used as both a precipitator for PO_4^{3-} and as an oxidant for aniline. The Fe^{3+} on the outer surface of $FePO_4$ deposits resulted in the oxidization polymerization of aniline. The green polyaniline (PANI) shell can effectively restricted the size growth of $FePO_4$ particles. Secondly, with heat treatment, the prepared $FePO_4$-PANI composite was combined with

a lithium salt and some sugar to form a $LiFePO_4$-carbon composite, thereby transforming the polymer shell into a carbon shell that in situ restricted the crystallite growth of $LiFePO_4$. The prepared $LiFePO_4$/carbon nanocomposite achieved a high C-rate performance with a capacity of 90 mAh g^{-1} at the current density of 10 A g^{-1} (rate of about 60 C), and excellent cycling performance, with less than 5% discharge capacity loss over 1100 cycles.

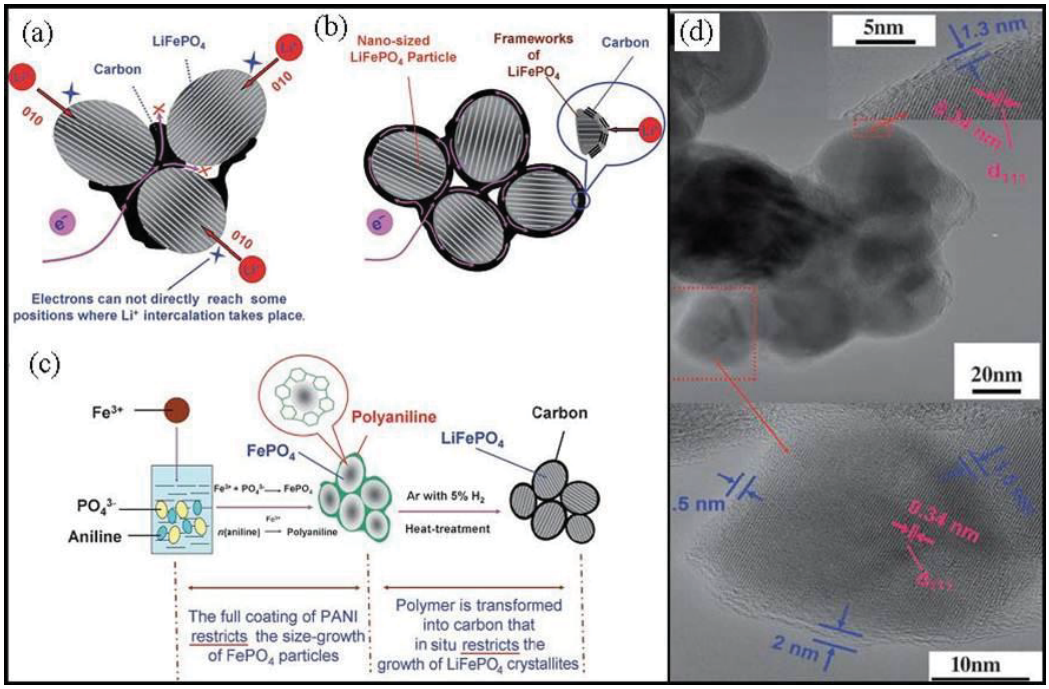

Figure 1-9 (a) Electron-transfer pathway for $LiFePO_4$ particles partially coated with carbon. (b) Designed ideal structure for $LiFePO_4$ particles with typical nano-size and a complete carbon coating. (c) Preparation process for the $LiFePO_4$/carbon composite. (d) TEM image for $LiFePO_4$/carbon particle containing several primary crystallites.[114]

Besides the carbon, other materials have also been used for surface coating to increase electronic and ionic conductivity. Conductive polymers such as polypyrrole,[115] polyaniline,[116] polyethylene glycol[117] and polyacene,[118] have been used to coat the surface of $LiFePO_4$ particles. After surface modification with those polymers, $LiFePO_4$

can achieve excellent high C-rate performance and good cycle stability. Nano-metal particles such as Cu or Ag particles have been dispersed on the surface of $LiFePO_4$ to enhance the electronic conductivity.[119,120] Some metal oxide such as ZrO_2, RuO_2, ZnO and CuO have been used for surface coating by some groups. The thin coating layer of metal oxide can increase the surface ionic conductivity and protect $LiFePO_4$ from volume change during cycling.[121-124]

Recently, Lslam's group found that the lowest Li migration energy is for the pathway along the [010] channel.[125] This computational prediction was later confirmed by experimental evidence. The Li^+ diffusion along the [010] direction in olivine type $LiFePO_4$ material has been clearly visualized by combining high-temperature powder neutron diffraction and the maximum entropy method.[126] Therefore, ionic conductivity of $LiFePO_4$ can be improved by reducing the length of the [010] direction and increasing the (010) facet. $LiFePO_4$ nanocrystals with a high percentage (010) facet have been synthesized through a solvothermal method and have shown excellent electrochemical performance.[127,128] In this thesis, $LiFePO_4$ nanoplates/graphene hybrid materials with a large (010) surface were also prepared and will be discussed in Chapter 3.

For practical application to large-scale lithium-ion power batteries, the volume energy density is quite important. Although the above down-sizing strategy combined with carbon coating is effective at increasing the electrochemical performance of a $LiFePO_4$

electrode, it also significantly reduces the tap density and volumetric energy density.[129] Recently, several reports have shown that $LiFePO_4$ with a porous secondary microsphere structure can deliver high-rate capacity.[130-132] Since the microspheres can easily form close packed arrays, a three-dimensional micro-nano porous hierarchical sphere structure is the ideal structure for $LiFePO_4$ cathode materials. The nanosized primary particles with carbon coating can ensure the high rate capability and the micro-sized secondary structures can achieve a high tap density. In Chapter 4, the use of as-prepared mesoporous nanolayer carbon coated $LiFePO_4$ microspheres as high power cathode materials for lithium-ion batteries will be discussed.

1.1.4.2 Nanostructure Anode Materials

In a lithium-ion battery, the anode material is the active materials in the negative electrode and is associated with the oxidation reaction. It gives electrons from the external circuit during cell discharge process. A successful anode material for lithium ion battery should meet the following requirements:

- The material should react with lithium ions reversibly.
- The material should react with lithium at a low operating voltage.
- The material should have high electronic conductivity for electron transportation and high ionic conductivity for lithium ion transportation.
- The material should be stable and safe over the entire operation environment.
- The material should be low cost and friendly to the environment.

A brief review of the development of selected nanostructure anode materials for

lithium-ion batteries is given below.

Nanostructure Carbonaceous Anode Materials

Lithium metal with a high specific capacity of 3860 mAh g^{-1} was first considered as the anode material in rechargeable batteries. However, the low melting point, dendritic growth during the charging process and high reactivity toward electrolytes make it unsafe for commercialization. The use of lithium insertion compounds (e.g. carbonaceous materials) instead of metallic lithium resulted in great success in battery industry since the commercialization of lithium-ion batteries by Sony in 1991. Carbonaceous materials, especially graphite, are the most widely used anode materials in current lithium-ion batteries. The intercalation mechanism of graphite is well understood. Each Li atom stored between every six C atoms permits a theoretical storage capacity of 372 mAh g^{-1}. The low storage capacity results in only a small volumetric change of about 10 % and allows for a life of more than 500 cycles. Today, graphite-based anodes are still used in most conventional lithium-ion batteries. Despite the graphite, several novel nanostructure carbon materials, such as carbon nanotubes (CNTs), carbon nanofibers (CNFs), ordered mesoporous carbon and graphene, have gained enormous attention during the past few years.[133]

Carbon nanotubes (CNTs) are an attractive anode material for use in lithium-ion batteries due to their outstanding electrical properties, high mechanical strength, high chemical stability and highly activated surface areas. Carbon nanotubes are graphene

sheets rolled-up into cylinders with diameters as small as one nanometer (Figure 1-10). A single-walled carbon nanotube (SWCNT) is a graphene sheet rolled-over into a cylinder with a typical diameter of about 1.4 nm, similar to that of a C_{60} buckyball. A multi-walled carbon nanotube (MWCNT) consists of concentric cylinders with an interlayer spacing of 3.4 Å and a diameter typically in the order of 10-20 nm. The lengths of the two types of tubes can be up to hundreds of microns or even centimeters.[134,135] The potential of CNTs to be anode materials in lithium-ion batteries was initially evaluated by many research groups, as early as the 1990s.[136-138] The measured reversible lithium ion capacities for some CNT-based anodes can exceed 1000 mAh g^{-1}, which is 3 times higher than conventional graphite anodes. Li ions can be stored in electrodes comprising CNTs via the following different ways: intercalation (LiC_6 stoichiometry); adsorption and accumulation on the outer surface and/or in the inner channel when CNTs are open; storage in the void space between bundles of tubes. The lithium storage can be further improved by adsorption on the surface of modified CNTs via reaction with heteroatoms or functional groups.[55] In all cases to date, a large irreversible capacity was observed in the first discharge and charge process, which is due to the formation of a solid electrolyte interphase (SEI) layer at around 0.9 V. This effect has been attributed to the high specific surface area of CNTs affecting the extent of solvent decomposition, leading to the SEI layer formation. CNTs have the capability to be assembled into free-standing electrodes (a role as both the active material and current collector) for lithium-ion batteries.[139] CNTs films can also be used as a physical support for ultra high capacity anode materials.[140]

Carbon nanofibers (CNFs) are also one-dimensional carbon nanostructures with graphitic layers inclined at any angle with respect to the fiber axis. Their structure arises from the stacking of very small graphene basic structural units to a tower-like morphology instead of from wrapping large graphene units in a tubular structure.[133] CNFs are usually fabricated by chemical vapor decomposition of hydrocarbons or by electrospinning of bicomponent polymer solutions, followed by thermal treatment.[141-143] The advantage of using CNFs as electrode materials for lithium-ion batteries, like that of using CNTs, is that they can be assembled into free-standing electrodes without any other additives. The lithium storage mechanism in CNFs is similar to that in CNTs (described above). The major problems are the low Coulombic efficiency of the first cycle and instability during lithium intercalation/deintercalation.[144,145]

Ordered mesoporous carbons with large surface area (more than 1000 m^2 g^{-1}) and ordered open pores have been investigated as anode materials for lithium-ion batteries and displayed an enormous lithium storage capacity. Zhou et al. reported the ordered mesoporous carbon (CMK-3) exhibited an initial discharge capacity of 3100 mAh g^{-1}, corresponding to a composition of $Li_{8.4}C_6$ and a reversible capacity of 850-1100 mAh g^{-1}, corresponding to a composition of Li_3C_6.[146] The extremely high reversible capacity is most probably due to a combination of several Li storage mechanisms discussed above. The enhanced electrode performance should arise from the three-dimensional ordered porous structure. The disadvantages associated with application of mesoporous

materials to lithium-ion batteries are the large irreversible capacity in the first cycle, the hysteresis in the charge-discharge curves and the complex synthesis method.

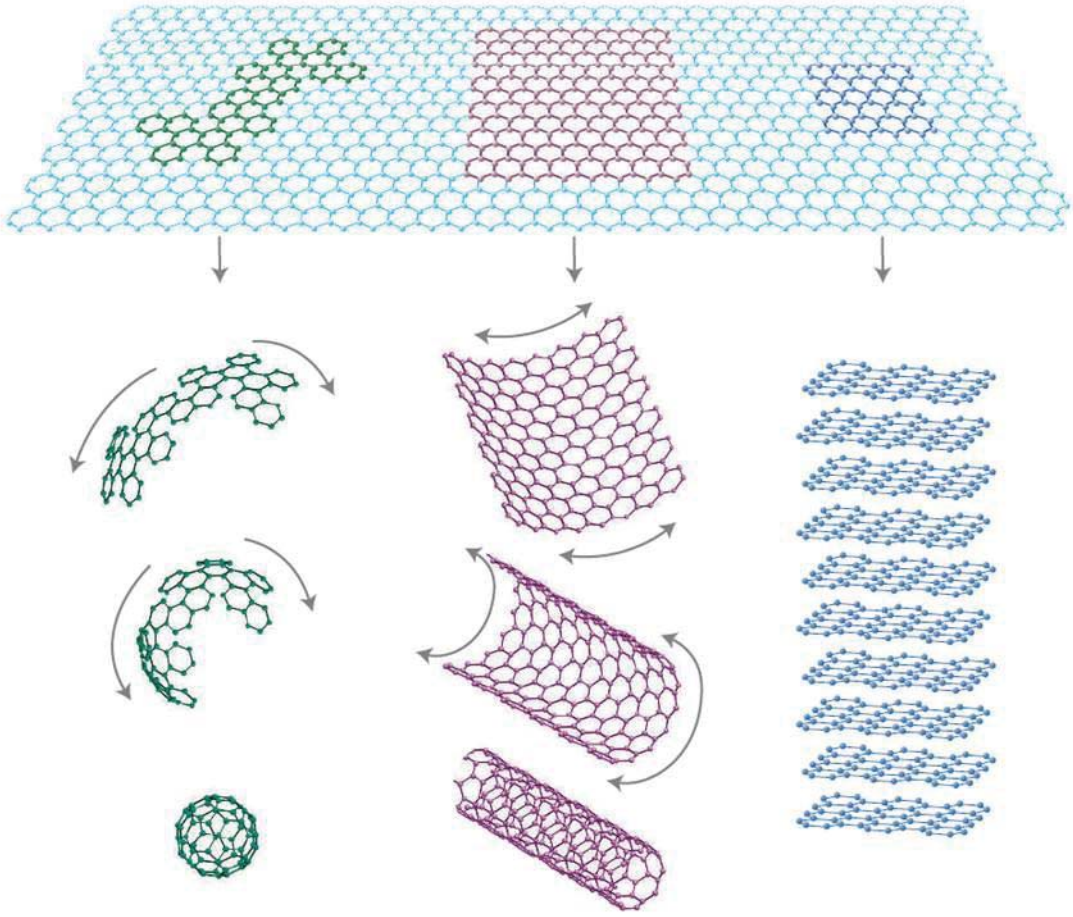

Figure 1-10 Mother of all graphitic forms. Graphene is a 2D building material for carbon materials of all other dimensionalities. It can be wrapped up into 0D buckyballs, rolled into 1D nanotubes or stacked into 3D graphite.[147]

Graphene is a two-dimensional (2D) carbon sheet of one atom thickness representing the basic structural unit of graphite as shown in Figure 1-10. The chemical synthesis of graphene includes the oxidation of graphite to graphene oxide and the chemical reduction of graphene oxide.[148] Graphene materials obtained by exfoliation of graphite exhibit a large surface area and more prismatic edge sites anchoring functional groups through the chemical treatment. The loose graphene nanosheets tend to stick together to

form fluffy agglomerates with a flower-like appearance and contain lots of void spaces as shown in Figure 1-11a.

Recently, graphene and graphene-based materials have been attracting enormous attention for their use as electrode materials in lithium-ion batteries due to their superior high electronic conductivity, large surface area and flexibility. A free-standing graphene sheet can supply two surfaces for hosting Li ions (via adsorption rather than intercalation; Figure 1-11b). Therefore, the theoretical capacity of single layer graphene should be 744 mAh g^{-1}, corresponding to a chemical composition of LiC_3. Wang et al. reported that graphene nanosheets obtained from a soft-chemistry approach had a high discharge capacity of 945 mAh g^{-1} in the first cycle and 460 mAh g^{-1} after 100 cycles.[149] The disadvantages of graphene for its application to lithium-ion batteries are the large irreversible capacity in the first cycle and the continuous capacity loss during cycling. A strategy that has been used to increase the capacity and cycling stability is to introduce another element to form graphene sandwich composites, such as SnO_2/graphene, Sn/graphene, Co_3O_4/graphene, et al.[150-154]

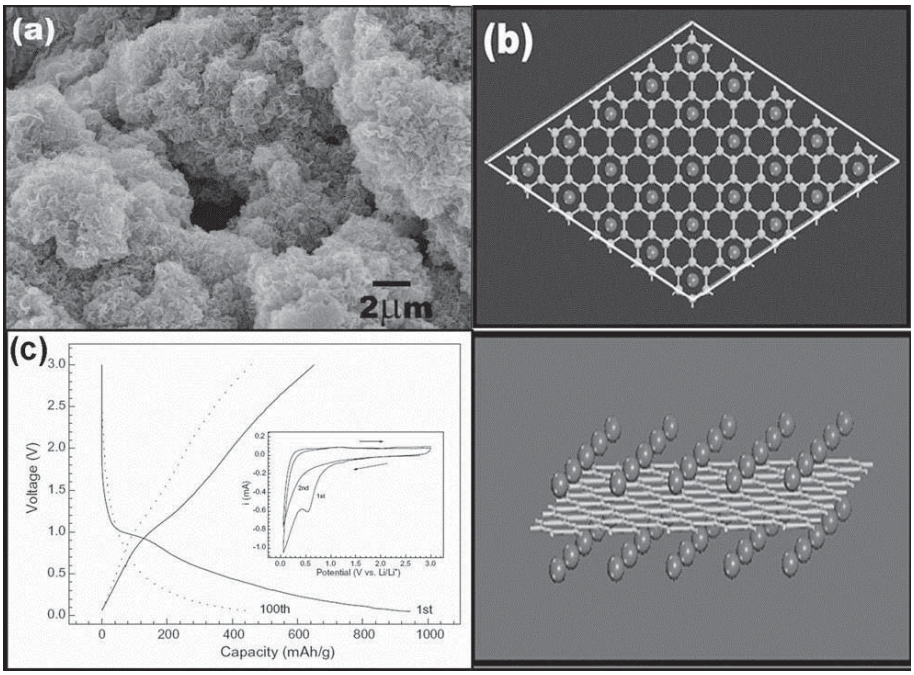

Figure 1-11 (a) Low magnification FESEM image of loose graphene nanosheets powders. (b) Atomic model of LiC_3 graphene. Top: top view; bottom: side view. (c) Charge and discharge curves of graphene nanosheets as anode in lithium-ion cells.[149,152]

Nanostructure Lithium-Metal Alloy materials

Since Dey first demonstrated in 1997 that lithium metal can electrochemically alloy with other metals to form intermetallic compounds at ambient temperature in an organic electrolyte, lithium metal alloys have been intensively investigated as high capacity anode materials for lithium-ion batteries.[155] Although such alloys have specific capacities far exceeding that of the conventional graphite anode, they still suffer from the large irreversible capacity in the first cycle and poor cycling stability. The large volume change during the lithium insertion and extraction leads rapidly to electrode deterioration (cracks, and eventually, pulverization).[49] Significant research efforts, by many groups, have been devoted to overcoming this problem. The commonly used strategies to improve the electrochemical performances of lithium alloy materials are

reducing the primary particles to nanoscale and/or forming nanostructure composites with other elements.[156] In this section, the developments of two selected Group Ⅳ elements, Si and Sn, are reviewed below.

Silicon (Si) is a very promising candidate for the anode materials of lithium-ion batteries because of its extremely high theoretical capacity. Electrochemical reactions of lithium with silicon at elevated temperatures have demonstrated that silicon can alloy with lithium up to $Li_{22}Si_4$, corresponding to a capacity of 4212 mAh g^{-1}.[157] The structure changes during lithium reacting with silicon have been studied by ex situ and in situ X-ray powder diffraction. [158,159] Crystalline silicon becomes amorphous during lithium insertion. Highly lithiated, amorphous silicon suddenly crystallizes at 50 mV to form a new lithium-silicon phase, identified as $Li_{15}Si_4$ at room temperature. This phase is the fully lithiated phase for silicon at room temperature. Delithiation of the $Li_{15}Si_4$ phase results in the formation of amorphous silicon. Poor cycling performance is a big challenge for the application of silicon in lithium-ion batteries. During the discharge process, lithium alloys with silicon, causing the volume expansion up to 270 % for the $Li_{15}Si_4$ phase. During the charge process, lithium cannot fully extract from the alloys due to the increased internal resistance. The huge volume contraction of the silicon particles after lithium extraction causes the loss of the contact area between silicon and the conducting agent. One strategy to solve this problem is to use nanostructure materials to accommodate large strain and maintain good electrical contact during discharge-charge cycling.

The enhanced electrochemical performance of silicon nanoparticles (78 nm) as anode materials for lithium-ion batteries was first reported by Li et al.[160] The nano-silicon showed a high reversible capacity, over 1700 mAh g^{-1}, at the tenth cycle, with a flat and smooth plateau ranged from 0.4 to 0.0 V *vs.* Li/Li^+, due to the distribution of nanoparticles experiencing smaller volume variation. Furthermore, coating the silicon nanoparticles with carbon or conducting polymer can increase the electrical conductivity and prevent the electrode pulverization by buffering the volume changes.[161-163]

One-dimensional nanostructure materials, such as nanowires and nanotubes, have been demonstrated to have outstanding electrochemical performance. Chan et al. reported the synthesis of silicon nanowires grown directly on a stainless steel current collector using a gold catalyzed vapor – liquid – solid (VLS) process.[164] Each silicon nanowire was directly grown on the current collector without binder and conductive additives. The silicon nanowire electrodes exhibited a very high initial discharge capacity with a coulombic efficiency of 73 % and nearly no charge-discharge capacity degradation for up to 10 cycles. The excellent electrochemical performance should benefit from the one-dimensional nanowire structure, which allows better accommodation of the large volume variations induced by the lithium insertion/removal process. Park et al. fabricated silicon nanotubes by reductive decomposition of the silicon precursor inside anodic alumina templates and etching.[165] The nanotube structure can increase the

contact surface area with the electrolyte, allowing lithium ions to intercalate from both the interior and the exterior of the nanotubes. The nanotube electrodes demonstrated a very high reversible charge capacity of 3247 mAh g^{-1}, with Coulombic efficiency of 89 % after 200 cycles at a rate of 1 C in a lithium-ion full cell consisting of a $LiCoO_2$-based cathode and a silicon-nanotube-based anode.

Tin (Sn) is an attractive anode material due to its high volumetric capacity of about 2000 mAh cm^{-3}, which is higher than that of lithium and is comparable to silicon.[166] It can alloy with lithium up to a chemical composition of $Li_{17}Sn_4$, with a theoretical specific capacity of 959.5 mAh g^{-1}.[167] However, like other lithium alloying materials, its commercialization is limited by its poor capacity retention, caused by large volume variation during lithium insertion/extractiom from Sn phase.

Encapsulating Sn nanoparticles into a conductive matrix can significantly enhance the electrochemical performance. A carbon matrix can provide sufficient mechanical strength to buffer the volume expansion, preventing disintegration and aggregation of Sn particles. Darrien et al. reported Sn/C nanostructured composites with Sn nanoparticles (10-50 nm) uniformly dispersed in a supporting carbon matrix.[168] The novel Sn/C nanocomposite exhibited a specific capacity of 500 mAh g^{-1} for 200 cycles at 0.8 C and 200 mAh g^{-1} at 5 C, thus demonstrating significantly excellent electrochemical performance. Wang et al. reported a three-dimensional Sn/graphene composite with Sn nanoparticles distributed in a graphene nanosheets matrix. The

Sn/graphene nanocomposite electrode gave high reversible lithium storage capacities (795 mAh g^{-1} in the second cycle and 508 mAh g^{-1} in the hundredth cycle), which represents a much improved performance compared to a bare graphene electrode or a bare Sn electrode.[152]

Tin oxide (SnO_2) based materials have also been considered as promising candidates for anode materials in terms of their high theoretical reversible capacity (790 mAh g^{-1}). The basic reaction mechanisms of SnO_2 have been reported as follows:[169,170]

$$SnO_2 + 4Li^+ + 4e^- \rightarrow Sn + 2Li_2O + 4.4Li^+ + 4.4e^- \leftrightarrow 2Li_{4.4}Sn + 2Li_2O \qquad \text{(Eq. 1-12)}$$

However, the formation of an undesirable Li_2O phase and the large volume variation of the Sn phase are the main barriers that have to be overcome. However, the electrochemical performance of SnO_2 can be significantly increased by reducing SnO_2 nanoparticles to the nanoscale and/or distributing the SnO_2 particles in a carbon matrix.

Park et al. reported the synthesis of SnO_2 nanotubes, nanowires, and nanopowders and demonstrated that the electrochemical performance of SnO_2 nanomaterials is likely to be related to their morphological features.[171,172] The SnO_2 nanomaterials with high specific surface areas and single-crystalline structures are better for maintaining electronic conductivity and at allowing enhancement of lithium ion diffusion into the SnO_2 structure.

Paek et al reported the fabrication of SnO_2/graphene nanosheets in an ethylene glycol

solution in the presence of rutile SnO_2 nanoparticles.[151] The SnO_2 nanoparticles were distributed between the loose graphene nanosheets with large amounts of void spaces. The SnO_2/graphene obtained exhibited a reversible capacity of 810 mAh g^{-1} and enhanced cycling performance in comparison with that of the bare SnO_2 nanoparticle. The three-dimensional configuration limits the volume expansion upon lithium insertion, and the developed pores between SnO_2 and GNS could be used as buffered spaces during charge/discharge, resulting in the superior electrochemical performances.

Nanostructure Transition Metal Oxide

In 2000, Poizot et al. reported that electrodes made of nanoparticles of transition-metal oxides demonstrated electrochemical specific capacities near 1000 mAh g^{-1}, with 100% capacity retention for up to 100 cycles.[173] The mechanism involves the formation and decomposition of Li_2O, accompanied by, the reduction and oxidation of metal nanoparticles, respectively, following the equation below:

$$MO + yLi^+ + ye^- \leftrightarrow Li_yO + M \qquad \text{(Eq. 1-13)}$$

where M=Fe, Co, Ni, Cu, Mn, etc.

This conversion reaction allows the storage of more than two lithium ions per molecule, which offers high specific capacity and good reversibility. The enhanced electrochemical reactivity of Li_2O is attributed to the unique nanostructure consisting of uniformly dispersed nanomatric metallic particles (2-8 nm) dispersed in an amorphous Li_2O matrix (Figure 1-12), which shorts the diffusion lengths and supplies large contact areas. The major drawbacks of the application of transition metal oxide to practical

Li-ion batteries, are the large irreversible capacity loss in the first cycle and poor kinetics (that is, the rate at which lithium ions and electrons can reach the interfacial regions within the nanoparticle and react with the active domains).[49]

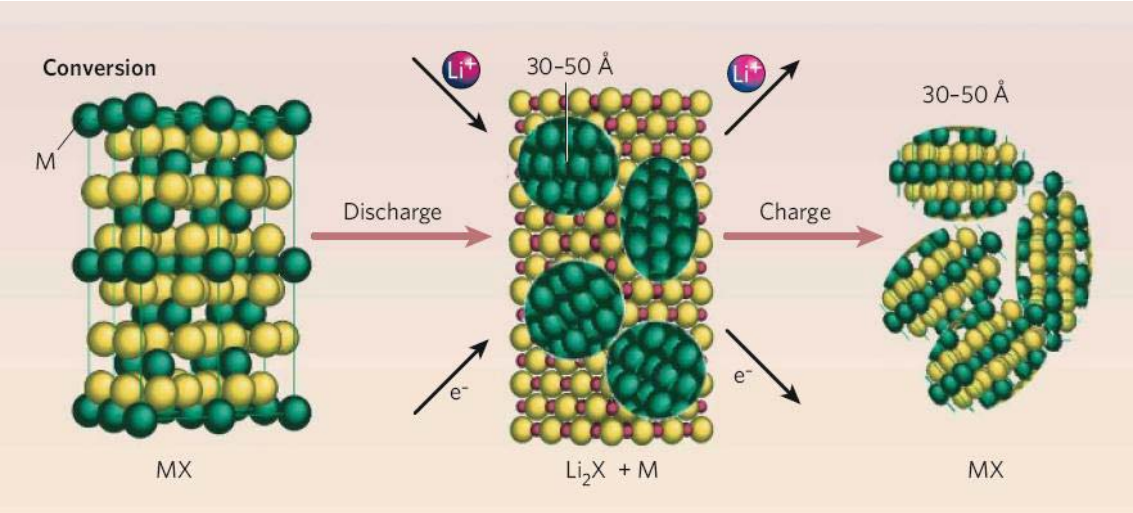

Figure 1-12 Schematic representation conversion reaction mechanism. The insertion reaction demonstrates a maximum of 1 electron transfer per transition metal (here designated M), whereas the conversion reaction can transfer 2 to 6 electrons.[1,174]

One strategy to enhance the electrochemical performance of transition metal oxide is to use nanostructure materials, such as nanowires, nanorods, nanotubes, and three-dimensional mesoporous particles.

In 2009, Liu et al. reported the synthesis of α-Fe_2O_3 nanowires by a facile hydrothermal method.[175] The SEM image shown in Figure 1-13a of the as-prepared material revealed that the prepared α-Fe_2O_3 product was uniform nanowires with the length/diameter ratio as high as 500. The TEM image shown in Figure 1-13b showed that the as-prepared nanowires have a polycrystalline structure with a width around 200 nm and a high

specific surface area of 152 m^2 g^{-1}. The initial discharge capacity of the electrode made of α-Fe_2O_3 nanowires can reach 1303 mAh g^{-1} at the rate of 0.1 C (C=1000 mA g^{-1}) and the lithium storage capacity can still maintain 456 mAh g^{-1} after 100 cycles. This good electrochemical performance is attributed to the large surface area and short pathways for lithium ion migration in nanowires. Liu et al. also reported the synthesis of α-Fe_2O_3 nanorods with diameters in the range of 60~80nm and lengths extending from 300 to 500 nm as shown in Figure 1-13c.[176] The α-Fe_2O_3 nanorod anodes exhibit a stable specific capacity of 800 mAh g^{-1}, a significantly improved electrochemical performance compared to that of commercial products in lithium ion batteries.

Chen's group reported the synthesis of a series of transition metal oxide nanotubes, such as Fe_2O_3 and Co_3O_4.[177-179] The nanotubes were synthesized by a hard template method using porous anodic aluminum oxide (AAO) as the template. The as-prepared nanotubes were a uniform size and had a tube shape structure with a large surface area as shown in Figure 1-13 d and e. It was found that the as-preparedα-Fe_2O_3 nanotubes exhibit excellent electrochemical performance with a discharge capacity of 1415 mAh g^{-1} at 100 mA g^{-1} and 20 C.

Three-dimensional mesoporous transition metal oxides have been synthesized by our group through both the hard template method and soft template method. Highly ordered mesoporous Co_3O_4, NiO and Cr_2O_3 were synthesized by a nanocasting method using mesoporous silica SBA-15 and KIT-6 as the hard templates.[180-182] The as-prepared

materials showed high specific surface area, large pore volume and periodically distributed pores. When used as anode materials for lithium storage in lithium ion batteries, mesoporous Co_3O_4 electrode materials (shown in Figure 1-13e and f) have demonstrated the high lithium storage capacity of more than 1200 mAh g^{-1} with an excellent cycle life. Mesoporous α-Fe_2O_3 was also synthesized by a soft template method. The details will be discussed in Chapter 5.

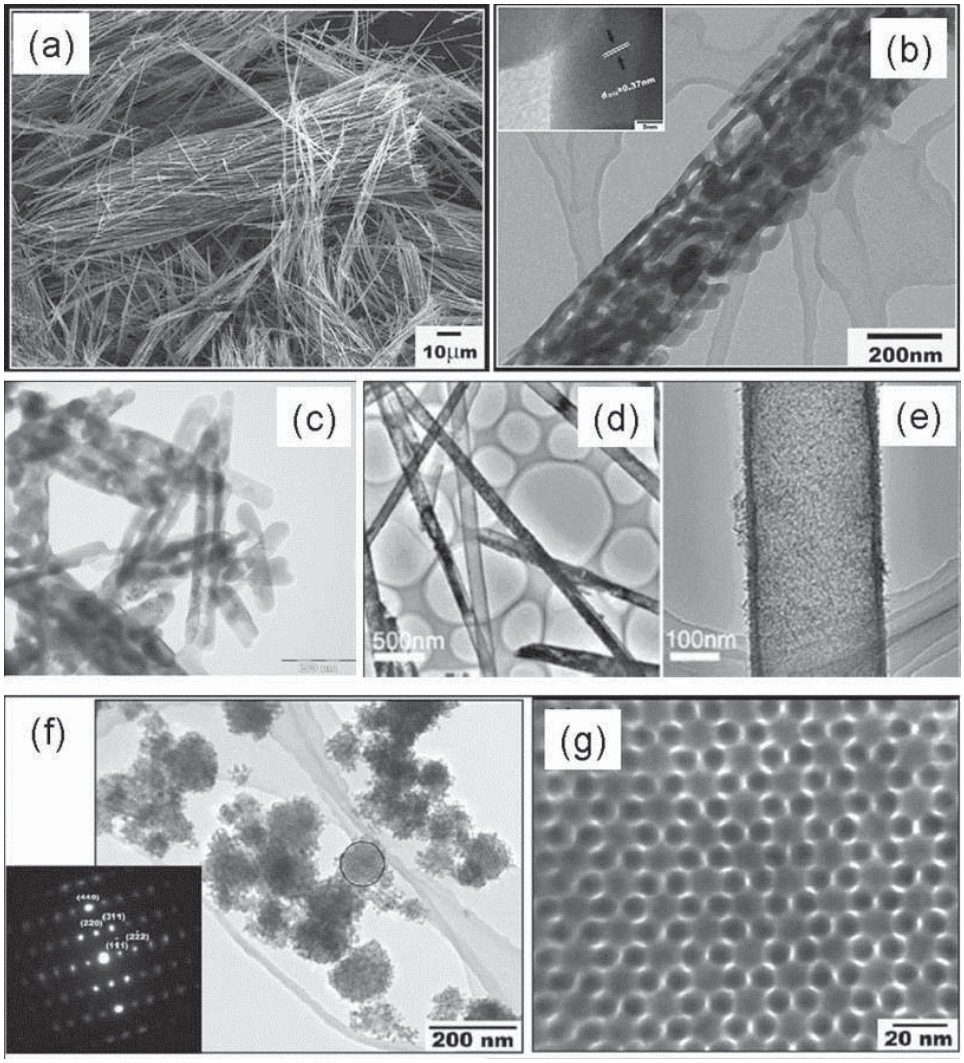

Figure 1-13 (a) SEM and (b) TEM images of Fe_2O_3 nanowires.[175] (c) TEM image of Fe_2O_3 nanorods.[176] (d) and (e) TEM images of Fe_2O_3 nanotubes.[177] (f) and (g) TEM images of highly ordered mesoporous Co_3O_4.[180]

Other strategies to enhance the electrochemical performance of transition metal oxides include using carbon coating or distribution of metal oxide nanoparticles into a porous carbon matrix.

Carbon coated Co_3O_4 was recently synthesized through solid-state pyrolysis of structurally defined organic cobalt precursors under an inert atmosphere, followed by mild thermal oxidation.[183] The Co_3O_4 nanoparticles (20 nm) obtained were covered by thin carbon layers. The initial reversible charge capacity was about 940 mAh g^{-1} at 0.2 C-rate. After 20 cycles, the reversible capacity of the carbon coated Co_3O_4 nanoparticles could still be maintained at about 940 mAh g^{-1} (almost 100 % capacity retention), whereas the reversible capacity of the pure Co_3O_4 nanoparticles decayed to around 120 mAh g^{-1}. The good cycling performance arose from the action of the carbon coating layers that can significantly increase the surface electronic conductivity of Co_3O_4 nanoparticles.

Liu et al. reported the synthesis of carbon coated magnetite (Fe_3O_4) core-shell nanorods by a hydrothermal method using Fe_2O_3 nanorods as the precursor.[184] The initial discharge capacity of the carbon coated magnetite is as high as 1126 mAh g^{-1} and the capacity remains at 394 mAh g^{-1} after 100 cycles. MnO/C core-shell nanorods were also synthesized by our group and will be discussed in Chapter 6.

Wang et al. reported the synthesis of carbon nanotube/cobalt oxide core-shell

one-dimensional nanostructures via a hydrothermal method.[185] The nanosize cobalt oxide crystals were homogeneously coated on the surface of carbon nanotubes. When applied as the anode material in lithium-ion batteries, carbon nanotube/cobalt oxide composite exhibited an initial lithium storage capacity of 1250 mAh g^{-1} and a stable capacity of 530 mAh g^{-1} over 100 cycles.

Recently, loading of transition metal oxide nanoparticles onto flexible graphene nanosheets to form three-dimensional laminate composites for use as anode materials has been intensively investigated worldwide.[153,186-188] Wang et al. prepared a Co_3O_4/graphene nanocomposite by an in-situ solution-based method under reflux conditions.[189] The prepared material consists of uniform Co_3O_4 nanoparticles (15-25 nm), which are well dispersed on the surfaces of graphene nanosheets. The prepared composite material exhibits an initial reversible lithium storage capacity of 722 mAh g^{-1} in lithium-ion batteries. This is higher than that of the pure graphene nanosheets and Co_3O_4 nanoparticles.

1.2 Lithium-Oxygen Batteries

It is well known that the energy density and power density of current lithium ion batteries cannot meet the stringent requirements of applications for EVs application.[190] They are limited mainly by the inherent low energy density of the available cathode materials and the conventional intercalation compounds.[191] Since Abraham and Jiang first reported the lithium-oxygen batteries using an organic electrolyte in 1996, this new

configuration of lithium batteries has attracted enormous attention.[192] Lithium-oxygen batteries have the highest energy density among all rechargeable battery systems; they could achieve an energy density more than 4 times higher than that of current lithium-ion batteries.[7,193-196] A lithium-oxygen battery consists of a porous oxygen-breathing electrode as the cathode and a lithium metal as the anode, as schematically shown in Figure 1-14. During the discharge process, lithium ions transport from the negative electrode to the positive electrode and react with oxygen to form Li_2O or Li_2O_2 inside the porous positive electrode. This is very different from the current lithium-ion batteries. If the oxygen comes from the atmosphere, we denote them lithium-air batteries. In order to avoid the negative effect of humidity and CO_2, most of the fundamental works was carried out in pure oxygen.

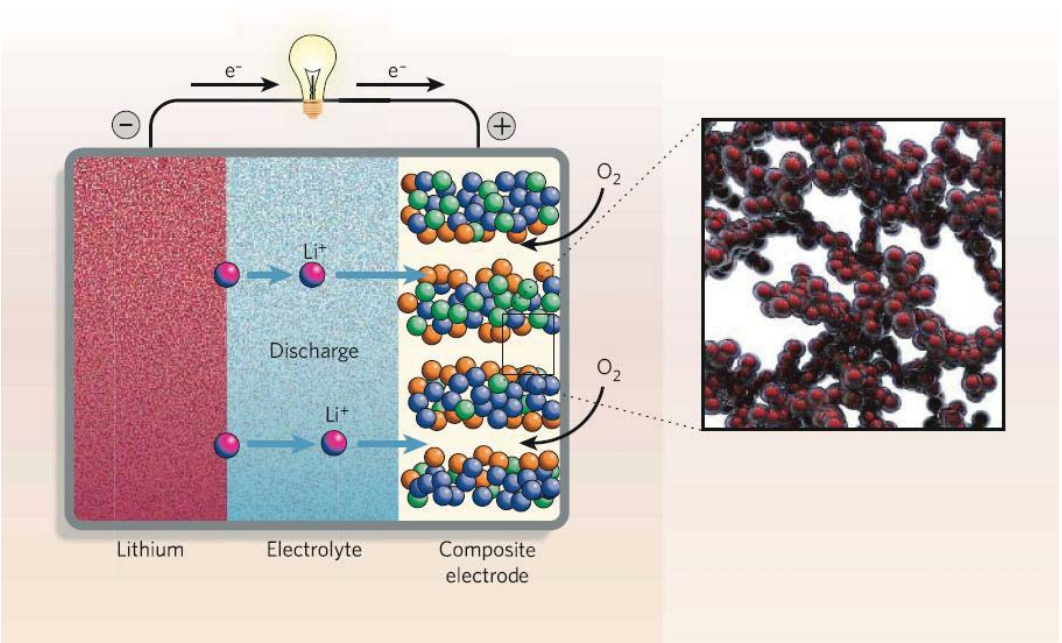

Figure 1-14 Schematic illustration of a lithium-air battery.[1]

Usually, the theoretical energy density of lithium-oxygen batteries is calculated to 11,586 Wh kg^{-1} based on the mass of lithium only. All the metal oxygen batteries gain

mass (O_2) during the discharge process, so the mass of oxygen should be included. The theoretical energy density of lithium-oxygen batteries with a non-aqueous electrolyte is 3,505 Wh kg^{-1}, based on the sum of the volume of Li at the beginning and Li_2O_2 at the end of discharge.[6] For practical applications, there are always several factors that conspire to lower the energy density. The porous cathode continues to absorb oxygen from the outside atmosphere during the discharge process, adding mass and volume to the cell. More lithium metal is required to compensate for the inefficiency of lithium metal during cycling. Furthermore, the gas diffusion channel, current collectors and packaging will also reduce the energy density. However, if we can control the reduction in energy density by a factor of 4-7, the estimated practical specific energy is in the range of ~500-900 Wh kg^{-1}, which would be sufficient to deliver a driving range of more than 550 km.[6]

Although lithium-oxygen batteries have already shown great potential for offering energy density much higher than those of current lithium-ion batteries, many fundamental questions need to be addressed to realize the practical application of lithium-oxygen batteries. Recent developments in research into lithium-oxygen batteries will be reviewed in the following section.

1.2.1 Architectures of Lithium-Oxygen Batteries

To date, four different chemical architectures of lithium-oxygen batteries, based on the types of electrolyte, have been developed worldwide, as shown in Figure 1-15. These

include a fully aprotic liquid (nonaqueous organic) electrolyte, an aqueous electrolyte, a solid state electrolyte and an aqueous/nonaqueous hybrid electrolyte. Each configuration has specific advantages and also faces scientific and engineering challenges, so that the ultimate choice for the best configuration is still an open question.

The aprotic version was first reported by Abrahan and Jiang in 1996.[192] The lithium anode is in contact with the electrolyte and forms a stable solid electrolyte interface (SEI). It is thought that, during the discharge process, insoluble Li_2O_2 (and perhaps Li_2O) is thought to form at the porous oxygen-breathing cathode via the oxygen reduction reaction (ORR). During the charge process, Li_2O_2 decomposes to release oxygen by undergoing the oxygen evolution reaction (OER).[197,198] Reactions for all solid lithium-oxygen batteries are presumed to be the same as those for the aprotic version. The presumed electrochemical reactions can be described as follows:

$$2Li + O_2 \leftrightarrow Li_2O_2 \qquad E^0=2.96 \text{ V } \textit{vs.} \text{ Li/Li}^+ \qquad \text{(Eq. 1-14)}$$

$$4Li + O_2 \rightarrow 2Li_2O \qquad E^0=2.91 \text{ V } \textit{vs.} \text{ Li/Li}^+ \qquad \text{(Eq. 1-15)}$$

The fully aqueous and hybrid electrolyte version was developed by Polyplus, Wang and Zhou.[193,199] In an aqueous electrolyte, the chemistry reactions have been identical and depend on the pH values of the electrolyte, as shown below:

$$4Li + O_2 + 2H_2O \leftrightarrow 4LiOH \qquad E^0=3.45 \text{ V vs Li/Li}^+ \quad \text{(Alkaline media)} \quad \text{(Eq. 1-16)}$$

$$4Li + O_2 + 4H^- \leftrightarrow 4Li^+ + 2H_2O \qquad E^0=3.45 \text{ V vs Li/Li}^+ \quad \text{(Alkaline media)} \quad \text{(Eq. 1-17)}$$

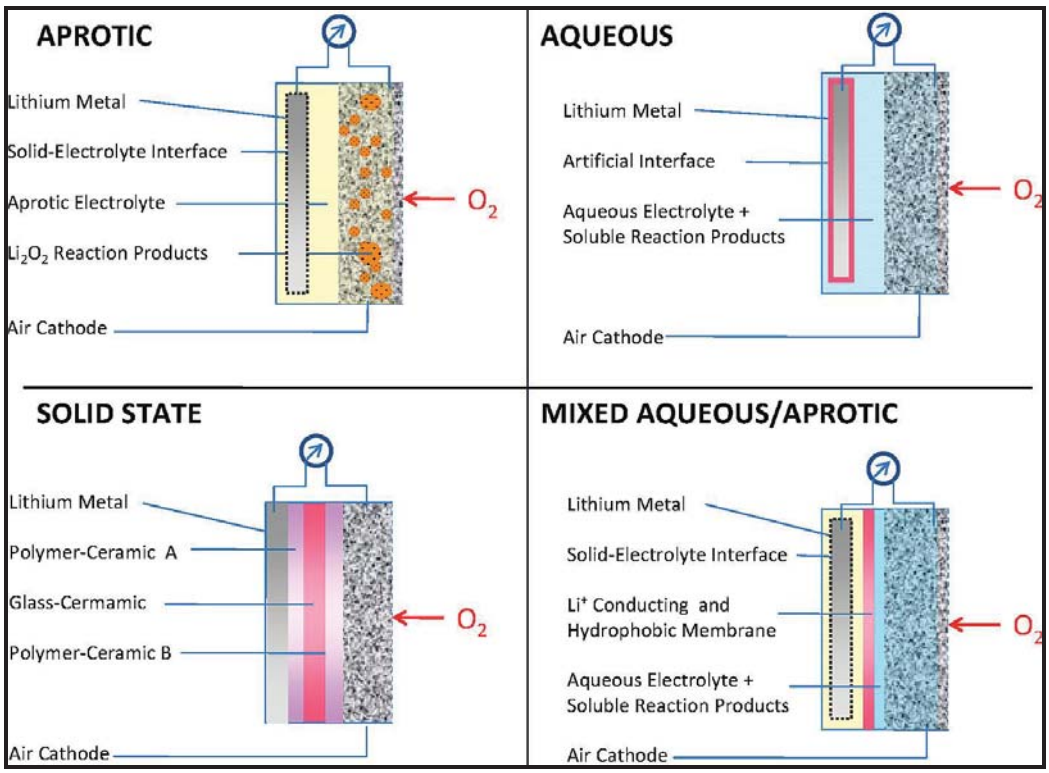

Figure 1-15. Four different architectures of lithium-oxygen/air batteries based on the types of electrolytes, which all assume the use of lithium metal as the anode.[7]

The great advantage of the aqueous or hybrid electrolyte configuration is that the discharge reaction product is soluble in the electrolyte, eliminating clogging of the cathode, volume expansion, and electrical conductivity issues. A big challenge for aqueous and hybrid electrolyte systems is the development of stable lithium-ion conducting membranes, which protect the lithium anode from reacting vigorously with water.[200]

Of the four configurations, the aprotic version has shown the most promise in terms of electrical rechargeability and this configuration has attracted the most effort worldwide to date. In this PhD work, we focus only on the lithium-oxygen batteries with a

nonaqueous (aprotic liquid) electrolyte. The actual electrode reactions and recent developments in research into rechargeable lithium-oxygen batteries with a nonaqueous electrolyte will be presented in the next three sections.

1.2.2 Electrochemical Reaction in a Nonaqueous Li^+ Electrolyte

The electrochemical reaction in rechargeable lithium-oxygen batteries with a nonaqueous electrolyte was first proposed by Bruce's group.[197] They used an in situ mass spectrometry measurement to demonstrate two essential prerequisites for the successful operation of a rechargeable lithium-oxygen battery. During the discharge process, the discharge product Li_2O_2 should be formed first on discharging in the porous oxygen breathing electrode with or without a catalyst. During the charging process, the Li_2O_2 must be decomposed to Li and O_2, with or without a catalyst. Later, Bruce's group used an in situ spectroscopic method to study the oxygen reduction reaction and oxygen evolution reaction in a non-aqueous solvent (acetonitrile solution), in the presence and absence of Li^+ ions.[201] Direct evidence has been provided that LiO_2 is an intermediate on oxygen reduction, and that it then disproportionates to Li_2O_2, during the discharge process. During the charging process, in situ spectroscopic studies reveal that Li_2O_2 decomposes to release oxygen and does not pass through LiO_2 as an intermediate. The electrochemical reactions are shown below:

Oxygen reduction reaction (ORR):

$$O_2 + e^- \rightarrow O_2^- \qquad \text{(Eq. 1-18)}$$

$$O_2^- + Li^+ \rightarrow LiO_2 \quad \text{(Eq. 1-19)}$$

$$2LiO_2 \rightarrow Li_2O_2 + O_2 \quad \text{(Eq. 1-20)}$$

Oxygen evolution reaction (OER):

$$Li_2O_2 \rightarrow O_2 + 2Li^+ + 2e^- \quad \text{(Eq. 1-21)}$$

However, the real reaction in practical lithium oxygen batteries differs from this. Most lithium-oxygen batteries use organic carbonate-based electrolytes, e.g. $LiPF_6$ in propylene carbonate, like those widely used in current lithium-ion batteries. However, such electrolytes are not stable in lithium-oxygen batteries and will decompose during the discharge process. The real redox electrochemical reactions in lithium-oxygen batteries have attracted enormous attention worldwide.[202-205] Bruce's group used Fourier transform infrared spectroscopy (FTTR) and nuclear magnetic resonance (NMR) to analyze the discharge products in the air electrode after discharge and could not detect any of the desired Li_2O_2 in the discharge products. The actual discharge products observed were $C_3H_6(OCO_2Li)_2$, Li_2CO_3, HCO_2Li, CH_3CO_2Li, CO_2, and H_2O at the cathode, due to electrolyte decomposition. The charging process of lithium-oxygen batteries involves the oxidation of $C_3H_6(OCO_2Li)_2$, Li_2CO_3, HCO_2Li, CH_3CO_2Li accompanied by CO_2 and H_2O evolution.[206] The proposed mechanisms for the charge and discharge reactions in lithium-oxygen batteries are shown in Figure 1-16. The different pathways for discharge and charge are consistent with the widely observed large charge/discharge voltage gap in lithium-oxygen batteries. The battery cycling involves repeated decomposition of the electrolyte in the discharge process and the oxidation of the decomposition products in the charge process. The capacity fading of

lithium-oxygen batteries is associated with the starvation of the electrolyte and the accumulation of the discharge products, such as Li_2CO_3, CH_3CO_2Li, HCO_2Li, in the cathode.

Later, the electrochemical reactions in ether based electrolytes in lithium-oxygen batteries were also investigated by Bruce's group.[207] They combined electrochemical measurements with powder X-ray diffraction (XRD), FTIR and NMR spectroscopy and demonstrated that ether based electrolytes are more stable than carbonate electrolyte and Li_2O_2 was detected in the discharge products. However, the ether based electrolytes still exhibited electrolyte decomposition for both the linear-chain and cyclic ethers. In our experiments, we found that oxygen can more easily diffuse through the ether based electrolyte than that in carbonate electrolyte and react with lithium metal, which will reduce the cycling stability. In this PhD work, $LiClO_4$ is used in propylene carbonate as the electrolyte for lithium-oxygen batteries. The relevant electrochemical reactions will be discussed in Chapter 7 and Chapter 8.

1.2.3 Porous Carbon Based Cathode

The oxygen-breathing cathode of lithium-oxygen batteries is usually composed of carbon, a catalyst and a polymer binder. As mentioned above, the electrochemical reactions in nonaqueous electrolyte systems are different from the aqueous electrolyte systems. The discharge products, such as Li_2O_2, Li_2O_3, etc. are insoluble in the

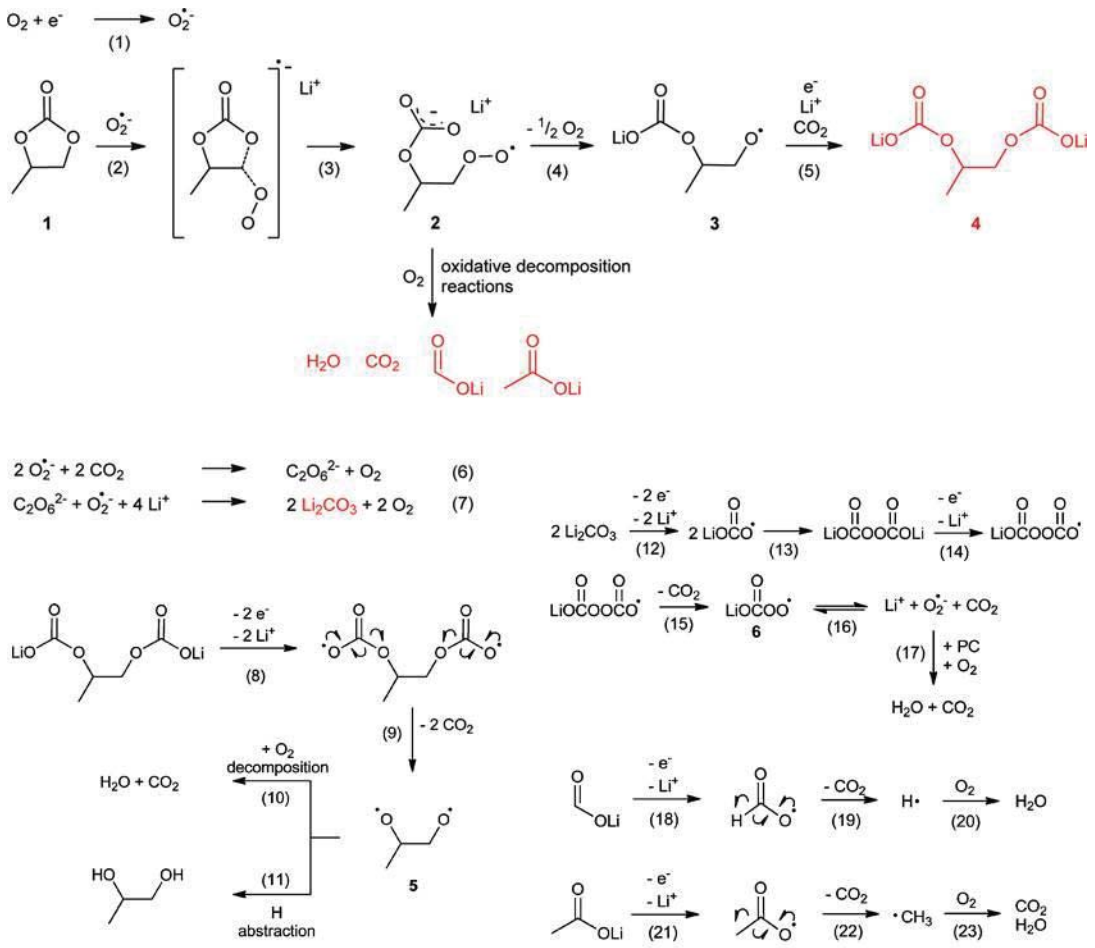

Figure 1-16 Schematic illustration of reactions. (1)~(7) Proposed reaction on discharge to explain formation of $C_3H_6(OCO_2Li)_2$, Li_2CO_3, HCO_2Li, CH_3CO_2Li, CO_2, and H_2O. (8)~(23) Proposed mechanisms of charging $C_3H_6(OCO_2Li)_2$, Li_2CO_3, HCO_2Li and CH_3CO_2Li.[206]

electrolyte. The pores of air cathodes in lithium-oxygen batteries become increasingly blocked by the discharge products during the discharge process. Impedance analysis revealing increased cell resistance and SEM observation of the discharged electrode support this finding.[198,208-210] Therefore, the real capacity of a lithium-oxygen battery cannot be calculated from the electrochemical reactions in Eq. 1-14 and 1-15. Instead, the real capacity of a lithium-oxygen battery is determined by the air cathodes, especially with respect to the pore volume available for the deposition of discharge products. The choice of carbon source is critical to the air cathode's ability to facilitate

the Li/O_2 reaction and provide enough pores to hold a maximum amount of discharge products. A variety of carbon materials with different surface areas, such as Super-p carbon black, acetylene black, Ketjenblack, mesocellular carbon foam, carbon nanotubes graphite, graphene, etc. have been investigated by several groups.[211-214] The results have demonstrated that having a carbon source with a high surface area does not mean the electrode will have a high discharge capacity. The most important factor to achieve high electrochemical performance is the pore volume rather than the surface area. If the pore size is too small (e.g. micropores), the pore entrance will be easily blocked by insoluble discharge products at the beginning of the discharge process. Consequently, the inner surface of those pores will not be accessed by oxygen and electrolyte, making them unavailable for the electrochemical reaction and unable to contribute to the discharge capacity.[215]

To optimize the air cathode, the porous electrode should contained micrometer-sized open pores for rapid oxygen diffusion and substantial mesopores (2-50 nm) to hold the maximum amount of discharge products. Recently Xiao et al. reported a novel air electrode that can deliver an exceptionally high discharge capacity of 15000 mAh g^{-1} in lithium-oxygen batteries.[216] It consisted of an unusual hierarchical arrangement of functionalized graphene sheets without any other catalyst (as shown in Figure 1-17). This excellent performance is attributed to the unique porous structure of the air cathode: microporous channels facilitate rapid O_2 diffusion and the highly connected nanoscale pores provide large surface areas for oxygen reduction reactions. Furthermore, Xiao et

al. discovered that defects and functional groups on graphene nanosheets favor the formation of isolated nanosized Li_2O_2 particles and help prevent electrode passivation. However, in this study, only the discharge performance of the graphene electrode were studied. The charge-discharge performance and cycling stability of graphene electrodes in lithium-oxygen batteries is discussed in Chapter 7.

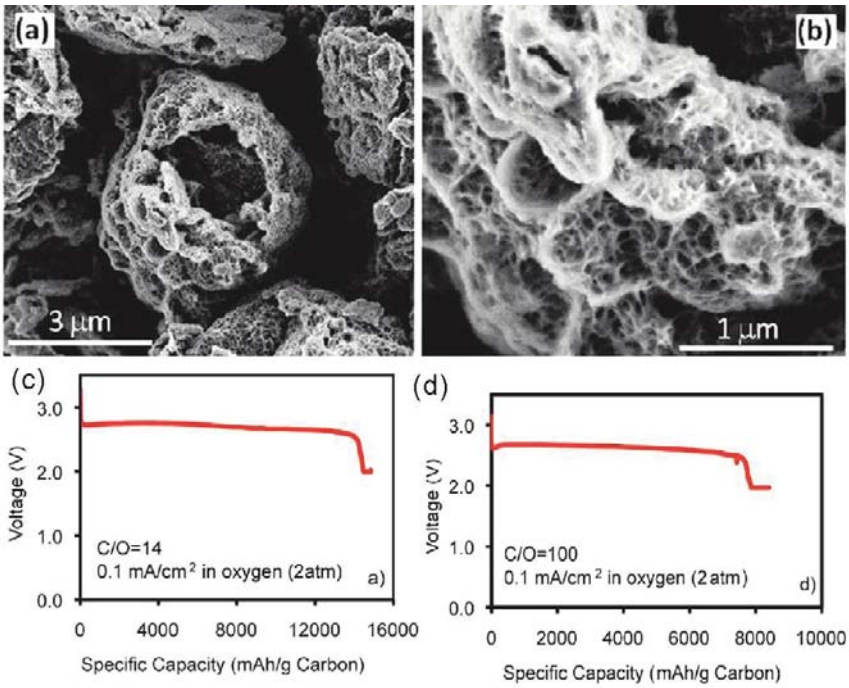

Figure 1-17 (a, b) SEM images of as-prepared functionalized graphene sheets (FGS) (C/O = 14) air electrodes at different magnifications. (c, d) Discharge curves of lithium-oxygen batteries using FGS as the air electrodes (P_{O2} = 2 atm).[216]

Another strategy to increase the electrochemical performance of lithium oxygen batteries is to tail the electrode structure to form a novel three-dimensional electrode. Mitchell et al. reported that an all-carbon-nanofiber electrode can yield high gravimetric energies up to 2500 Wh $kg_{discharge}^{-1}$, which is 4 times greater than the current lithium ion batteries (e.g. LiCoO2 600 Wh $kg_{electrode}^{-1}$).[217] The three-dimensional electrode was

synthesized by growing the hollow carbon nanofibers directly on a ceramic porous substrate. The electrode morphologies at different depth of discharge are shown in Figure 1-18. The discharge product, Li_2O_2 particles, grew on the sidewalls of the aligned carbon fibers with a toroidal structure. The high electrochemical performance achieved in Mitchell's study can be attributed to low carbon packing in the grown carbon-fiber electrodes and highly efficient utilization of the available voids for the accommodation of the discharge products.

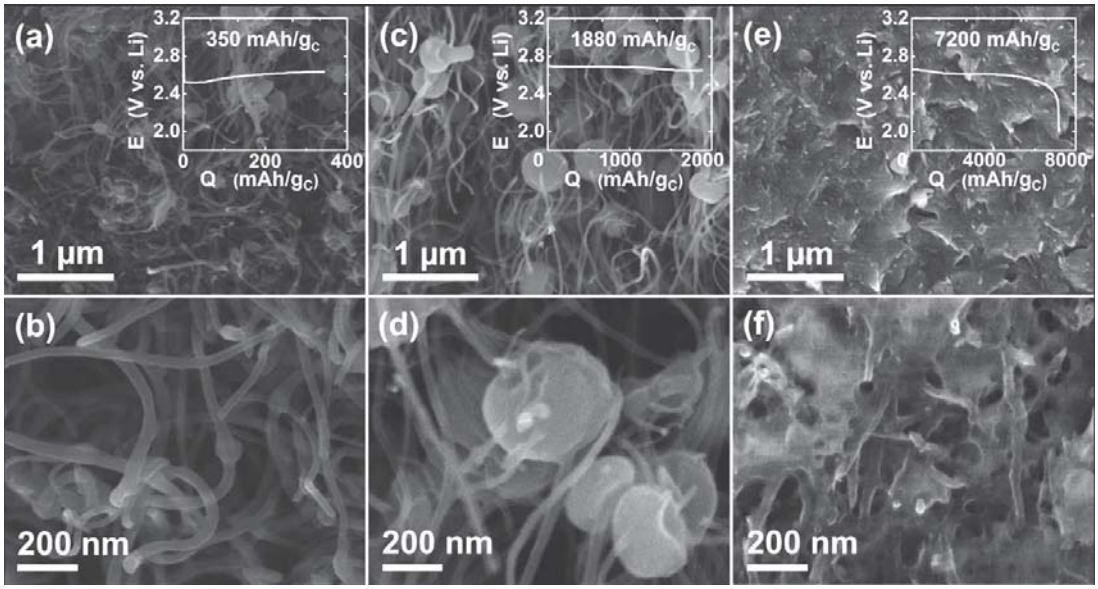

Figure 1-18 Evolution of Li_2O_x discharge product morphology at different depth of discharge.[217]

1.2.4 Catalysts for Lithium-Oxygen Batteries

Although it has been demonstrated that lithium-oxygen batteries with nonaqueous electrolytes can be cycled over 100 cycles,[218] the large charge-discharge voltage gap significantly reduces the electrical efficiency for one discharge-charge cycle. Recently, several reports demonstrated that electrocatalysts are able to reduce the

charge-discharge over-potentials and increase the round-trip efficiency.

Debart et al. explored the use of several catalysts for lithium-oxygen batteries with nonaqueous electrolyte. These catalysts have already been widely investigated as electrocatalysts for O_2 electrochemistry in aqueous media and they included Pt, $La_{0.8}Sr_{0.2}MnO_3$, Fe_2O_3, Fe_3O_4, NiO, CuO, $CoFe_2O_4$.[219] The preliminary study demonstrated that Pt, $La_{0.8}Sr_{0.2}MnO_3$, Fe_2O_3 and NiO do not perform well as catalysts for lithium-oxygen batteries with nonaqueous electrolytes. However, Fe_3O_4, CuO and $CoFe_2O_4$ gave much improved capacity retention. Co_3O_4 gave the best performance, exhibiting reduced charge potential, the highest discharge capacity and the best cycling performance. Later, Debart et al. examined different forms of manganese oxides for their use as the catalysts in lithium-oxygen batteries. These included EMD, commercial Mn_3O_4, bulk Mn_2O_3, bulk α, β, λ, γ-MnO_2, α-MnO_2 nanowires and β-MnO_2 nanowires.[191] The air cathode with α-MnO_2 as the catalyst showed the highest capacity (about 3000 mAh g_{carbon}^{-1}) and the best capacity retention compared with air cathodes using other MnO_2 polymorphs. Debart et al. concluded that the enhanced performance of the α-MnO_2 nanowires was due to the crystal structure and the nanowire structure with its high surface area. They also discovered that the capacity retention could be improved by avoiding a high level depth of discharge.

Lu et al. studied Pt, Au, and Pt-Au alloy nanoparticles loaded onto Vulcan carbon (XC-72) as electrocatalysts for rechargeable lithium-oxygen batteries.[220-224] They found

that Au showed very high activity for the oxygen reduction reaction (ORR) and Pt/C exhibited remarkable activity for the oxygen evolution reaction (OER). Pt-Au/C can act as a bifunctional catalyst for lithium-oxygen batteries. This novel catalyst was shown to a higher discharge voltage and a much lower charge voltage than that of pure carbon, as showed in Figure 1-19. Very recently, Lu et al. reported the intrinsic ORR activity of polycrystalline palladium, platinum, ruthenium, gold, and glassy carbon surfaces in a nonaqueous electrolyte.[225] They found that the ORR activities on the surface of these polycrystallines correlate to the oxygen adsorption energy and the order of ORR activity is Pd > Pt > Ru $\approx$ Au > GC on bulk surfaces.

Thapa et al pointed out that the carbon materials in the air cathode are not stable and could be oxidized to CO_2. [226] To study the activity of various metals or metal oxides as catalysts for lithium-oxygen batteries, they used a carbon free air cathode in their electrochemical measurements and found that a Pd/MnO_2 composite showed the highest activity for the ORR and OER. Although the Pd/MnO_2 air electrode without a carbon binder exhibited low discharge capacity, the round trip efficiency of the electrode increased from 60 to 89 %. Later, Thapa et al. reported air electrodes using mesoporous α-MnO_2/Pd or mesoporous β-MnO_2/Pd with a high surface area can significantly increase the discharge capacities compare with the air electrode using Pd/MnO_2.[227,228]

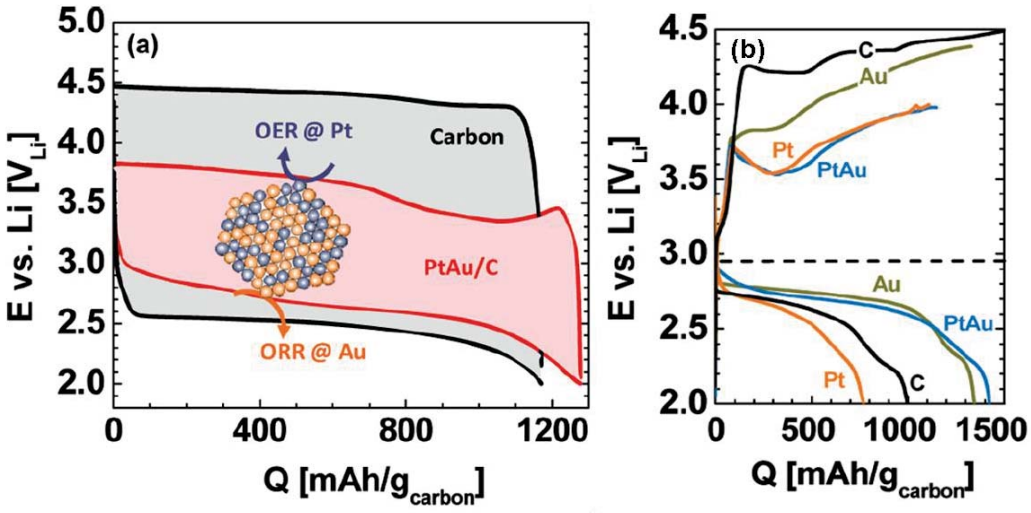

Figure 1-19 (a) Lithium-oxygen cell discharge-charge profiles of carbon and Pt-Au/C in the third cycle at 0.04 mA $cm^2_{electrode}$. (b) First discharge-charge profiles of carbon at 85 mA g^{-1}_{carbon} and of Au/C, Pt/C, and PtAu/C at 100 mA g^{-1}_{carbon}.[221]

Recently, a novel free-standing Co_3O_4@Ni electrode has been reported by Cui et al..[229] The electrode was synthesized by simple chemical deposition of a Co_3O_4 catalyst on a Ni foam current collector without any additional carbon or binder. The free-standing air cathode exhibited much higher specific capacity and improved cycle efficiency than the conventional carbon-supported Co_3O_4/carbon/binder electrode. It showed a discharge voltage of around 2.95 V and a charge voltage of around 3.44 V with the highest round trip efficiency (about 85.7 %) reported to date.

Lithium-oxygen (air) batteries have shown great potential for offering much higher energy density than that of current lithium-ion batteries. Rechargeable lithium-oxygen batteries with a nonaqueous electrolyte have attracted the most attention because of their high energy density and rechargeability. However, lots of fundamental research is needed to address the current challenges before the realization of practical

lithium-oxygen batteries. Promising ways of improving the electrochemical performance of lithium-oxygen batteries include optimization of the pore structures of the air cathode and combination with a nanostructure catalyst.

1.3 Summary

To further increase the energy density and power density of current lithium-ion batteries, the biggest barriers are the development of electrode material with high capacity and high rate performance. From the above literature review, nanotechnology can greatly enhance the electrochemical performance of the current developed electrode materials. $LiFePO_4$ was chosen and studies as the cathode material for lithium-ion batteries in this doctoral work. Nanostructure $LiFePO_4$ nanoplates/graphene composite and porous $LiFePO_4$/C microspheres were investigated in Chapter 3 and Chapter 4, respectively. Furthermore, two nanostructured transition metal oxides, mesoporous α-Fe_2O_3 and MnO/C core-shell nanorods, were studied in Chapter 5 and Chapter 6, respectively. For the future commercialization of lithium-oxygen batteries, we must improve the cycling life and the charge-discharge efficiency of lithium-oxygen batteries to catch up with the current lithium-ion batteries. The electrochemical performances of lithium-oxygen batteries are mainly depended on the cathode performance. In this doctoral work, graphene and mesoporous CoO/CMK-3 nanocomposite were investigated as high performance cathode catalyst for lithium-oxygen batteries in Chapter 7 and Chapter 8, respectively.

CHAPTER 2 EXPERIMENTAL METHODS

2.1 Overview

The overall experimental procedures for designing nanostructure materials are shown in Figure 2-1. This research work mainly consists of three steps: (1) the preparation of nanostructure materials; (2) the characterization of as-prepared materials; (3) testing of the electrochemical performances of the as-prepared nanostructure materials for lithium-ion batteries or lithium-oxygen batteries — after galvanostatic charge-discharge cycling, the electrodes for the lithium-ion batteries or lithium-oxygen batteries were analyzed by XRD, FT-IR and SEM.

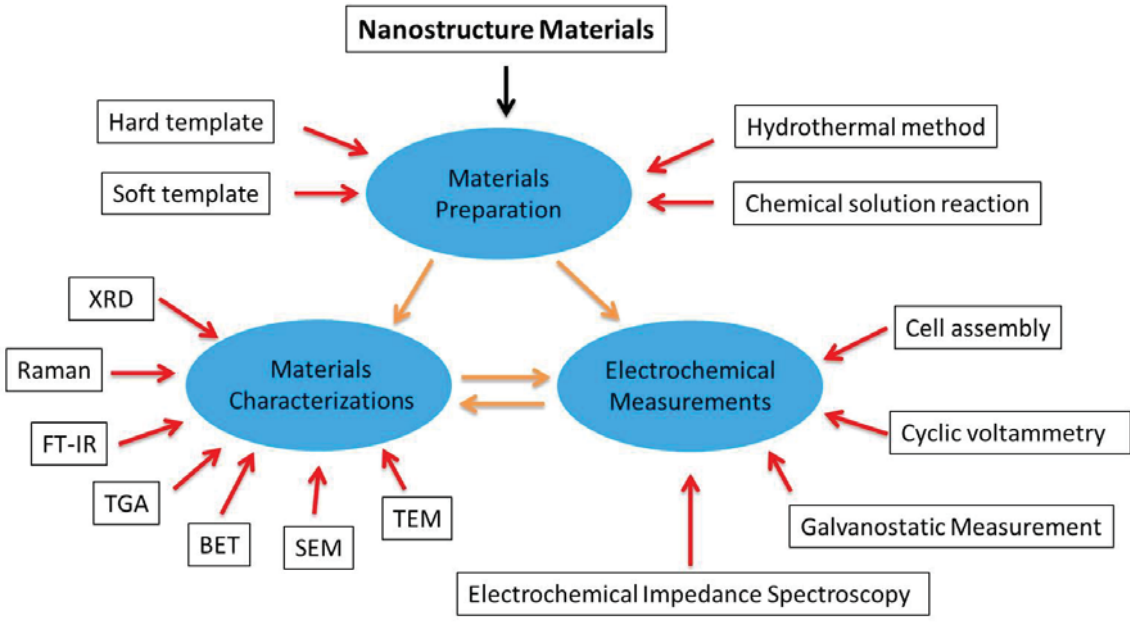

Figure 2-1 Framework of the overall procedures of the experiments.

2.2 Materials Preparation

In this thesis, several methods were used to synthesize nanostructure materials for lithium-ion batteries and lithium-oxygen batteries. These methods include: (1) hydrothermal method; (2) chemical solution reaction; (3) hard template method and (4) soft template method.

2.2.1 Hydrothermal Method

Hydrothermal synthesis can be defined as a method of synthesis of single crystals that depends on the solubility of minerals in hot water under high pressure. The experimental reaction must be take place in an autoclave. The hydrothermal autoclave used in this doctoral work is made of stainless steel and the inside contains a polytetrafluoroethylene (PTFE) liner with 30 ml capacity as shown in Figure 2-2. The reaction temperature can reach up to 220 °C.

This technique is particularly suitable for the growth of large good-quality crystals while maintaining good control over their composition. It is a current, widely used, method for the synthesis of nanostructure materials. Several synthesis conditions can affect the composition, morphology and crystal structure of the products. These include the concentration of the precursors, the volume of the solvent, temperature, the use of a surfactant and the use of a solvent other than water. In this doctoral work, a hydrothermal method was used to synthesize $LiFePO_4$ nanoplates (Chapter 3), porous $LiFePO_4$ microspheres (Chapter 4), MnO_2 nanowires (Chapter 6) and SBA-15 silica

template (Chapter 8).

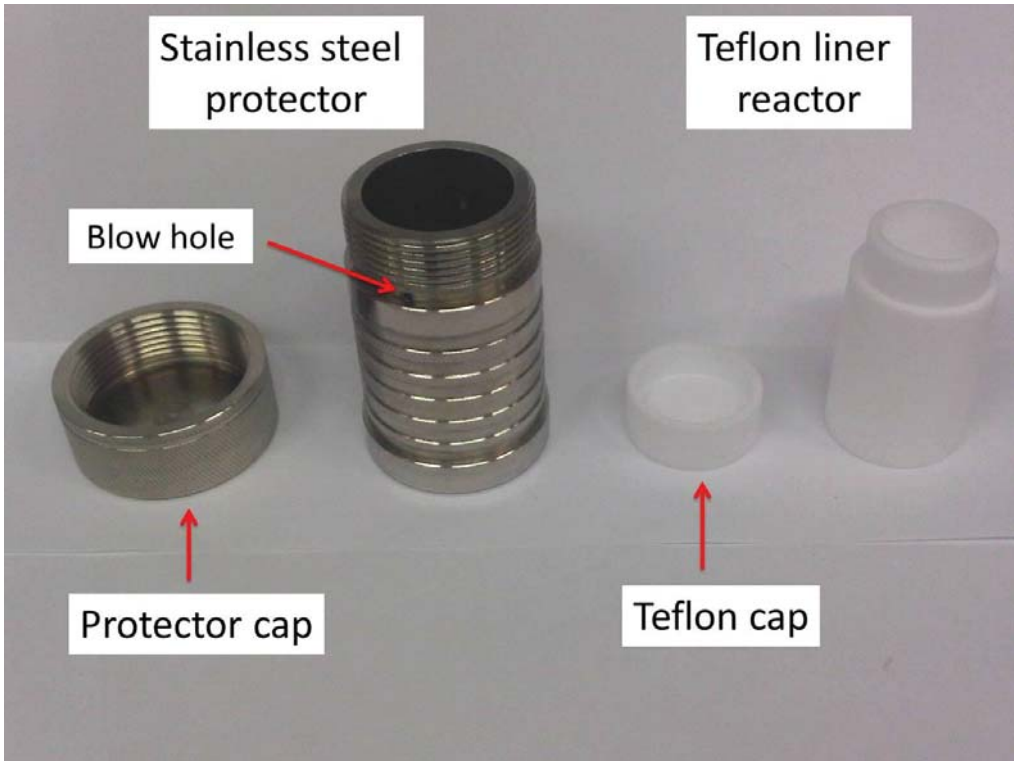

Figure 2-2 Photograph of an autoclave used in this doctoral work.

2.2.2 Chemical Redox Reaction

A chemical redox reaction was used to synthesize of graphene nanosheets. A typical synthesis method is described as follows. Graphene oxide was derived from the modified Hummers method.[148] Graphite powder (1 g) and sodium nitrate (0.5 g) were poured into 70 ml concentrated H_2SO_4 (under an ice bath). Then 3 g $KMnO_4$ was gradually added. The mixture was stirred for 2 h and then diluted with de-ionised (DI) water. After that, 5% H_2O_2 was added into the solution until the colour of the mixture changed to brilliant yellow. The as-obtained graphite oxide was re-dispersed in DI water

and then exfoliated by ultrasonication using a Brandson Digital Sonifer (S450D, 40 % amplitude) to generate a suspension of graphene oxide nanosheets. The graphene oxide suspension obtained was reduced by hydrazine hydrate at 90 °C for 2-3h to yield a graphene sheets suspension.

2.2.3 Soft Template Method

The template method has been widely used to synthesize nanostructure materials.[179] Various lithium storage materials can be obtained through the template method, as we described in Chapter 1. For example, one-dimensional nanowires/nanotubes, two-dimensional films/nanoplates, and three dimensional porous structures have been obtained by using different types of templates and have been shown to significantly enhance electrochemical performance compared with their bulk forms. The overall synthesis process generally included three steps: (1) combine precursors with templates by impregnation or incorporation; (2) form solid species through reaction, nucleation and growth; and (3) removal the template by thermal treatment or chemical dissolution to get the final products.

Template methods are usually classified into hard template methods and soft template methods. A soft template method usually uses organic surfactants, polymers, and even biological viruses as the soft templates, these being relatively flexible in shape. Under certain conditions, these materials are assembled into aggregating entities such as micelle-vesicle aggregates or liquid crystal phases, which restrict and direct the growth

of guest structures. Spherelike, wirelike or porous materials can be obtained after the removal of the template. The soft template synthesis strategies are illustrated in Figure 2-3. In this doctoral work, mesoporous α-Fe_2O_3 (Chapter 5) and silica template SBA-15 (Chapter 8) were synthesized through a soft template method.

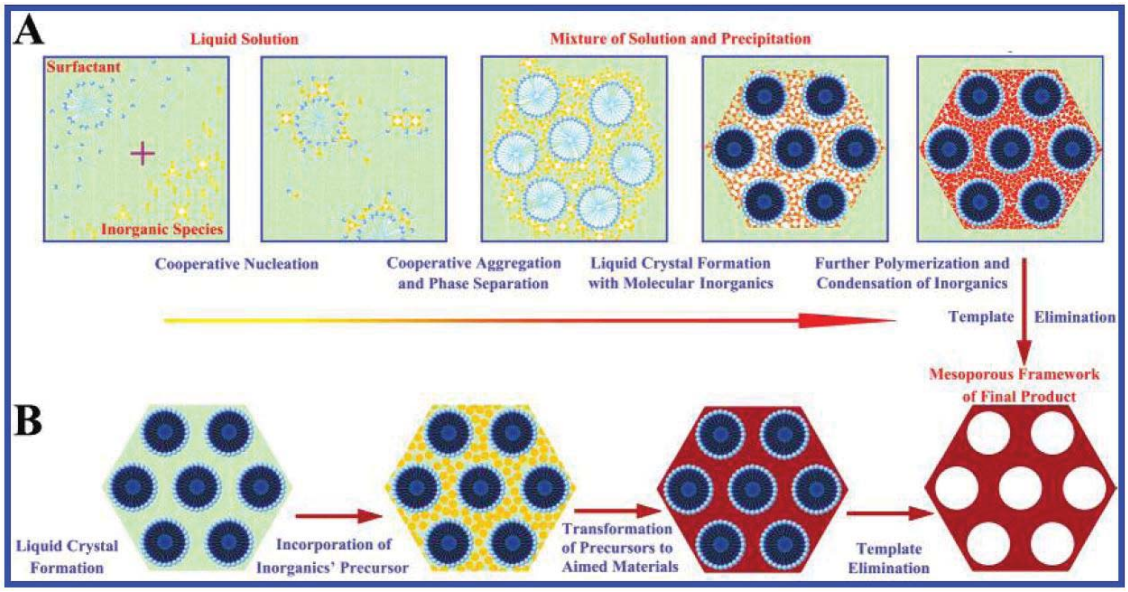

Figure 2-3 Two synthetic strategies of mesoporous materials through soft template method: (A) cooperative self-assembly; (B) "true" liquid-crystal templating process.[230]

2.2.4 Hard Template Method

A hard template method usually uses a template with a well-confined void in the form of channels, pores, or connected hollow spaces (e.g. anodic aluminum oxide (AAO) membranes or mesoporous silica). The connectivity of the pores or channels can strongly influence the structures of the final products. Many inorganic materials can grow inside the pores of the templates and negatively replicate the porous networks.

In this doctoral work, the mesoporous carbon CMK-3 was synthesized by a hard template method through a nanocasting pathway. Two-dimensional hexagonal mesoporous silica SBA-15 was used as the hard template. First, the precursor (e.g. sucrose) was infiltrated into the mesoporous template. Then, the sucrose was converted to carbon by thermal treatment in an inert atmosphere. The final mesoporous carbon was obtained after the removal of the silica template by etching with HF or NaOH. The schematic illustration of the synthesis process of mesoporous carbon CMK-3 is shown in Figure 2-4. More synthesis details are described in Chapter 8.

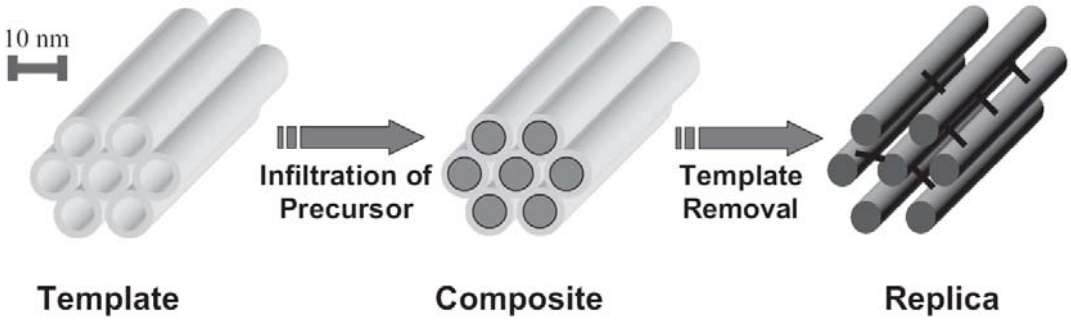

Figure 2-4 Schematic illustration of the synthesis processes of mesoporous carbon CMK-3.[231]

2.3 Structural and Physical Characterization Method

2.3.1 X-ray Diffraction (XRD)

X-ray diffraction (XRD) is a non-destructive and versatile technique that reveals detailed information about the chemical composition and crystallographic structure of a wide range of materials. The sample can be reused for other tests after XRD measurement. Each crystal has a unique, characteristic X-ray diffraction pattern based on Bragg's law (Eq. 2-1) and this can be used to identify the crystal structure of

materials. A schematic drawing of the theory of Bragg's law is shown in Figure 2-5.

$$n\lambda = 2d \sin\theta \qquad \text{(Eq. 2-1)}$$

where n is any integer, λ is the wavelength of the incident X-ray beam, d is the distance between atomic layers in a crystal and θ is the incident angle.

The crystal size *d* of polycrystalline particles can be obtained from the broadening of the peaks according to the Scherrer equation:

$$d = k\lambda / \beta\cos\theta \qquad \text{(Eq. 2-2)}$$

where *k* is the shape factor of the average crystallite (normally assigned a value of 0.89), λ is the wavelength of the incident X-ray beam, β is the half-peak width and θ is the incident angle.

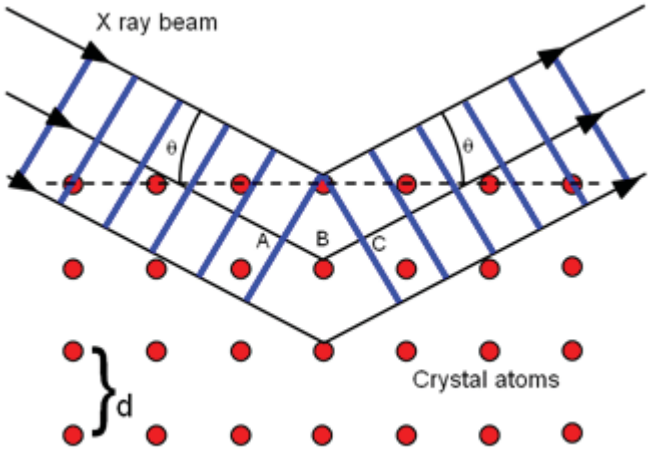

Figure 2-5 Schematic drawing of theory of Bragg's law.[173]

The XRD instruments used in this doctoral work were GBC MMA and Siemens D5000, with a monochromatized Cu Kα radiation (λ=0.15406 nm) at a scan rate of 1° min^{-1} and

step size of 0.02 °.

2.3.2 Raman Spectroscopy

Raman spectroscopy is a spectroscopic technique used to study vibrational, rotational, and other low-frequency modes in a system.[232] It relies on inelastic scattering, or Raman scattering, of monochromatic light, such as a laser. The laser light interacts with molecular vibrations, phonons or other excitations in the system, resulting in the energy of the laser photons being shifted up or down. The shift in energy gives information about the vibrational modes in the system. Figure 2-6 illustrated the concepts of a simplified energy diagram. In this doctoral work, the structure information of the as-prepared materials was obtained by using a JOBIN Yvon Horiba Confocal Mico Raman spectrometer (HR 800) with 632.8 nm diode laser excitation on a 300 lines/mm grating at room temperature.

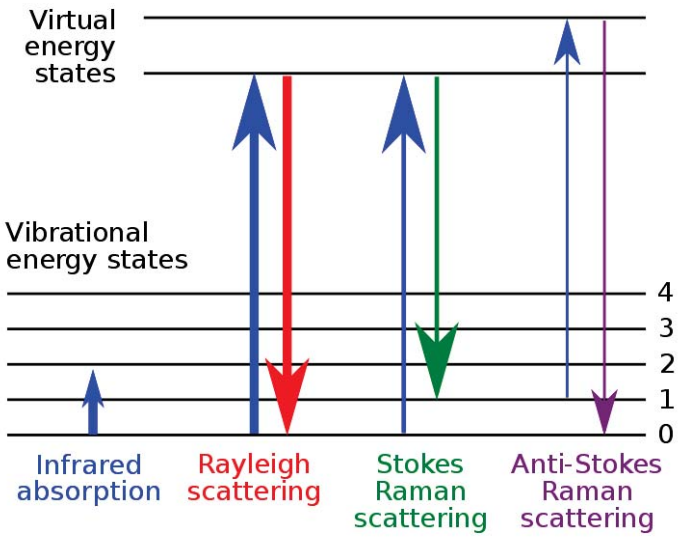

Figure 2-6 Energy diagram illustrating the concept of Raman spectroscopy.[233]

2.3.3 Fourier Transform Infrared (FT-IR) Spectroscopy

Fourier transform infrared spectroscopy (FTIR) is a technique used to obtain an infrared spectrum of absorption of a solid, liquid or gas. An FTIR spectrometer simultaneously collects spectral data in a wide spectral range. This confers a significant advantage over a dispersive spectrometer that measures intensity over a narrow range of wavelengths at a time. FT-IR spectra produced with Nicolet Magna 6700 FT-IR spectrometer was used to analyze the discharge products in the air cathode of lithium-oxygen batteries.

2.3.4 Brunauer Emmett Teller (BET)

BET method, first proposed by Stephen Brunauer, Paul Hugh Emmett and Edward Teller, is an important technique for the measurement of the specific surface area of a variety of solid materials, which was.[234] The initial concept of the theory was based on the Langmuir theory for monolayer molecular adsorption and later it was extended to multilayer adsorption. The BET equation is expressed as follows:

$$\frac{1}{\upsilon[\left(\frac{p_0}{p}\right)-1]}=\frac{c-1}{\upsilon_m c}\left(\frac{p}{p_0}\right)+\frac{1}{\upsilon_m c} \qquad \text{(Eq. 2-3)}$$

Where P and P_0 are the equilibrium and the saturation pressure of adsorbates at the temperature of adsorption, υ is the adsorbed gas quantity, and υ_m is the monolayer adsorbed gas quantity and c is the BET constant, which is expressed as follow:

$$C=\exp(\frac{E_1-E_L}{RT}) \qquad \text{(Eq. 2-4)}$$

Where E_1 is the heat of adsorption for the first layer and E_L is the heat adsorption for the second and higher layers.

A total BET surface area S_{total} and a specific BET surface area S can be calculated by the following equations:

$$S_{BET,\ total} = \frac{(\upsilon_m N_s)}{V} \quad \text{(Eq. 2-5)}$$

$$S_{BET} = \frac{S_{total}}{a} \quad \text{(Eq. 2-6)}$$

Where N is Avogadro's number, s is adsorption cross section of the adsorbing species, V is molar volume of adsorbate gas and a is the mass of adsorbent.

In this work, nitrogen adsorption/desorption was applied by using a Quadrasorb SI analyzer at 77 K in liquid nitrogen. The BET surface area was calculated using the experimental points at a relative pressure of P/P_0 = 0.05-0.25. The pore size distribution was derived from the adsorption or desorption branch using the Barrett-Joyner-Halenda (BJH) method. The total pore volume was calculated by the nitrogen amount adsorbed at a relative pressure of (P/P_0) 0.99.

2.3.5 Thermogravimetric Analysis (TGA)

Thermogravimetric analysis or thermal gravimetric analysis (TGA) is a type of testing

performed on samples that determines changes in weight in relation to a temperature program in a controlled atmosphere. Such analysis relies on a high degree of precision in three measurements: weight, temperature, and temperature change. In this work, the TGA was used to determine the carbon content of in the carbon composite materials. The TGA instrument used here was Simultaneous TG-DTA (SDT 2960) with a platinum plate as the sample holder. The temperature can increase up to 1000 °C in air or N_2 atmosphere with a speed of 5-10 C min^{-1}.

2.3.6 Ultraviolet-Visible Spectroscopy

Ultraviolet–visible (UV-vis) spectroscopy refers to absorption spectroscopy or reflectance spectroscopy in the ultraviolet-visible spectral region. In this work, the band gap energy of the as-prepared mesoporous α-Fe_2O_3 was calculated via ultraviolet-visible (UV-vis) spectroscopy on a Shimadzu UV-1700 spectrophotometer.

2.3.7 Scanning Electron Microscopy (SEM)

The scanning electron microscope (SEM) is a type of electron microscope that images a sample by scanning it with a high-energy beam of electrons in a raster scan pattern. The electrons interact with the atoms that make up the sample producing signals that contain information about the sample's surface topography, composition, and other properties such as electrical conductivity. The morphology of as-prepared materials and electrodes before and after cycling were observed by field emission SEM (Zeiss Supra 55VP) in this work. An accelerating voltage of 5–20 kV was used with 10–30 mm aperture and

images were obtained using an in-lens secondary detector. A thin layer of carbon was deposited on the surface of the materials if the conductivity of the materials was low.

2.3.8 Transmission Electron Microscopy (TEM)

Transmission electron microscopy (TEM) is a microscopy technique that can be used to observe morphology, crystal structure and electronic structure of a wide range of materials. Transmission electron microscopies can produce good images at a significantly higher resolution than light microscopes, owing to the small de Broglie wavelength of electrons. A beam of electrons is transmitted through an ultra-thin specimen, interacting with the specimen as it passes through. An image can be formed from the interaction of the electrons transmitted through the specimen; the image is magnified and focused onto an imaging device, (e.g. a fluorescent screen, layer of photographic film), or detected by a sensor such as a CCD camera. Selected area electron diffraction (SAED) is a crystallographic experimental technique that can be performed inside a TEM. Chemical analysis of CoO/CMK-3 nanocomposite was performed using an energy dispersive X-ray spectroscopy (EDX) system interfaced to the TEM. The TEM model used in this work was JEOL 2011 with a normal operation accelerating voltage of 2000 kV. Samples were prepared by loading the as-prepared materials onto a holey carbon support film on a copper grid.

2.4 Electrode Preparation and Cell Assembly

2.4.1 Lithium-Ion Batteries

The electrodes for lithium-ion batteries tests were fabricated by mixing the as-prepared materials with 10-40 wt% carbon black and 10 wt% polyvinylidene fluoride (PVDF) in N-methyl-2-pyrrolidone (NMP). The slurry was uniformly pasted onto Al foil (for cathode) or Cu foil (for anode) by a doctor blade and dried in an oven at 80-100 °C overnight under vacuum. Electrodes prepared in this way were then pressed under 200 kg cm^{-2} and kept in an argon filled glove box. For testing the electrochemical properties of the as-prepared electrodes, coin-type cells (CR2032) were used. The cells contained the as-prepared electrode as the working electrode, lithium foil as the counter and reference electrode, a porous polypropylene (Celgard 2300) as the separator, and 1M $LiPF_6$ in a mixed aprotic liquid as the electrolyte. A schematic diagram of the configuration of the coin-type cell is shown in Figure 2-7. Two kinds of electrolyte solutions purchased from Zhangjiagang Guotai-Huarong New Chemical Materials Co., Ltd were used in this study. LB301 is 1M $LiPF_6$ in a 1:1 mixture of ethylene carbonate (EC) and dimethyl carbonate (DMC). LB303 is 1M LiPF6 in a 1:1:1 mixture of ethylene carbonate (EC), diethyl carbonate carbonate (DEC) and dimethyl carbonate (DMC). The cells were assembled in an argon filled glove box (Unilab, Mbraun, Germany) with O_2 and H_2O levels less than 0.1 ppm.

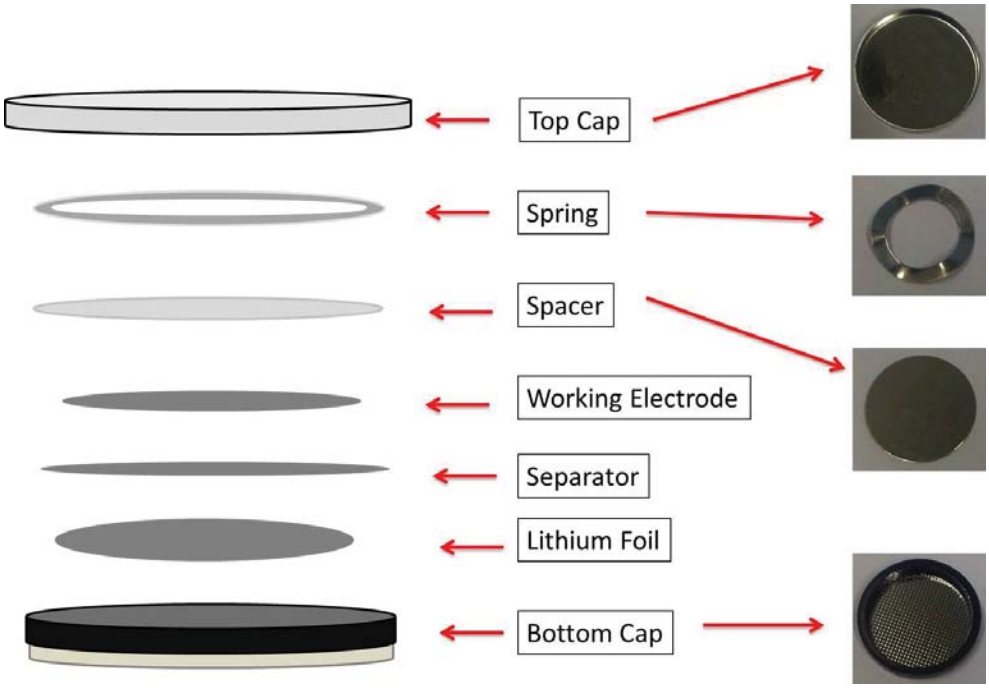

Figure 2-7 Schematic diagram of the coin type cell configuration.

2.4.2 Lithium-Oxygen Batteries

The air cathode for lithium-oxygen batteries was fabricated as follows: the catalyst mash was prepared by mixing the as-prepared materials (90 wt%) with poly(tetrafluoroethylene) (PTFE) (10 wt%) in isopropanol with continuous stirring. The mixture was then pressed onto the stainless steel mesh to form the air cathode. The cathode film was punched into discs with a diameter of 14 mm and dried at 80°C in a vacuum oven for 12 h and then kept in the glove box. The typical loading of the air electrode is about 2 mg cm^{-2}. A Swagelog type cell with an air hole (0.785 cm^2) on the cathode side was used to investigate the electrochemical performance. A schematic diagram of the configuration of the lithium-oxygen battery is shown in Figure 2-8. The cell was assembled in an Ar filled glove box (UniLab, Mbraun, Germany) with water

and oxygen level less than 0.1 ppm. The as-prepared air cathode was used as the working electrode and a lithium foil was used as the counter and reference electrode. The electrodes were separated by a glass microfiber filter (No. 1825-257, Whatman). The electrolyte was 1 M $LiClO_4$ (>99.99%, Aldrich) in propylene carbonate (PC, Sigma-aldrich). The cell was gas-tight except for the stainless steel mesh window that exposed the porous cathode film to the oxygen atmosphere. All experiments were tested in 1 atm dry oxygen atmosphere to avoid any negative effects of humidity and CO_2.

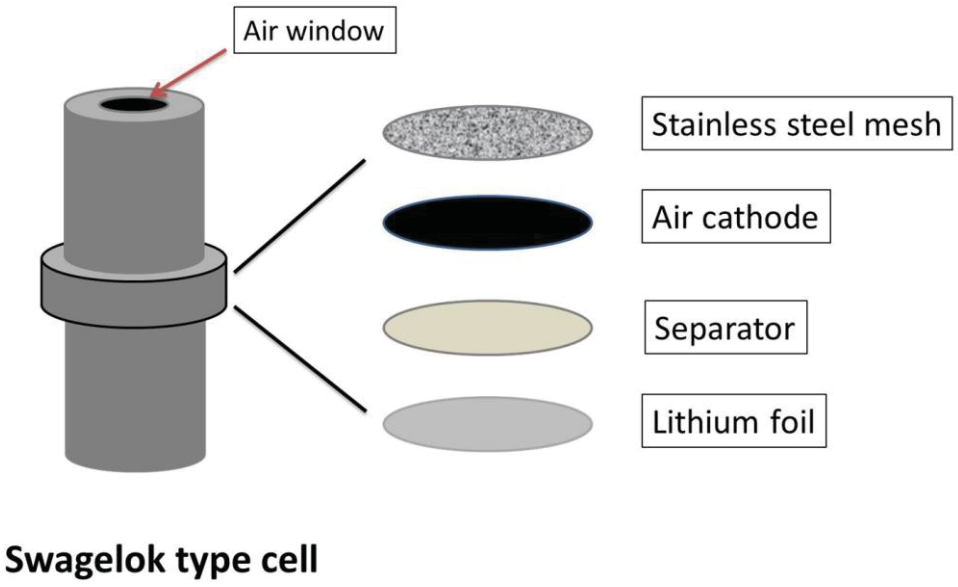

Figure 2-8 A schematic diagram of lithium-oxygen battery.

2.5 Electrochemical Characterization

The electrochemical measurements for evaluating the electrochemical performance of lithium-ion batteries and lithium-oxygen batteries included galvanostatic charge-discharge testing cyclic voltammetry and electrochemical impedance spectroscopy.

2.5.1 Galvanostatic Charge and Discharge

Generally, the capacity of the electrode material was calculated by galvanostatic charge and discharge testing. The measurement was conducted under a constant current density. The charge/discharge capacities (Q) can be calculated using the following formula:

$$Q = I \times t \qquad \text{(Eq. 2-7)}$$

where I is current density and t is the charge/discharge time. The galvanostatic testing voltage cut-offs for lithium-ion batteries were 2.0-4.3 V for cathode materials and 0.01-3.0 V for anode materials. The galvanostatic testing voltage cut-offs for lithium-oxygen batteries were 2.0-4.6 V. In lithium-ion battery testing, the C-rate performance was used to evaluate the capacity of the electrode at different charge/discharge current densities. Charge/discharge the cell at C/n rate means completely charge/discharge the cell within n hour. In this doctoral work, the galvanostatic charge-discharge measurements were collected on a computer-controlled Neware battery testing system and a Land Battery testing system.

2.5.2 Cyclic Voltammetry

Cyclic voltammetry or CV is a type of potentiodynamic electrochemical measurement and has been widely used to characterize the electrochemical performance of lithium-ion batteries.[235] In a cyclic voltammetry experiment the working electrode potential is ramped linearly versus time. This ramping is known as the experiment's scan rate (V/s). In three electrodes systems, the potential is applied between a reference

electrode and a working electrode and the current is measured between a working electrode and a counter electrode. In this doctoral work, the CV measurements were conducted in two electrode systems, where a lithium anode was acting as both counter and reference electrode. This collected data was plotted as current (i) vs. potential (E). The current peaks appear as the potential reaches the reduction or oxidation potential of the analyte. As a result, information about the redox potential and the electrochemical reaction rates of the electrode materials can be obtained. The CV measurements in this doctoral work were conducted via a CHI 660 C or CHI 660D electrochemical workstation (CH Instrument, Cordova, TN).

2.5.3 Electrochemical Impedance Spectroscopy (EIS)

Electrochemical impedance spectroscopy (EIS) has been widely used to examine a complex sequence of coupled electrochemical processes, such as electron transfer and mass transfer. A very small amplitude signal is applied to the testing system over a range of frequencies from 0.001 Hz to 100,000 Hz. By monitoring the current response, the variation of resistance with frequency can be examined. Charge-transfer resistance (R_{ct}), which can qualitatively characterize the electrode reaction speed, can be calculated through EIS measurements. A typical impedance Nyquist curve of a lithium-ion battery system consists of a compressed semicircle in the medium-frequency region which is assigned to be the charge-transfer resistance R_{ct} and an inclined line in the low frequency range which is assigned to be Warburg impedance, as shown in Figure 2-9.

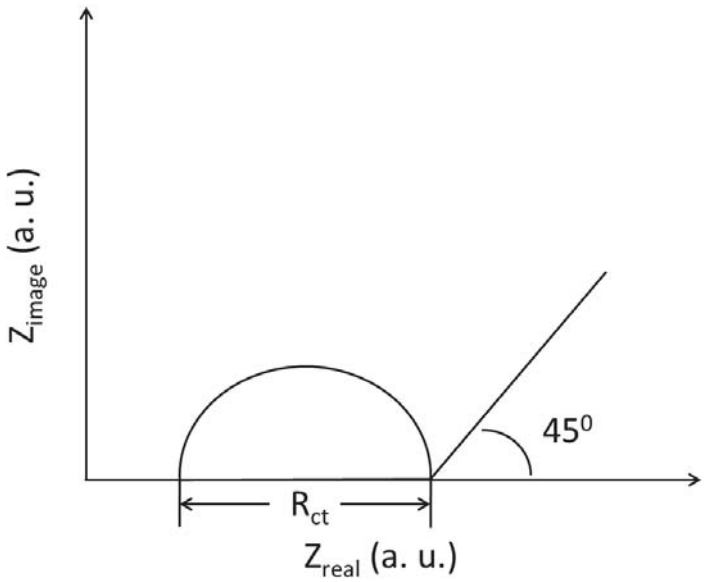

Figure 2-9 Typical EIS Nyquist curve of lithium-ion battery.

In this doctoral work, the EIS data were collected from a CHI 660 C or CHI 660D electrochemical workstation (CH Instrument, Cordova, TN). The amplitude of the AC signal applied to the cells was 5 mV and the frequency range was between 100 kHz and 10 mHz at controlled temperature.

CHAPTER 3 $LiFePO_4$ FACET NANOPLATES/GRAPHENE HYBRID MATERIALS FOR LITHIUM-ION BATTERIES

3.1 Introduction

Since its discovery in 1997, olivine $LiFePO_4$ has emerged as a promising cathode material for lithium ion batteries, in particular for high power application.[56,101,105,236] However, $LiFePO_4$ is insulating in nature with low electronic and ionic conductivity, inducing poor electrochemical performance. Tremendous efforts have been applied to overcome these obstacles including doping $LiFePO_4$ with foreign atoms, minimizing the $LiFePO_4$ particle size to the nanoscale and coating the particles with conductive materials, such as carbon, conductive polymers, metal or metal oxide.[108,110,114,116,119-122,237,238] Decreasing the $LiFePO_4$ particle size is now widely recognized as a way to improve the transport issues.[49] $LiFePO_4$ with different nanostructures such as nanoparticles, nanoplates, nanowires, and hierarchical porous spheres, has been synthesized to decrease the primary particle size of $LiFePO_4$.[114,127,131,239-242]

Recently, Islam's group found that the lowest Li migration energy is along the [010] channel.[125] This computational prediction was later confirmed by experimental investigation. The Li^+ diffusion along the [010] direction in olivine type $LiFePO_4$ material has been clearly visualized by combining high-temperature powder neutron

diffraction and the maximum entropy method.[126] Therefore, lithium ion conductivity of $LiFePO_4$ can be improved by reducing the length of the [010] direction and increasing the (010) facet. $LiFePO_4$ nanocrystals with a high percentage of (010) facets have been synthesized through a solvothermal method.[127,128]

Furthermore, it is crucial to increase the electronic conductivity of $LiFePO_4$ material. Graphene is an ideal carbon additive to increase the electronic conductivity of insulating materials due to its excellent electronic conductivity, large surface area and flexibility.[147] When used as an anode material, graphene based composites (such as graphene modified Fe_2O_3, Co_3O_4, Mn_3O_4, SnO_2 and Sn nanoparticles) have shown significant improvement on cycling stability and high rate capability than that of the pristine materials in lithium-ion batteries.[151,152,186,188,243,244] Modification of $LiFePO_4$ nanoparticles by graphene nanosheets as cathode materials has also achieved high electronic conductivity and high-rate performance.[245,246]

In this chapter, $LiFePO_4$ facet nanoplates/graphene hybrid materials were synthesized by a hydrothermal reaction combined with high temperature heat treatment. Application of $LiFePO_4$ facet nanoplates/graphene hybrid materials as cathode materials for lithium-ion batteries was also investigated.

3.2 Synthesis of $LiFePO_4$ Nanoplates/Graphene Hybrid Material

The synthesis process of $LiFePO_4$ nanoplates/graphene hybrid material is illustrated in Figure 3-1. $LiFePO_4$ nanoplates were synthesized first by a hydrothermal method. In a typical synthesis process, 2 mmol iron (II) sulfate heptahydrate ($FeSO_4 \cdot 7H_2O$, Sigma Aldrich) was dissolved in 10 ml pre-heated ethylene glycol at 50 °C. Two mmol phosphoric acid (H_3PO_4, Sigma Aldrich) and 200 mg PVP were dissolved in another 10 ml pre-heated ethylene glycol at 50 °C. Meanwhile, 5.4 mmol lithium hydroxide (LiOH, Sigma Aldrich) was dissolved in 5 ml ethylene glycol at 50 °C. After complete dissolution, those solutions were mixed together by stirring. The mixture was then transferred to a 30 ml Teflon-lined stainless steel autoclave and kept at 180 °C for 10 h. After cooling naturally to room temperature, the precipitate was washed with water and ethanol several times, and dried at 60 °C, under vacuum, overnight.

The synthesis of graphene oxide suspension was derived from the modified Hummers method as described in Chapter 2. Graphene oxide suspension (80 ml, 0.5 mg ml^{-1}) was reduced by hydrazine hydrate to yield a graphene sheets suspension at 90 °C for 2h. Eighty mg as-prepared $LiFePO_4$ nanoplates were dispersed in 40 ml distilled water by ultrasonification and quickly added to the freshly prepared graphene sheets suspension under vigorous stirring. The mixed suspension was filtrated by continuous stirring. The graphene sheets wrapped $LiFePO_4$ nanoplate hybrid materials were obtained by sintering the precipitate at 650 °C for 2 h under Ar atmosphere. For comparison, $LiFePO_4$ nanoplates without graphene were also calcinated under the same condition.

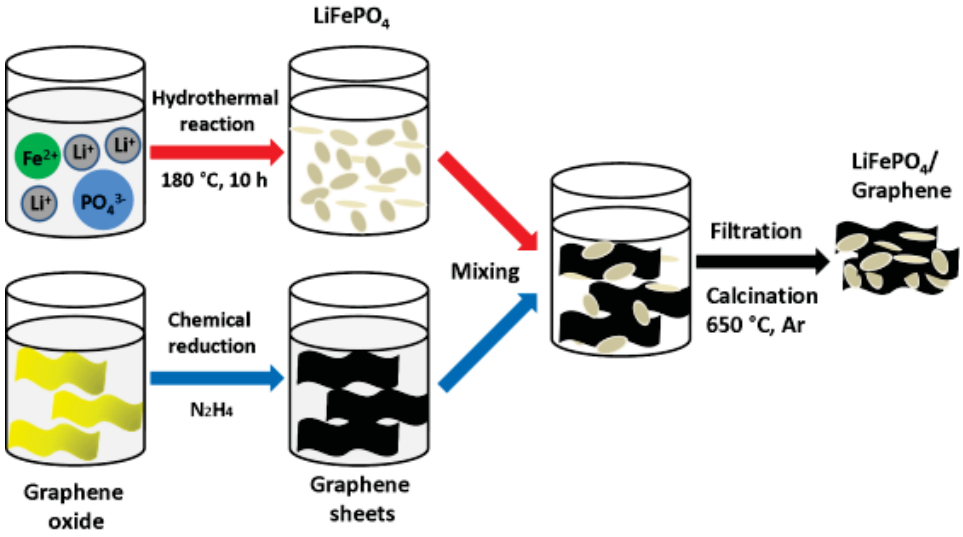

Figure 3-1 Illustration of the synthesis processes of $LiFePO_4$ nanoplates/graphene hybrid material.

3.3 Physical and Structural Characterization

3.3.1 X-ray Diffraction and Raman Spectroscopy

In this chapter, $LiFePO_4$ nanoplates that were obtained after hydrothermal reaction are denoted as LFP-180; $LiFePO_4$ nanoplates/graphene hybrid material that was obtained after calcination at 650 °C is denoted as LFP-GE650 and $LiFePO_4$ nanoplates without graphene that was obtained after calcination at 650 °C is denoted as LFP-650. The crystalline phases of the as-prepared materials were determined by powder X-ray diffraction (Siemens D5000) using Cu-Kα radiation in the range of 10°-50° with a scanning rate of 1° min^{-1}. Figure 3-2a shows XRD patterns of three as-prepared materials. All diffraction peaks can be indexed to an orthorhombic olivine phase, which matches well with the standard data (JCPDS card No: 81-1173). For $LiFePO_4$ obtained from a hydrothermal reaction (LFP-180), the intensity of the (020) diffraction line is much higher than other diffraction peaks, indicating that $LiFePO_4$ nanoplates have the

(020) face orientation (corresponding to the (010) facet). After sintered at 650 °C in Ar, the XRD pattern of $LiFePO_4$ nanoplates/graphene hybrid material (LFP-GE650) shows pure olivine phase with the strongest (020) peak.

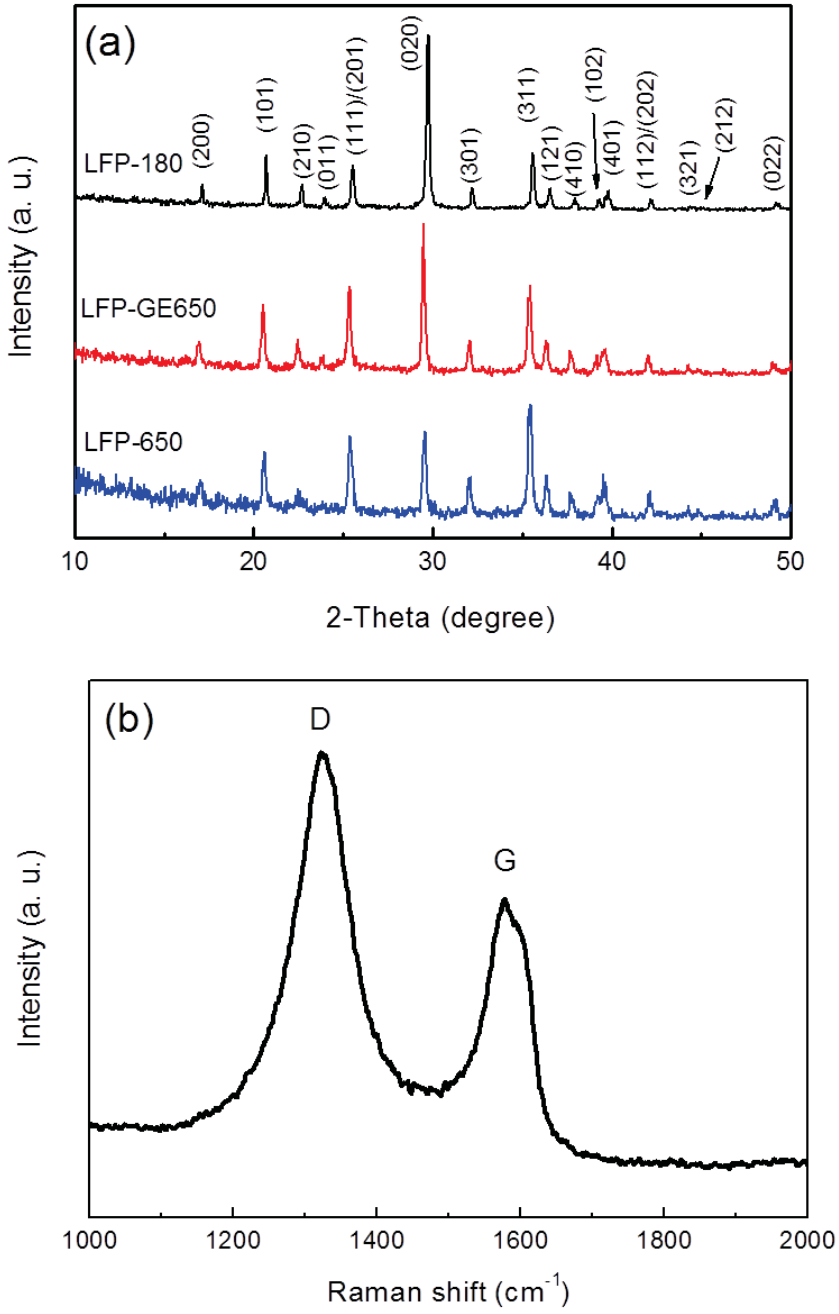

Figure 3-2 (a) XRD patterns of the as-prepared materials. (b) Raman spectrum of the $LiFePO_4$ nanoplates/graphene hybrid material.

Therefore, the sintering process did not change the crystal orientation. In comparison,

$LiFePO_4$ nanoplates without graphene were also sintered at 650 °C and the XRD pattern shows the strongest (311) diffraction peak, indicating a significant structure change without graphene. No obvious peaks corresponding to graphene are found in the XRD pattern of LFP-GE650 possibly due to its low content and homogeneous distribution among the $LiFePO_4$ nanoplates. However, the Raman spectrum of $LiFePO_4$ nanoplates/graphene hybrid materials (Figure 3-2b) clearly shows two carbon peaks, the D line and G line, at 1333 cm^{-1} and 1598 cm^{-1}, respectively. The D/G intensity ratio in the spectrum is significantly larger than that of well-crystallized graphite indicating the presence of exfoliated graphene layers.[247]

3.3.2 Thermogravimetric Analysis (TGA)

Thermogravimetric analysis (TGA) was used to determine the carbon content in the hybrid materials; the weight loss was 13.52 wt % at 600 °C in air (Figure 3-3). Based on the oxidation products of $Li_3Fe_2(PO_4)_3$ and Fe_2O_3, the weight gain should have been 5.07 wt % for pure $LiFePO_4$.[248] Therefore, the carbon content was about 18.59 wt % in $LiFePO_4$ nanoplates/graphene hybrid material. The weight changes of the $LiFePO_4$ nanoplates before and after calcination was -1.36 wt% and +3.65 wt%, respectively. The reduced weight loss indicates the PVP surfactant had decomposed into carbon during the calcination process. During the hydrothermal reaction, the highly viscous ethylene glycol with low ion diffusion rate can slow down the particle growth and prevent the oxidation of Fe^{2+} to Fe^{3+}. The PVP surfactant acted as the morphology directing agent for the formation of nanoplates.

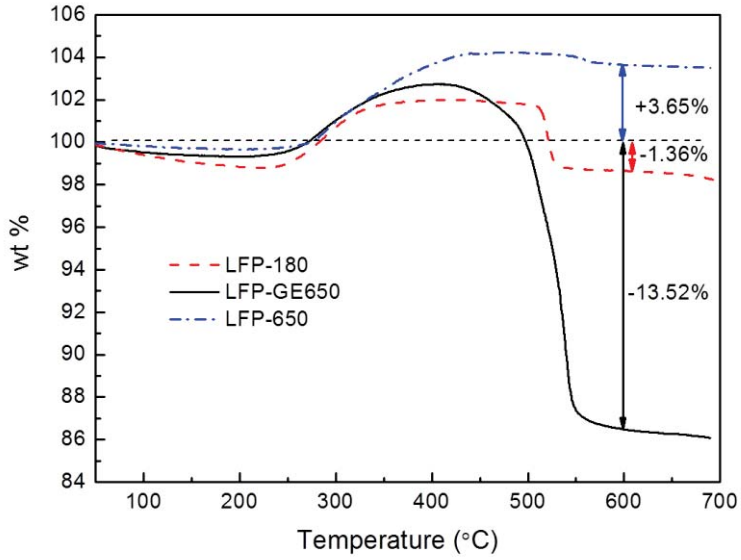

Figure 3-3 Thermogravimetric analysis (TGA) curves of the as-prepared materials.

3.3.3 Scanning Electron Microscopy (SEM)

The morphologies of as-prepared materials were observed by field-emission scanning electron microscopy (FESEM, Zeiss Supra 55VP) (Figure 3-4). The $LiFePO_4$ nanoplates obtained after a hydrothermal reaction showed an oval plate shape with the length of ~200 nm. Figure 3-4b shows the flexible graphene sheets surrounding $LiFePO_4$ nanoplates. After sintering, the nanoplate shape was preserved. A high magnification FESEM image (Figure 3-4c) clearly shows that a single $LiFePO_4$ nanoplate was wrapped by graphene nanosheets. The morphology of $LiFePO_4$ nanoplates without graphene was also investigated by FESEM. In Figure 3-4d, the nanoplates agglomerate to big particles and lose plate shape. The addition of graphene nanosheets can effectively inhibit agglomeration during the sintering process.

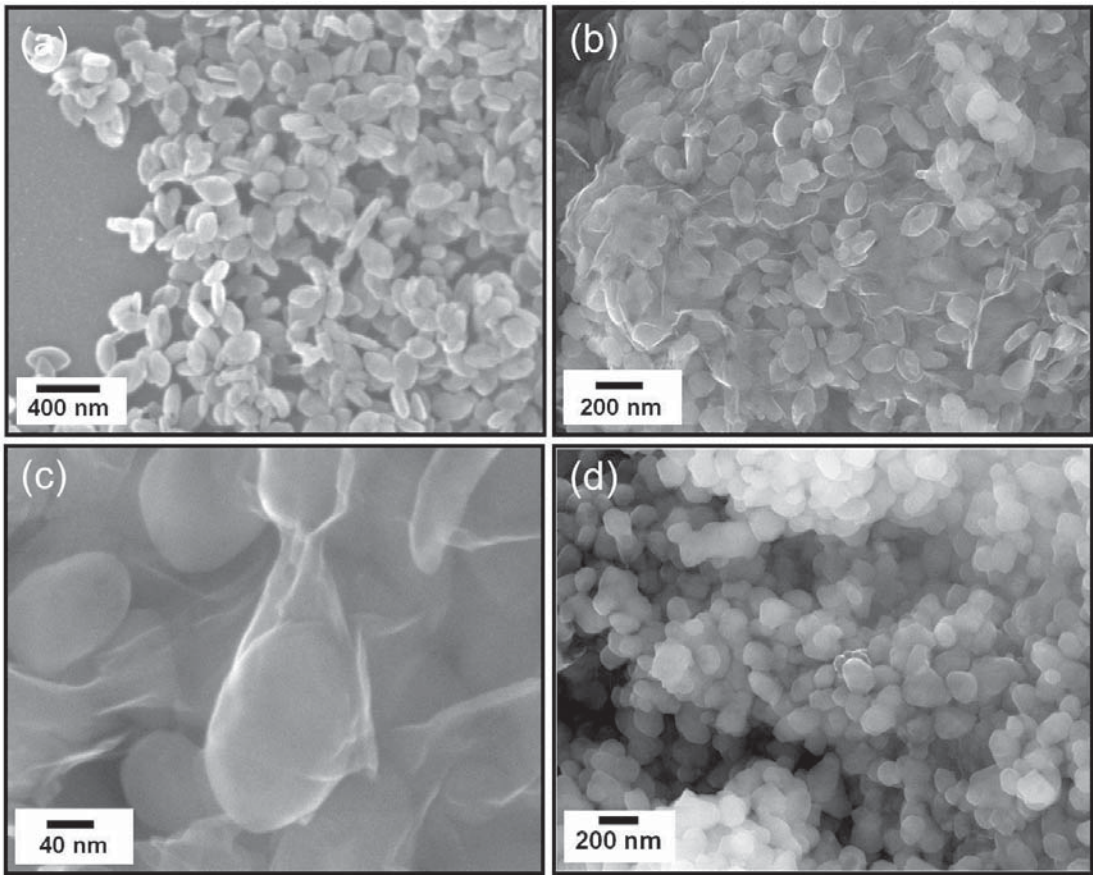

Figure 3-4 FESEM images of (a) LFP-180, (b) and (c) LFP-GE650 and (d) LFP-650 at different magnification.

3.3.4 Transmission Electron Microscopy (TEM)

More structure details were observed by transmission electron microscopy (TEM, JEOL 2011). A low magnification TEM image of $LiFePO_4$ nanoplates/graphene hybrid materials (Figure 3-5a) clearly illustrates that individual $LiFePO_4$ nanoplates are embedded in graphene networks. The thickness of the nanoplate was measured to be about 40 nm. Figure 3-5b shows a single $LiFePO_4$ nanoplate, which was surrounded by graphene nanosheets. Notably, the surface of a $LiFePO_4$ nanoplate is not smooth, resembling craters. These craters could be formed by the decomposition of the PVP surfactants, which were adsorbed on the surface during the hydrothermal process.[128]

The thickness of the nanoplate inside those craters was been further reduced compared with the rest of the nanoplate, which would be beneficial for fast lithium ion migration. A TEM image of another $LiFePO_4$ nanoplate (Figure 3-5c) shows a similar shape. Figure 3-5d shows a lattice resolved HRTEM image of a $LiFePO_4$ nanoplate, in which a (100) crystal plane with a d-spacing of 1.03 nm can be determined. The selected area electron diffraction (SAED) pattern (the inset in Figure 3-5d) shows regular diffraction spot arrays along the [010] zone axis, indicating the single crystalline nature of $LiFePO_4$ nanoplates. Therefore, the dominantly exposed crystal planes are the two (010) basal

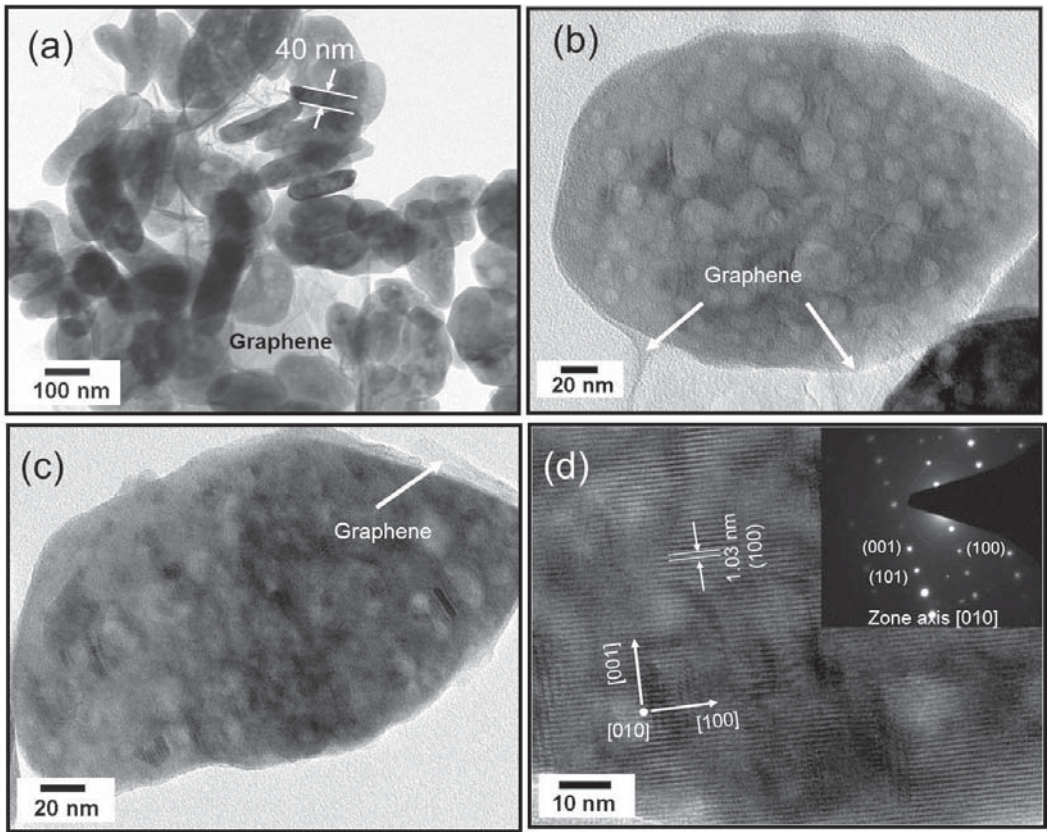

Figure 3-5 (a),(b), (c) TEM images and (d) HRTEM image of LFP-GE650. Inset is the corresponding selected area electron diffraction (SAED) pattern.

facets. Since Li ions diffuse fast along the [010] direction, the $LiFePO_4$ nanoplates with

dominantly exposed (010) planes could achieve fast Li ion transport, leading to high rate capacity.

3.4 Electrochemical Performance

The electrochemical performance of the as-prepared materials was evaluated by galvanostatic charge-discharge and cyclic voltammetry (CV). The experiments were carried out in coin cells (CR2032). The electrode composition was 80 wt % of the as-prepared materials, 10 wt % of carbon black, and 10 wt % of polyvinylidene fluoride (PVDF). The electrolyte solution was 1M $LiPF_6$ in a 1:1:1 mixture of ethylene carbonate (EC), diethyl carbonate (DEC) and dimethyl carbonate (DMC).

3.4.1 Cyclic Voltammetry

The cyclic voltammetry (CV) measurements of the cells were carried out using a CHI-660D electrochemical workstation. The scan rate of CV was 0.1 mV s^{-1} between 2.0-4.5 V. Figure 3-6 shows the CV curves of the electrodes made from as-prepared cathode materials. A single pair of defined redox peaks was observed for all the samples, which can be attributed to the Fe^{3+}/Fe^{2+} redox couple. For $LiFePO_4$ nanoplates obtained after hydrothermal reaction, the potentials of anodic and cathodic peaks were located at 3.63 V and 3.13 V vs Li/Li^+, respectively, with a potential separation (ΔV) of 500 mV. The potentials of the sintered sample shifted to 3.53 V and 3.35 V vs Li/Li^+, with a smaller ΔV of 180 mV. Moreover, the $LiFePO_4$ nanoplates/graphene electrode showed similar peak positions to the calcinated $LiFePO_4$ nanoplates, but with very sharp and

high redox current peaks. The smaller ΔV and higher current peak reflected the reduced over-potential. This implies that the hybrid materials have significantly improved electrode kinetics.

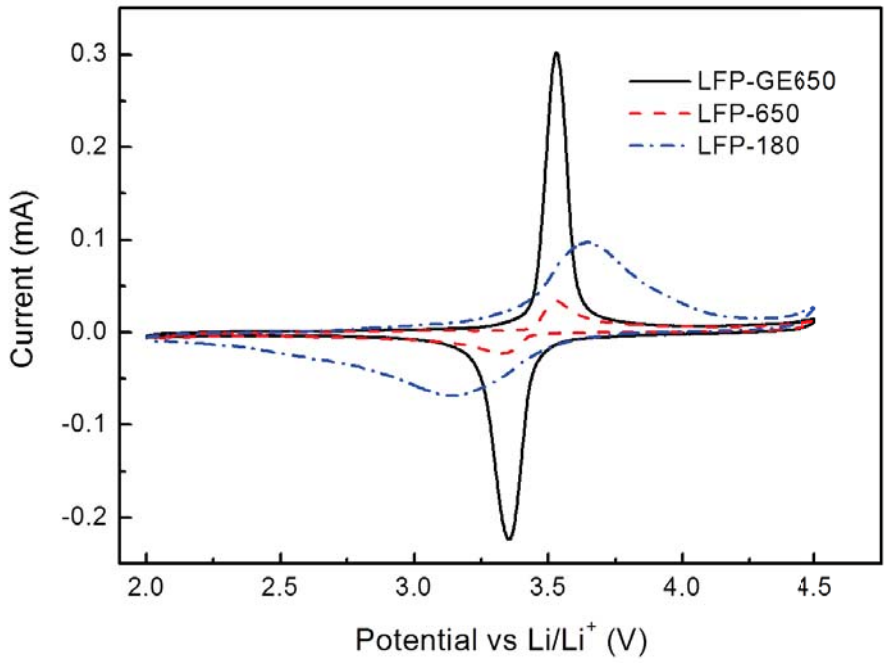

Figure 3-6 Cyclic voltammetry of the electrodes made of as-prepared materials, scan rate 0.1 mV s^{-1}, from 2.0 to 4.5 V vs Li/Li^+.

3.4.2 Galvanostatic Charge-Discharge

The electrochemical performances of the as-prepared materials were further investigated by galvanostatic charge-discharge. The galvanostatic charge and discharge experiment was performed between 2.0-4.3 V at room temperature using a battery testing system (Neware). Figure 3-7 shows the charge-discharge curves and cycling performance of the electrodes made of as-prepared materials at different C-rates. The charge process was carried out at the same rate as the discharge process to 4.3 V followed by a constant voltage charge at 4.3 V until the current was less than 8.5 mA g^{-1}

(C/20). For a $LiFePO_4$ nanoplates/graphene electrode, typical single plateaus were observed at 3.4 V and 3.5 V during the discharge and charge process at 0.2 C, corresponding to the oxidation and reduction of Fe^{2+} and Fe^{3+}, respectively. Furthermore, the discharge plateau could be maintained up to 10 C. The $LiFePO_4$ nanoplates/graphene electrode showed a discharge specific capacity of 163 mAh g^{-1} at 0.2 C, which was very close to the theoretical capacity (170 mAh g^{-1}). The electrode delivered a discharge capacity of 160 mAh g^{-1} at 1 C. Even at a high rate of 50 C, the hybrid materials achieved a discharge capacity of 75 mAh g^{-1}. Furthermore, the $LiFePO_4$ nanoplates/graphene hybrid materials delivered a specific energy of 554 Wh g-1 at 0.2 C (Figure 3-7e) and specific power >20 kW g^{-1} at 50 C (Figure 3-7f), respectively. For comparison, the charge-discharge performance of $LiFePO_4$ nanoplates obtained after hydrothermal reaction (LFP-180) and sintered $LiFePO_4$ nanoplates without graphene (LFP-650) were also tested (Figure 3-7b, c and d). The $LiFePO_4$ nanoplates obtained after hydrothermal reaction only exhibited a discharge capacity of 106 mAh g^{-1} at 0.2 C and 16 mAh g^{-1} at 5 C. The sintered $LiFePO_4$ nanoplates without graphene showed even lower discharge capacity of 42 mAh g^{-1} at 0.2 C, which may be due to the poor electronic conductivity and particle aggregation after calcination.

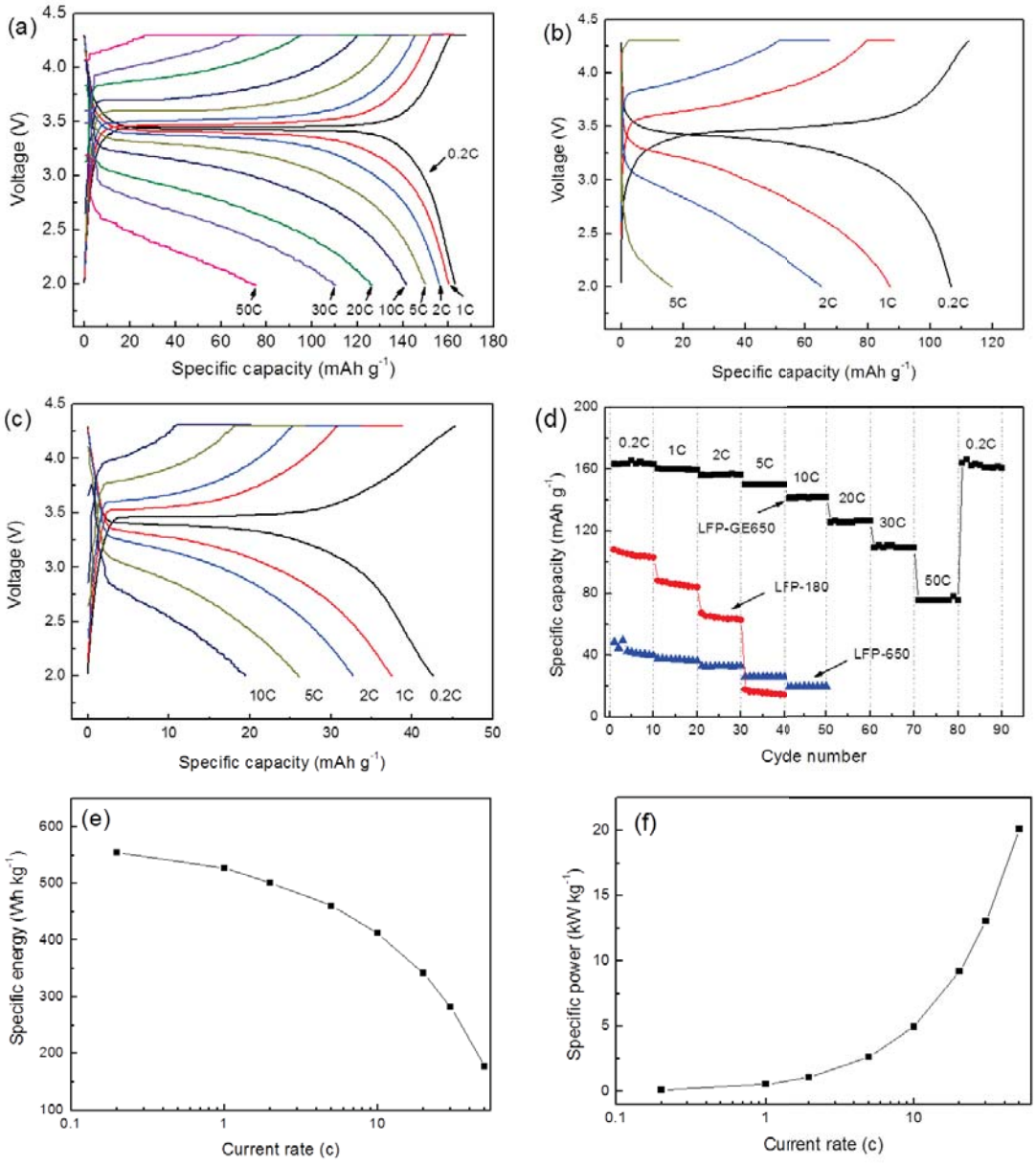

Figure 3-7 Charge and discharge profiles (a) LFP-GE650, (b) LFP-180 and (c) LFP-650. (d) High C-rate cycling performance of LFP-GE650. (e) Specific energy and (f) specific power of $LiFePO_4$ nanoplates/graphene electrode at different C-rate.

The long cycling stabilities of the $LiFePO_4$ nanoplates/graphene (LFP-GE650) electrodes at 5 C and 10 C are shown in Figure 3-8. The first discharge capacities of $LiFePO_4$ nanoplates/graphene hybrid materials (LFP-GE650) were 152 mAh g^{-1} at 5 C and 138 mAh g^{-1} at 10 C, respectively. After 200 cycles, the capacities were 147 mAh

g^{-1} and 132 mAh g^{-1}. These correspond to about 96.7% and 95.6 % of the initial cycle capacities and represent 0.016 % and 0.022 % capacity decrease per cycle, respectively.

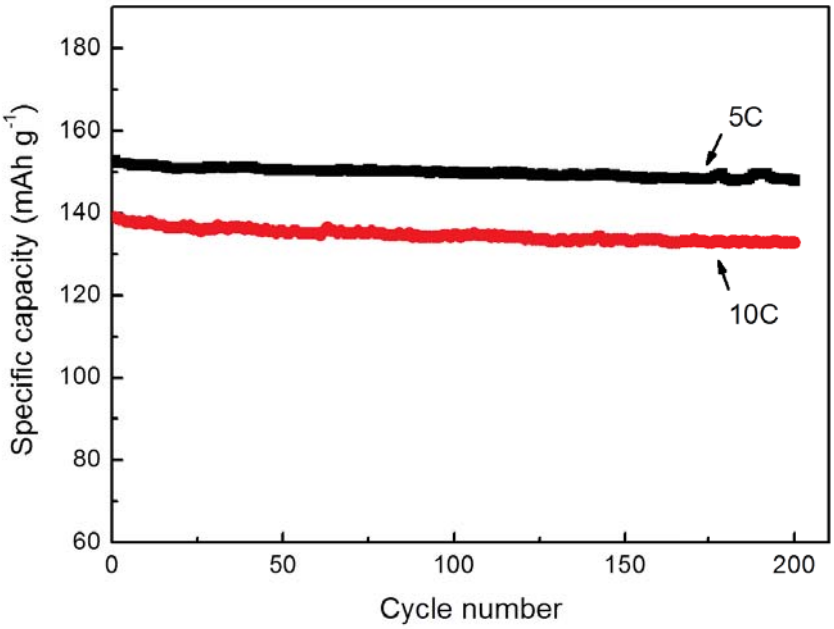

Figure 3-8 Cycling stability of LFP-GE650 electrodes at 5 C and 10 C rates at room temperature.

The $LiFePO_4$ nanoplates/graphene (LFP-GE650) in this work showed higher C-rate performance than the graphene modified $LiFePO_4$ reported by other groups through the co-precipitation method and spry pyrolysis method.[245, 246] The adding of graphene nanosheets could significantly increase the conductivity of the as-prepared $LiFePO_4$. Furthermore, the $LiFePO_4$ nanoplate with dominantly exposed (010) facets showed the shortest Li-ion diffusion length compared with that of other $LiFePO_4$/graphene composites in previous reports, which also should be contributed to the high C-rate performance.

3.5 Summary

$LiFePO_4$ facet nanoplates/graphene hybrid materials were successfully synthesized by a

hydrothermal method combined with high temperature treatment. The as-prepared materials display a plate structure with dominated (010) surfaces that could enhance the lithium diffusion efficient through the solid state phase. The graphene nanosheets can form a three dimensional conductive network which significantly increased the electronic conductivity of the as-prepared composites. The nanoplates/graphene electrodes exhibit very high discharge capacities of 163 mAh g^{-1} at 0.2 C and 75 mAh g^{-1} at 50 C. These results suggest that the synthesis of nanocrystals with preferred facets and integration with graphene nanosheets is a promising strategy to increase both ionic conductivity and electronic conductivity of insulating $LiFePO_4$ for lithium ion batteries.

CHAPTER 4 MESOPOROUS NANOLAYER CARBON COATED $LiFePO_4$ MICROSPHERES FOR LITHIUM-ION BATTERIES

4.1 Introduction

As described in previous chapters, reducing the particles of $LiFePO_4$ to the nanometer scale can significantly enhance its high C-rate performance. Although the down-sizing strategy combined with carbon coating is effective at increasing the electrochemical performance of a $LiFePO_4$ electrode, it also significantly reduces the tap density and volumetric energy density.[129] Recently, several reports have shown that $LiFePO_4$ with mesoporous structures and microsphere structures can deliver high-rate capacity.[105,130,242,249,250] Since the microspheres can easily form close packed arrays, a three-dimensional micro-nano porous hierarchical sphere structure is considered the ideal structure for $LiFePO_4$ cathode materials. The nanosized primary particles with carbon coating can ensure the high rate capability and the micro-sized secondary structures can achieve a high tap density.[131,132,251]

In this chapter, nanolayer carbon coated $LiFePO_4$ cathode material with a mesoporous microsphere structure was prepared using a hydrothermal method combined with high temperature calcination. The electrochemical performance of carbon coated $LiFePO_4$ microspheres as cathode material for lithium-ion batteries was investigated by

galvanostatic charge and discharge testing. The effect of calcination temperature on the kinetic behaviors of a carbon coated $LiFePO_4$ microsphere electrode was further investigated by cyclic voltammetry and electrochemical impedance spectroscopy.

4.2 Preparation of Mesoporous Carbon Coated $LiFePO_4$ Microspheres

In a typical synthesis process, 2 mmol iron nitrate ($Fe(NO_3)_3 \cdot 9H_2O$, Sigma Aldrich), 2 mmol ammonium phosphate ($NH_4H_2PO_4$, Sigma Aldrich) and 1 mmol citric acid ($C_6H_8O_7$, Sigma Aldrich) were dissolved in 10 ml distilled water. Meanwhile, 2 mmol lithium hydroxide (LiOH, Sigma Aldrich) was dissolved in 10 ml distilled water. After complete dissolution, the two solutions were mixed together by stirring. Two ml ethylene glycol was then added to the mixture. The mixture was then transferred to a 25 ml Teflon-lined stainless steel autoclave and kept at 180 °C for 3h. After cooling naturally to room temperature, the suspension and precipitate were heated on a hotplate at 80 °C under stirring to obtain the dried precursor. The precursor was finally calcinated from 600 °C to 750 °C for 10 h under 5% H_2/Ar atmosphere.

4.3 Physical and Structural Characterization

4.3.1 X-ray Diffraction

The mesoporous carbon coated $LiFePO_4$ microspheres were synthesized by using a hydrothermal method combined with high temperature calcination. The samples obtained after calcination at 600 °C, 650 °C, 700 °C and 750 °C, are denoted by

LFP-600, LFP-650, LFP-700, LFP-750, respectively. The crystalline phases of the as-prepared materials were determined by powder X-ray diffraction (Siemens D5000) using Cu-Kα radiation in the range of 10°-50° with a scanning rate of 1° min^{-1}. X-ray diffraction patterns of the precursor obtained after the hydrothermal reaction and the sintered $LiFePO_4$ samples are presented in Figure 4-1. The XRD matches well with the standard data JCPDS card No. 01-070-6442 for the precursor ($Fe_3(PO_4)_2(OH)_2$). All the calcinated samples are $LiFePO_4$ phase with an ordered olivine structure (orthorhombic *Pnma* (JCPDS No. 83-2092)). The lattice parameters of the as-prepared carbon coated $LiFePO_4$ calculated from the XRD patterns, are listed in Table 4-1. The crystallite size of $LiFePO_4$ increased from 60.2 nm to 92.9 nm when the calcination temperature increased from 650 °C to 750 °C. Impurity phases started to appear when the sintering temperature increased above 700 °C, which can be identified to Fe_2P and Li_3PO_4. According to previous reports, Fe_2P is a high-electronic conductivity phase leading to high rate charge-discharge.[103,252] Diffraction lines from carbon did not appear in the XRD pattern, possibly due to its amorphous state. The carbon content calculated by thermal gravimetric analysis was about 4.3 wt% for sample LFP-700.

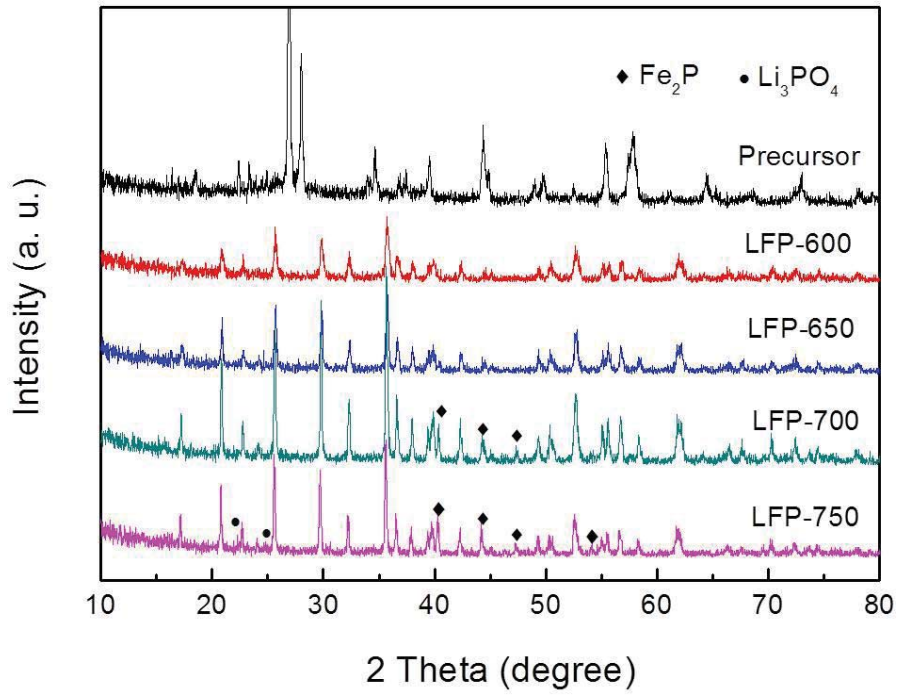

Figure 4-1 XRD patterns of $LiFePO_4$ precursor and carbon coated $LiFePO_4$ synthesized at different temperature.

Table 4-1 The lattice parameters and the crystallite size of the as-prepared $LiFePO_4$ samples.

Samples	Lattice parameters (Å)			Crystallite size
	a	b	c	(311) facet (nm)
LFP-600	10.30(4)	5.98(9)	4.68(2)	60.2
LFP-650	10.30(7)	6.00(1)	4.67(6)	79.5
LFP-700	10.30(9)	6.00(0)	4.68(5)	81.8
LFP-750	10.33(6)	6.00(9)	4.69(6)	92.9

4.3.2 Brunauer-Emmett-Teller

Nitrogen adsorption-desorption measurements were conducted using a Quadrasorb SI

analyzer at 77 K. Figure 4-2 shows the nitrogen adsorption-desorption isotherm and the corresponding Barret-Joyner-Halenda (BJH) pore size distribution curve of mesoporous carbon coated $LiFePO_4$ microspheres (LFP-700). The adsorption isotherm is a type IV adsorption-desorption isotherm with H3-type hysteresis, which is a feature of mesoporous materials. The measured Brunauer-Emmett-Teller (BET) area was 18.1 m^2 g^{-1}. The average pore diameters was 3.65 nm, calculated from the desorption branch of the nitrogen isotherm using the BJH method. The corresponding BJH desorption cumulative pore volumes was 0.078 cm^3 g^{-1}. The mesoporous structure allows the facile infiltration of electrolyte into the pores of the microspheres and is beneficial for enhancing the electrochemical performance of $LiFePO_4$.

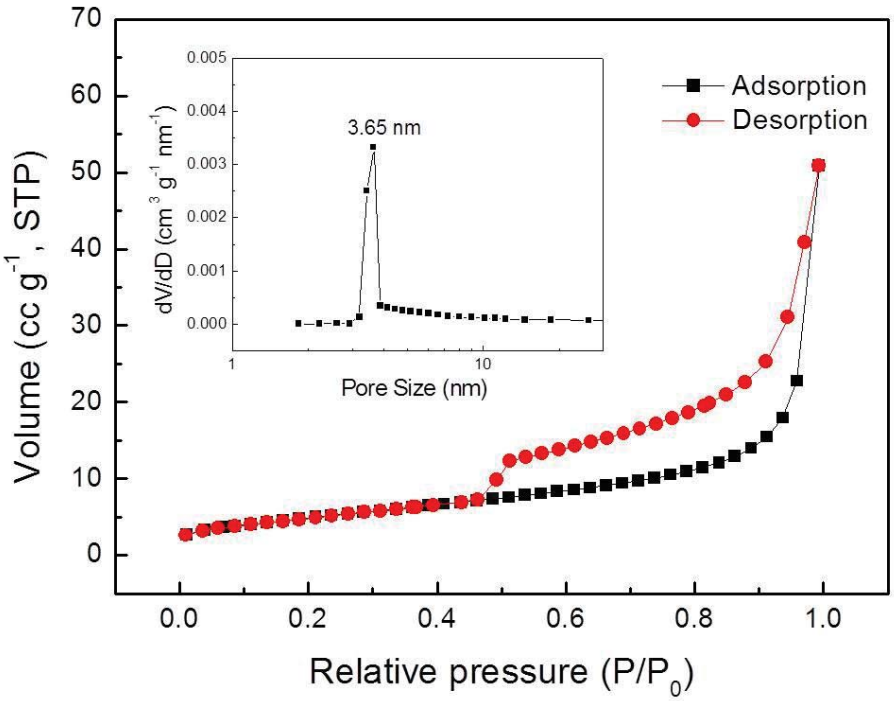

Figure 4-2 Adsorption-desorption isotherms of mesoporous $LiFePO_4$/C microspheres (LFP-700). The insert is the pore size distribution calculated from the desorption isotherm.

4.3.3 Scanning Electron Microscopy

The size and morphology of the $LiFePO_4$ precursor obtained after hydrothermal reaction and carbon coated $LiFePO_4$ microspheres (LFP-700) were observed by field emission scanning electron microscopy (FESEM, Zeiss Supra 55VP). From Figure 4-3a, we can observe that the $LiFePO_4$ precursor consists of spherical microparticles with diameters of 1-3 μm. A higher magnification FESEM image (Figure 4-3b) reveals that each microsphere is actually a random aggregate of primary nanoparticles. After calcination, the as-prepared materials could still keep a microsphere structure, as shown in Figure 4-3c. Furthermore, the high magnification FESEM image in Figure 4-3d shows each microsphere is actually an aggregate of primary $LiFePO_4$ nanoparticles. The high-temperature calcination process didn't significantly change the nanostructure, probably due to the carbon nanolayer that coated the primary $LiFePO_4$ nanoparticles. The amorphous carbon coating layer, which was formed by the pyrolysis of citric acid during the calcination process, can inhibit particle growth during the calcination process.

4.3.4 Transmission Electron Microscopy

The morphology and structure of carbon coated $LiFePO_4$ microspheres (LFP-700) was further analysed by transmission electron microscopy (TEM, JEOL 2011) and high resolution TEM (HRTEM). Figure 4-4a shows a TEM image of a carbon coated $LiFePO_4$ microsphere, which reveals the porous structure characteristic of the $LiFePO_4$ microsphere. The HRTEM image (Figure 4-4b) clearly illustrates the crystal lattice with

a d-spacing of 0.393 nm, corresponding to the (120) planes of orthorhombic $LiFePO_4$. Furthermore, amorphous carbon coating layer with a thickness of about 2 nm covering the surface of the $LiFePO_4$ nanoparticles is clearly distinguishable. The amorphous carbon coating layer was formed by the pyrolysis of citric acid during the calcination process.

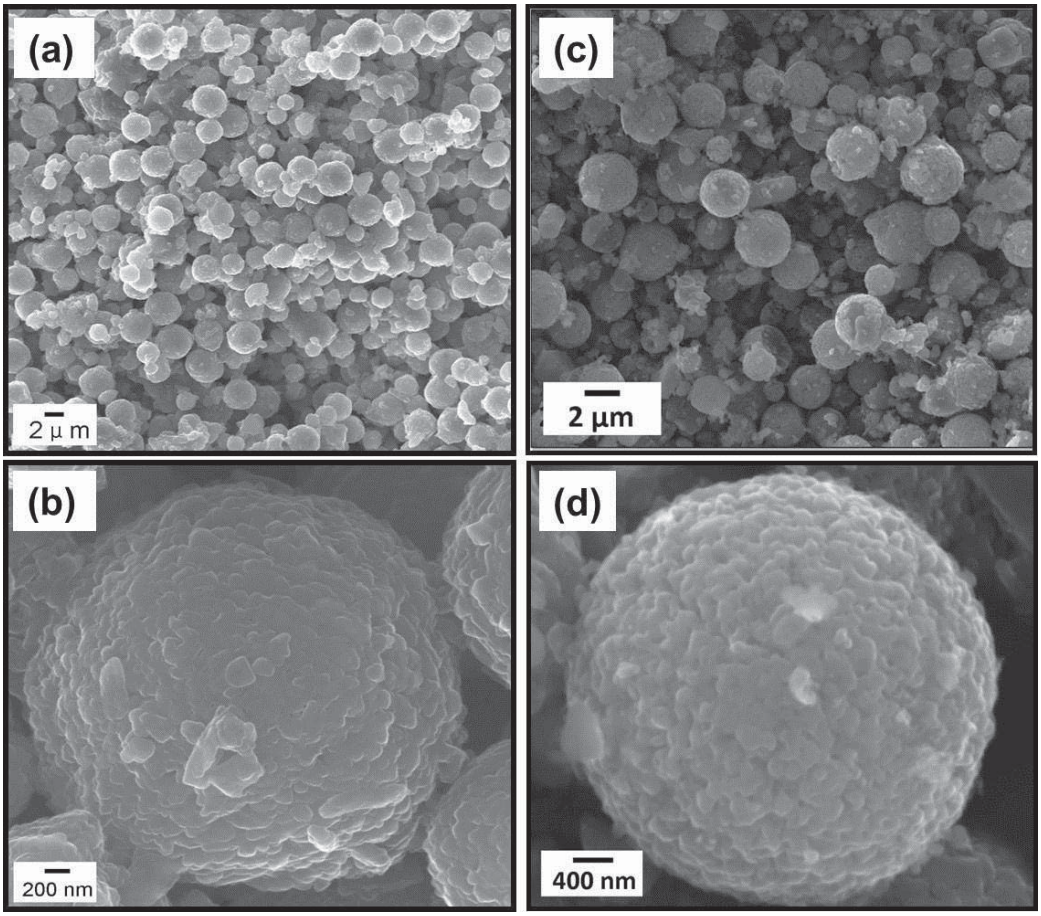

Figure 4-3 (a) and (b) FESEM images of $LiFePO_4$ microspheres precursor after hydrothermal reaction. (c) and (d) FESEM images of the as-prepared carbon coated $LiFePO_4$ microspheres (LFP-700).

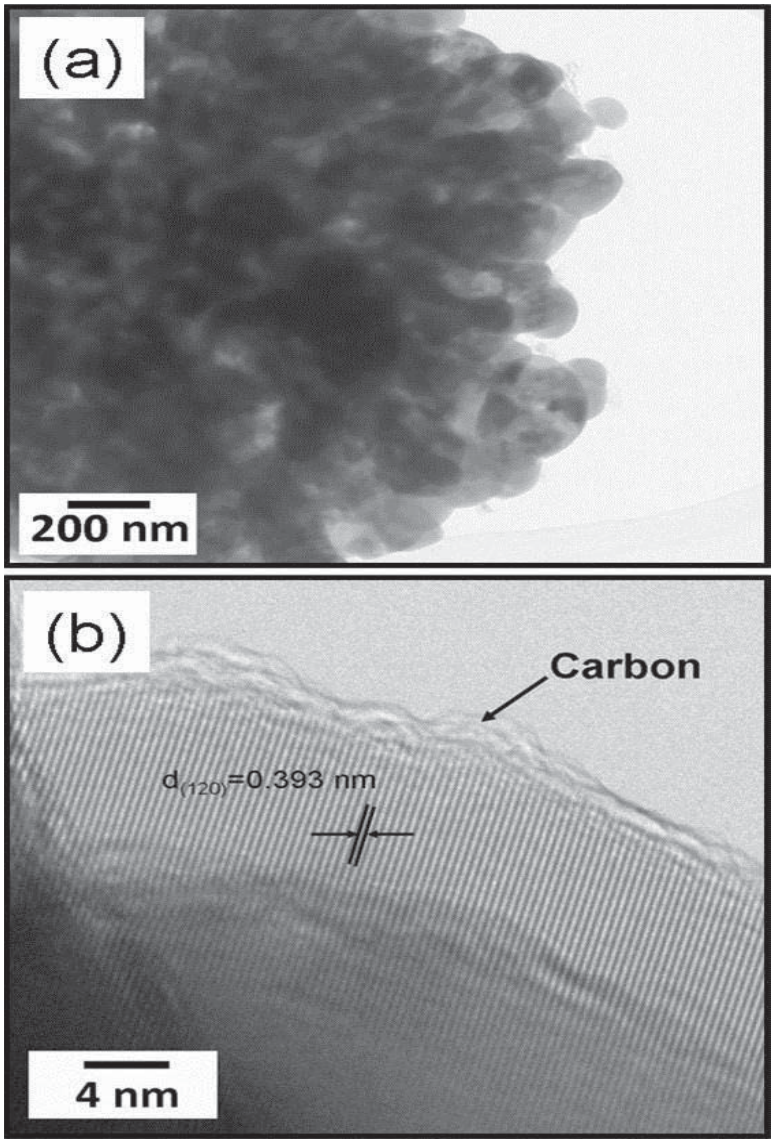

Figure 4-4 (a) TEM and (b) HRTEM images of the carbon coated $LiFePO_4$ microspheres (LFP-700).

4.4 Electrochemical Performance

The electrochemical performance of the as-prepared carbon coated mesoporous $LiFePO_4$ microspheres was evaluated by galvanostatic charge-discharge, cyclic voltammetry (CV) and electrochemical impedance spectra. The experiments were carried out in coin cells (CR2032). The electrode composition was 80 wt % of the

as-prepared materials, 10 wt % of carbon black, and 10 wt % of polyvinylidene fluoride (PVDF). The electrolyte solution was 1M $LiPF_6$ in a 1:1:1 mixture of ethylene carbonate (EC), diethyl carbonate (DEC) and dimethyl carbonate (DMC).

4.4.1 Galvanostatic Charge-Discharge

The galvanostatic charge and discharge experiment was performed between 2.0-4.3 V at room temperature using a battery testing system (Neware). Figure 4-5a shows the charge-discharge voltage curves of carbon coated $LiFePO_4$ microspheres electrodes at 0.2 C (C=170 mAh g^{-1}). Two typical plateaus were observed at 3.4 V and 3.5 V for all the samples during the discharge and charge process. Carbon coated $LiFePO_4$ sintered at 700 °C delivered the highest specific capacity. The lengthened voltage plateau and increased capacity should be attributed to the lower degree of polarization of the electrode materials during the charge-discharge process. The discharge capacities of the $LiFePO_4$ electrode at 0.2 C were 115 mAh g^{-1}, 144 mAh g^{-1}, 150 mAh g^{-1} and 137 mAh g^{-1} for the electrodes made of LFP-600, LFP-650, LFP-700 and LFP-750, respectively. The cycling stabilities of the as-prepared $LiFePO_4$ electrodes are shown in Figure 4-5b. The first cycle discharge capacity of carbon coated $LiFePO_4$ (LFP-600) was 42 mAh g^{-1} at the current rate of 10 C. After cycling for 200 cycles, the specific discharge capacity decreased to 29 mAh g^{-1}. The capacity retention is about 69%. The first cycle discharge capacity of carbon coated $LiFePO_4$ (LFP-650) was 99 mAh g^{-1} at the current rate of 10 C. After cycling for 200 cycles, the specific discharge capacity decreased to 67 mAh g^{-1}, which represents capacity retention of about 67.7%. The first cycle discharge capacity

of carbon coated $LiFePO_4$ (LFP-700) was 112 mAh g^{-1} at the current rate of 10 C. After cycling for 200 cycles, the specific discharge capacity decreased to 108 mAh g^{-1}. The capacity retention is about 96.4% and the electrode has a 0.018% capacity decrease per cycle. The first cycle discharge capacity of carbon coated $LiFePO_4$ (LFP-750) was 100 mAh g^{-1} at the current rate of 10 C. After cycling for 200 cycles, the specific discharge capacity decreased to 87 mAh g^{-1}. The capacity retention is about 87%. The carbon coated $LiFePO_4$ calcinated at 700 °C (LFP-700) showed the highest discharge capacity and best cycle stability.

Different rates of charge-discharge were also used to evaluate the electrochemical performance of the as-prepared carbon coated $LiFePO_4$ microspheres. The charge-discharge voltage curves, cycle stability and power density of the as-prepared mesoporous $LiFePO_4$/C microspheres at different current rates are shown in Figure 4-6. The charge-discharge plateaus of the LFP-600 and LFP-650 electrodes started to slope with the increase of the charge-discharge current rate, while the electrodes made of LFP-700 and LFP-750 still showed discharge voltage plateau even discharge at 30 C. The sample LFP-600 delivered discharge capacities of 115 mAh g^{-1}, 104 mAh g^{-1}, 89 mAh g^{-1}, 81 mAh g^{-1}, 64 mAh g^{-1}, 42 mAh g^{-1}, 21 mAh g^{-1} and 12 mAh g^{-1} at the discharge current rates from 0.2 C to 30 C with the rate capacity retention of 10.4 %. The sample LFP-650 showed discharge capacities of 144 mAh g^{-1}, 143 mAh g^{-1}, 140 mAh g^{-1}, 132 mAh g^{-1}, 118 mAh g^{-1}, 101 mAh g^{-1}, 66 mAh g^{-1} and 38 mAh g^{-1} at the discharge current rates from 0.2 C to 30 C with the rate capacity retention of 26.3 %.

The sample LFP-700 showed similar discharge capacity to the sample LFP-650 at low C-rate (<2 C), but showed much higher discharge capacity at high C-rate (>10 C) with a rate capacity retention of 60.6 % from 0.2 C to 30 C. The sample LFP-750 showed lower discharge capacity than the sample LFP-650 and LFP-700 at low C-rate (<2 C). However, at a high C-rate (>10 C), sample LFP-750 showed a higher discharge capacity than the sample LFP-650 with a rate capacity retention of 51.1 % from 0.2 C to 30 C. The improved high C-rate performance may be due to the high electronic conductivity Fe_2P impurity phase for the sample LFP-700 and LFP-750. As Fe_2P and Li_3PO_4 are inactive phases for lithium ion insertion-extraction during the charge-discharge process and the Fe_2P and Li_3PO_4 content will rise with increasing the calcination temperature, the $LiFePO_4$ sample synthesized at 750 °C showed lower discharge capacity than the sample synthesized at 650 °C and 700 °C at low C-rate (<2 C). Figure 4-6f shows the energy and power density of sample LFP-700 at different C-rates. Sample LFP-700 can deliver specific energy of 485 Wh g^{-1} at 0.2 C and specific power >14.3 kW g^{-1} at 30 C, respectively. The excellent high-rate performance of sample LFP-700 should be related to the higher crystallinity, the small particle size, the carbon coating treatment and high electronic conductivity Fe_2P impurity phase, which facilitates the diffusion of the lithium ion within the intercalation host and increases the electric conductivity of the electrode. The mesoporous structure of the material also facilitates the penetration of the electrolyte into the electrode.

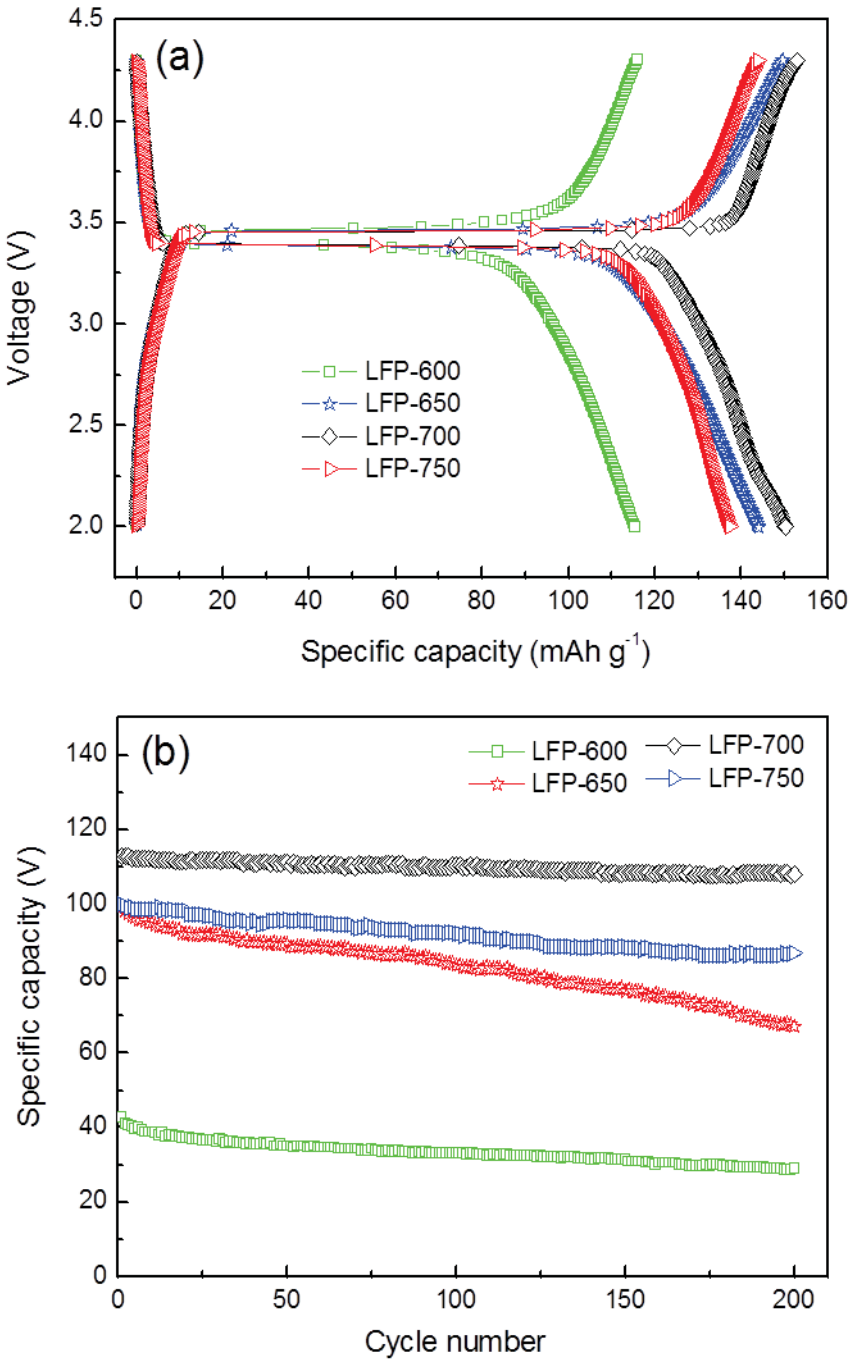

Figure 4-5 (a) The charge-discharge voltage curves of the as-prepared mesoporous carbon coated $LiFePO_4$ microspheres electrodes in the voltage range from 2.0 to 4.3 V at 0.2C. (b) The discharge capacity vs cycle number for mesoporous carbon coated $LiFePO_4$ microspheres electrodes at the high rate of 10 C (C=170 mA g^{-1}).

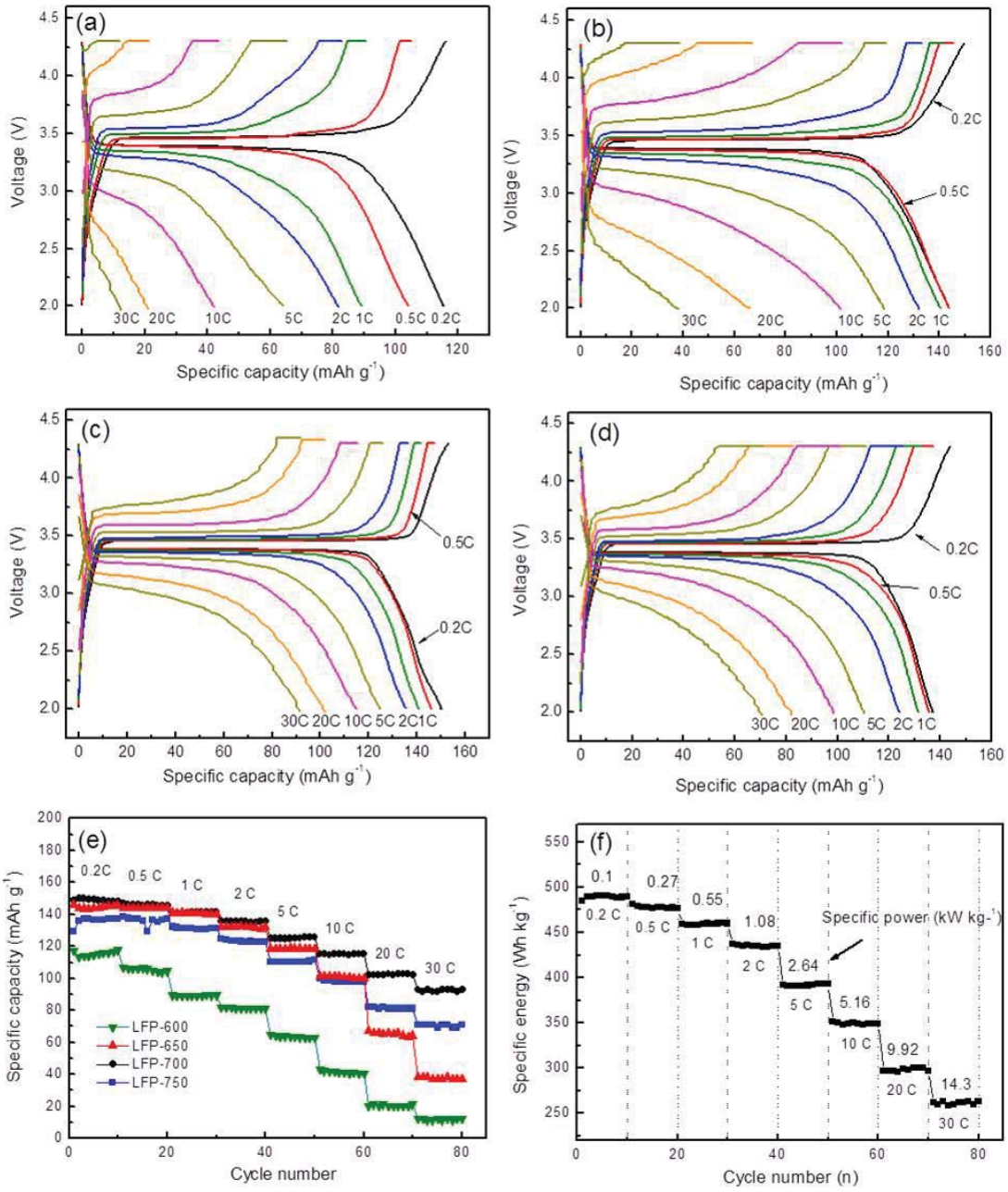

Figure 4-6 The charge-discharge voltage curves of the electrodes made of as-prepared carbon coated $LiFePO_4$ microspheres (a) LFP-600, (b) LFP-650, (c) LFP-700 and (d) LFP-750, in the voltage range from 2.0 to 4.3 V at different current rates (C=170 mAh g^{-1}). (e) Cycle life of as-prepared carbon coated $LiFePO_4$ microspheres at different current rate. (f) Specific energy and specific power of sample LFP-700 electrode at different current rate.

4.4.2 Cyclic Voltammetry and Electrochemical Impedance Spectra

To further investigate the electrode kinetics of the as-prepared mesoporous $LiFePO_4$/C microspheres, cyclic voltammetry (CV) and electrochemical impedance spectra (EIS) were used to calculate the apparent activation energies and the Li-ion diffusion coefficient. Cyclic voltammetry (CV) measurements and electrochemical impedance spectroscopy (EIS) of the cells were carried out using a CHI-660D electrochemical workstation. The scan rate of CV was from 0.1~2.0 mV s^{-1} between 2.0-4.5 V. For EIS measurements, the amplitude of the AC signal applied to the cells was 5 mV and the frequency range was between 100 kHz and 10 mHz.

Figure 4-7 shows the CV curves of the as-prepared $LiFePO_4$ electrodes at various scanning rates between 2.0 and 4.5 V. A single pair of well-defined redox peaks is observed for all the samples, which can be attributed to the Fe^{3+}/Fe^{2+} redox couple. The height and area of the redox peaks increased with increased scanning rates. Meanwhile, the anodic and cathodic peaks move to the higher and lower potentials, respectively, as scanning rates increased. Even at high scanning rate of 2.0 mV s^{-1}, the very well-defined sharp redox reaction peaks are still maintained for sample LFP-650, LFP-700, LFP-750, indicating good kinetics for lithium intercalation and de-intercalation. A Li-ion diffusion coefficient D (cm^2 s^{-1}) can be calculated from the Randles Sevcik equation:[235]

$$I_p = 2.69\times10^5 A C D^{1/2} n^{3/2} v^{1/2} \qquad \text{(Eq. 4-1)}$$

where I_p is the peak current (A), A is the surface area of the electrode (1 cm^2), C is the

concentration of Li-ion in solid (0.0228 mol cm^{-3}), n is the number of electrons involved in the half-reaction for the redox couple (n = 1 for Fe^{2+}/Fe^{3+} redox couple), and v is the potential scan rate (V s^{-1}). As shown in Figure 4-8, I_p is indeed proportional to $v^{1/2}$, confirming a diffusion-controlled behavior. From the slope of the lines and based on Eq. 4-1, the diffusion coefficients D_a (a peak) are 9.12×10^{-12} cm^2 S^{-1}, 2.28×10^{-11} cm^2 S^{-1}, 2.34×10^{-11} cm^2 S^{-1}, 3.32×10^{-11} cm^2 S^{-1} for electrodes made of LFP-600, LFP-650, LFP-700 and LFP-750, respectively. The diffusion coefficients $D_{a'}$ (a' peak) are 5.05×10^{-12} cm^2 S^{-1}, 1.45×10^{-11} cm^2 S^{-1}, 1.64×10^{-11} cm^2 S^{-1}, 1.81×10^{-11} cm^2 S^{-1} for electrodes made of LFP-600, LFP-650, LFP-700 and LFP-750, respectively. The lithium diffusion coefficient calculated from CV is increased with increased calcination temperature, indicating that high temperature treatment can greatly increase the lithium diffusion kinetics of $LiFePO_4$.

The electrochemical impedance spectra were measured at the discharge potential of 3.4 V (*vs* Li/Li^+) at different temperatures from 100 kHz to 10 mHz. The Nyquist plots are shown in Figure 4-9. All the profiles exhibit a semicircle in the medium frequency region and an inclined line in the low frequency range. The numerical value of the diameter of the semicircle on the Z_{re} axis gives an approximate indication of the charge transfer resistance (R_{ct}). From the Nyquist plots in Figure 4-9, the electrode made of LFP-700 showed the lowest charge transfer resistance, indicating its good electrode kinetics, consistent with the galvanostatic charge-discharge testing results. The inclined line can be considered to be the Warburg impedance (Z_w), which is associated with

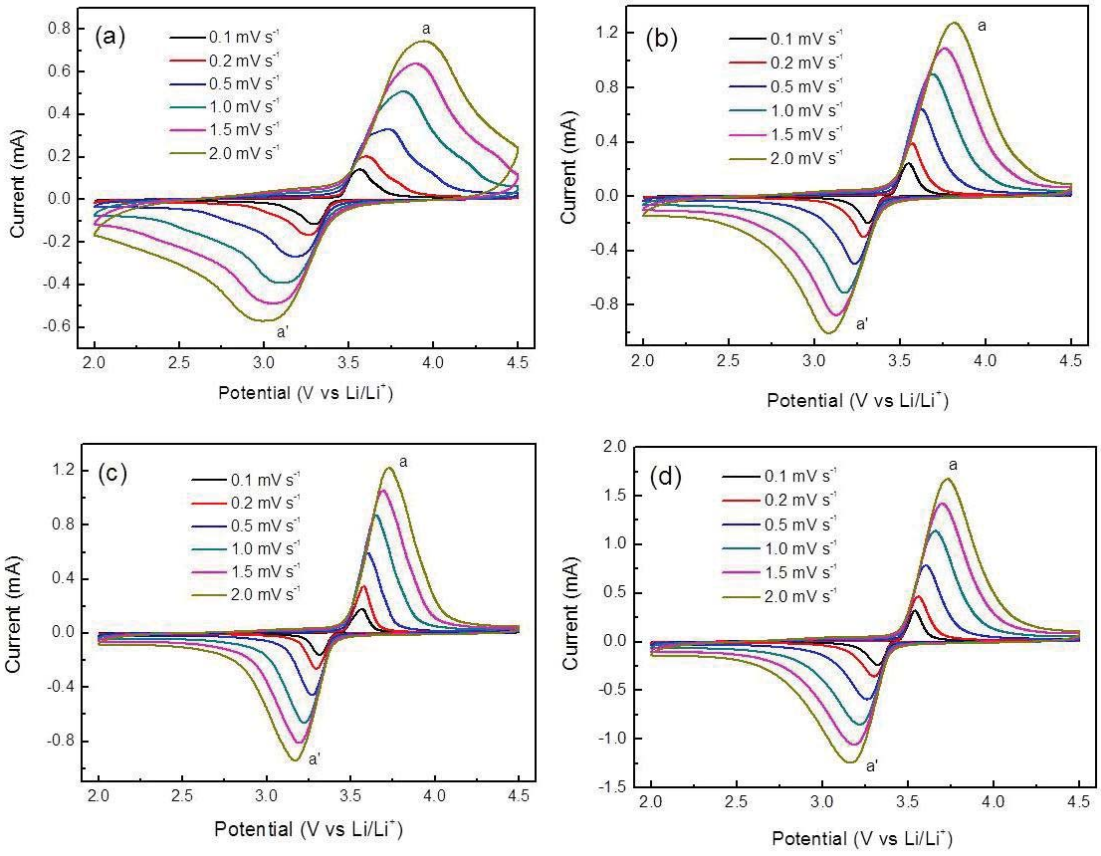

Figure 4-7 CV curves of the carbon-coated $LiFePO_4$ microsphere electrodes at different scan rate. (a) LFP-600, (b) LFP-650, (c) LFP-700 and (d) LFP-750.

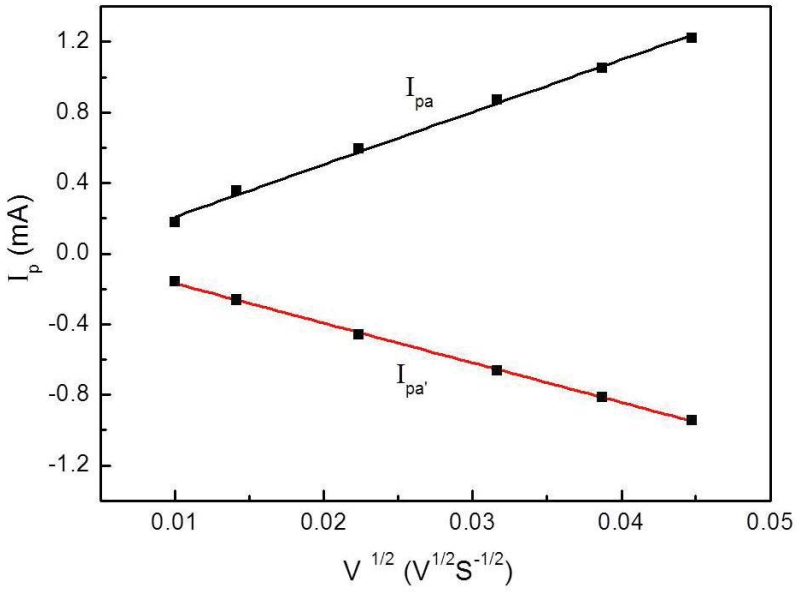

Figure 4-8 Peak current I_p versus square root of scan rate $v^{-1/2}$ at 25 °C for the electrodes made of the mesoporous carbon coated $LiFePO_4$ microspheres (LFP-700).

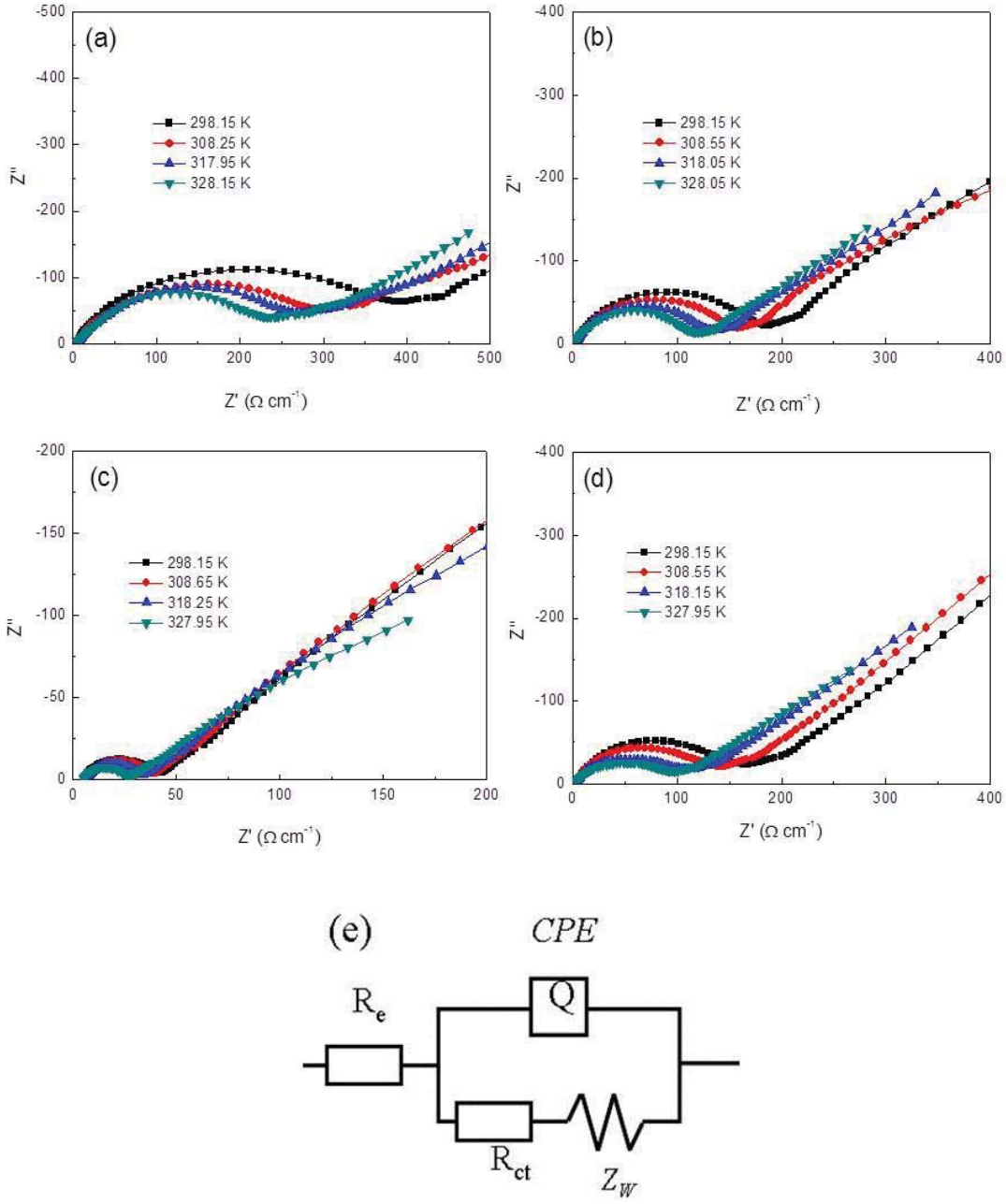

Figure 4-9 Nyquist plots of electrodes made of as-prepared mesoporous carbon coated $LiFePO_4$ microspheres synthesized at (a) LFP-600, (b) LFP-650, (c) LFP-700 and (d) LFP-750 at 3.4 V (discharge) at different temperatures from 100 kHz to 10 mHz. (e) Equivalent circuit used for fitting the experimental EIS data.

lithium ion diffusion in the $LiFePO_4$ particles. The R_{ct} is calculated using the equivalent

circuit shown in Figure 4-9e. The exchange current (i_0) and the apparent activation energy (E_a) for the $LiFePO_4$ samples synthesized at different temperature can be calculated from Eq. 4-2 and the Arrhenius equation, Eq. 4-3, respectively.

$$i_0 = RT / nFR_{ct} \quad \text{(Eq. 4-2)}$$

$$i_0 = A \exp(-E_a / RT) \quad \text{(Eq. 4-3)}$$

where R is the gas constant, T is the absolute temperature, n is the number of transferred electrons, and F is the Faraday constant, A is a temperature-independent coefficient.

Figure 4-10 shows the Arrhenius plots of log i_0 as a function of 1/T. The activation energies of the electrodes made of sample LFP-600, LFP-650, LFP-700 and LFP-750 are 15.73, 14.31, 13.50 and 14.07 kJ mol^{-1} (error is within 2%), respectively. These values are comparable to the previously reported activation energy (13 kJ mol^{-1}) derived from the Avrami-Johnson-Mehl-Eroofev equation.[253] The electrode made of mesoporous $LiFePO_4$ microspheres synthesized at 700 °C shows the lowest activation energy.

The EIS is also an important method for calculating the lithium diffusion coefficient. The Warburg impedance in the low frequency is directly related to the lithium ion diffusion process. The lithium ion diffusion coefficient D_{Li+} can be calculated by using the following equation:

$$D_{Li+} = R^2T^2 / 2An^4F^4C^2\sigma^2 \quad \text{(Eq. 4-4)}$$

where R is the gas constant, T is the absolute temperature, A is the surface area of the

cathode (1 cm^2), n is the number of electrons per molecule during oxidization, which is

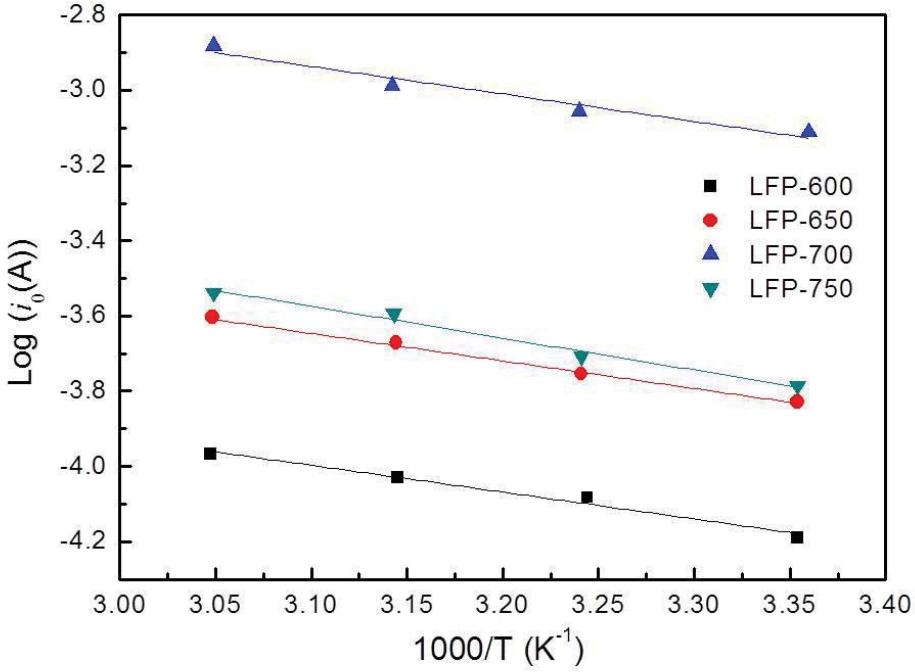

Figure 4-10 Arhenius plots of log i_0 versus 1/T for the electrodes made of as-prepared mesoporous carbon coated $LiFePO_4$ microspheres synthesized at different temperatures. The lines are the linear fitting results.

equal to 1, F is the Faraday constant, C is the concentration of Li-ion in solid (0.0228 mol cm^{-3}),[254] and σ is the Warburg factor, which is relative to Z'_{re}. σ can be obtained from the slope of the lines in Figure 4-11. The lithium diffusion coefficients were 3.47 $\times 10^{-14}$ cm^2 S^{-1}, 4.49$\times 10^{-14}$ cm^2 S^{-1}, 6. 57$\times 10^{-14}$ cm^2 S^{-1} and 6. 33$\times 10^{-14}$ cm^2 S^{-1} for the electrodes made of sample LFP-600, LFP-650, LFP-700 and LFP-750, respectively, at 25 °C. The lithium diffusion coefficient increases when the calcination temperature increases from 600 °C to 700 °C and slightly decreases after calcinations at 750 °C. The increasing lithium ion diffusion kinetics should be attributed to the improved crystallinity after calcination. The lithium diffusion coefficient calculated from the EIS measurement is lower than that calculated from the CV measurement, which is

consistent with the experimental results from another group.[255] The EIS measurements were carried out at a certain voltage with constant material composition. The lithium diffusion coefficient decreases with the lithium ions extracting from the olivine $LiFePO_4$ structure.[256] The lithium diffusion coefficient calculated from the CV measurement is from the peak current which should be the largest lithium diffusion coefficient of the $Li_{1-x}FePO_4$ ($0<x<1$).

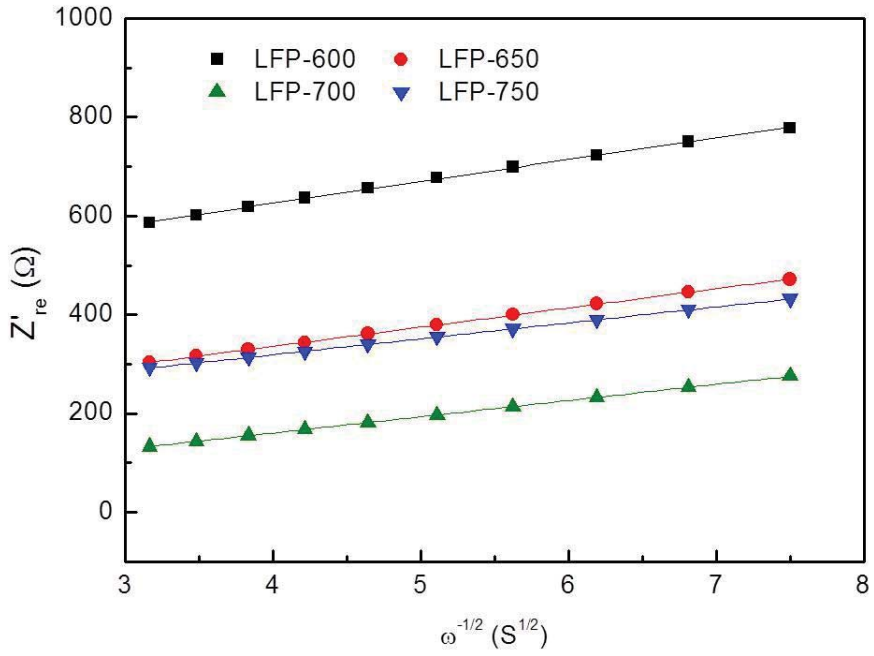

Figure 4-11 Real parts of the complex impedance versus $\omega^{-1/2}$ at 25 °C at 3.4 V (discharge) for the electrodes made of the mesoporous carbon coated $LiFePO_4$ microspheres synthesized at different temperatures.

4.5 Summary

Porous $LiFePO_4$/C microspheres were successfully synthesized by a hydrothermal reaction combined with high-temperature calcinations. The as-prepared materials showed secondary mesoporous microsphere morphology with sphere diameters of 1-3

μm. Each microsphere is actually a random aggregate of primary 100-200 nm carbon coated $LiFePO_4$ nanoparticles. The $LiFePO_4$ /C microspheres synthesized at 700 °C delivered a discharge capacity of 150 mAh g^{-1} at 0.2 C and 91 mAh g^{-1} at 30 C. The excellent high C-rate performance may be due to the mesoporous secondary sphere structure facilitating penetration of the electrolyte and to the small amount of Fe_2P impurity increasing the electronic conductivity of the materials. Through material architecture design, $LiFePO_4$ cathode material can meet the stringent requirements for high power applications such as electric vehicles and energy storage for smart grids.

Both the $LiFePO_4$ nanoplates/graphene composite in Chapter 3 and the porous $LiFePO_4$/C microspheres in this chapter showed high discharge capacities, high C-rate performances and good cycling stabilities. Both of them are promising cathode materials for lithium-ion batteries. The C-rate performance of $LiFePO_4$ nanoplates/graphene composite is higher than that of $LiFePO_4$/C microsphere, which makes it more suitable for high power lithium-ion batteries. While the tape density of the porous $LiFePO_4$/C microsphere is much higher than that of the $LiFePO_4$ nanoplates/graphene composite, which makes it more suitable for high energy lithium-ion batteries in energy storage application.

CHAPTER 5 MESOPOROUS HEMATITE NANOSTRUCTURES FOR HIGH CAPACITY ANODE MATERIALS IN LITHIUM-ION BATTERIES

5.1 Introduction

As an n-type semiconductor, hematite (α-Fe_2O_3) has attracted a great deal of attention from researchers in different fields because of its non-toxicity, low cost, high stability under ambient conditions, and multiple functions. It has been intensively investigated for applications in lithium batteries, sensors, catalysts, pigments, and magnetic devices.[257-262] The performance of α-Fe_2O_3 strongly depends on the particle size, morphology, and structure. For use as an anode material in lithium-ion battery, the reversibility of lithium intercalation in α-Fe_2O_3 depends strongly on the nanostructure and particle size.[263,264] Nanosize α-Fe_2O_3 exhibits better performance than microscale samples as the smaller particle size can greatly reduce the diffusion length of the lithium ions. There is growing interest in the preparation of nanostructure materials with specially designed structures. Nanostructured α-Fe_2O_3 with one-dimensional nanowire/nanotube structures,[177,265] two-dimensional flake/film structures,[266,267] and three-dimensional hollow/porous structures[262,268] has already been synthesized by a variety of methods, such as a sol-gel method,[269,270] electrostatic spray deposition,[271] a hydrothermal method,[272,273] and a template method.[179,274]

Since the discovery of MCM-41 mesoporous silica in 1992, mesoporous materials have been developed into an important class of materials and occupy a very important position in materials science.[275] The mesopore structure can dramatically increase the surface area/volume ratio, which makes mesoporous materials very useful surface-related applications. There is intense interest in preparing mesoporous transition-metal oxides because of their unique catalytic, magnetic, adsorptive, and electrochemical properties in applications as catalysts, magnetic materials, absorbents, and energy conversion and storage materials.[57,276-278] Several mesoporous transition metal oxides have already been synthesized, such as Co_3O_4, Mn_2O_3, Fe_2O_3, TiO_2, and V_2O_5, etc.[277,279-282] Nonetheless, it is still much more difficult to synthesize mesoporous transition-metal oxides than mesoporous silica. The materials with three-dimensional mesoporous architectures are normally obtained through template directed methods, which can be simply classified into the hard template method and the soft template method. The hard templates (usually mesoporous silica or carbon) normally possess well-defined channels and pores, which strongly influence the structure of the resulting solid product. Soft templates are usually surfactants, long-chain polymers, and viruses, which function as structure-directing agents that assist in the assembly of reacting species.[179] Yang et al. first reported the synthesis of a series of metal oxides by employing nonionic polymer surfactants as templates which could be easily removed by solvent extraction or thermal treatment.[283,284] The hard template methods usually involve a multistep synthesis process. Mesoporous silica or carbon must be prepared first. Then, the inorganic precursors are combined with the templates by impregnation

or incorporation. The final product can be obtained by template removal after the solid species has formed through reaction, nucleation, and growth. However, for the soft template methods, the templates can form by self-assembly in liquid solution and can be easily removed by solvent or calcination. Therefore, the soft template method is, generally, more easily scaled up for large-scale production than the hard template method. However, it is difficult to control the regularity, pore size, and pore structure using the soft template method. In this chapter, use of a soft template method in a nonaqueous solution to synthesize of mesoporous α-Fe_2O_3 nanostructures with large mesopores is reported. The as-prepared mesoporous α-Fe_2O_3 materials exhibit excellent high reversible lithium storage capacity in lithium ion cells.

5.2 Preparation of Mesoporous α-Fe_2O_3

In a typical synthesis, the triblock copolymer ($HO(CH_2CH_2O)_{106}(CH_2\text{-}CH(CH_3)O)_{70}(CH_2CH_2O)_{106}H$) (F127) and iron nitrate were used as the template and inorganic source, respectively. F127 block copolymer (1 g) was dissolved in a mixture of isopropanol (5 g) and ethylene glycol (EG; 5 g). To this solution, 0.01 mol $Fe(NO_3)_3 \cdot 9H_2O$ was added with vigorous stirring over 2 h. The resulting sol solution was then aged in air at 40 °C for 7 days before being gradually heated to 150 °C (1 °C min^{-1}) and then maintained at 150 °C for 24 h. Finally, the samples were further sintered at 400 °C for 5 h to remove the block copolymer surfactant (heating rate: 1 °C min^{-1}).

5.3 Physical and Structural Characterization

5.3.1 X-ray Diffraction

The crystal structure of the as-prepared material was first characterized by X-ray diffraction (XRD, GBC MMA) using Cu KR radiation with 2θ ranging from 20° to 70°. Figure 5-1 shows the powder X-ray diffraction (XRD) pattern of the as-prepared mesoporous α-Fe_2O_3 and the commercial α-Fe_2O_3 powder (Sigma-Aldrich). All diffraction peaks could be indexed to the standard hematite (α-Fe_2O_3) crystal structure (JCPDS card number 33-0664)[265] indicating that a pure and highly crystalline product was obtained by calcinating an iron oxide precursor. The average crystal size of mesoporous α-Fe_2O_3 was calculated to be about 20.6 nm on the basis of the broadening of the (104) diffraction peak using the Scherrer formula.

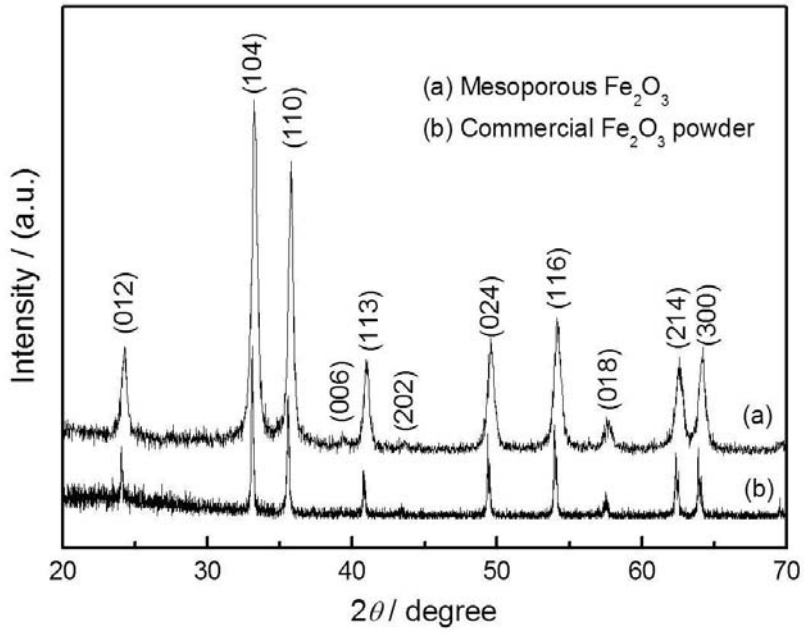

Figure 5-1 X-ray diffraction pattern of the as-prepared mesoporous and commercial α-Fe_2O_3.

5.3.2 Raman Spectroscopy

Raman spectra were collected on a JOBIN Yvon Horiba Confocal Mico Raman spectrometer model HR 800 with 632.8 nm diode laser excitation on a 300 lines mm^{-1} grating at room temperature. Figure 5-2 shows the Raman spectrum of the as-prepared mesoporous α-Fe_2O_3 along with a hematite reference spectrum (RRUFF ID R050300).[285] The spectrum indicates a typical α-Fe_2O_3 crystal structure showing Raman peaks at 224, 292, 410, 496, and 613 cm^{-1}, which matches well with the hematite reference spectrum. Compared to a previous report on α-Fe_2O_3 microcrystalline powders, all Raman peaks of our mesoporous α-Fe_2O_3 are slightly blue-shifted.[286] This may be due to the small size of the component nanocrystals. The Raman peak around 660 cm^{-1} in the spectrum has been reported in several published papers and is attributed

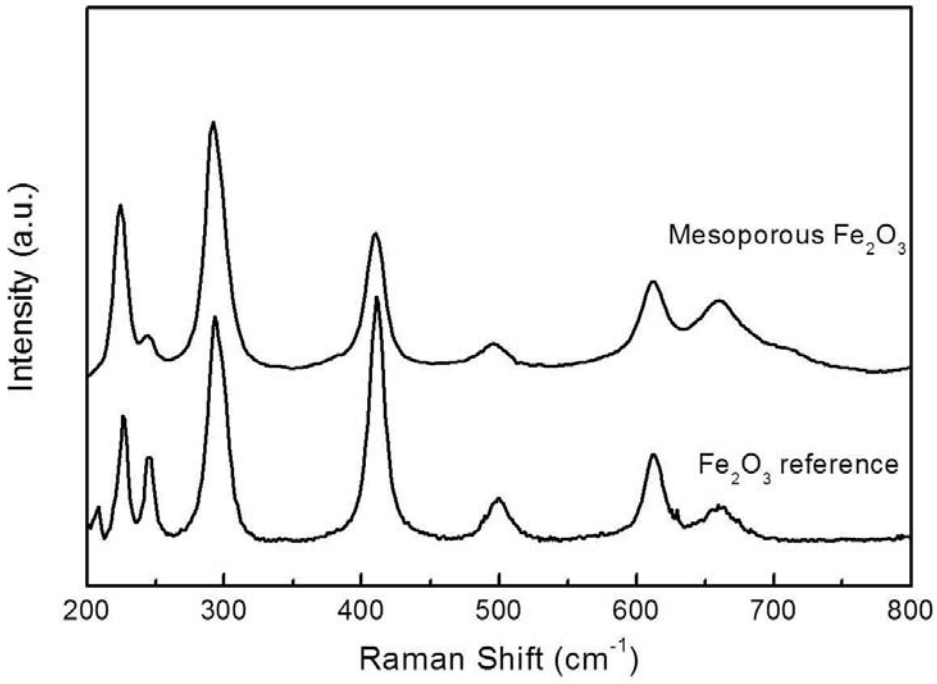

Figure 5-2 Raman spectrum of as-prepared mesoporous α-Fe_2O_3 and a hematite reference spectrum.

to a large amount of defects and local lattice disorder at the interfaces and interior faces, which leads to a reduction of space symmetry and the appearance of the new peak.[267,287] Both the XRD and Raman spectroscopy measurements confirmed the pure phase nature of mesoporous α-Fe_2O_3.

5.3.3 Ultraviolet-Visible Spectroscopy

The optical absorption property of the as-prepared mesoporous α-Fe_2O_3 was investigated at room temperature by UV-vis spectroscopy on a Shimadzu UV-1700 spectrophotometer (Figure 5-3). The band gap of hematite can be calculated by the following equation:

$$(\alpha h\nu)^2 = B \times (h\nu - E_g) \qquad \text{(Eq. 5-1)}$$

Where α is the absorption coefficient, $h\nu$ is the photon energy, B is a constant, and E_g is the band gap. The $(\alpha h\nu)^2$ versus $h\nu$ curve is shown as the inset in Figure 5-3. The band gap of the as-prepared mesoporous α-Fe_2O_3 calculated from Eq. 5-1 is 2.14 eV, which agrees well with previously reported values of 1.9-2.2 eV for n-type semiconductor α-Fe_2O_3.[288,289]

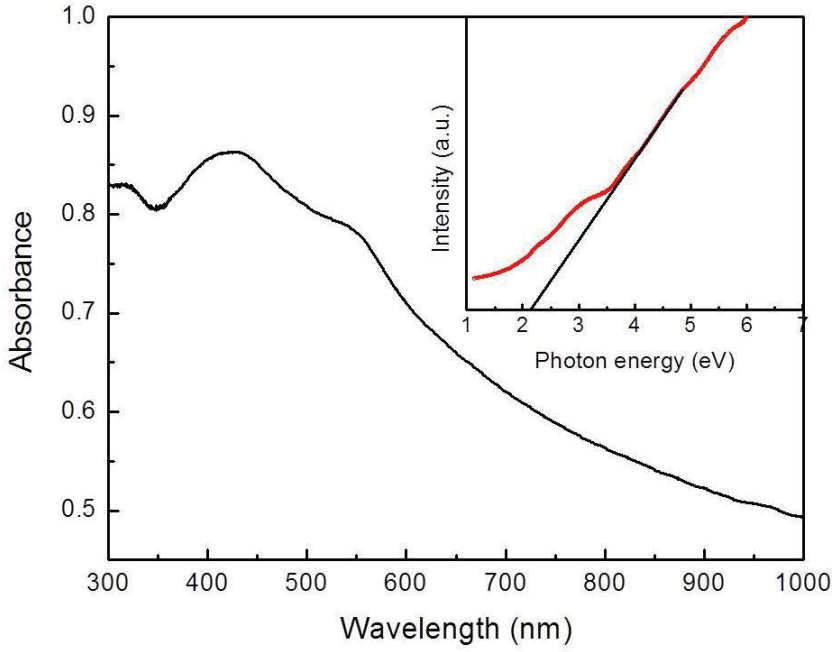

Figure 5-3 UV-vis spectrum of mesoporous α-Fe_2O_3.

5.3.4 Brunauer-Emmett-Teller

To examine the specific surface area and the pore size distribution, N_2 adsorption-desorption isotherm measurements were carried out on a Quantachrome Autosorb analyzer at 77 K with the samples degassed at 120 °C overnight under vacuum before measurements. The curve shown in Figure 5-4a depicts a typical H2-type hysteresis loop, which makes it clear that the distribution of the pore sizes and shapes is heterogeneous.[262] The pore size distribution, obtained from the Barrett-Joyner-Halenda (BJH) method, is shown in Figure 5-4b. The plot shows that the dominant peaks are in the mesoporous range with a wide main peak around 7 nm and a small narrow peak at 15 nm.[290] The two main peaks in pore size distribution suggest that the mesopores are distributed over a wide range of sizes. The surface area estimated

from the Brunauer-Emmett-Teller (BET) method is 128 m^2 g^{-1}. The high surface area of the mesoporous structures will be of benefit for increasing reversible lithium storage capacity as anode material in lithium-ion batteries.

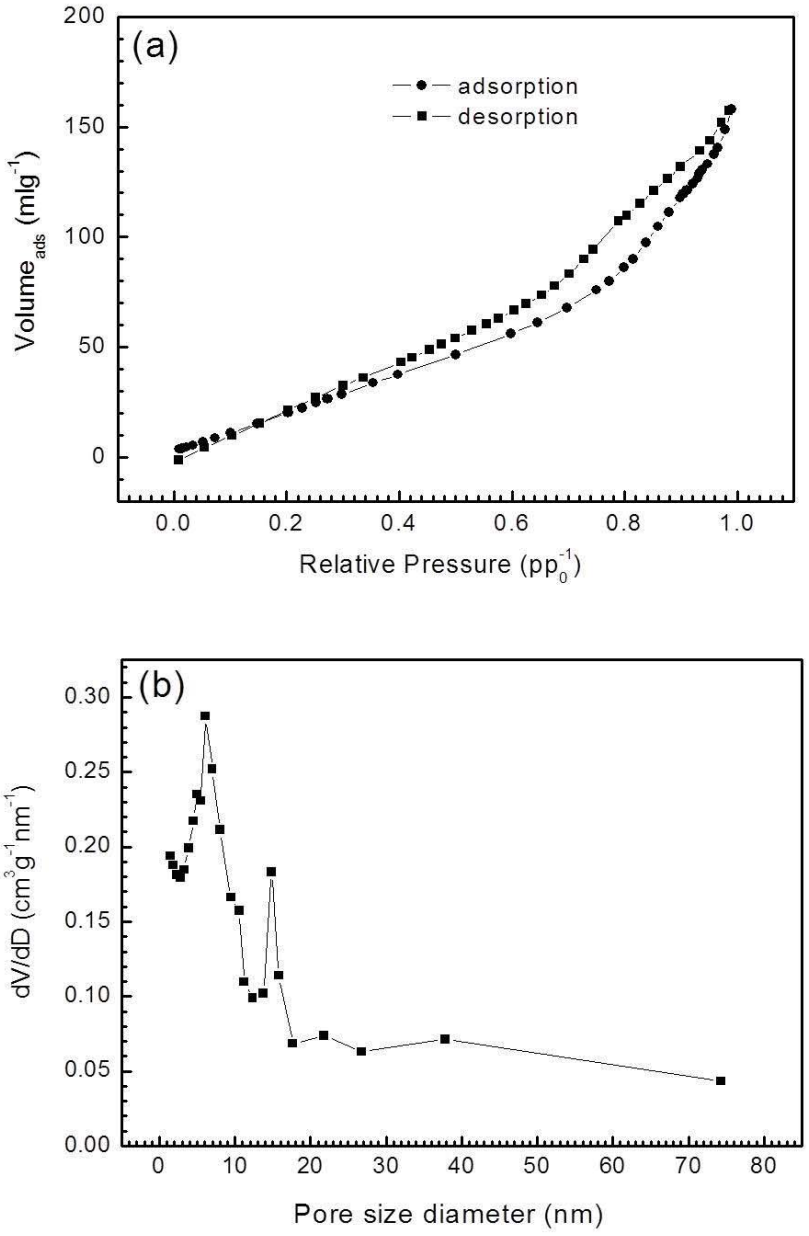

Figure 5-4 (a) Adsorption-desorption isotherms of mesoporous α-Fe_2O_3, and (b) Pore size distribution calculated from the desorption isotherm.

5.3.5 Transmission Electron Microscopy

The morphology and microstructures were characterized by transmission electron microscopy (TEM) and high-resolution TEM (HRTEM, JEOL 2011). Figure 5-5 shows the TEM and HRTEM images of the as-prepared mesoporous α-Fe_2O_3 powders. The prepared material exhibits an ordered porous structure with different shapes of pores as shown in Figure 5-5a. Pores in the iron oxide materials originate from the regions previously occupied by the polymer surfactants. After the removal of the surfactant, some walls of the porous structure collapse and form a wormhole-like morphology. The selected area electron diffraction (SAED) pattern is presented in the inset of Figure 5-5a showing a single crystalline-like SAED dot pattern. The HRTEM image in Figure 5-5b clearly presents the lattice fringes of the (110) and (102) planes of α-Fe_2O_3 corresponding to *d*-spacings of 0.250 and 0.388 nm. Both the HRTEM images and the SAED pattern confirm the formation of single-crystalline mesoporous α-Fe_2O_3.

5.4 Electrochemical Performance

The electrochemical performance of the as-prepared mesoporous α-Fe_2O_3 and commercial α-Fe_2O_3 (mico-size particles) was evaluated by cyclic voltammetry (CV) and galvanostatic charge-discharge. The experiments were carried out in coin cells (CR2032). The electrode composition was 50 wt % of the as-prepared materials, 40 wt % of carbon black, and 10 wt % of polyvinylidene fluoride (PVDF). The electrolyte solution was 1 M $LiPF_6$ dissolved in a mixture of ethylene carbonate (EC) and dimethyl carbonate (DMC) with a volume ratio of 1:1.

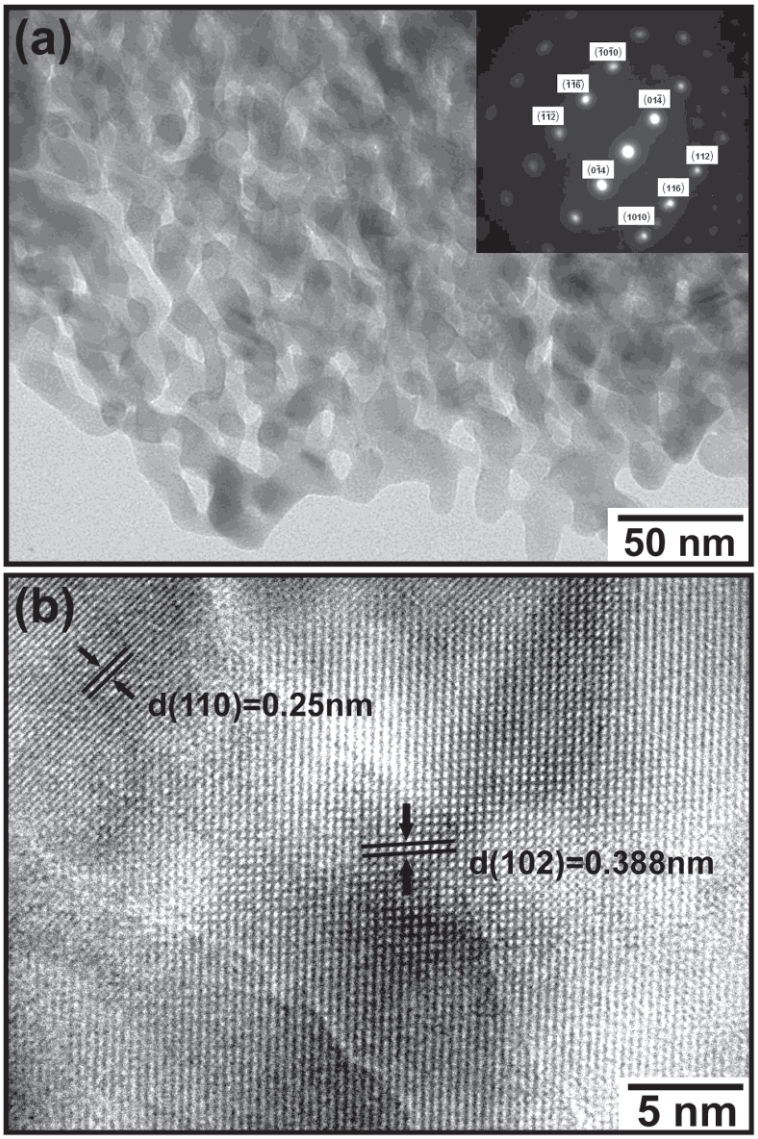

Figure 5-5 (a) TEM image of mesoporous α-Fe_2O_3. The inset is the corresponding selected area electron diffraction (SAED) pattern. (b) HRTEM image of mesoporous α-Fe_2O_3, in which the Fe_2O_3 lattice can be clearly resolved.

5.4.1 Cyclic Voltammetry

The electrochemical behavior of the electrode made from the as-prepared mesoporous α-Fe_2O_3 was first evaluated by cyclic voltammetry (CV), which was carried out on a CHI 660C electrochemistry workstation with a scan rate of 0.1 mV s^{-1} from 0.005 to 3.0

V in a two-electrode system. Figure 5-6 shows the CV curves of the mesoporous α-Fe_2O_3 and commercial α-Fe_2O_3 anode. During the cathodic polarization in the first cycle, a spiky peak was observed at 0.65 V with two small peaks appearing at 1.0 and 1.6 V indicating the following three lithiation steps.[263,264]

$$\alpha\text{-}Fe_2O_3 + xLi^+ + xe^- \rightarrow \alpha\text{-}Li_xFe_2O_3 \quad \text{(Eq. 5-2)}$$

$$\alpha\text{-}Li_xFe_2O_3 + (2\text{-}x)Li^+ + (2\text{-}x)e^- \rightarrow Li_2Fe_2O_3 \text{ (cubic)} \quad \text{(Eq. 5-3)}$$

$$Li_2Fe_2O_3 \text{ (cubic)} + 4Li^+ + 4e^- \leftrightarrow 2Fe^0 + 3Li_2O \quad \text{(Eq. 5-4)}$$

$$\alpha\text{-}Fe_2O_3 + 6Li^+ + 6e^- \rightarrow 2Fe^0 + 3Li_2O \quad \text{(Eq. 5-5)}$$

At the initial stage of lithium intercalation (peak I), a small amount of lithium can be inserted into the crystal structure of the as-prepared mesoporous α-Fe_2O_3 without causing change in the structure. In the next step of lithium intercalation (peak II), the hexagonal α-$Li_xFe_2O_3$ is transformed to cubic $Li_2Fe_2O_3$. The spiky peak (peak III) corresponds to the complete reduction of iron from Fe^{2+} to Fe^{0+} and decomposition of the electrolyte. On the other hand, in the anodic polarization process, two broad overlapping peaks were recorded at about 1.7 and 1.85 V corresponding to the oxidation of Fe^0 to Fe^{2+} and further oxidization to Fe^{3+}.[291] The curves of the subsequent cycles are significantly different from that of the first cycle as only one cathodic peak appears at about 0.8 V with decreased peak intensity, while the anodic polarization only showed one broad peak with a little decrease in peak intensity. The difference between the first and the second cathodic curves is due to an irreversible phase transformation during the process of lithium insertion and extraction in the initial cycle. After the first discharge

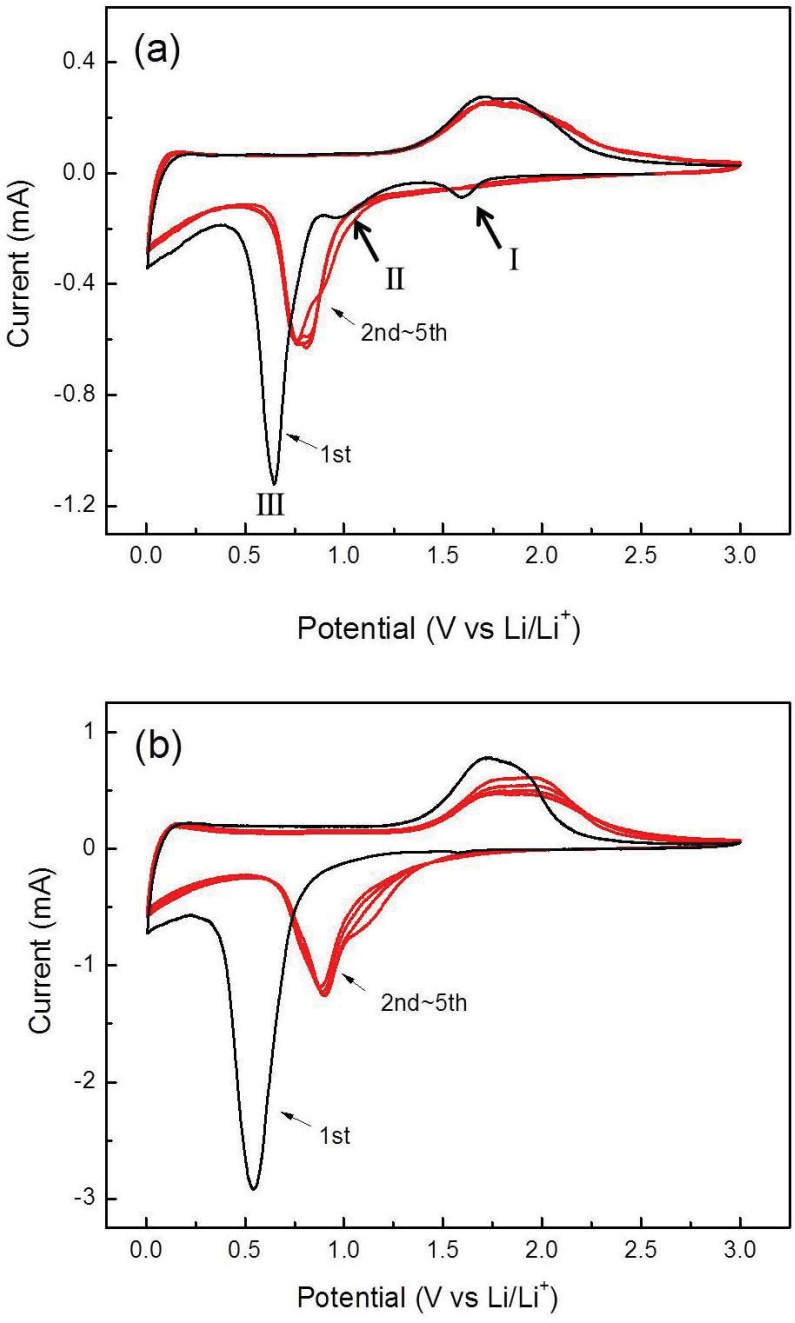

Figure 5-6 Cyclic voltammentry (CV) curves of the cell with anode prepared from (a) mesoporous and (b) commercialα-Fe_2O_3 (scanning rate: 0.1 mV s^{-1} in the range of 0.005-3.0 V).

process, α-Fe_2O_3 was completely reduced to iron nanoparticles and was dispersed in a Li_2O matrix.[173] The disappearance of the peaks at 1.6 V and 1.0 V from the second cathodic process indicates that the lithium insertion reaction and phase transformation

from hexagonal α-$Li_xFe_2O_3$ to cubic $Li_2Fe_2O_3$ are irreversible.[291] The decrease of the redox peak intensity implies that the capacity is decreased during cycling. After the second cycle, the CV curves are very stable for the mesoporous α-Fe_2O_3 electrode indicating enhanced stability during the lithiation and delithiation processes.

The CV curves of the commercial electrode also showed a spiky cathodic peak at about 0.55 V and two broad anodic peaks around 1.7~1.8 V, corresponding to the reduction and oxidation of Fe^{3+}. The peak position also significantly changed from the second cycle indicating an irreversible structure change after first cycle lithiuation and delithiation. From the second cycle, the current peaks continue to decrease for the commercial α-Fe_2O_3 electrode indicating capacity loss during cycling. The electrode made of mesoporous α-Fe_2O_3 showed higher electrochemical activity than the commercial product.

5.4.2 Galvanostatic Charge-Discharge

The charge-discharge measurements were carried out at ambient temperature at different current densities in the voltage range from 0.005 to 3.0. The charge-discharge curves of the mesoporous and commercial α-Fe_2O_3 electrode during the first and second cycles are shown in Figure 5-7, and these are typical charge-discharge curves for transition metal anode materials.[173] For the discharge curve of the mesoporous α-Fe_2O_3 electrode in the first cycle, the voltage initially decreased quickly to approximately 1.6

V followed by a weak slope corresponding to the initial lithium insertion into the α-Fe_2O_3 without causing any change of the α-Fe_2O_3 structure. There was also a wide slope located at 1.2-0.85 V, where there was a phase transformation from the hexagonal α-$Li_xFe_2O_3$ to the cubic $Li_2Fe_2O_3$. An obvious plateau was observed at 0.85 V indicating the complete reduction of iron from Fe^{2+} to Fe^{0+}. This electrochemical behavior is consistent with the results of the CV measurement. The capacity obtained above 0.8 V was 940 mAh g^{-1} (5.6 mol of Li per mole of α-Fe2O3), which is very close to the theoretical capacity of 1007 mAh g^{-1} (6 mol of Li per mole of α-Fe_2O_3). After discharging the voltage to 0.005 V, the total specific capacity of the as-prepared mesoporous α-Fe_2O_3 was 1730 mAh g^{-1} corresponding to 10.3 mol of Li per mole of α-Fe_2O_3, which is much higher than the theoretical capacity. For the discharge curve of the commercial α-Fe_2O_3 electrode in the first cycle, the voltage quickly decreased to 0.85 V and then sloped to 0.005 V. The initial discharge capacity of the commercial α-Fe_2O_3 was 1435 mAh g^{-1} corresponding to 8.5 mol of Li per mole of α-Fe_2O_3, which is much lower than the mesoporous α-Fe_2O_3, but still higher than the theoretical capacity of α-Fe_2O_3. The large excess capacity could be ascribed to decomposition of the electrolyte at low voltage (generally below 0.8 V vs Li^+/Li) to form a solid electrolyte interphase (SEI) layer and to further lithium storage via interfacial charging at the metal/Li_2O interface.[51,52,292,293] During the second cycle, the discharge curve only showed a slope at 1.0-0.8 V, and the capacities were reduced to 1360 mAh g^{-1} for mesoporous α-Fe_2O_3 electrode and 999 mAh g^{-1} for commercial α-Fe_2O_3 electrode. Usually, the slope behavior during the discharge process of metal oxide anode materials

is considered to relate to the irreversible formation of a nanocomposite of crystalline grains of metals and amorphous Li_2O matrix.[51,294] For the charge curves of the first and second cycles of mesoporous α-Fe_2O_3 electrode, no obvious plateau can be observed and the charge capacities are 1200 mAh g^{-1} and 1250 mAh g^{-1}, respectively, corresponding to the oxidation of Fe^0 to Fe^{2+}, with part of the Fe further oxidized to Fe^{3+}, along with some contribution from the reversible surface layer formed during the discharge process. The commercial α-Fe_2O_3 exhibited much lower charge capacity, with a charge capacity of 974 mAh g^{-1} in the first cycle and 958 mAh g^{-1} in the second cycle, respectively. It has been demonstrated in previous reports that the morphology of Fe_2O_3 plays a significant role in the discharge performance.[266,295] Materials that have small particles with high surface area always yield high charge-discharge capacities indicating that high surface area can enhance the interfacial charge storage. Our experimental results are consistent with those previous reports.

The cycling performances of the mesoporous α-Fe_2O_3 electrode and the commercial electrode are shown in Figure 5-8. The mesoporous α-Fe_2O_3 electrode demonstrates an excellent cycling performance. The second discharge cycle for the mesoporous α-Fe_2O_3 electrode capacity was 1360 mAh g^{-1} at a current rate of 200 mA g^{-1} (0.2C). After 50 cycles, the specific discharge capacity was 1293 mAh g^{-1}, which is about 95% of the second cycle discharge capacity and represents a 0.1% capacity drop per cycle if the first cycle is excluded. In contrast, the cycle discharge capacity of the commercial α-Fe_2O_3 electrode, continued decreasing as the cycle number increased: from 999 mAh

g^{-1} at the second cycle to 656 mAh g^{-1} at the fiftieth cycle, with the capacity loss more than 34% of the second cycle discharge capacity. Both samples showed good coulombic efficiencies from the fifth cycle, above 95%. The excellent capacity retention of mesoporous α-Fe_2O_3 should be related to the mesoporous structure of the material, which can accommodate the volume change of the Li^+ insertion/extraction during the charge-discharge process and prevent the active materials from falling off the current collector.[52,296]

The charge-discharge performances of mesoporous α-Fe_2O_3 and commercial α-Fe_2O_3 electrodes at different current densities were also investigated (as shown in Figure 5-9). The discharge capacities of the electrodes made of mesoporous α-Fe_2O_3 were 1381 mAh g^{-1}, 1259 mAh g^{-1}, 1150 mAh g^{-1}, 1087 mAh g^{-1} and 877 mAh g^{-1}, at 0.1 C, 0.2 C, 0.5 C, 1 C and 2 C, respectively, which is much higher than the theoretical capacity of graphite (372 mAh g^{-1}). The capacity retention of mesoporous α-Fe_2O_3 was 63.5 % from 0.1 C to 2 C. The discharge capacities of the electrodes made of commercial α-Fe_2O_3 were 1021 mAh g^{-1}, 843 mAh g^{-1}, 629 mAh g^{-1}, 557 mAh g^{-1} and 309 mAh g^{-1}, at 0.1 C, 0.2 C, 0.5 C, 1 C and 2 C, respectively, with a capacity retention of 30.2 % from 0.1 C to 2 C. The mesoporous α-Fe_2O_3 showed much better C-rate performance than the commercial micro-size α-Fe_2O_3. The mesoporous structure with its high surface area provides high surface contact with the electrolyte and decreases the current density per unit area. The excellent cycling stability and high rate specific capacity of the as-prepared mesoporous

α-Fe_2O_3 indicate its attractive potential for use as an anode material in lithium-ion batteries.

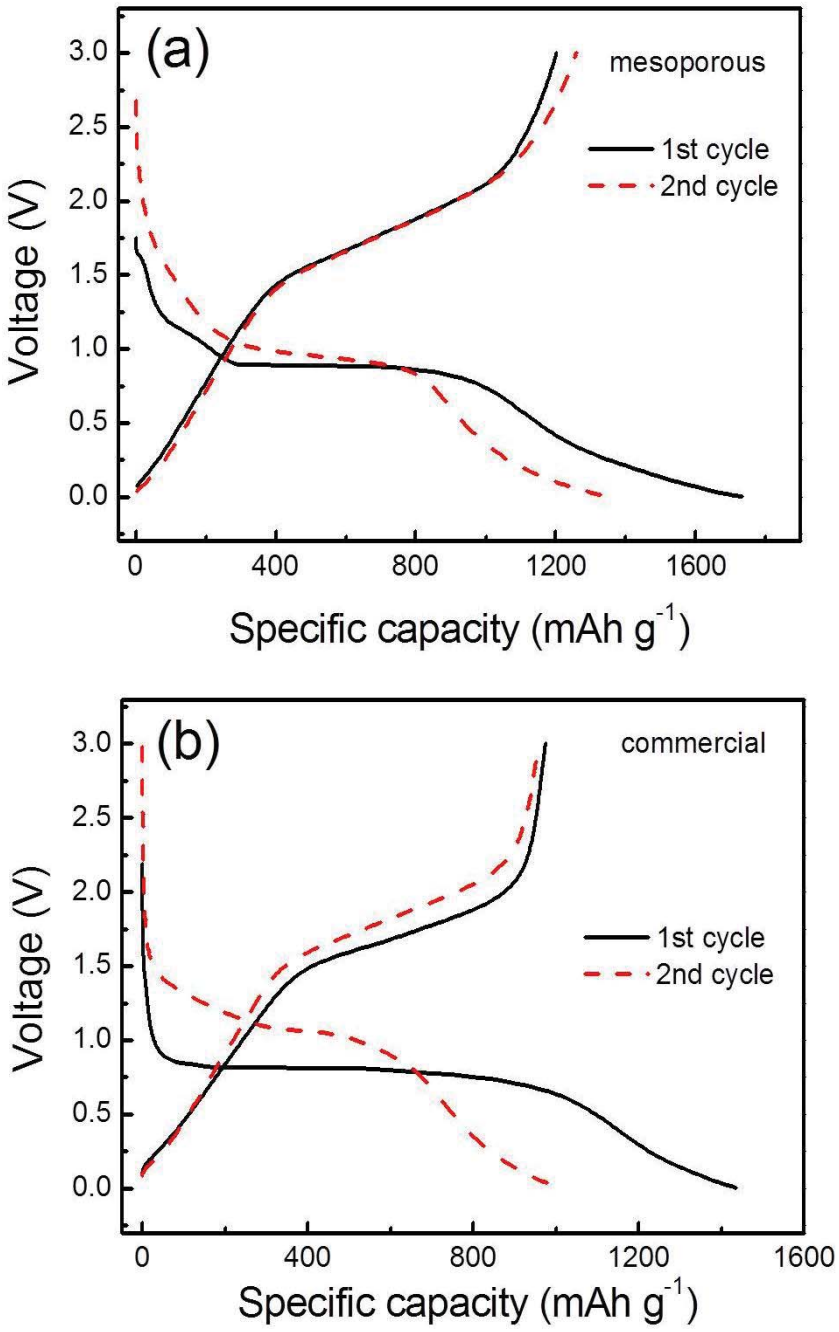

Figure 5-7 Charge-discharge voltage profiles of the electrodes made of (a) mesoporous α-Fe_2O_3 and (b) commercial α-Fe_2O_3.

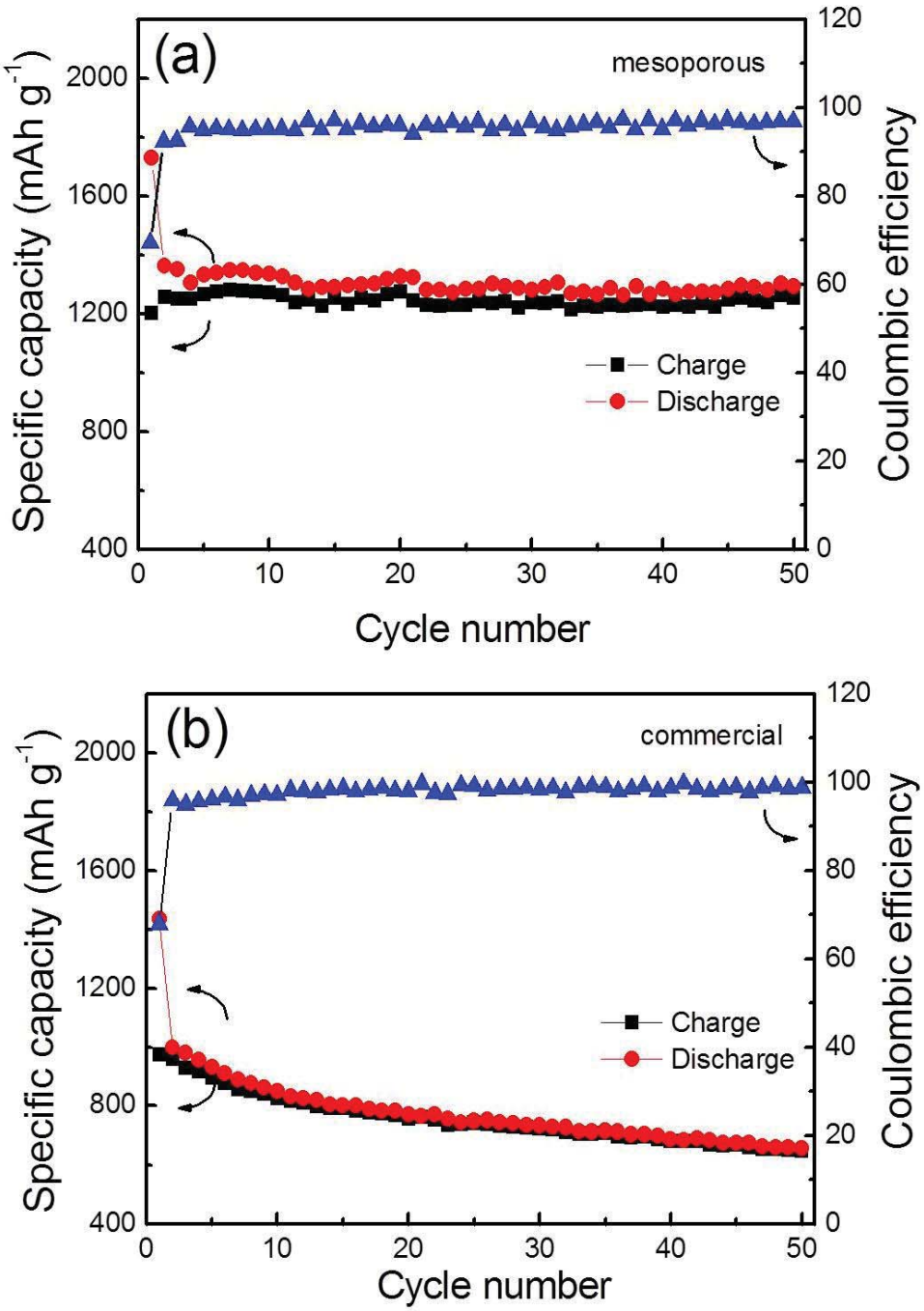

Figure 5-8 Cycling performance and coulombic efficiencies of the electrodes made of (a) mesoporous α-Fe_2O_3 and (b) commercial α-Fe_2O_3.

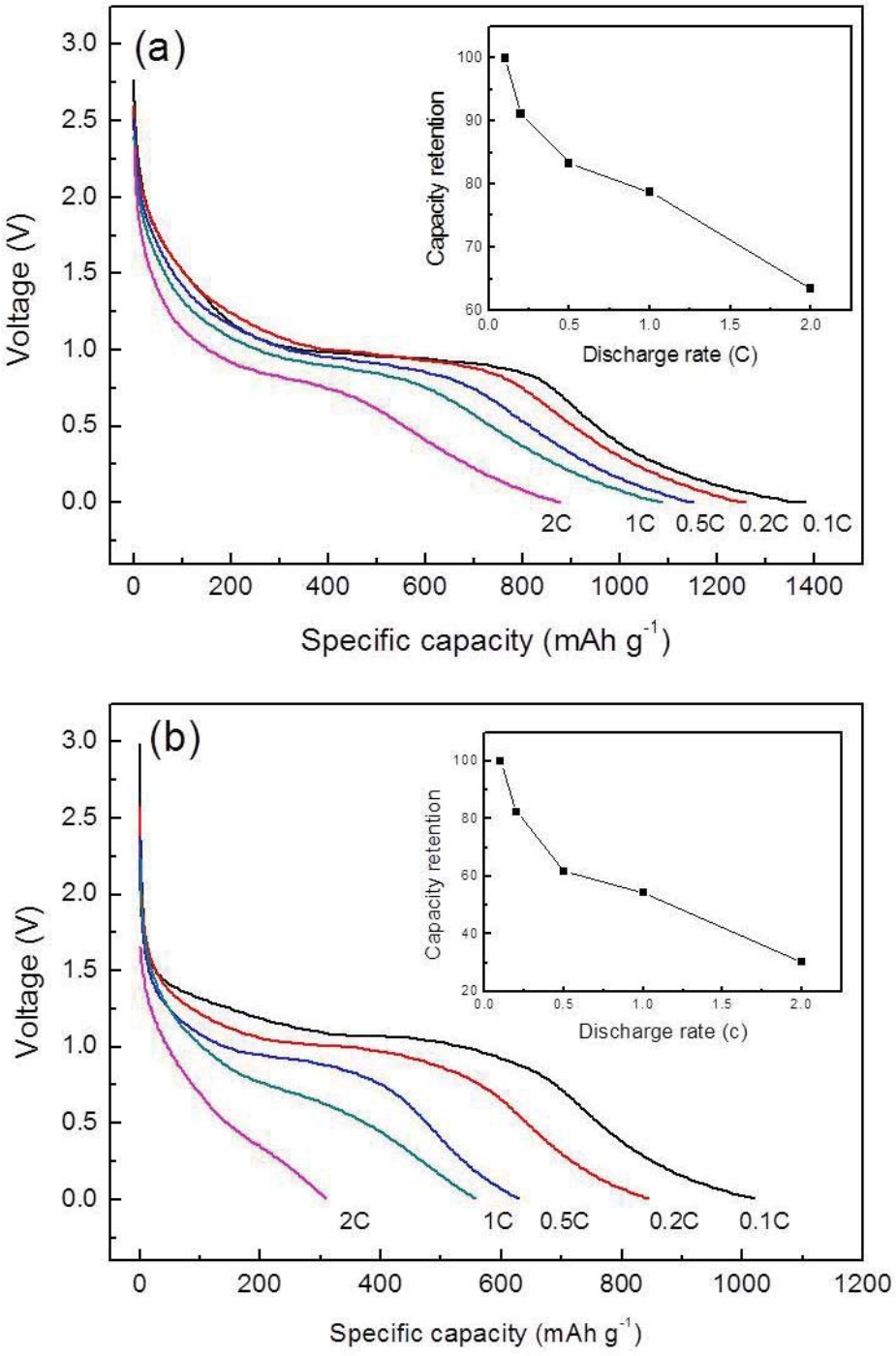

Figure 5-9. Discharge voltage profiles of the electrode made of (a) mesoporous and (b) commercial α-Fe_2O_3 at different C-rates (1 C=1000 mA g^{-1}). The insert is the capacity retention at different C-rates.

5.5 Summary

A soft template synthesis method was used to successfully prepare mesoporous α-Fe_2O_3. The as-prepared material shows a highly porous structure with a large surface area of 128 m^2 g^{-1}. As an anode material in lithium-ion batteries, the as-prepared mesoporous α-Fe_2O_3 shows much better electrochemical performance than the commercial micro-sized α-Fe_2O_3, with a high discharge specific capacity of 1730 mAh g^{-1} at the first cycle and 1293 mAh g^{-1} at the fiftieth cycles. The mesoporous α-Fe_2O_3 also showed excellent high-rate performance with a discharge capacity of 877 mAh g^{-1} at 2 C-rate. The good cycling stability and high rate specific capacity indicate it could potentially be applied to the lithium-ion battery industry.

CHAPTER 6 MnO/C CORE-SHELL NANORODS FOR LITHIUM-ION BATTERIES

6.1 Introduction

Transition metal oxides have attracted great attention as anode materials for lithium-ion batteries. However, there are still many challenges in using them as anode materials for lithium-ion batteries. One of them is the poor cycling performance, resulting from large volume expansion during the charge-discharge process due to the generation of Li_2O. Another obstacle is their poor electronic conductivity, which limits their power performance. It has been demonstrated that electrode materials with a deliberately designed nanostructure can partly accommodate the strains of Li^+ intercalation and de-intercalation, and the cycling performance can be improved.[271] Furthermore, coating these semiconducting materials with carbon or a conductive polymer can significantly enhance the electronic conductivity of the electrode materials with a resultant improvement in rate performance.[297,298] Recently, various manganese oxides (MnO_x) (e.g. MnO_2, Mn_2O_3, Mn_3O_4 and MnO) have been investigated for their potential use as anode materials. Fang et al. reported that, for all the different manganese oxides, metallic Mn and Li_2O are the end discharge products at 0.01 V and MnO is the end charge product at 3.0 V. MnO is the most promising anode material among all the manganese oxides for lithium-ion batteries due to its high reversible capacity.[299] Furthermore, MnO has a relatively low electromotive force (emf) value (1.032 V vs.

Li^+/Li) and high density (5.43 g cm^{-3}).[300,301] In this chapter, MnO/C core-shell nanorod material was prepared through a thermal reduction reaction and its electrochemical performance as an anode material for lithium-ion batteries. In use as an anode material for lithium-ion battery, the prepared MnO/C core-shell nanorods showed much higher specific capacity than that of MnO microparticles and MnO_2 nanowires.

6.2 Preparation of MnO_2 Nanowires, MnO/C Core-Shell Nanorods and MnO Microparticles

MnO/C core-shell nanorods were synthesized by the reduction of carbon precursor coated MnO_2 nanowires. The MnO_2 nanowires were synthesized by a typical hydrothermal method according to previously reported procedures.[302] Thirty five ml of distilled water was used in dissolving 0.7 mmol $KMnO_4$ (Sigma-Aldrich) and 0.7 mmol NH_4Cl to form a transparent solution under stirring. The solution was sealed in a Teflon-lined stainless steel autoclave and kept at 140 °C for 24 h. After cooling down to room temperature, the precipitate was collected by filtration and rinsed with distilled water and absolute alcohol several times, and then dried in a vacuum oven at 60 °C overnight. Non-ionic block co-polymer poly (ethylene oxide)-block-poly (propylene oxide)-block-poly (ethylene oxide)-($EO_{106}PO_{70}EO_{106}$) Pluronic® F127 (Sigma-Aldrich) was used as the carbon precursor for carbon coating in this work. Twenty nine mg F127 was first dissolved in 10 ml ethanol to form a transparent solution. Then, 56 mg MnO_2 nanowires were added to the solution and ultrasonicated for 30 min in a sealed bottle. After drying under stirring at room temperature, the product was ground into powder

and sintered at 500 °C for 5 h in flowing Ar containing 5 vol.% H_2.

6.3 Physical and Structural Characterization

6.3.1 X-ray Diffraction

The crystal structure of the as-prepared materials was characterized by X-ray diffraction (XRD, GBC MMA) using Cu Kα radiation, with 2θ ranging from 10° to 80°. The XRD patterns of as-prepared MnO_2 nanowires, MnO/C nanorods and MnO microparticles are shown in Figure 6-1. For the MnO_2 nanowires, all the diffraction peaks of the XRD pattern can be indexed to the body-centered tetragonal α-MnO_2 phase (JCPDS 44-0141). MnO/C nanorods and MnO microparticles were obtained from the reduction of MnO_2 nanowires in flowing Ar containing 5 vol.% H_2. As shown in Figure 6-1, the crystal structure of both the MnO/C nanorods and the MnO microparticles can be indexed to the face-centered cubic phase of MnO (JCPDS 07-0230).

6.3.2 Field Emission Scanning Electron Microscopy

The morphologies of the as-prepared materials were observed by field emission scanning electron microscopy (FESEM, JEOL 7500) and are shown in Fig. 6-2. The as-prepared MnO_2 shows a nanowire structure with length up to several micrometers and diameters ranging from 20-50 nm (Figure 6-2a and b). After reducing to carbon coated MnO, the nanowire structures fractured into nanorod structures (Figure 6-2c). There was no significant change in diameter. Figure 6-2d shows the morphology of

MnO obtained from the reduction of MnO_2 nanowires without carbon coating. The nanowire structure agglomerated into big microsized particles, indicating the carbon coating technique can prohibit particle growth during the calcination process.

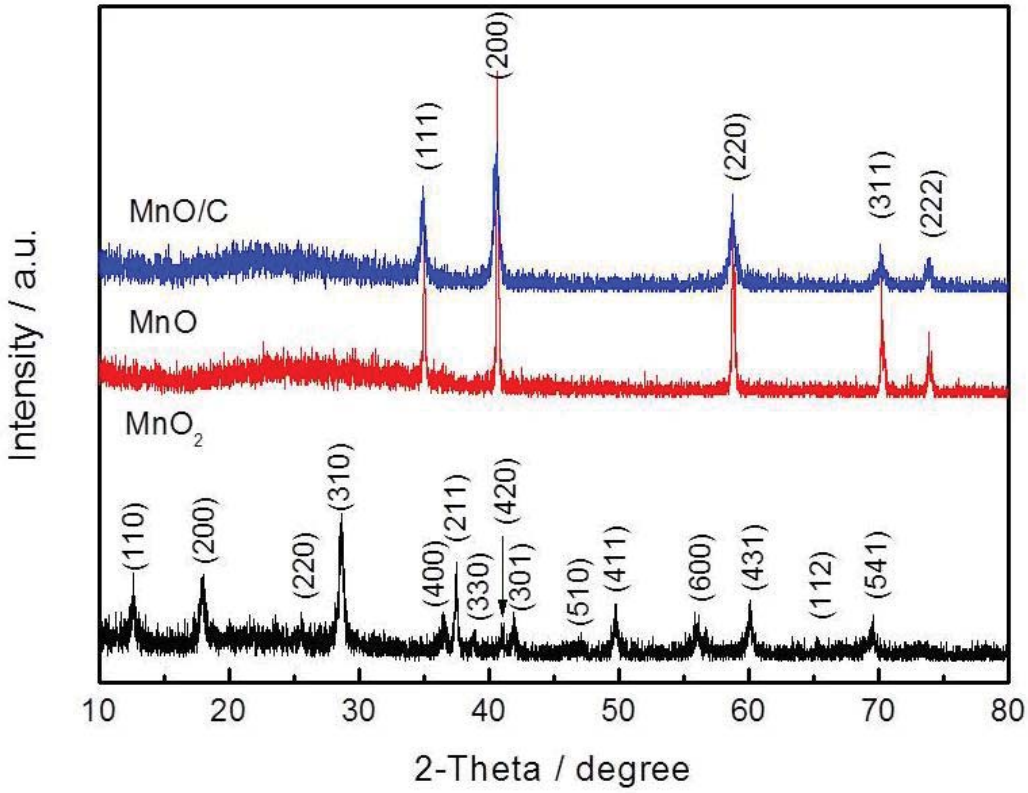

Figure 6-1 X-ray diffraction patterns of the as-prepared MnO/C core-shell nanorods, MnO microparticles and MnO_2 nanowires.

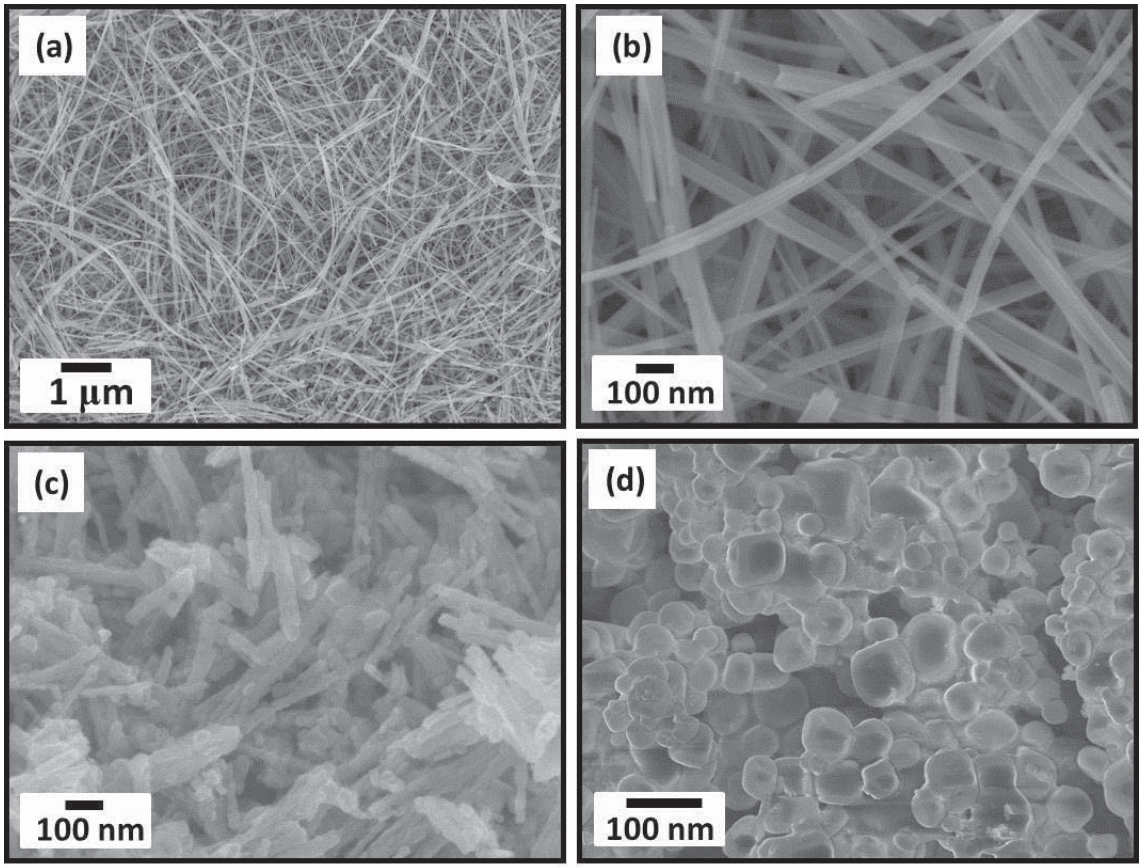

Figure 6-2 FESEM images of (a) and (b) MnO_2 nanowires, (c) MnO/C core-shell nanorods and (d) MnO microparticles.

6.3.3 Transmission Electron Microscopy

More structural details of the MnO/C core-shell nanorods were further analyzed by transmission electron microscopy (TEM, JEOL 2011) and selected area electron diffraction (SAED). Low magnification TEM images are shown in Figure 6-3a and b. The nanorods show a polycrystalline feature and are agglomerated into bundles with a length extending to a few hundred nanometers. The fracturing of the nanowire structure into nanorods may be caused by the reduction of MnO_2 to MnO. An individual nanorod consists of nanoparticles with diameters from 20nm to 30 nm. The corresponding SAED pattern is shown as the inset in Figure 6-3b. All the diffraction rings can be indexed to

the face-centered cubic Fm-3m crystal structure. A HRTEM image is presented in Figure 6-3c. In the region A, we can clearly observe that the image is in focus on the surface of the MnO crystal, and the lattice can be clearly resolved with a d-spacing of 0.255nm for the (1 1 1) planes. However, in region B at the same level, the image is focused on the carbon layer, which presents numerous black spots, indicating that the surface of the nanorod is covered with a thin layer of amorphous carbon. On the edge of the nanorod, a thin carbon layer with a thickness of 1-2 nm is clearly visible.

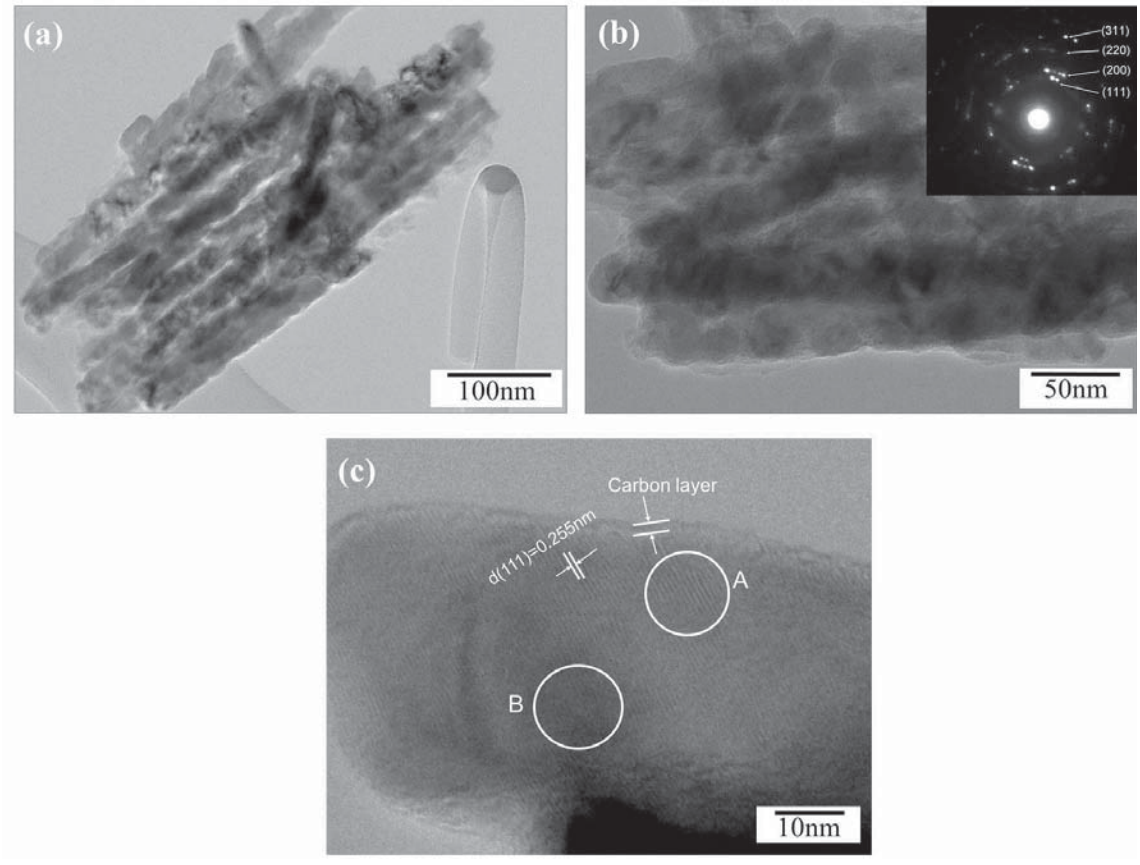

Figure 6-3 (a and b) TEM images of MnO/C core-shell nanorods, with the inset in (b) showing the corresponding SAED pattern, and (c) HRTEM image of MnO/C core-shell nanorods.

6.4 Electrochemical Performance for Lithium-Ion Batteries

The electrochemical performance of the as-prepared materials was evaluated by galvanostatic charge-discharge and cyclic voltammetry (CV). The experiments were carried out in coin cells (CR2032). The electrode composition was 70 wt % of the as-prepared materials, 20 wt % of carbon black, and 10 wt % of polyvinylidene fluoride (PVDF). The electrolyte solution was 1M $LiPF_6$ in a 1:1 mixture of ethylene carbonate (EC) and dimethyl carbonate (DMC).

The electrochemical behavior of the prepared MnO/C nanorods, MnO microparticles and MnO_2 nanowires were initially characterized by cyclic voltammetry (CV) using a CHI660C electrochemical workstation, as shown in Figure 6-4. The CV curves of MnO/C core-shell nanorod electrode showed two small peaks at 1.86 V and 1.53 V in the first negative scan process; these disappeared in the subsequent cycles. These reduction peaks may correspond to the reduction of Mn^{3+} or Mn^{4+} to Mn^{2+}; the Mn^{3+} or Mn^{4+} could have originated from a trace MnO_{1+x} impurity resulting from the incomplete reduction of MnO_2 in the sintering process. The main cathodic peak was close to 0.1 V, corresponding to the complete reduction of Mn^{2+} to Mn^0 and the formation of a solid electrolyte interphase (SEI) layer with a reversible polymer/gel like film.[303,304] From the second cycle, the reduction current peaks shifted to 0.3 V, indicating an irreversible phase transformation due to the formation of Li_2O and metallic manganese. In the anodic polarization process, one main peak appeared at around 1.3 V, and a weak peak was recorded at 2.1 V, corresponding to the oxidation of Mn^0 to Mn^{2+} and the

decomposition of the polymer/gel layer at a high oxidation potential above 2.0 V.[303] After the second cycle, the CV curves became stable and overlapped. The MnO microparticle electrode and the MnO_2 nanowire electrode showed CV curves similar to the MnO/C nanorod electrode. However, the peak intensities of the MnO microparticle electrode and MnO_2 nanowire electrode continued to decrease with cycling, indicating poor cycling stability.

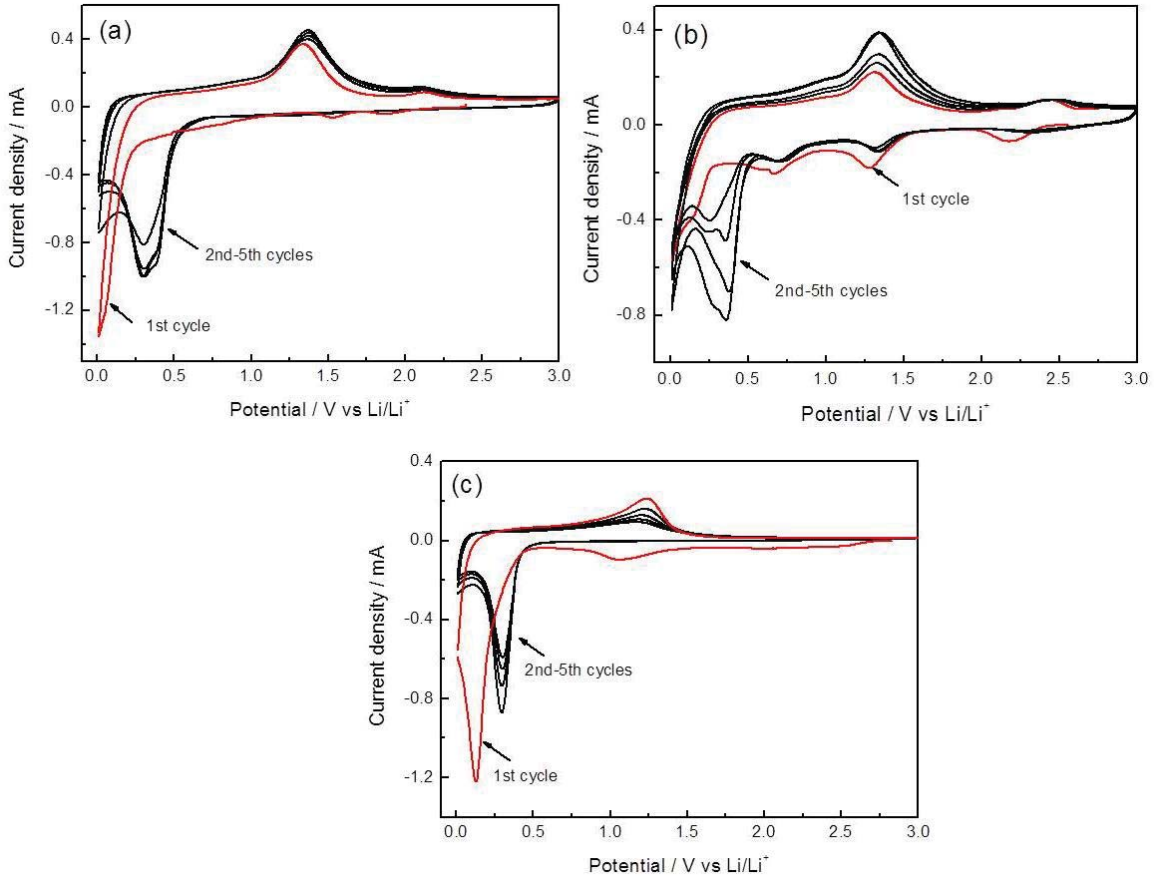

Figure 6-4 Cyclic voltammetry (CV) curves of (a) MnO/C core–shell nanorod electrode, (b) MnO microparticle electrode and (c) MnO_2 nanowire electrode. Scanning rate: 0.2 mV s^{-1} in the range of 0.01-3.0V.

The electrochemical performances were further investigated by charge-discharge measurements with cycling at a current density of 200 mA g^{-1} between 0.01 and 3.0 V

at ambient temperature. In the first discharge curve of the MnO/C core-shell nanorod electrode shown in Figure 6-5a, the voltage dropped quickly to a plateau at about 0.28 V, and then decreased slowly to 0.01 V, associated with the complete reduction of Mn^{2+} to Mn^0. The initial charge curve of the MnO/C core-shell nanorod electrode showed a slope in the voltage range between 1.0 and 1.5 V, related to the oxidation of Mn^0 to Mn^{2+}. The voltage plateau for this reaction should be at the emf value of 1.032V vs. Li^+/Li at 298K for perfect bulk materials.[300,301] The difference in the plateau position is considered to be caused by the cathodic over-potential, which has already been studied by Zhong et al. using the galvanostatic intermittent titration technique (GITT).[305] The voltage profiles of the MnO microparticle electrode and MnO_2 nanowire electrode were similar to the MnO/C core-shell nanorod electrode except for the position of the charge-discharge plateau (Figure 6-5b and c). The initial discharge capacities of the MnO/C nanorods, MnO microparticles and MnO_2 nanowires were 1090 mAh g^{-1}, 881 mAh g^{-1} and 1319 mAh g^{-1}, respectively, which are larger than their theoretical capacities. The theoretical capacity for MnO is 755 mAh g^{-1} and MnO_2 has a theoretical capacity of 1232 mAh g^{-1}. The exceeding capacities could be ascribed to the decomposition of the electrolyte at low voltage (generally below 0.8 V vs Li^+/Li) to form a solid electrolyte interphase (SEI) layer and further lithium storage via interfacial charging at the metal/Li_2O interface.[51] As shown in Figure 6, the discharge plateaus of the MnO/C core-shell nanorod electrode, MnO microparticle electrode and MnO_2 nanowire electrode shifted to about 0.5 V from the second cycle, indicative of the irreversible formation of crystalline metal nanoparticles and an amorphous Li_2O matrix.

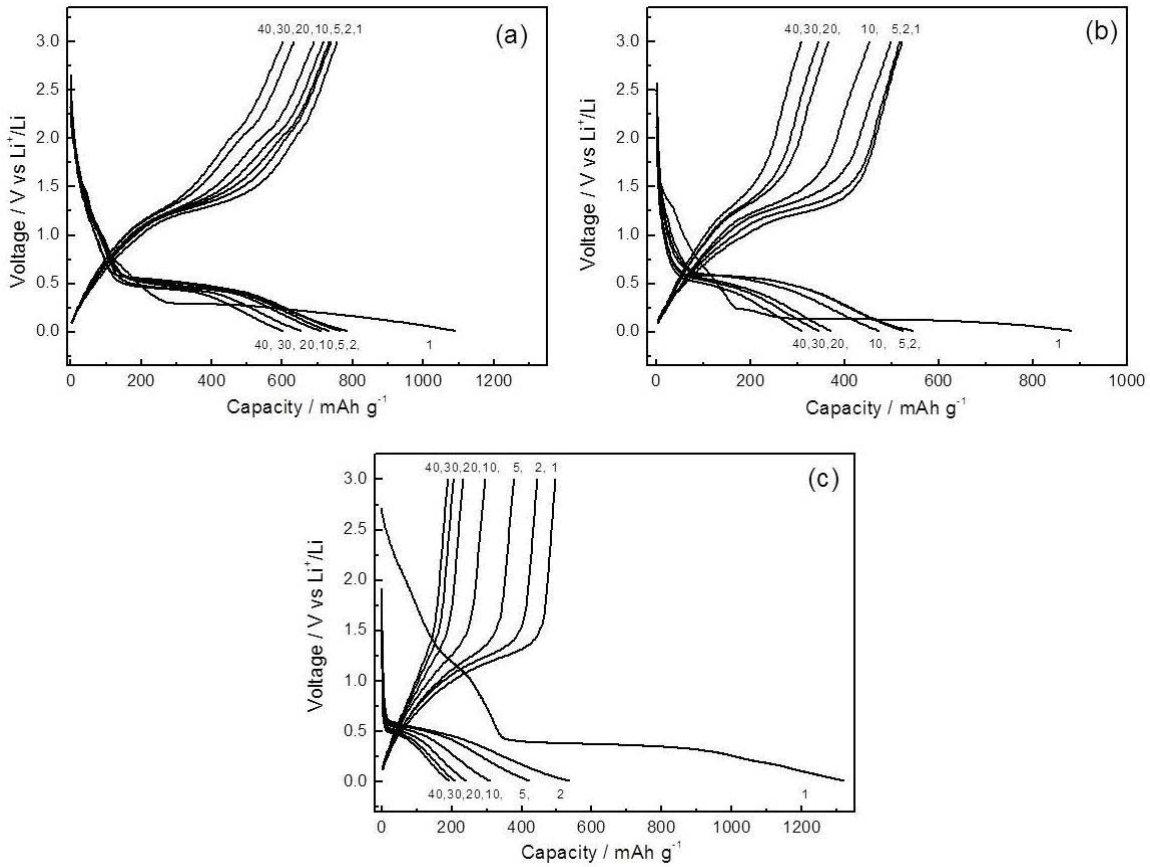

Figure 6-5 Voltage profiles of the electrodes made of (a) MnO/C core–shell nanorods, (b) MnO microparticles and (c) MnO_2 nanowires. Current density: 200 mA g^{-1}.

The long cycling performance results of MnO/C nanorod, MnO microparticle and MnO_2 nanowire electrodes are shown in Figure 6-6. The MnO/C core-shell nanorod electrode exhibited much higher capacity retention than that of the MnO microparticle and MnO_2 nanowire electrode after 40 cycles. The second cycle discharge capacity of the MnO/C core-shell nanorod electrode is 783 mAh g^{-1} at a current rate of 200 mA g^{-1}. After 40 cycles, the specific discharge capacity was 602 mAh g^{-1}, which is about 77 % of the second cycle discharge capacity. In contrast, the capacities of the MnO microparticle and MnO_2 nanowire electrodes, continued decreasing to 309 mAh g^{-1} and

191 mAh g^{-1} as the number of cycles increased, with the capacity retention of 35 % and 14 % of the second cycle discharge capacity, respectively. The C-rate performances of the as-prepared materials were also investigated and are shown in Figure 6-7. The MnO/C core-shell nanorod electrode also showed much better C-rate performance than the MnO microparticle and MnO_2 nanowire electrodes. The good electrochemical performance of MnO/C core-shell nanorod electrode is a result of the combined advantages of the nanorod structure and the porous carbon coating layer. Nanosize materials with a large surface area can provide more active sites for Li^+ intercalation/de-intercalation and shorten the diffusion length for lithium ions in the solid phase. The nanoporous carbon coating layer with mesopores can form a mixed conducting three-dimensional network that facilitates the migration of both the Li^+ and the e^-, so that they reach each surface of the MnO nanorods.[56]

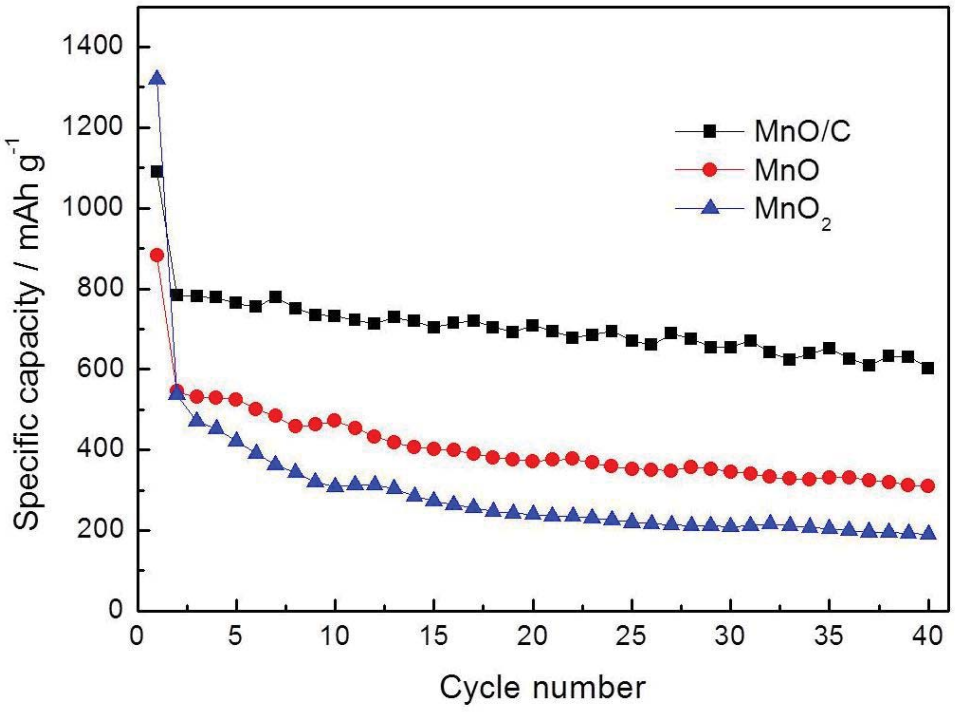

Figure 6-6 Cycling performance of MnO/C core–shell nanorod, MnO microparticle and MnO_2 nanowire electrodes at discharge and charge current rate of 200 mA g^{-1}.

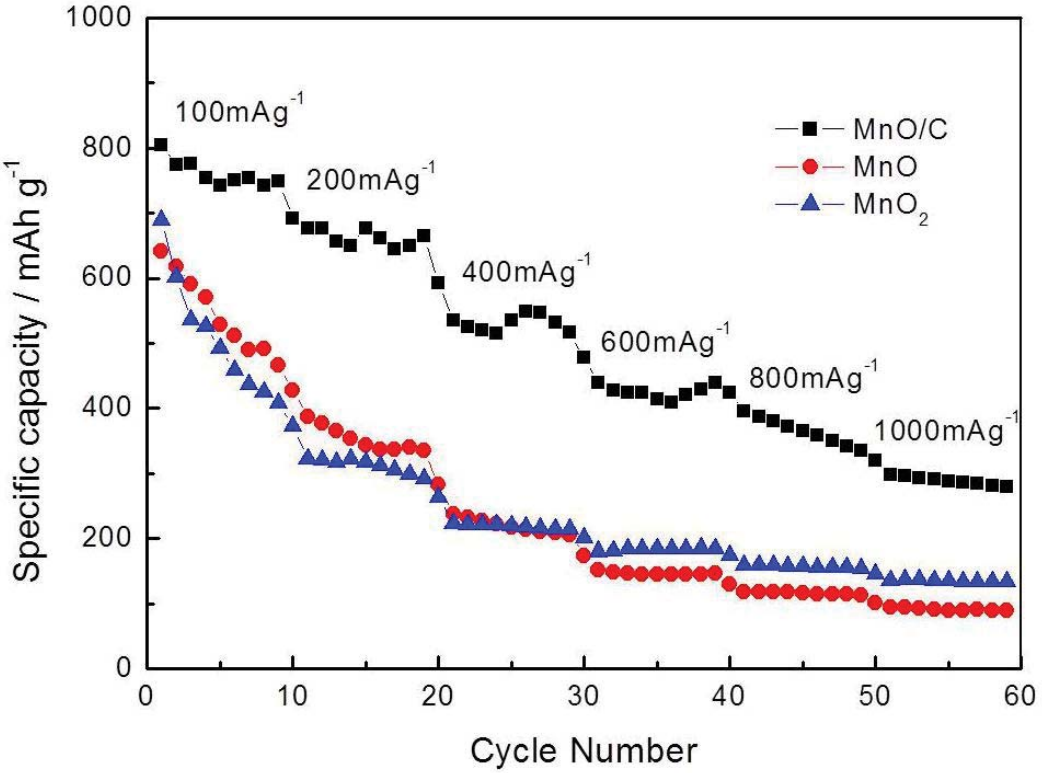

Figure 6-7 Cycling performance of MnO/C core–shell nanorod, MnO microparticle and MnO_2 nanowire electrodes at different discharge and charge current rate.

6.5 Summary

Using block copolymer F127 as the carbon source, MnO/C core-shell nanorods were successfully prepared from MnO_2 nanowires by calcination in a gas flow of 5 vol.% H_2 in Ar. The XRD pattern shows that the product has a face-centered cubic phase structure. FESEM and TEM images showed that a thin carbon layer was coated on the surfaces of the MnO nanorods. The MnO/C core-shell nanorod electrodes delivered a higher capacity retention and better C-rate capability than that of MnO microparticle electrodes and MnO_2 nanowire electrodes.

Both of the mesoporous α-Fe_2O_3 in Chapter 5 and the MnO/C core-shell nanorods in

this chapter showed higher discharge capacities than the commercial graphite, which demonstrated that nanostructure transition metal oxides are suitable as anode materials for high energy lithium-ion batteries. Three-dimensional mesoporous structure and one-dimensional nanowire structure can both significantly increase the surface area and reduce the lithium ion diffusion length in the solid state of the as-prepared materials. The mesoporous α-Fe_2O_3 electrode showed higher discharge capacity than that of the MnO/C core-shell nanorods electrode at 0.2 C, which is benefit to increase the energy density of lithium-ion batteries. While the MnO/C core-shell nanorods showed lower discharge voltage plateau, which can increase the out-put voltage for whole-cell lithium-ion batteries.

CHAPTER 7 GRAPHENE NANOSHEETS AS CATHODE CATALYSTS FOR LITHIUM-OXYGEN BATTERIES

7.1 Introduction

Various approaches to improving the electrochemical performance of rechargeable lithium-oxygen batteries have been reported, including the use of nanostructured transition metal oxide;[191,211,219,306] mesocellular carbon foam;[213] superfine platinum particles;[307] bi-functional platinum–gold nanoparticles loaded onto carbon[221] and carbon modified by long-chain hydrophobic molecules.[308] Recently, Zhou's group firstly successfully fabricated multilayer graphene electrodes for lithium-oxygen batteries by drawing the pencil rods on a ceramic separator.[309] They also examined metal free graphene nanosheets (GNSs) for use in air electrodes in a lithium-oxygen battery with a hybrid aqueous/nonaqueous electrolyte. As the cathode, the GNSs exhibited higher catalytic activity than that of acetylene carbon black and were considered to be a promising candidate for use in an air electrode for rechargeable lithium-oxygen batteries.[310] Although GNSs have been widely investigated as the catalyst or catalyst hosts in an air electrode with an aqueous electrolyte, the electrochemical performance of GNSs as a cathode catalyst in a lithium-oxygen battery with a non-aqueous electrolyte has not yet been studied.

In this chapter, the use of GNSs as high efficiency cathode catalysts for rechargeable

lithium-oxygen batteries in an alkyl carbonate electrolyte was investigated. The GNSs were prepared by the chemical reduction of exfoliated graphite oxide nanosheets. The electrochemical properties of GNSs as cathode electrode materials were studied in lithium-oxygen batteries with an alkyl carbonate electrolyte.

7.2 Preparation of Graphene

The synthesis of GNSs was derived from the modified Hummers method as described in chapter 2; graphene oxide was first prepared and then reduced to yield GNSs by hydrazine hydrate. Vulcan XC-72 carbon was purchased from Cabot Australia.

7.3 Physical and Structural Characterization

7.3.1 Scanning Electron Microscopy and Transmission Electron Microscopy

The microstructure of the as-prepared GNSs agglomerate was observed by field emission scanning electron microscope (FESEM, Zeiss Supra 55VP) (shown in Figure 7-1a). The as-prepared GNSs consist of almost transparent, wrinkle-like, thin nanosheets. Vulcan XC-72 carbon, another widely used catalyst host, was also observed, for comparison. Figure 7-1b shows that the Vulcan XC-72 carbon consists of nanoparticles around 100 nm. The morphology of the as-prepared GNSs was further investigated by transmission electron microscope (TEM, JEOL 2011) and high resolution TEM (HRTEM). Figure 7-1c shows a bright-field TEM image of graphene nanosheets, which resemble repelled and entangled silk veil waves. Figure 7-1d further

presents a HRTEM image of the as-prepared GNSs, in which the featureless basal planes of graphene nanosheets are clearly visible.

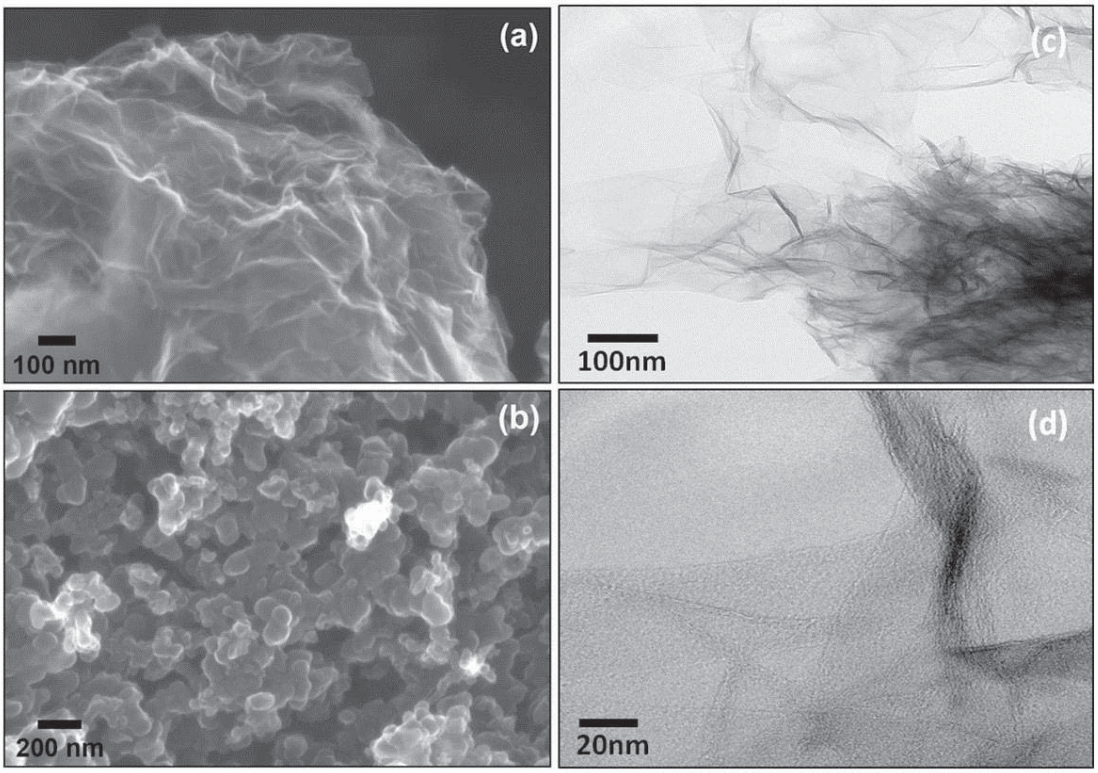

Figure 7-1 FESEM images of the as-prepared GNSs (a) and commercial Vulcan XC-72 carbon (b). TEM images of the as-prepared GNSs (c) and (d) at different magnifications.

7.3.2 X-ray Diffraction and Raman Spectroscopy

X-ray diffraction (XRD) of as-prepared GNSs was conducted on a Siemens D5000 X-ray diffraction meter (Figure 7-2a). The as-prepared GNSs display broad a (002) peak and a weak (100) peak, implying breaking of the inter-planar carbon bonds of the pristine graphite and the formation of graphene nanosheets.[311,312] The Raman spectrum was acquired on a Jobin Yvon HR800 confocal Raman system with 632.81 nm diode laser excitation on a 300 lines per mm grating at room temperature. Figure 7-2b shows

the Raman spectrum of the as-prepared GNSs. Two typical Raman peaks of carbon are observed at 1330 and 1592 cm^{-1}, corresponding to the D line and G line, respectively. The D line is stronger than the G line, and the D/G intensity ratio in the spectrum is significantly higher than that of well-crystallized graphite, indicating the graphene nanosheets have smaller sized in-plane sp^2 domains than that of graphite and a partially disordered crystal structure.[149,247]

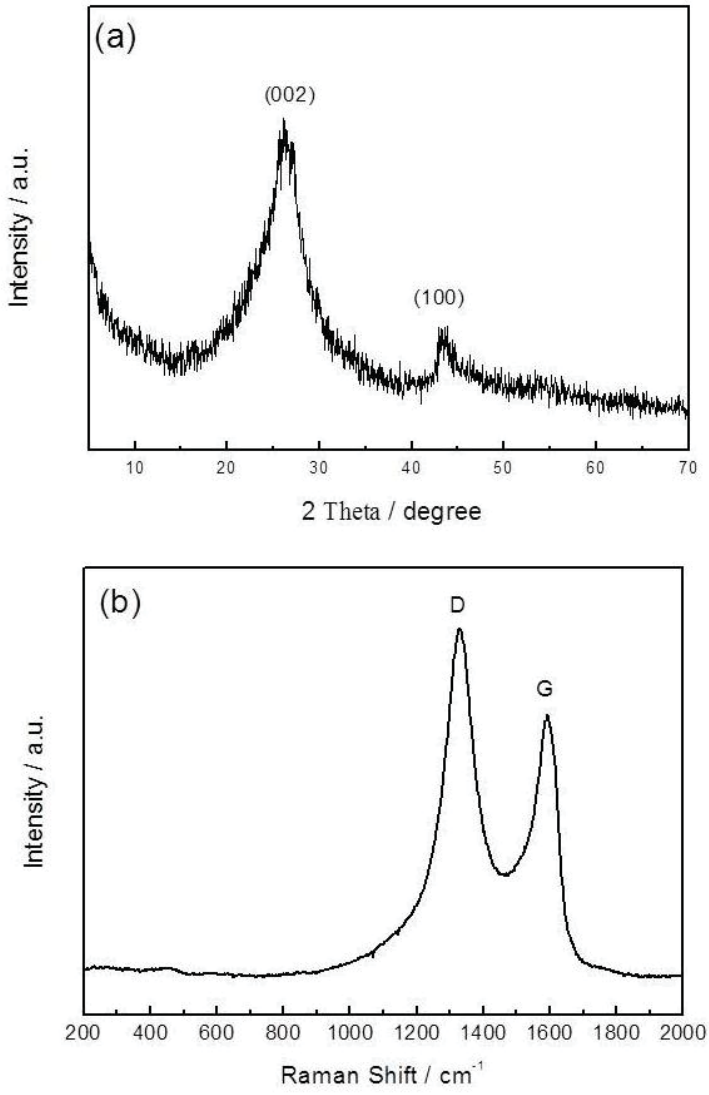

Figure 7-2 (a) XRD pattern and (b) Raman spectrum of the as-prepared GNSs.

7.3.3 Brunauer-Emmett-Teller

The surface area and microstructure of the carbon source play an important role in the electrochemical performance of lithium-oxygen batteries.[212] In order to examine the specific surface area and the pore size distribution of the as-prepared GNSs and Vulcan XC-72 carbon, N_2 adsorption–desorption isotherm measurements were carried out. In Figure 7-3a, the GNSs exhibit a typical IV shape, indicating theey are mesoporous. The pore size distribution, obtained from the Barrett-Joyner-Halenda (BJH) method, is shown as the inset in Figure 7-3a. The plot shows that the dominant peaks are in the mesoporous range with a peak around 3.63 nm. The surface area of the GNSs, estimated from the Brunauer-Emmett-Teller (BET) method, is 309 m^2 g^{-1} and the pore volume is 0.3666 cm^3 g^{-1}. The nitrogen adsorption/desorption isotherm of Vulcan XC-72 carbon is shown in Figure 7-3b. The pore size distribution of Vulcan XC-72 carbon exhibits mesoporous structure with broad pore size distribution. The surface area estimated from the BET method is 240m^2 g^{-1} and the pore volume is 0.3834 cm^3 g^{-1}.

7.4 Lithium-Oxygen Batteries Performance

The electrocatalytic activity of graphene nanosheets was examined in lithium-oxygen cells and compared with Vulcan XC-72 carbon. The charge–discharge measurement was carried out in the voltage range of 2.0–4.4 V for graphene nanosheet electrodes and 2.0–4.6 V for Vulcan XC-72 carbon electrodes at room temperature. The third cycle charge/discharge voltage profiles are shown in Figure 7-4. The discharge capacity of the as-prepared GNSs electrode was 2332 mAh g^{-1}; whereas the Vulcan XC-72 carbon

electrode showed a lower discharge capacity of 1645 mAh g^{-1}. During the discharge process, the GNSs electrode showed a discharge potential plateau of 2.75 V vs. Li/Li^+, which was higher than that of the Vulcan XC-72 carbon electrode (2.60 V vs. Li/Li^+). During the charge process, the charge potential plateau of the GNSs electrode was 3.97 V vs. Li/Li^+ (half charge capacity), which was much lower than that of the

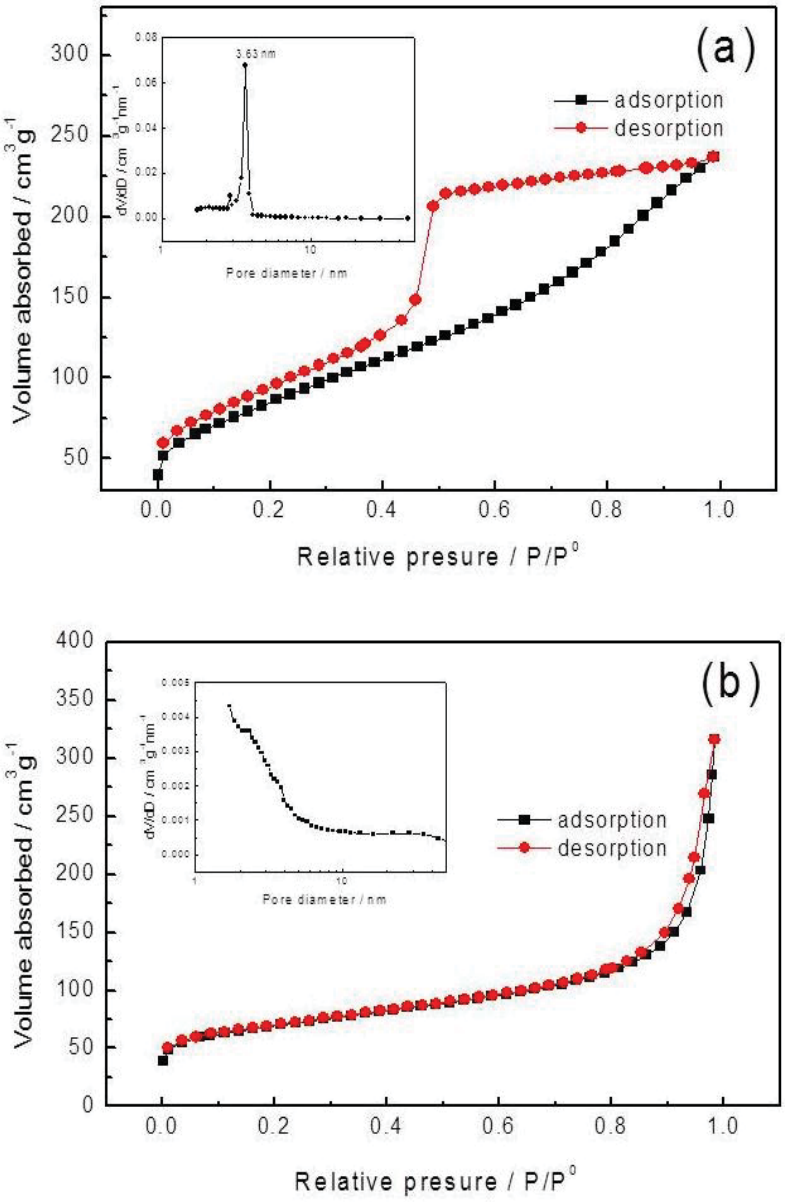

Figure 7-3 The nitrogen adsorption/desorption isotherm of (a) GNSs and (b) Vulcan XC-72 carbon. The insets are the pore size distribution curves.

Vulcan XC-72 carbon electrode (4.29 V vs. Li/Li^+). The GNSs electrode exhibited a charge potential similar to that of a α-MnO_2 nanowires electrode,[191] which is lower than that of any other pure carbon material reported previously.[219,220] Using the data shown in Figure 7-4, we can determine that the potential difference (ΔV) between the charge and discharge potentials of the GNSs electrode was 1.22 V, which is significantly lower than that of the Vulcan XC-72 carbon electrode (1.69 V). Therefore, the air electrode with GNSs was found to have a higher round-trip efficiency than that of the Vulcan XC-72 carbon electrode. The significant difference in the electrochemical performance between the GNSs and the Vulcan XC-72 carbon in lithium-oxygen cells could be ascribed to the differences in their catalytic activities.

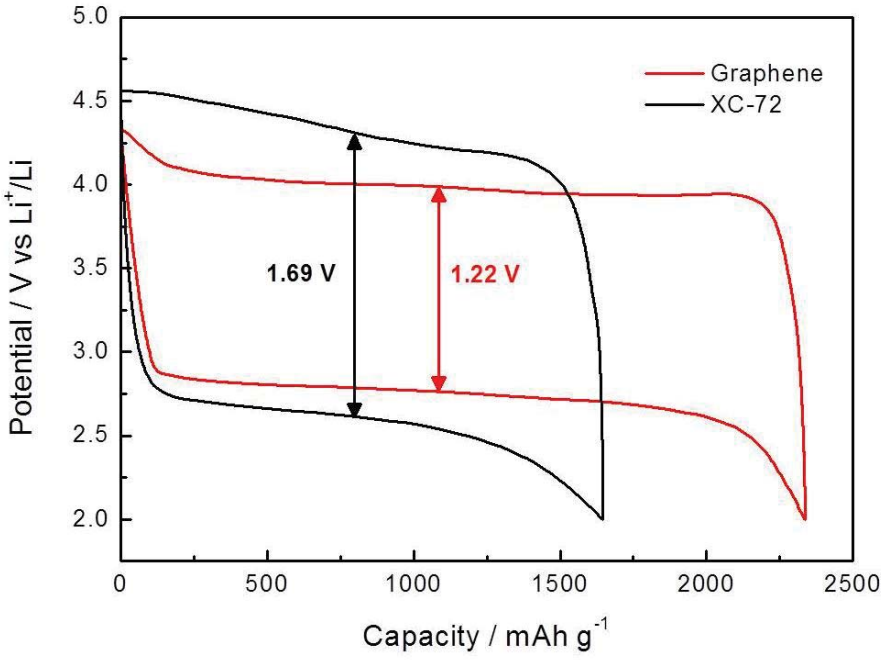

Figure 7-4 Charge-discharge voltage profiles (third cycle) of the as-prepared GNSs and Vulcan XC-72 carbon. Capacities are per gram of carbon in the electrode. Cycling was carried out at a current density of 50 mA g^{-1} (0.1 mA cm^{-2}) in 1 atm O_2 atmosphere at room temperature (20 °C). The cut voltage ranges were 2.0-4.4 V for the GNSs electrode and 2.0-4.6 V for the Vulcan carbon electrode, respectively.

Previous studies described the electrochemical reaction of lithium-oxygen batteries, during discharge, as the reduction of oxygen by lithium ions to form Li_2O or Li_2O_2 and, during the charging process, as the electrochemical decomposition these oxides to lithium ions and oxygen.[197] To identify the reaction products on the GNSs and Vulcan XC-72 carbon electrodes in the Li-air cell, we performed FTIR measurements on the cathode in both the discharge and charge states. Figure 7-5 shows the FTIR spectra of GNSs and Vulcan XC-72 cathodes. The FTIR spectrum of the discharged electrodes showed that the discharge products were dominated by Li_2CO_3 instead of the expected Li_2O_2, and that peaks associated with C=O, C-O, C-C and C-H groups were also present. These absorbance peaks associated with Li_2CO_3 and the above mentioned functional groups disappeared after charging. The XRD patterns in Figure 7-6 further confirmed that Li_2CO_3 is the dominant phase of the discharged electrode. In the discharged state, the Li_2CO_3 phase can be identified on both the GNSs and the Vulcan carbon electrodes; whereas in the charged state it cannot be seen on either of these electrodes. This result is consistent with the FTIR measurement. Recently, several publications have demonstrated that when alkyl carbonate electrolytes are used in the lithium-oxygen batteries, the electrochemistry is much more complicated than a simple combination reaction.[204,206] The discharge reaction is the decomposition of the electrolyte, with oxygen involved, leading to the formation of Li_2CO_3, $CH3CO_2Li$, HCO_2Li, $C_3H_6(OCO_2Li)_2$, CO_2 and H_2O. The charge reaction is the oxidation of Li_2CO_3, CH_3CO_2Li, HCO_2Li, $C_3H_6(OCO_2Li)_2$. This explains the large over-potential between the charge and discharge curves of the Li-air batteries. Our results are consistent with

the recent report by Bruce et al.[206] The reduced over-potential indicates the as-prepared GNSs used with an alkyl carbonate electrolyte are more electrochemically active for the above reactions than Vulcan XC-72. The increased electrocatalytic activity probably arises from the presence of many carbon vacancies and defects on the surface of GNSs. These vacancies and defects are formed during the preparation process by chemical reduction of exfoliated graphite oxide sheets. The zigzag edges of graphene nanoribbons have been reported to have a unique edge state's electronic structure.[313] The carbon atoms at the edge of graphene nanosheets are considered to be ''partially radical'', which can offer special chemical reactivity, differing from that of non-edge carbon atoms. This means that the sp^3-bonded carbon atoms in GNSs contribute to edge states and defects and might serve as active sites for the electrochemical reaction of oxygen. Although the detailed mechanism for the oxygen involved electrochemical reaction in alkyl carbonate electrolytes is still not completely clear and is under intense investigation, graphene nanosheets have shown an efficient catalytic effect as the air electrode in rechargeable lithium-oxygen batteries with an organic electrolyte.

The cycling performance of the GNSs and the Vulcan carbon electrodes is shown in Figure 7-7. The initial capacity of the electrode made of GNSs was 1597 mAh g^{-1}. It then dramatically increased to 2332 mAh g^{-1} on the second cycle and was sustained at 2359 mAh g^{-1} on the fifth cycle. Whereas, the 1918 mAh g^{-1} initial capacity of the Vulcan XC-72 carbon electrode steadily declined to 1342 mAh g^{-1} by the fifth cycle. The GNSs electrode exhibited a better cycling performance than that of the Vulcan

XC-72 carbon electrode. For the lithium-oxygen batteries with alkyl carbonate electrolytes, the cycling involves the repeated decomposition of the electrolyte during discharge and oxidation of the decomposed products during charge.[206] The fading of the lithium-oxygen cell during cycling is associated with the accumulation of these products in the electrode and the starvation of the electrolyte. The FTIR spectrum of the charged

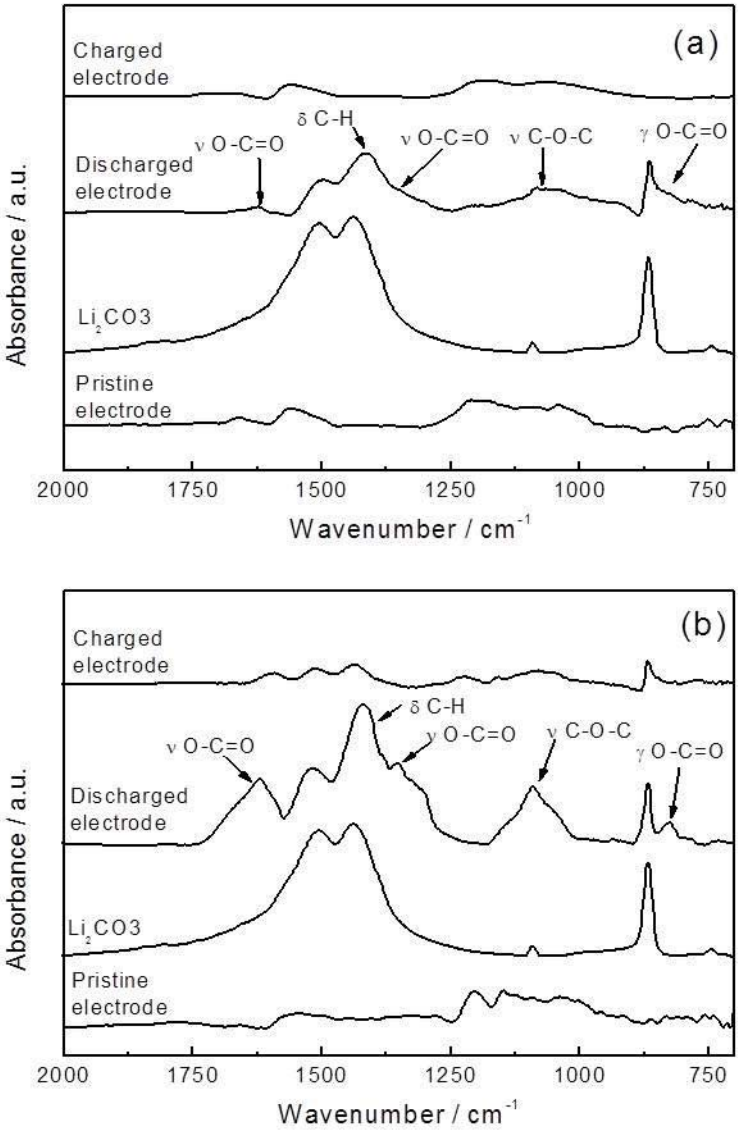

Figure 7-5 FTIR spectra of the pristine air electrode and after first discharge, then recharge in 1 M $LiClO_4$ in PC under O_2. (a) As-prepared GNSs electrode and (b) Vulcan XC-72 carbon electrode.

electrode in Figure 7-5 demonstrated the decomposition of the discharge products of GNSs and Vulcan XC-72 electrode. However, there are still weak peaks associated with discharged products present in the Vulcan XC-72 electrode due to incomplete decomposition of the discharge products. The accumulation of the discharge product on the GNSs electrode is slower, and less, than on the Vulcan XC-72 electrode. Therefore, the GNSs electrode shows better cyclability.

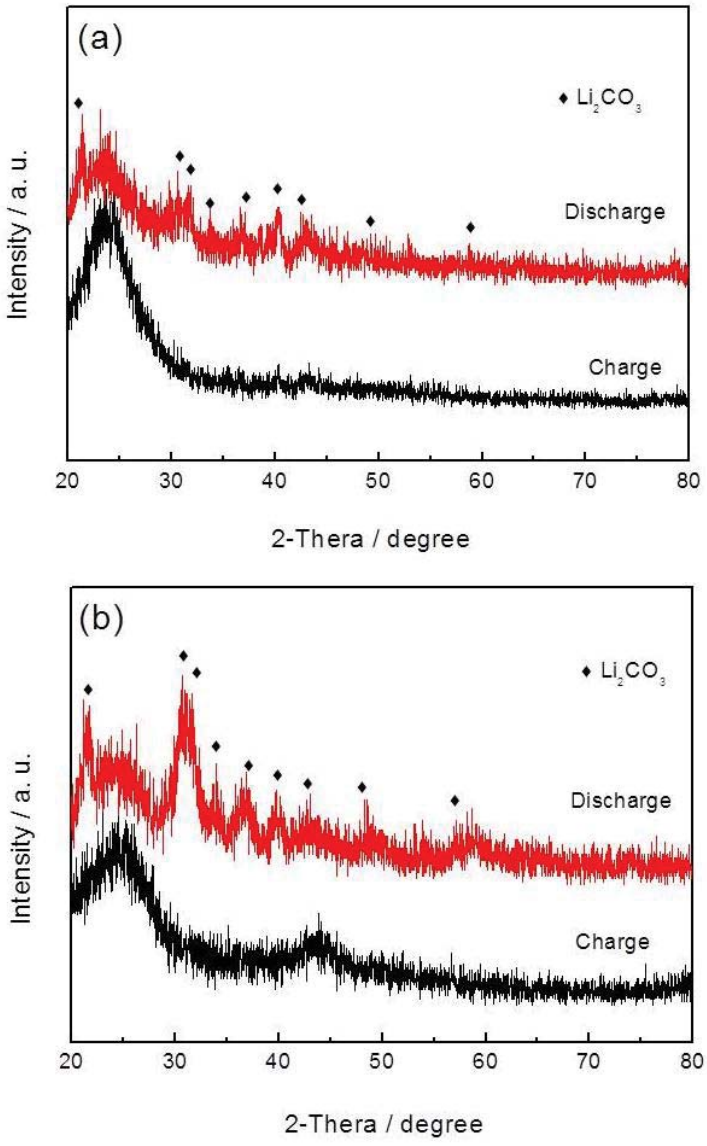

Figure 7-6 XRD patterns of the air electrodes in the first discharged and charged states: (a) the as-prepared GNSs electrode and (b) the Vulcan XC-72 carbon electrode.

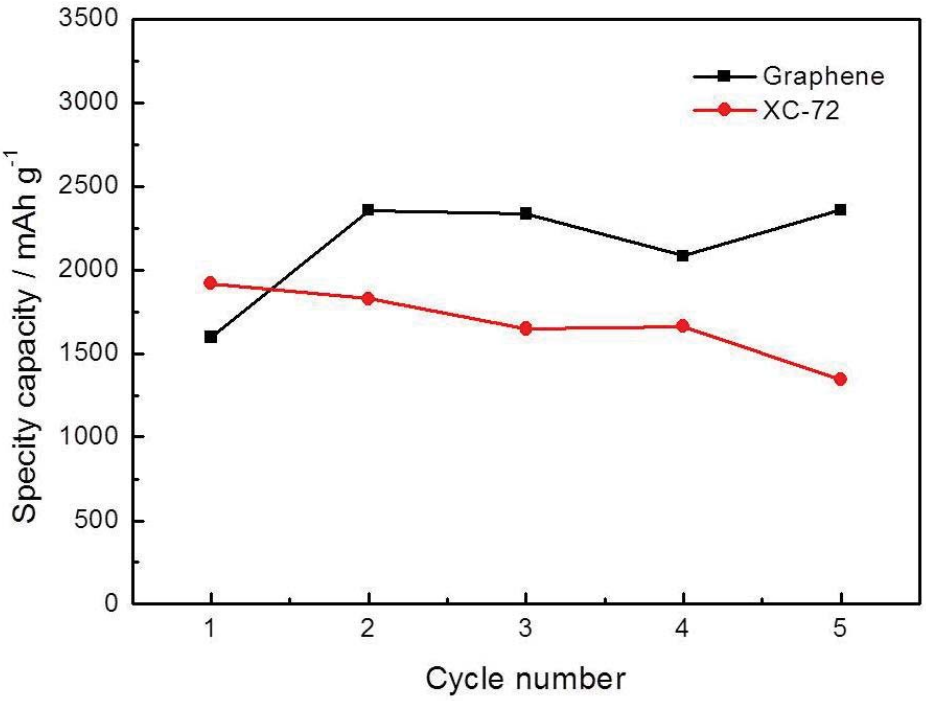

Figure 7-7 Cycling performances of the as-prepared GNSs and Vulcan XC-72 carbon electrode. Capacities are per gram of carbon in the electrode. Cycling was carried out at a current density of 50 mA g^{-1} (0.1 mA cm^{-2}) in 1 atm O_2 atmosphere.

The morphologies of the GNSs and Vulcan XC-72 air electrodes before and after cycling were investigated by FESEM (as shown in Figure 7-8). The GNSs air electrode before cycling presents sufficient pores between GNSs agglomerates. These pores can facilitate oxygen diffusion and electrolyte impregnation. After cycling, the pores inside the air electrode were partially filled by insoluble reduction products (Figure 7-8b). The pores between the carbon nanoparticles of the Vulcan XC-72 air electrode were similarly filled by the reduction products after discharge. This filling of pores with insoluble reduction products could reduce further oxygen diffusion, leading to increased polarization of the air electrode and is a phenomenon that remains a big challenge for

lithium-oxygen batteries.

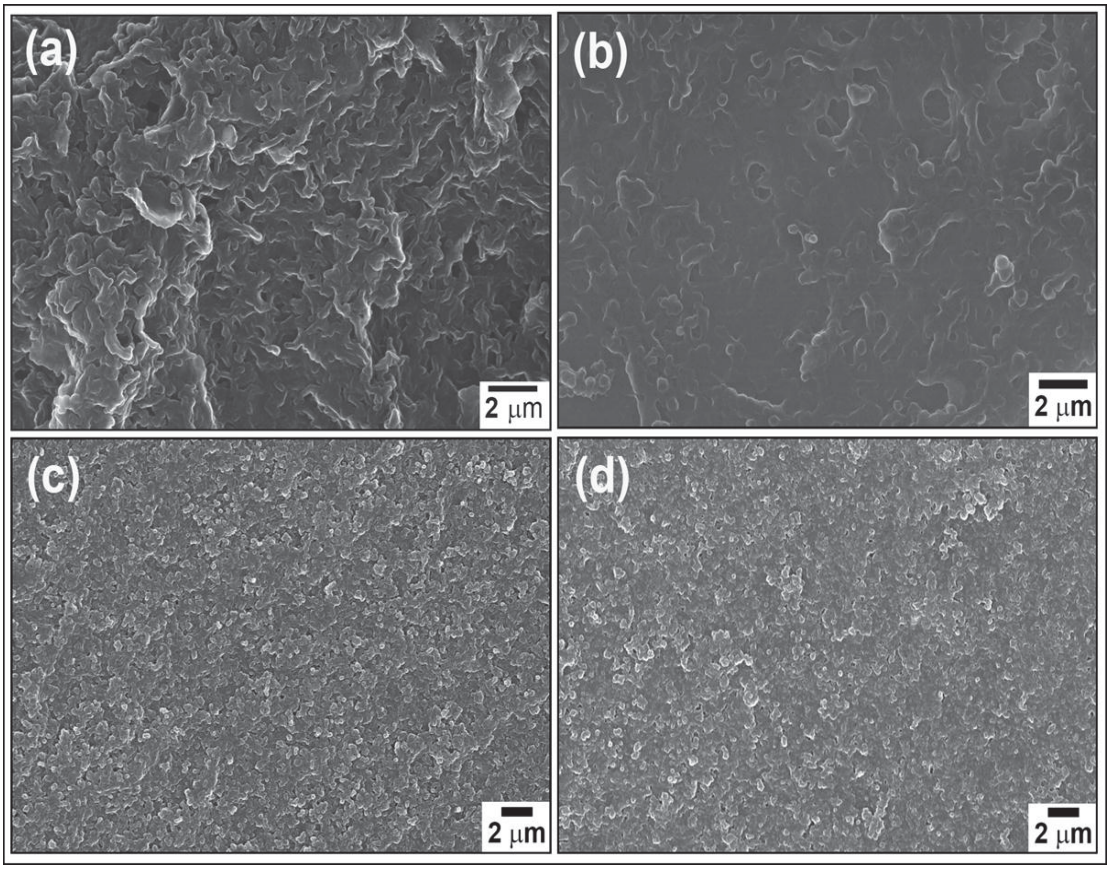

Figure 7-8 FESEM images of the GNSs electrode before (a) and after (b) discharge and the Vulcan XC-72 carbon electrode before (c) and after (d) discharge.

7.5 Summary

Graphene nanosheets have been prepared and applied as cathode catalysts for lithium-oxygen batteries with an alkyl carbonate electrolyte. The as-prepared GNSs electrode exhibited better cyclability and lower over-potential than that of the Vulcan XC-72 electrode. The reduced over-potential is indicative of the high electrochemical activity of the GNSs towards oxygen involved reactions in lithium-oxygen cells which could arise from the presence of many carbon vacancies and defects on the GNSs

surface. It is expected that graphene nanosheets could be an efficient cathode catalyst for lithium-air batteries.

CHAPTER 8 MESOPOROUS CoO/CMK-3 NANOCOMPOSITE FOR LITHIUM OXYGEN BATTERIES

8.1 Introduction

For practical application of lithium-oxygen batteries, there are still many challenges that need to be overcome. These include reducing the charge-discharge over-potential in order to increase the round-trip efficiency, improving the rate capability, and enhancing the cycle life stability. The lithium anode has very little polarization, thus the large over-potential observed during cell charge-discharge is mainly caused by the cathode. Many studies have been devoted to exploring cathode catalysts for the oxygen reduction reaction (ORR) and the oxygen evolution reaction (OER) as described in previous chapters. The structure of the carbon material used in the air electrode is another critical factor that affects the electrochemical performance of lithium-oxygen batteries. The insoluble discharge products will accumulate inside the pores of the porous electrode and will eventually clog the oxygen diffusion path inside the electrode. Therefore, the capacity of a lithium-oxygen battery is determined by the carbon air electrode. It is critical to choose a carbon source with the appropriate microstructure to facilitate the ORR and accommodate the maximum amount of discharge products. Xiao et al. showed that the capacities can increase with increasing mesopore volume of the carbon materials.[212] Yang et al. used a mesocellular carbon foam as the cathode electrode

materials and achieved a high discharge capacity.[213]

In the past few years, the development of self-ordered mesoporous carbon materials with uniform hexagonal or cubic mesopore structures as electrode materials for lithium-ion batteries, fuel cells and supercapacitors has attracted attention.[105,146,314-319] Wang et al. reported high electrocatalytic performance of a mesoporous carbon Mn_3O_4/CMK-3 nanocomposite for oxygen reduction in an alkaline solution.[320] The good performance of the Mn_3O_4/CMK-3 nanocomposite as the air diffusion electrode material is due to the unique arrangement of ordered and interconnected pores within the bulk CMK-3 carbon which can provide effective gas diffusion channels. The electrochemical performance of mesoporous CMK-3 carbon as an air electrode for a lithium oxygen battery with a nonaqueous electrolyte has not yet been studied. In this chapter, the use of mesoporous CMK-3 carbon and CMK-3 carbon loaded with CoO nanoparticles as cathode catalysts for lithium-oxygen batteries is reported. The mesoporous CoO/CMK-3 nanocomposite exhibited excellent capacity retention in nonaqueous electrolytes, when compared with bare mesoporous CMK-3 carbon, Super-P carbon and CoO/Super-P composites.

8.2 Preparation of a CoO/CMK-3 Nanocomposite

Mesoporous silica SBA-15 was used as the template to synthesize CMK-3 and was prepared according to a previous report.[321] In the first step, Pluronic P123 ($EO_{20}PO_{70}EO_{20}$) (12.0 g, 0.0207 mol, Aldrich) and potassium chloride (KCl, 99%,

Aldrich) were dissolved in 360.0 g of 2 M HCl. Then, 24.96 g (0.119 mol) tetraethylorthosilicate (TEOS, 99%, Aldrich) was added to the transparent solution with vigorous stirring for 8 min and the mixture was left quiescent at 40 °C for 24 h. The mixture was subsequently treated at 130 °C for another 24 h in a Teflon lined autoclave. The as-synthesized SBA-15 was collected by filtration, dried and calcinated at 550 °C for 6 h in air.

Mesoporous carbon CMK-3 was synthesized by a similar method to that reported by Jun et al.[322] In a typical preparation process, 1.25 g (3.63 mmol) of sucrose (99.5%, Sigma) was dissolved in 5.0 mL of water containing 0.14 g (1.4 mmol) of H_2SO_4 (98%, Aldrich). SBA-15 template (1.0 g) was then dispersed in the above solution and the mixture was ultrasonicated for 1 h. The mixture was then heat-treated at 100 °C for 6 h and subsequently at 160 °C for another 6 h. The impregnation process was repeated again with another aqueous solution containing 5 g of water, 0.8 g (2.32 mmol) of sucrose and 0.09 g (0.90 mmol) of H_2SO_4. The composite was completely carbonized at 900 °C for 5 h in an inert argon atmosphere. To remove the SBA-15 silica template, the composite was stirred in 2 M hot NaOH (98%, pellets, Aldrich) solution and the process then repeated.

CoO/CMK-3 nanocomposite was prepared by a the wet impregnation method. An ethanolic solution (50 mL) of cobalt nitrate (8 mmol) was stirred for 24 h at room temperature with 100 mg of dried CMK-3 template. The carbon–cobalt nitrate mixture

was separated from the solution by centrifugation (3000 revolutions/min, 5 min). After drying in air at room temperature for 24 h, the resulting material was sintered at 873 K for 2 h under flowing Ar gas. The CoO/Super-P carbon composite was obtained by the following procedures. First, 100 mg Super-P carbon (TIMCAL) was dispersed in 20 ml of ethanolic cobalt nitrate solution (0.022mol L^{-1}). Then, the suspension was dried at 333 K under stirring. The resulting powders were sintered at 873 K for 2 h under flowing Ar to obtain the final product.

8.3 Physical and Structure Characterization

8.3.1 X-Ray Diffraction

Mesoporous CMK-3 carbon before and after loading with CoO nanoparticles was characterized by X-ray diffraction (XRD) (as shown in Figure 8-1). The XRD pattern of CMK-3 (Figure 8-1a) shows two very broad weak diffraction peaks (002) and (100) of the graphite structure – indicating that the CMK-3 is not highly graphitized. After impregnation with CoO nanoparticles, two broad weak diffraction peaks appeared in the XRD pattern of CoO/CMK-3 nanocomposite and these can be indexed to the (111) and (200) crystal planes of the cubic CoO (PDF No. 43-1004). The low peak intensity was probably due to the small crystal size of CoO nanoparticles. Therefore, the XRD pattern confirmed the deposition of CoO in the nanocomposite. Small angle X-ray diffraction (SAXRD) measurements were performed on both the CMK-3 carbon and CoO/CMK-3 nanocomposite (as shown in Figure 8-1b). For the CMK-3 mesoporous carbon, the SAXRD peaks can be indexed to the (100), (110), and (200) diffraction lines of the

hexagonal mesoporous structure (p6mm), and confirm the long range regularity and highly ordered nature of the mesoporous structures. After impregnation with CoO nanoparticles, the (110) and (200) diffraction peaks disappeared, indicating that the pore channels inside the mesoporous carbon were partially filled by CoO nanoparticles.

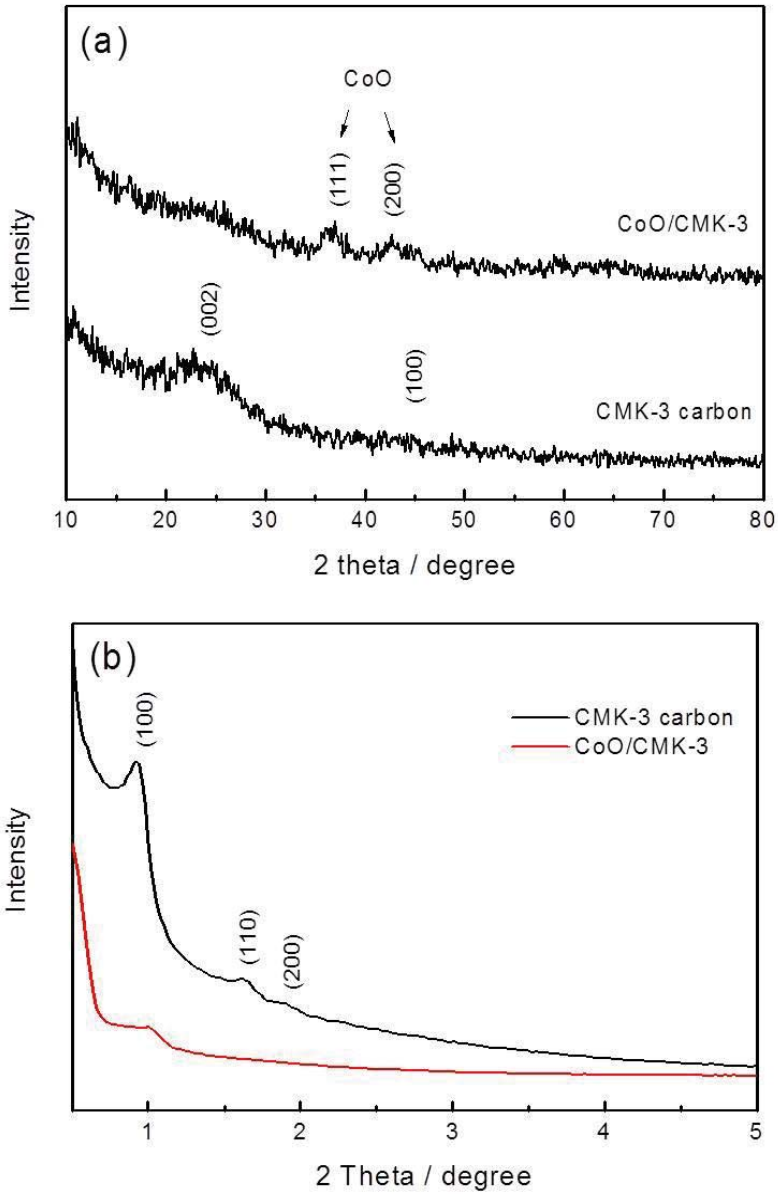

Figure 8-1 (a) Wide angle powder X-ray diffraction patterns and (b) Small angle X-ray diffraction patterns of mesoporous CMK-3 carbon and CoO/CMK-3 nanocomposite.

8.3.2 Brunauer-Emmett-Teller

In order to determine the Brunauer-Emmett-Teller (BET) surface area of mesoporous CMK-3 carbon, CoO/CMK-3 nanocomposite, Super-P carbon black and CoO/Super-P nanocomposite, N_2 adsorption-desorption isotherm measurements were carried out. As shown in Figure 8-2a, both the mesoporous CMK-3 carbon and CoO/CMK-3 nanocomposite exhibited a typical IV shape, indicating their mesoporous characteristic. The surface areas estimated by the BET method were 1264 $m^2 g^{-1}$ for the mesoporous CMK-3 carbon and 849 $m^2 g^{-1}$ for the CoO/CMK-3 nanocomposite. The decrease in the surface area for the CoO/CMK-3 nanocomposite further demonstrates that the pore channels inside the mesoporous carbon are partially filled by CoO nanoparticles. The Super-P carbon and CoO/Super-P composites showed a BET area of 881 $m^2 g^{-1}$ and 660 $m^2 g^{-1}$, respectively (Figure 8-2c).

The pore size distribution, obtained from the Barrett-Joyner-Halenda (BJH) method, is shown in Figure 8-2b and d. The mesoporous CMK-3 carbon has a primary pore size of 5.08 nm, and the CoO/CMK-3 nanocomposite has a similar pore size distribution. This result confirms that most of the pore channels in CMK-3 carbon are not blocked by the loading of CoO nanoparticles. Therefore, the mesopore channel nanoarchitecture is maintained in the CoO/CMK-3 nanocomposite, as is desirable for the air electrode in lithium-oxygen batteries. The Super-P carbon black and CoO/Super-P composite showed a broad pore size distribution as shown in Figure 8-2d. The pore size of CoO/Super-P decreased slightly after the impregnation of CoO nanoparticles.

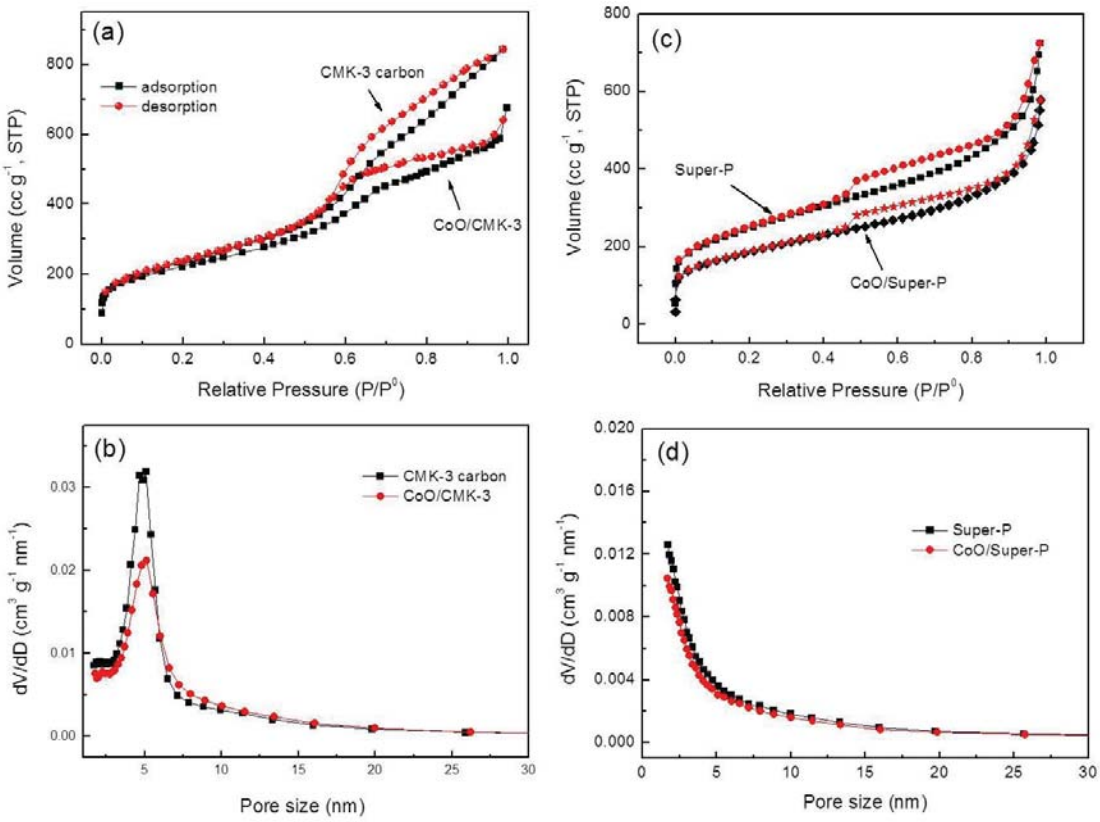

Figure 8-2 The nitrogen adsorption/desorption isotherm of (a) mesoporous CMK-3 carbon and CoO/CMK-3 nanocomposite; (b) Super-P and Super-P/CoO nanocomposite. (c) and (d) The corresponding pore size distribution curves.

8.3.3 Scanning Electron Microscopy and Transmission Electron Microscopy

The morphology and microstructure of the mesoporous CMK-3 carbon and CoO/CMK-3 nanocomposite were analyzed by field emission scanning electron microscopy (FESEM), transmission electron microscopy (TEM) and high resolution transmission electron microscopy (HRTEM). FESEM images of CMK-3 and CoO/CMK-3 nanocomposite are shown in Figure 8-3. The CMK-3 carbon template has a worm-like morphology and a porous structure. After loading with CoO nanoparticles, the CoO/CMK-3 nanocomposite maintained the same shape and morphology as that of the CMK-3 template.

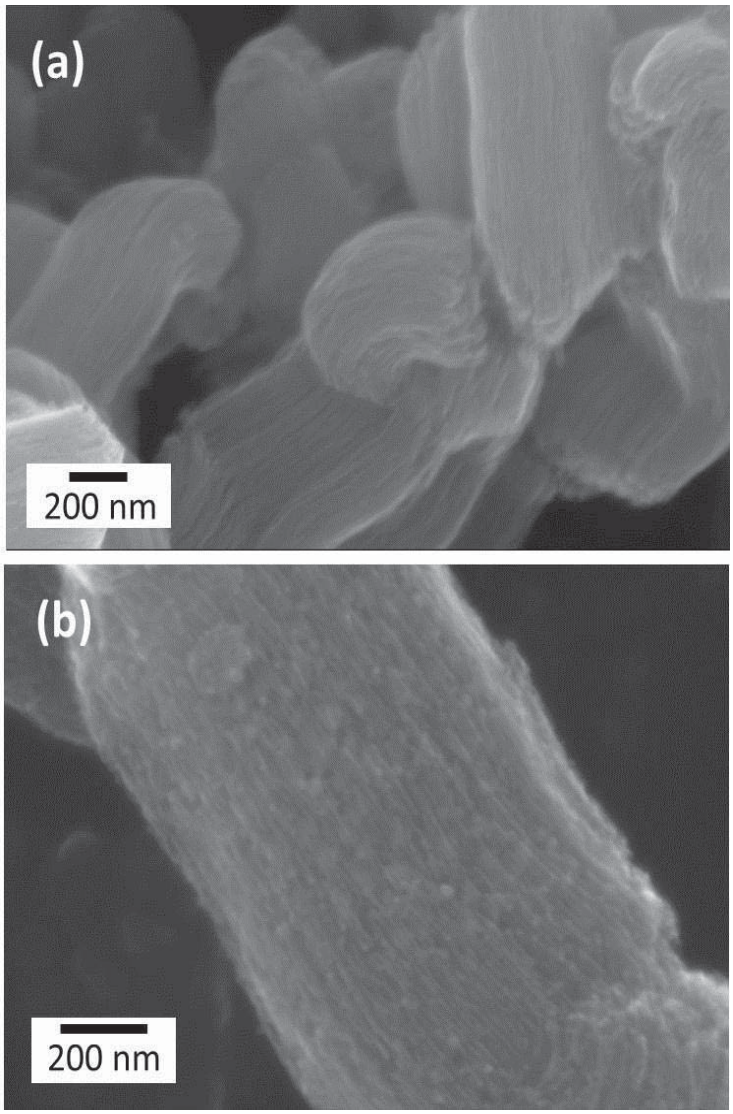

Figure 8-3 FESEM images of (a) CMK-3 and (b) CMK-3/CoO nanocomposite.

Figure 8-4 shows a TEM image of the mesoporous CMK-3 carbon, in which mesopore channel structures are clearly visible. To investigate the dispersion of CoO nanoparticles in the CMK-3 mesoporous carbon matrix, we performed TEM and HRTEM observations of the CoO/CMK-3 nanocomposite. Figures 8-4b and 8-4c present the TEM images of the CoO/CMK-3 nanocomposite at different magnifications. It can be clearly seen that CoO nanoparticles are homogeneously dispersed on the mesoporous carbon matrix. Elemental mapping by energy-dispersive X-ray (EDX) spectroscopy also

confirmed the presence and fine distribution of C, Co and O (Figure 8-5). Figure 8-4d illustrates a HRTEM image of the CoO/CMK-3 nanocomposite. Two CoO nanocrystals can be clearly identified with crystal sizes in the range of a few tens of nanometers. This illustrates that some CoO nanoparticles are loaded on the outer surface of the mesoporous CMK-3 carbon. Therefore, the BET results and TEM observations, confirm that the CoO nanoparticles are loaded both inside and outside the pore channels of the mesoporous CMK-3 carbon matrix. The mesopore channels still exist in the nanocomposite structure, which should ensure facile infiltration of the electrolyte and the diffusion of oxygen into mesopores in lithium-oxygen batteries.

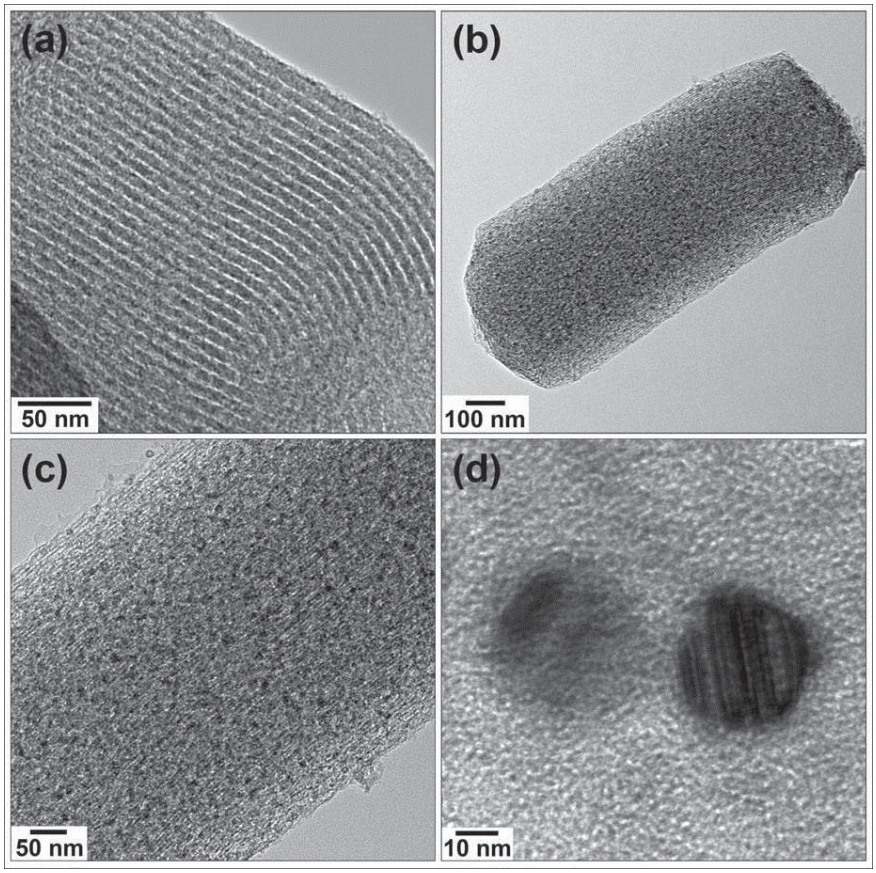

Figure 8-4 TEM images of (a) mesoporous CMK-3 carbon and (b, c) CoO/CMK-3 nanocomposite. (d) HRTEM image of CoO/CMK-3 nanocomposite.

8.3.4 Thermogravimetric analysis (TGA)

Thermogravimetric analysis (TGA) was used to determine the carbon content in the composite materials. The TGA curves of the CoO/CMK-3 and CoO/Super-P nanocomposites are shown in Figure 8-6. The CoO/CMK-3 nanocomposite started to lose weight from 100 °C, due to loss of absorbed water. The main weight loss was at about 450 °C corresponding to the oxidation of carbon to CO_2. The loading of CoO in the as-prepared CoO/CMK-3 nanocomposite was determined to be about 25 wt.%. For the CoO/Super-P nanocomposite, the temperature at which carbon is oxidized is lower than for the CoO/CMK-3 nanocomposite, which may because the Super-P carbon black is less graphite than the mesoporous CMK-3 carbon. The weight percentage of CoO in the as-prepared CoO/Super-P nanocomposite was determined to be about 17.5 wt.%.

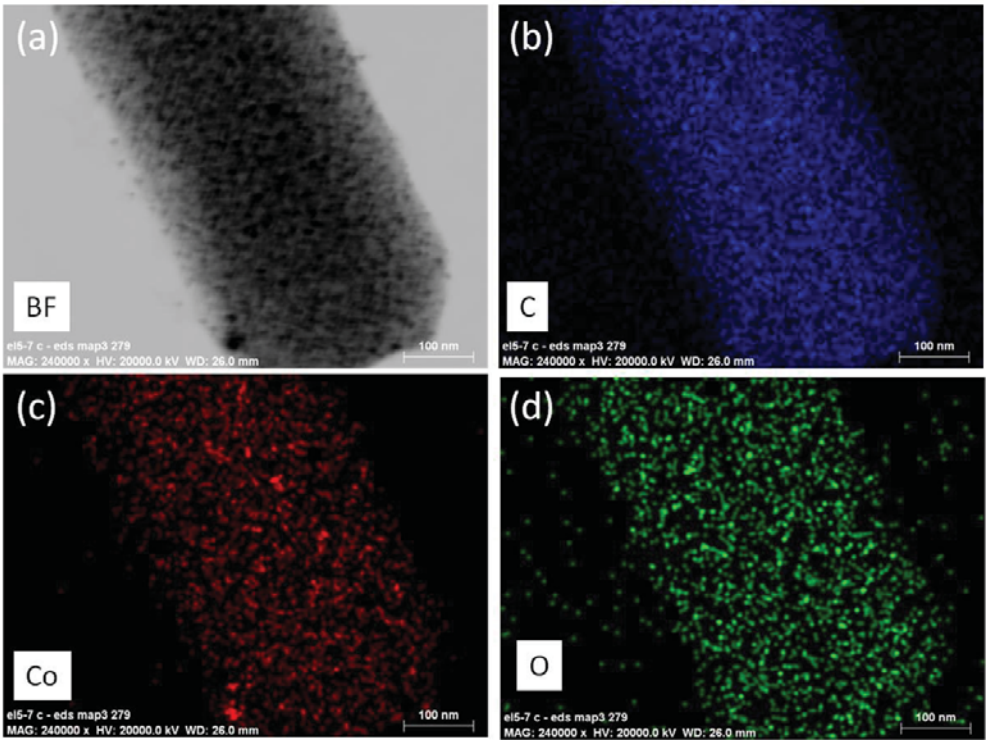

Figure 8-5 EDX elemental maps of the CoO/CMK-3 nanocomposites.

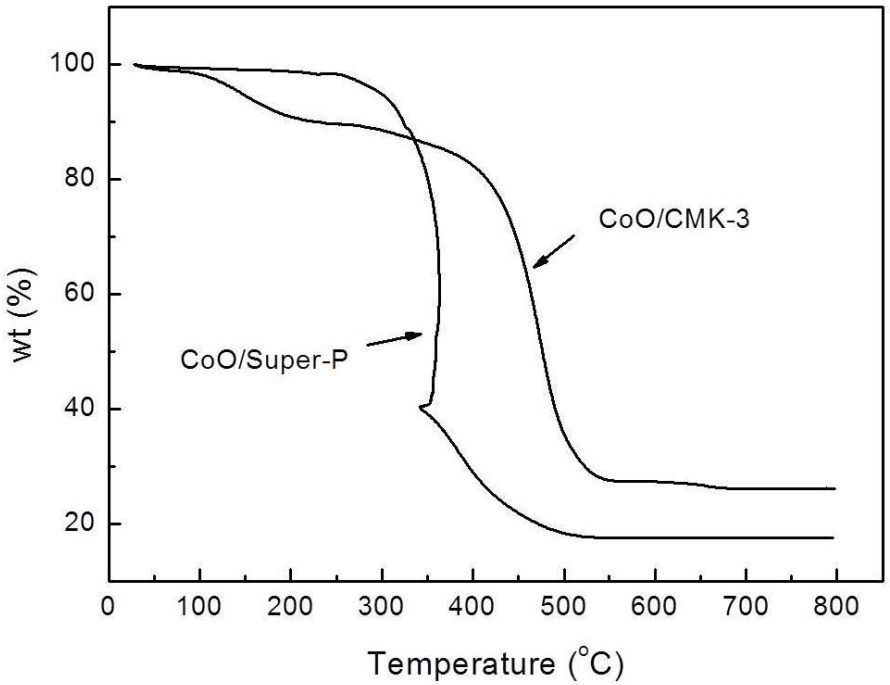

Figure 8-6 Thermogravimetric analysis (TGA) curve of the CoO/CMK-3 and CoO/Super-P nanocomposite.

8.4 Lithium-Oxygen Battery Performance

The electrocatalytic activities of the as-prepared samples as cathode catalysts were examined in lithium-oxygen cells. All the cells were discharged to 2.0 V and charged to 4.15~4.6 V. The charge-discharge voltage profiles are shown in Figure 8-7. During the first discharge process, the CMK-3 electrode exhibited a discharge plateau between 2.6-2.7 V. In the first charging process, the charge curve first reached a plateau at 4.15 V and then slowly increased to 4.5 V. During the following cycles, the discharge potential decreased quickly and the potential plateau disappeared at the 10th cycle. The first discharge plateau position for the Super-P electrode was similar to that for the CMK-3 electrode during the charging process. The charge potential of the Super-P electrode quickly increased to 4.5 V and reached a plateau between 4.5~4.6 V. The CMK-3

electrode showed a lower charge potential than the Super-P electrode. This may be due to the unique ordered mesopore structure of the former facilitating the infiltration of the electrolyte and the diffusion of the oxygen into the electrode. Previous studies have confirmed that transition metal oxides can efficiently reduce the charge over-potential.[191,219] The charge-discharge profiles of the CoO/CMK-3 electrode (in Fig. 8-7c) showed much lower charge over-potential than for the CMK-3 electrode. The charge voltage first increased to 4.0 V. It then reduced to 3.8 V and increased back to 4.15 V. This behavior is similar to the results reported by Lu. et al.[221] The CoO/Super-P electrode also showed much lower charge over-potential than the Super-P electrode as shown in Figure 8-7d.

The cycling performances of the as-prepared electrodes were further investigated and the results are shown in Figure 8-8. The initial discharge capacities of the mesoporous CMK-3 carbon and Super-P electrode were 1324 mAh g^{-1} and 964 mAh g^{-1}, respectively. The capacities quickly decreased for both samples from the second cycle. The discharge capacity of mesoporous CMK-3 carbon decreased to 521 mAh g^{-1} in the 15th cycle whilst the Super-P electrode could not survive more than 13 cycles. After loading with CoO nanoparticles, both mesoporous CMK-3 carbon and Super-P carbon electrodes showed improved capacity retention. The CoO/CMK-3 electrode exhibited an initial discharge capacity of 1021 mAh g^{-1} and 970 mAh g^{-1} at the 15th cycle, with a capacity retention of 95 %. However, the discharge capacity of the CoO/CMK-3 electrode decreased significantly after the 15th cycle. Therefore, improving the cyclability of

lithium-oxygen batteries remains a big challenge.

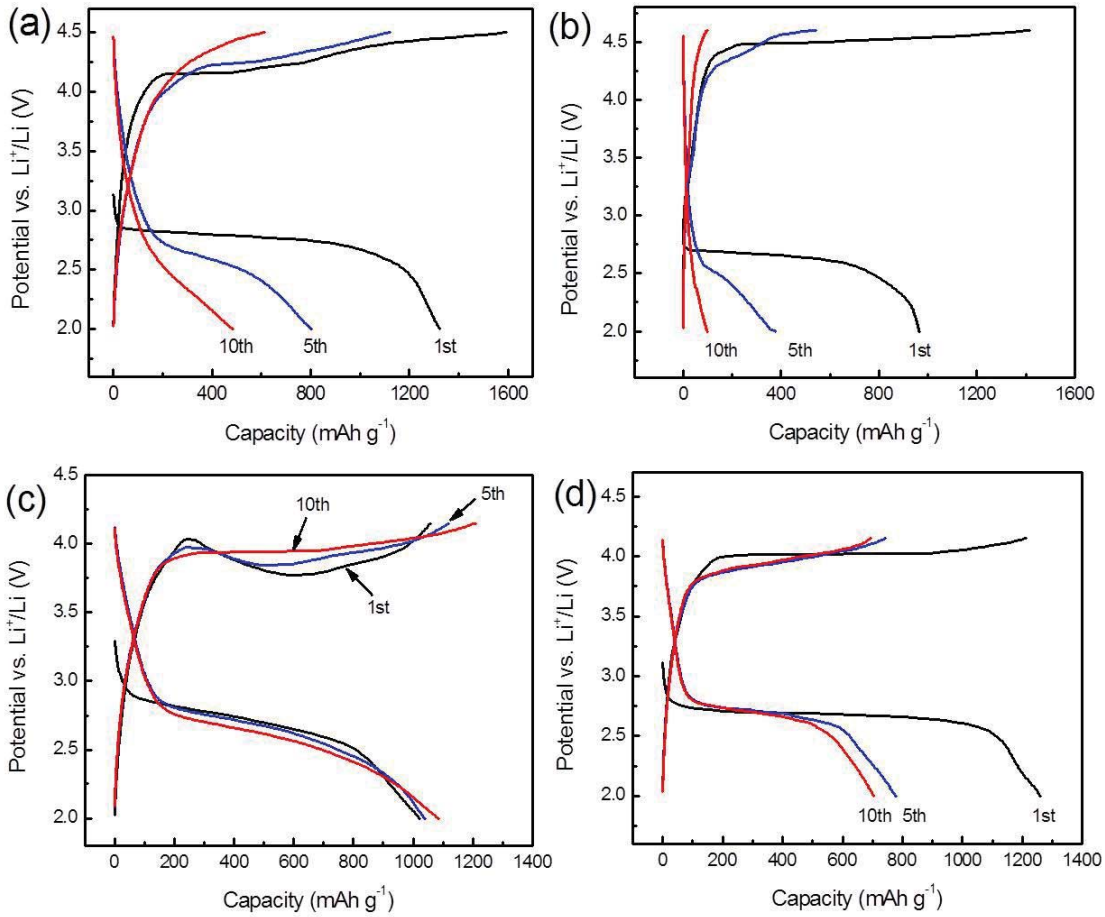

Figure 8-7 Charge-discharge voltage profiles of (a) mesoporous CMK-3 carbon, (b) Super-P, (c) CoO/CMK-3 nanocomposite and (d) CoO/Super-P nanocomposite. Capacities were calculated based on the weight of carbon in the electrode. Cycling was carried out at a current density of 100 mA g^{-1} (0.2 mA cm^{-2}) in 1 atm O_2 atmosphere.

The good electrochemical performance of the CoO/CMK-3 electrode may be due to the unique mesoporous nanostructure of CMK-3 carbon combined with the loading of CoO nanoparticles. There are several reasons for the capacity fading of an air electrode. The formation of a large amount of discharge products can cause the expansion of the electrode which will lead to a loss of the contact between electrode particles during the subsequent recharge process.[191] The morphologies of the CoO/CMK-3, CoO/Super-P,

CMK-3 and Super-P air electrodes before and after the first discharge were investigated by FESEM (as shown in Figure 8-9). The pores between the Super-P carbon black and CoO/Super-P particles in the air electrode were filled by the reduction products after discharge, which will cause large a volume expansion. The CoO/CMK-3 electrode consists of wormlike microsized particles. After discharge, the CoO/CMK-3 particles were covered by discharge products. The micropores between the CoO/CMK-3 particles were still present after discharge. The CMK-3 electrode showed similar morphology before and after discharge. Mesoporous CMK-3 carbon contains micro-sized particles, which are assemblies of hexagonally ordered carbon nanorods separated by meso-sized pore channels.[322,323] Due to the small pore size of around 5 nm, the capacity of CMK-3 electrode mainly comes from the outer surface of CMK-3 and the mesopores near the outer surface; not all of the interior surface of the mesopores can be used. Therefore, the good cycling performance of the CoO/CMK-3 electrode may be due to the catalytic effect of CoO nanoparticles and the unique mesoporous nanostructure of CMK-3 carbon.

Another reason for the capacity fading of the air electrodes is the decomposition of the electrolyte during the charge and discharge processes. Several recent publications have demonstrated that the lithium-oxygen electrochemistry when alkyl carbonate electrolytes are used is much more complicated than a simple combination reaction.[204,206,207,324,325] A recent report by Bruce et al. demonstrated that the discharge reaction in the most widely used alkyl carbonate electrolyte is the oxygen-involved

decomposition of the electrolyte and the formation of Li_2CO_3, CH_3CO_2Li, HCO_2Li, $C_3H_6(OCO_2Li)_2$, CO_2 and

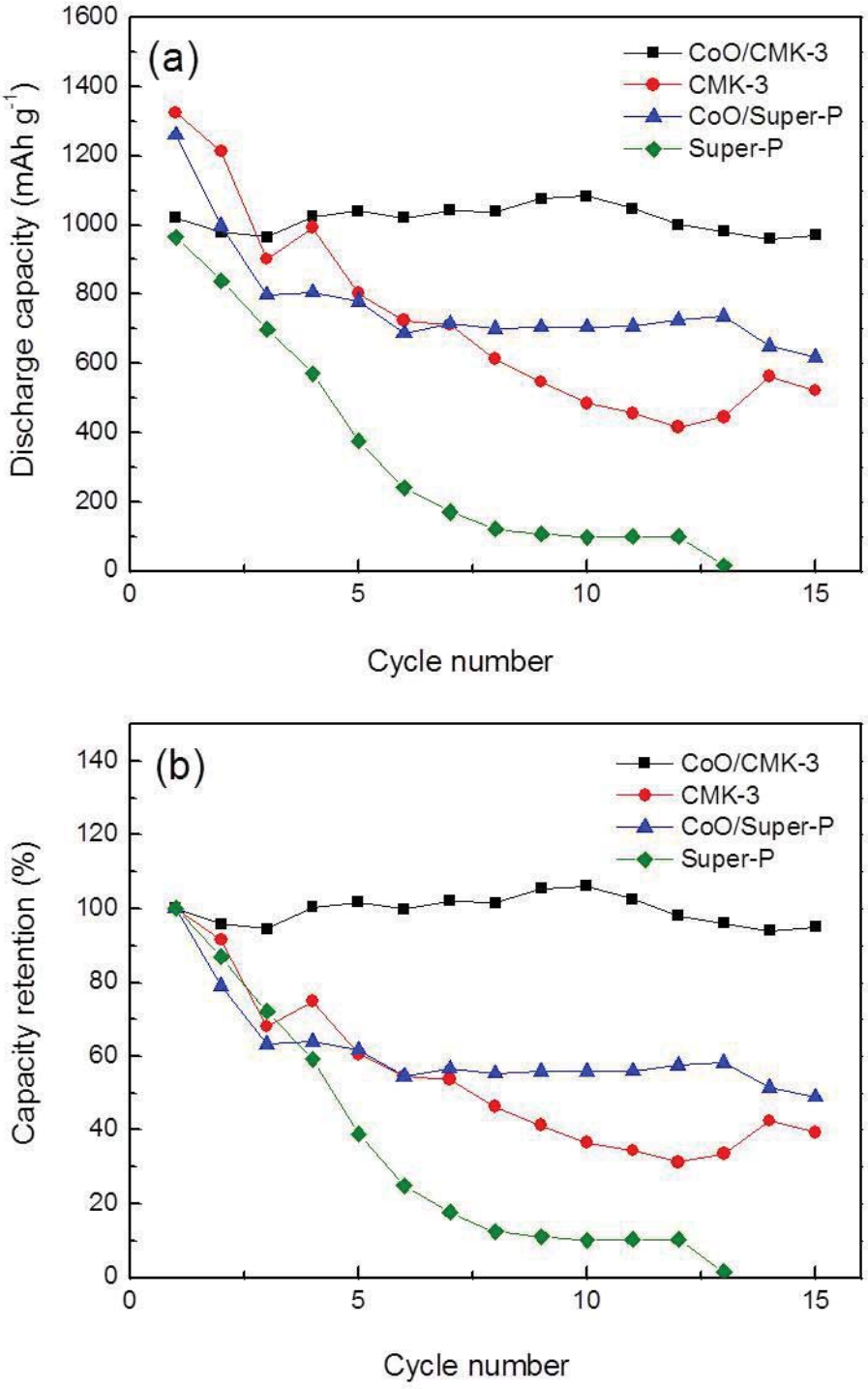

Figure 8-8 (a) Cycling performances and (b) capacity retention of the CMK-3, CoO/CMK-3, Super-P and CoO/Super-P nanocomposite electrodes. Cycling was carried out at a current density of 100 mA g^{-1} (0.2 mA cm^{-2}) in 1 atm O_2 atmosphere.

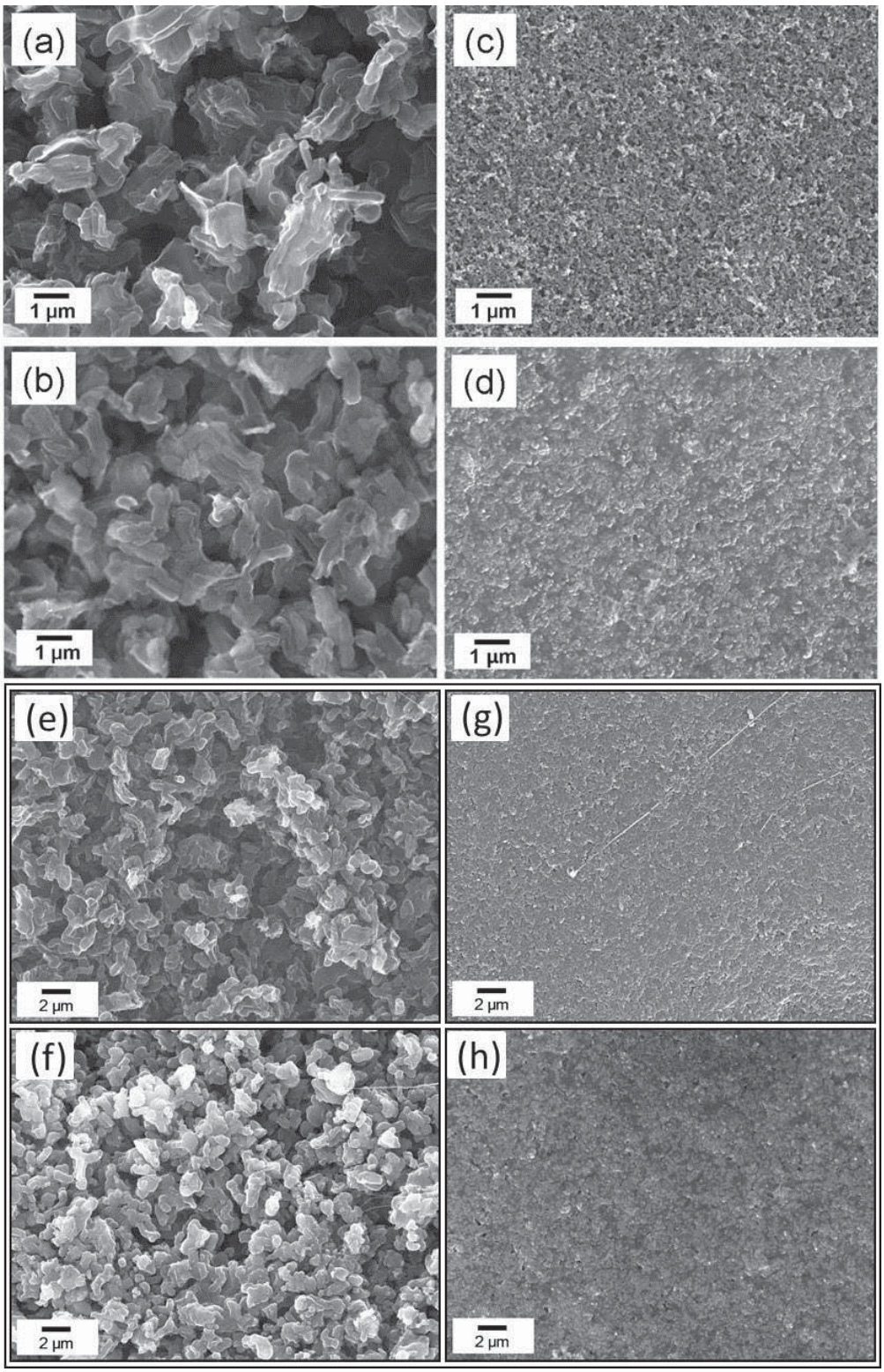

Figure 8-9 FESEM images of the mesoporous CoO/CMK-3 nanocomposite electrode before (a) and after (b) discharge, the CoO/Super-P nanocomposite electrode before (c) and after (d) discharge, mesoporous carbon CMK-3 electrode before (e) and after (f) discharge and the Super-P electrode before (g) and after (h) discharge.

H_2O. The charging reaction is the oxidation of the discharge products accompanied by CO_2 and H_2O evolution and the continuous decomposition of the electrolyte at high charged voltage.[206] Cycling involves the repeated decomposition of the electrolyte during discharge and oxidation of the deposited products during charge. The capacity fading of a lithium-oxygen cell during cycling is associated with the accumulation of these products in the air electrode and the starvation of the electrolyte. Bruce et al. also investigated the electrochemical reaction in lithium-oxygen batteries with ether-based electrolytes.[207] The ether-based electrolytes are more stable than carbonate electrolytes and can generate Li_2O_2 as the discharge product in the first cycle. However, the electrolytes also decompose to Li_2CO_3, HCO_2Li, CH_3CO_2Li, CO_2, and H_2O. The oxygen diffusion coefficient in an ether-based electrolyte is much higher than that of a carbonate electrolyte. This leads to an increase in capacity and rate performance. However, oxygen more easily diffuses through an ether-based electrolyte and reacts with lithium metal, which will reduce the cycling stability. Therefore, PC was used as the electrolyte in this investigation. The reaction products on the air electrodes in the lithium-oxygen cell were examined by Fourier transform infrared spectroscopy (FT-IR). The FT-IR spectra (Figure 8-10) of the discharged electrodes showed that the discharge products were dominated by Li_2CO_3 instead of the expected Li_2O_2, and that peaks associated with C=O, C-O, C-C and C-H groups were also present. Notably, the absorbance peaks associated with Li_2CO_3 and the above mentioned functional groups almost disappeared after charging of the mesoporous CMK-3 carbon electrode. The CoO/CMK-3 nanocomposite electrode showed similar FT-IR spectra after discharge and

recharge (Figure 8-10a). However, for the Super-P carbon black and CoO/Super-P nanocomposite electrodes, the absorbance peaks associated with the discharge products were still observed after recharge (Figure 8-10b and Figure 8-10d). These differences demonstrate that a mesoporous CMK-3 carbon electrode can more easily decompose the discharge products, which may also be attributed to its unique nanostructure. The discharge products mainly deposit on the outer surface and the mesopores near the outer surface. The micropores between the CMK-3 carbon micro-particles are retained as shown by the FESEM images (Figure 8-9). The presence of micropores between the CMK-3 carbon particles and ordered open pores throughout the CMK-3 carbon particles can facilitate the diffusion of the CO_2 and H_2O during the charging process. Therefore, the discharge products can be efficiently decomposed. After decomposition of the discharge products during the charging process, the remaining electrolyte can more easily penetrate into the ordered open mesopores occupied by the discharge product. Furthermore, after loading CoO nanoparticles, the CoO/CMK-3 electrode showed much lower charge voltage compared with the pristine CMK-3 carbon electrode. This significantly increased the round-trip efficiency. The detailed mechanism of the oxygen-based electrochemical reaction in alkyl carbonate electrolytes is still not completely clear, and we are still searching for a stable electrolyte for lithium-oxygen batteries. However, the as-prepared CoO/CMK-3 nanocomposite has shown an efficient catalytic effect as the air electrode in rechargeable lithium-oxygen batteries with organic electrolytes.

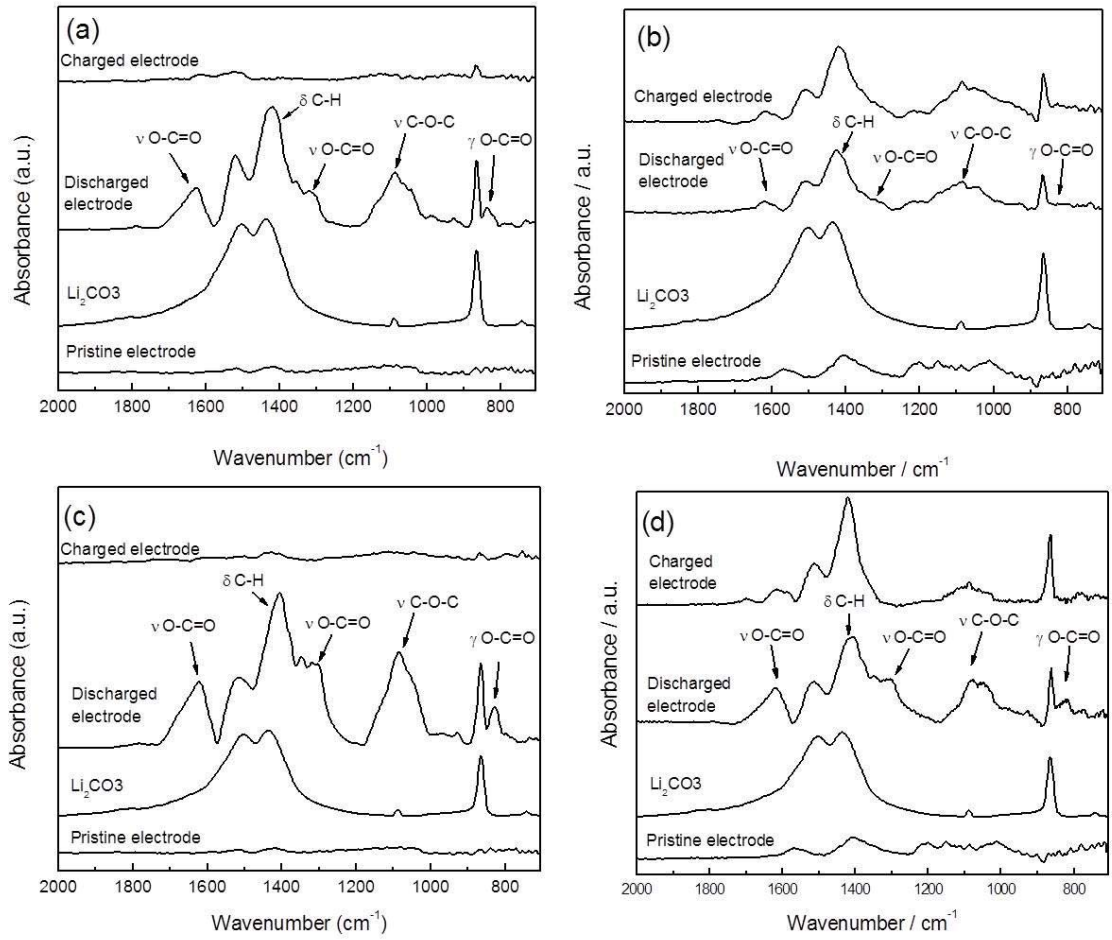

Figure 8-10 FT-IR spectra of pristine air electrodes, after the first discharge, and after subsequent recharge in 1 M $LiClO_4$ in PC under O_2. (a) mesoporous carbon CMK-3 electrode, (b) Super-P carbon black electrode，(c) mesoporous CoO/CMK-3 electrode and (d) CoO/Super-P electrode.

8.5 Summary

A mesoporous CoO/CMK-3 nanocomposite has been synthesised by an impregnation method. FESEM and TEM analysis confirmed that CoO nanoparticles were mainly loaded on the outer surface of the mesoporous CMK-3 carbon matrix. The as-prepared CoO/CMK-3 nanocomposite electrode exhibits better capacity retention than the bare mesoporous CMK-3 carbon, Super-P or the CoO/Super-P nanocomposite. The improved

catalytic performance can be attributed to the synergistic effect of the ordered open pore structure of CMK-3 carbon combined with the CoO nanocatalyst. The microsized CMK-3 carbon with its mesopores can facilitate the diffusion of oxygen during the discharge process and the release of the charge products (CO_2 and H_2O) during the charging process. The CoO nanoparticles can significantly reduce the charge over-potential and increase the round-trip efficiency. The use of microsized carbon particles with optimized mesopores as the supporting matrix and the loading of appropriate metal or metal oxide nanoparticles could be a promising strategy for the development of highly active catalyst materials for lithium-oxygen batteries.

Both of the graphene in Chapter 7 and the mesoporous CoO/CMK-3 nanocomposite in this chapter demonstrated that cathode catalyst can significantly enhance the electrochemical performance of lithium-oxygen batteries. The cathode catalysts can facilitate the oxygen reduction reaction, which can significantly increase the discharge capacities of lithium-oxygen batteries. They can also catalyse the decomposition of the discharge products during charge process, which greatly reduce the charge potential and increase the cycle efficiency.

CHAPTER 9 CONCLUSIONS

9.1 General Conclusion

This doctoral work has explored a series of methods for designing nanostructure materials for lithium-ion batteries and lithium-oxygen batteries, including a hydrothermal method, a soft template method, a hard template method and a chemical reduction method. Novel nanostructure materials were successfully synthesized, including one-dimensional nanorods, two-dimensional nanoplates and nanosheets, three-dimensional microsphere and mesoporous structures. The nanostructure materials show several advantages as the electrode materials or catalysts for lithium-ion batteries or lithium-oxygen batteries. The nanostructure materials for lithium-ion batteries can increase the electrode/electrolyte contact surface and shorten the lithium diffusion length. The nanostructure materials for lithium-oxygen batteries can reduce the charge-discharge over-potential and increase the round-trip efficiency.

9.1.1 Nanostructure $LiFePO_4$ as Cathode Materials for Lithium-Ion Batteries

$LiFePO_4$ facet nanoplates/graphene hybrid material with dominantly exposed (010) surfaces was successfully synthesized by a hydrothermal method and high temperature treatment. The as-prepared $LiFePO_4$ nanoplates were observed, via SEM, to be homogeneously distributed in a three-dimensional conductive graphene nanosheets

network. The carbon content of $LiFePO_4$ nanoplates/graphene hybrid material is about 18.59 wt% by thermogravimetric analysis. The $LiFePO_4$ nanoplates/graphene electrode showed discharge specific capacities of 163 mAh g^{-1}, 160 mAh g^{-1}, 138 mAh g^{-1}, 75 mAh g^{-1} at 0.2 C, 1 C, 10 C and 50 C, respectively. The hybrid material also delivered a specific energy of 554 Wh g^{-1} at 0.2 C and specific power >20 kW g^{-1} at 50 C. Further, the $LiFePO_4$ nanoplates/graphene hybrid material showed good cycle stability with a capacity retention of 96.7 % after 200 cycles at 5C. The excellent high-rate performance demonstrated that increasing the (010) surface and reducing the distance of the [010] direction of $LiFePO_4$ particles can significantly enhance lithium transport in the cell.

Porous $LiFePO_4$/C microspheres were successfully synthesized by a hydrothermal method and high temperature treatment. X-ray diffraction patterns showed Fe_2P and Li_3PO_4 impurities appeared when the calcination temperature increased higher than 700 °C. The as-prepared materials showed mesoporous microspheres morphology with a BET surface area of 18.1 m^2 g^{-1}. Each microsphere is actually a random aggregate of primary 100-200 nm carbon coated $LiFePO_4$ nanoparticles. The $LiFePO_4$/C microspheres synthesized at 700 °C delivered a discharge capacity of 150 mAh g^{-1} at 0.2 C and 91 mAh g^{-1} at 30 C. The mesoporous structure can facilitate the penetration of the electrolyte into the microspheres and the small amount of Fe_2P impurity can increase the electronic conductivity of the materials.

9.1.2 Nanostructure Transition Metal Oxide as Anode Materials for Lithium-Ion Batteries

Mesoporous α-Fe_2O_3 was successfully synthesized by a soft template method. The hematite crystal structure was confirmed by X-ray diffraction pattern and Raman spectroscopy. The as-prepared material exhibited an ordered porous structure with different shapes of pores and a large surface area of 128 m^2 g^{-1}. When used as an anode material in lithium-ion batteries, the as-prepared mesoporous α-Fe_2O_3 electrodes showed a high discharge specific capacity of 1730 mAh g^{-1} for the first cycle and 1293 mAh g^{-1} at the fiftieth cycle. The mesoporous α-Fe_2O_3 electrode also showed excellent high-rate performance with a discharge capacity of 877 mAh g^{-1} at 2 C. The higher surface area of mesoporous α-Fe_2O_3 can provide high surface contact with the electrolyte and decreases the current density per unit area. The porous structure can accommodate the volume change of the Li^+ insertion/extraction during the charge-discharge process, which can prevent the active materials falling off the current collector.

MnO/C core-shell nanorods were successfully prepared from the reduction of MnO_2 nanowires, which were synthesized by a hydrothermal method. Non-ionic block co-polymer poly (ethylene oxide)-block-poly (propylene oxide)-block-poly (ethylene oxide)-($EO_{106}PO_{70}EO_{106}$) Pluronic® F127 (Sigma-Aldrich) was used as the carbon source for carbon coating. The X-ray diffraction pattern shows that after calcination α-MnO_2 converted to body-centered tetragonal MnO. Transmission electron microscopy images showed that a thin carbon layer was coated on the surfaces of the MnO nanorods.

The initial discharge capacity of the MnO/C nanorod electrode was 1090 mAh g^{-1}. After 40 cycles, the specific capacity decreased to 602 mAh g^{-1}, which is higher than that of the MnO microparticle and MnO_2 nanowire electrodes. A one-dimension nanowire structure can greatly shorten the diffusion length for lithium ions in the solid phase. The nanoporous carbon coating layer with mesopores can form a mixed conducting three-dimensional network that facilitates the migration of both the Li^+ and the e^-, so that they each reach each the surface of the MnO nanorods.

9.1.3 Nanostructure Materials as Cathode Catalyst for Lithium-Oxygen Batteries

Graphene nanosheets (GNSs) have been prepared by a chemical reduction reaction. The SEM images showed the as-prepared GNSs consist of almost transparent wrinkle-like thin nanosheets. The specific surface area estimated from the BET method was 309 m^2 g^{-1}. When directly used as cathode catalysts for lithium-oxygen batteries in alkyl carbonate electrolyte, the as-prepared GNSs electrode exhibited better cyclability and lower over-potential than that of the Vulcan XC-72 electrode. The initial capacity of the electrode made of GNSs was 1597 mAh g^{-1}. It then dramatically increased to 2332 mAh g^{-1} on the second cycle and was sustained at 2359 mAh g^{-1} on the fifth cycle. The discharge reaction in the cathode electrode of the lithium-oxygen battery is the decomposition of the electrolyte and the charge reaction is the oxidation of those discharge products. The reduced over-potential shows the as-prepared GNSs are more electrochemically active than the Vulcan XC-72 towards those reactions in an alkyl carbonate electrolyte. The increased electrocatalytic activity of the as-prepared GNSs

was proposed to arise from the presence of many carbon vacancies and defects on the surface of GNSs.

Mesoporous CoO/CMK-3 nanocomposite was synthesised by an impregnation method using mesoporous carbon CMK-3 as the template. FESEM and TEM analysis confirmed that CoO nanoparticles were mainly loaded on the outer surface of the mesoporous CMK-3 carbon matrix. The loading of CoO in the as-prepared CoO/CMK-3 nanocomposite was determined to be about 25 wt% by thermogravimetric analysis. When used as the cathode catalyst in lithium-oxygen batteries, the as-prepared CoO/CMK-3 nanocomposite electrode exhibits better capacity retention than that of bare mesoporous CMK-3 carbon, Super-P or CoO/Super-P nanocomposite electrodes. The CoO/CMK-3 electrode exhibited an initial discharge capacity of 1021 mAh g^{-1} and 970 mAh g^{-1} at the 15th cycle with capacity retention of 95%. The improved catalytic performance was attributed to the synergistic effect of the ordered open pore structure of CMK-3 carbon conbined with the CoO nanocatalyst. The microsized CMK-3 carbon with mesopores can facilitate the diffusion of the oxygen during the discharge process and the release of the charge products (CO_2 and H_2O) during the charging process. The CoO nanoparticles can significantly reduce the charge over-potential and increase the round-trip efficiency.

9.2 Outlook

This doctoral work mainly focuses on the synthesis of nanostructure materials and their application in lithium-ion batteries and lithium-oxygen batteries. The synthesis methods presented are also applicable to the preparation of other nanostructure materials.

For facet $LiFePO_4$ nanoplates, the experimental results demonstrated that increasing the (010) surface can facilitate the lithium ion diffusion through the solid phase. This strategy can be applied to other olivine structure materials, such as $LiMnPO_4$, $LiCoPO_4$, Li_2FeSiO_4, etc. The hierarchical $LiFePO_4$ microsphere showed good electrochemical performance and relative high tap density; the technique for its synthesis can be used to synthesize other electrode materials with a hierarchical structure. For mesoporous transition metal oxides, the pores and the nanoscale walls are both beneficial for lithium diffusion. However, the electronic conductivity of the transient metal oxides is still poor. Coating a nano-layer of carbon inside the nanopores could be a promising strategy for increasing the electronic conductivity. It should be noted that the electrochemical performance testing only focused on the specific capacity, cycling life and rate capability. Other electrochemical performance, such as high/low temperature behaviour, has not been investigated. For the future commercialization of lithium-ion batteries, the synthesis processes for those materials in this doctoral work are also complicated, which makes it difficult to scale up.

Nanostructure catalyst materials have shown increased electrocatalytic activity in the

electrochemical reactions in lithium-oxygen batteries with organic electrolytes. However, the high activity may also accelerate the decomposition of the organic electrolyte. Searching for a stable electrolyte becomes a major challenge for rechargeable lithium-oxygen batteries. An ionic liquid electrolyte or a solid state electrolyte may serve as alternative electrolytes in the future development of lithium-oxygen batteries. For the future commercialization of lithium-oxygen batteries, the biggest barriers are the cycling life and the charge-discharge electricity efficiency.

REFERENCES

[1] Armand, M.; Tarascon, J. M.: Building better batteries. *Nature* **2008**, *451*, 652-657.

[2] Bashash, S.; Moura, S. J.; Forman, J. C.; Fathy, H. K.: Plug-in hybrid electric vehicle charge pattern optimization for energy cost and battery longevity. *J. Power Sources* **2011**, *196*, 541-549.

[3] Wadia, C.; Albertus, P.; Srinivasan, V.: Resource constraints on the battery energy storage potential for grid and transportation applications. *J. Power Sources* **2011**, *196*, 1593-1598.

[4] Tarascon, J. M.; Armand, M.: Issues and challenges facing rechargeable lithium batteries. *Nature* **2001**, *414*, 359-367.

[5] Etacheri, V.; Marom, R.; Elazari, R.; Salitra, G.; Aurbach, D.: Challenges in the development of advanced Li-ion batteries: a review. *Energy Environ. Sci.* **2011**, *4*, 3243-3262.

[6] Bruce, P. G.; Freunberger, S. A.; Hardwick, L. J.; Tarascon, J. M.: Li-O_2 and Li-S batteries with high energy storage. *Nat. Mater.* **2012**, *11*, 19-29.

[7] Girishkumar, G.; McCloskey, B.; Luntz, A. C.; Swanson, S.; Wilcke, W.: Lithium - air Battery: promise and challenges. *J. Phys. Chem. Lett.* **2010**, *1*, 2193-2203.

[8] Gamble, F. R.; Osiecki, J. H.; Cais, M.; Pisharod.R: Intercalation complexes of lewis bases and layered sulfides - large class of new superconductors. *Science* **1971**, *174*, 493-497.

[9] Whittingham, M. S.: Hydrated intercalation complexes of layered disulfides. *Mater. Res. Bull.* **1974**, *9*, 1681-1690.

[10] Whittingham, M. S.: Electrointercalation in transition-metal disulfides. *J. Chem. Soc., Chem. Commun.* **1974**, 328-329.

[11] Whittingham, M. S.: Electrical energy-storage and intercalation chemistry. *Science* **1976**, *192*, 1126-1127.

[12] Thompson, A. H.: Electron-electron scattering in TiS_2. *Phys. Rev. Lett.* **1975**, *35*, 1786-1789.

[13] Whittingham, M. S.: Role of ternary phases in cathode reactions. *J. Electrochem. Soc.* **1976**, *123*, 315-320.

[14] Whittingham, M. S.: Lithium batteries and cathode materials. *Chem. Rev.* **2004**, *104*, 4271-4301.

[15] Walk, C. R.; Gore, J. S.: Li-V_2O_5 secondary cell. *J. Electrochem. Soc.* **1975**, *122*, C68-C68.

[16] Delmas, C.; Cognacauradou, H.; Cocciantelli, J. M.; Menetrier, M.; Doumerc, J. P.: The $Li_xV_2O_5$ system - an overview of the structure modifications induced by the lithium intercalation. *Solid State Ionics* **1994**, *69*, 257-264.

[17] Dickens, P. G.; French, S. J.; Hight, A. T.; Pye, M. F.: Phase-relationships in the ambient-temperature $Li_xV_2O_5$ system ($0.1<x<1.0$). *Mater. Res. Bull.* **1979**, *14*, 1295-1299.

[18] Mizushima, K.; Jones, P. C.; Wiseman, P. J.; Goodenough, J. B.: Li_xCoO_2 ($0<x<-1$): a new cathode material for batteries of high-energy density. *Mater. Res. Bull.* **1980**, *15*, 783-789.

[19] Amatucci, G. G.; Tarascon, J. M.; Klein, L. C.: CoO_2, the end member of the Li_xCoO_2 solid solution. *J. Electrochem. Soc.* **1996**, *143*, 1114-1123.

[20] Yazami, R.; Touzain, P.: A reversible graphite-lithium negative electrode for electrochemical generators. *J. Power Sources* **1983**, *9*, 365-371.

[21] Ozawa, K.: Lithium-ion rechargeable batteries with $LiCoO_2$ and carbon electrodes: the $LiCoO_2$/C system. *Solid State Ionics* **1994**, *69*, 212-221.

[22] Bruce, P. G.: Energy storage beyond the horizon: Rechargeable lithium batteries. *Solid State Ionics* **2008**, *179*, 752-760.

[23] Winter, M.; Brodd, R. J.: What are batteries, fuel cells, and supercapacitors? *Chem. Rev.* **2004**, *104*, 4245-4269.

[24] Xu, K.: Nonaqueous liquid electrolytes for lithium-based rechargeable batteries. *Chem. Rev.* **2004**, *104*, 4303-4417.

[25] Goodenough, J. B.; Kim, Y.: Challenges for Rechargeable Li Batteries. *Chem. Mater.* **2010**, *22*, 587-603.

[26] Hayashi, K.; Nemoto, Y.; Tobishima, S.; Yamaki, J.: Mixed solvent electrolyte for high voltage lithium metal secondary cells. *Electrochim. Acta* **1999**, *44*, 2337-2344.

[27] Koch, V. R.; Dominey, L. A.; Nanjundiah, C.; Ondrechen, M. J.: The intrinsic anodic stability of several anions comprising solvent-free ionic liquids. *J. Electrochem. Soc.* **1996**, *143*, 798-803.

[28] Garcia, B.; Lavallee, S.; Perron, G.; Michot, C.; Armand, M.: Room temperature molten salts as lithium battery electrolyte. *Electrochim. Acta* **2004**, *49*, 4583-4588.

[29] Markevich, E.; Baranchugov, V.; Aurbach, D.: On the possibility of using ionic liquids as electrolyte solutions for rechargeable 5 V Li ion batteries. *Electrochem. Commun.* **2006**, *8*, 1331-1334.

[30] Wang, Y. D.; Zaghib, K.; Guerfi, A.; Bazito, F. F. C.; Torresi, R. M.; Dahn, J. R.: Accelerating rate calorimetry studies of the reactions between ionic liquids and charged lithium ion battery electrode materials. *Electrochim. Acta* **2007**, *52*, 6346-6352.

[31] Stassen, I.; Hambitzer, G.: Metallic lithium batteries for high power applications. *J. Power Sources* **2002**, *105*, 145-150.

[32] Zinck, L.; Borck, M.; Ripp, C.; Hambitzer, G.: Purification process for an inorganic rechargeable lithium battery and new safety concepts. *J. Appl. Electrochem.* **2006**, *36*, 1291-1295.

[33] Nishimoto, A.; Watanabe, M.; Ikeda, Y.; Kohjiya, S.: High ionic conductivity of new polymer electrolytes based on high molecular weight polyether comb polymers. *Electrochim. Acta* **1998**,

43, 1177-1184.

[34] Pradel, A.; Ribes, M.: Lithium chalcogenide conductive glasses. *Mater. Chem. Phys.* **1989**, *23*, 121-142.

[35] Adachi, G. Y.; Imanaka, N.; Aono, H.: Fast Li-circle plus conducting ceramic electrolytes. *Adv. Mater.* **1996**, *8*, 127-&.

[36] Minami, T.; Hayashi, A.; Tatsumisago, M.: Recent progress of glass and glass-ceramics as solid electrolytes for lithium secondary batteries. *Solid State Ionics* **2006**, *177*, 2715-2720.

[37] Kim, Y.; Saienga, J.; Martin, S. W.: Anomalous ionic conductivity increase in Li_2S+GeS_2+GeO_2 glasses. *J. Phys. Chem. B* **2006**, *110*, 16318-16325.

[38] Feuillade, G.; Perche, P.: Ion-conductive macromolecular gels and membranes for solid lithium cells. *J. Appl. Electrochem.* **1975**, *5*, 63-69.

[39] Croce, F.; Curini, R.; Martinelli, A.; Persi, L.; Ronci, F.; Scrosati, B.; Caminiti, R.: Physical and chemical properties of nanocomposite polymer electrolytes. *J. Phys. Chem. B* **1999**, *103*, 10632-10638.

[40] Fuller, J.; Breda, A. C.; Carlin, R. T.: Ionic liquid-polymer gel electrolytes. *J. Electrochem. Soc.* **1997**, *144*, L67-L70.

[41] Shin, J. H.; Henderson, W. A.; Passerini, S.: Ionic liquids to the rescue? Overcoming the ionic conductivity limitations of polymer electrolytes. *Electrochem. Commun.* **2003**, *5*, 1016-1020.

[42] Ye, H.; Huang, J.; Xu, J. J.; Khalfan, A.; Greenbaum, S. G.: Li ion conducting polymer gel electrolytes based on ionic liquid/PVDF-HFP blends. *J. Electrochem. Soc.* **2007**, *154*, A1048-A1057.

[43] Sirisopanaporn, C.; Fernicola, A.; Scrosati, B.: New, ionic liquid-based membranes for lithium

battery application. *J. Power Sources* **2009**, *186*, 490-495.

[44] Cho, J. P.; Liu, M. L.: Preparation and electrochemical properties of glass-polymer composite electrolytes for lithium batteries. *Electrochim. Acta* **1997**, *42*, 1481-1488.

[45] Hayashi, A.; Kitade, T.; Ikeda, Y.; Kohjiya, S.; Matsuda, A.; Tatsumisago, M.; Minami, T.: Preparation and characterization of lithium ion conducting glass-polymer composites. *Chem. Lett.* **2001**, 814-815.

[46] Inda, Y.; Katoh, T.; Baba, M.: Development of all-solid lithium-ion battery using Li-ion conducting glass-ceramics. *J. Power Sources* **2007**, *174*, 741-744.

[47] Arora, P.; Zhang, Z. M.: Battery separators. *Chem. Rev.* **2004**, *104*, 4419-4462.

[48] Arico, A. S.; Bruce, P.; Scrosati, B.; Tarascon, J. M.; Van Schalkwijk, W.: Nanostructured materials for advanced energy conversion and storage devices. *Nat. Mater.* **2005**, *4*, 366-377.

[49] Bruce, P. G.; Scrosati, B.; Tarascon, J. M.: Nanomaterials for rechargeable lithium batteries. *Angew. Chem. Int. Ed.* **2008**, *47*, 2930-2946.

[50] Guo, Y. G.; Hu, J. S.; Wan, L. J.: Nanostructured materials for electrochemical energy conversion and storage devices. *Adv. Mater.* **2008**, *20*, 2878-2887.

[51] Jamnik, J.; Maier, J.: Nanocrystallinity effects in lithium battery materials - Aspects of nano-ionics. Part IV. *Phys. Chem. Chem. Phys.* **2003**, *5*, 5215-5220.

[52] Maier, J.: Nanoionics: ion transport and electrochemical storage in confined systems. *Nat. Mater.* **2005**, *4*, 805-815.

[53] Balaya, P.: Size effects and nanostructured materials for energy applications. *Energy Environ. Sci.* **2008**, *1*, 645-654.

[54] Wang, Q.; Li, H.; Chen, L. Q.; Huang, X. J.: Monodispersed hard carbon spherules with uniform

nanopores. *Carbon* **2001**, *39*, 2211-2214.

[55] Kaskhedikar, N. A.; Maier, J.: Lithium storage in carbon nanostructures. *Adv. Mater.* **2009**, *21*, 2664-2680.

[56] Wu, X. L.; Jiang, L. Y.; Cao, F. F.; Guo, Y. G.; Wan, L. J.: $LiFePO_4$ Nanoparticles Embedded in a Nanoporous Carbon Matrix: Superior Cathode Material for Electrochemical Energy-Storage Devices. *Adv. Mater.* **2009**, *21*, 2710-+.

[57] Jiao, F.; Bruce, P. G.: Mesoporous crystalline beta-MnO_2- a reversible positive electrode for rechargeable lithium batteries. *Adv. Mater.* **2007**, *19*, 657-+.

[58] Balaya, P.; Bhattacharyya, A. J.; Jamnik, J.; Zhukovskii, Y. F.; Kotomin, E. A.; Maier, J.: Nano-ionics in the context of lithium batteries. *J. Power Sources* **2006**, *159*, 171-178.

[59] Delmer, O.; Balaya, P.; Kienle, L.; Maier, J.: Enhanced potential of amorphous electrode materials: Case study of RuO_2. *Adv. Mater.* **2008**, *20*, 501-+.

[60] Robertson, A. D.; Armstrong, A. R.; Bruce, P. G.: Layered $Li_xMn_{1-y}Co_yO_2$ intercalation electrodes-influence of ion exchange on capacity and structure upon cycling. *Chem. Mater.* **2001**, *13*, 2380-2386.

[61] Meethong, N.; Huang, H. Y. S.; Speakman, S. A.; Carter, W. C.; Chiang, Y. M.: Strain accommodation during phase transformations in olivine-based cathodes as a materials selection criterion for high-power rechargeable batteries. *Adv. Funct. Mater.* **2007**, *17*, 1115-1123.

[62] Reimers, J. N.; Dahn, J. R.: Electrochemical and in situ X-ray-diffraction studies of lithium intercalation in Li_xCoO_2. *J. Electrochem. Soc.* **1992**, *139*, 2091-2097.

[63] Shao-Horn, Y.; Croguennec, L.; Delmas, C.; Nelson, E. C.; O'Keefe, M. A.: Atomic resolution of lithium ions in $LiCoO_2$. *Nat. Mater.* **2003**, *2*, 464-467.

[64] Imanishi, N.; Fujiyoshi, M.; Takeda, Y.; Yamamoto, O.; Tabuchi, M.: Preparation and Li-7-NMR study of chemically delithiated $Li_{1-x}CoO_2$ ($0 < x < 0.5$). *Solid State Ionics* **1999**, *118*, 121-128.

[65] Levasseur, S.; Menetrier, M.; Suard, E.; Delmas, C.: Evidence for structural defects in non-stoichiometric HT-$LiCoO_2$: electrochemical, electronic properties and Li-7 NMR studies. *Solid State Ionics* **2000**, *128*, 11-24.

[66] Fu, L. J.; Liu, H.; Li, C.; Wu, Y. P.; Rahm, E.; Holze, R.; Wu, H. Q.: Surface modifications of electrode materials for lithium ion batteries. *Solid State Sci.* **2006**, *8*, 113-128.

[67] Cao, Q.; Zhang, H. P.; Wang, G. J.; Xia, Q.; Wu, Y. P.; Wu, H. Q.: A novel carbon-coated $LiCoO_2$ as cathode material for lithium ion battery. *Electrochem. Commun.* **2007**, *9*, 1228-1232.

[68] Cho, J.; Kim, Y. J.; Kim, T. J.; Park, B.: Zero-strain intercalation cathode for rechargeable Li-ion cell. *Angew. Chem. Int. Ed.* **2001**, *40*, 3367-+.

[69] Cho, J.; Kim, Y. W.; Kim, B.; Lee, J. G.; Park, B.: A breakthrough in the safety of lithium secondary batteries by coating the cathode material with AIPO(4) nanoparticles. *Angew. Chem. Int. Ed.* **2003**, *42*, 1618-1621.

[70] Kim, J.; Noh, M.; Cho, J.; Kim, H.; Kim, K. B.: Controlled nanoparticle metal phosphates (metal = Al, Fe, Ce, and Sr) coatings on $LiCoO_2$ cathode materials. *J. Electrochem. Soc.* **2005**, *152*, A1142-A1148.

[71] Zhou, Y. K.; Shen, C. M.; Li, H. L.: Synthesis of high-ordered $LiCoO_2$ nanowire arrays by AAO template. *Solid State Ionics* **2002**, *146*, 81-86.

[72] Li, X. X.; Cheng, F. Y.; Guo, B.; Chen, J.: Template-synthesized $LiCoO_2$, $LiMn_2O_4$, and $LiNi_{0.8}Co_{0.2}O_2$ nanotubes as the cathode materials of lithium ion batteries. *J. Phys. Chem. B* **2005**, *109*, 14017-14024.

[73] Chen, H. L.; Grey, C. P.: Molten salt synthesis and high rate performance of the "Desert-Rose" form of $LiCoO_2$. *Adv. Mater.* **2008**, *20*, 2206-+.

[74] Jiao, F.; Shaju, K. M.; Bruce, P. G.: Synthesis of nanowire and mesoporous low-temperature $LiCoO_2$ by a post-templating reaction. *Angew. Chem. Int. Ed.* **2005**, *44*, 6550-6553.

[75] Manthiram, A.; Murugan, A. V.; Sarkar, A.; Muraliganth, T.: Nanostructured electrode materials for electrochemical energy storage and conversion. *Energy Environ. Sci.* **2008**, *1*, 621-638.

[76] Dahn, J. R.; Vonsacken, U.; Michal, C. A.: Structure and electrochemistry of $Li_{1+/-y}NiO_2$ and a new Li_2NiO_2 phase with the $Ni(OH)_2$ structure. *Solid State Ionics* **1990**, *44*, 87-97.

[77] Armstrong, A. R.; Bruce, P. G.: Synthesis of layered $LiMnO_2$ as an electrode for rechargeable lithium batteries. *Nature* **1996**, *381*, 499-500.

[78] Capitaine, F.; Gravereau, P.; Delmas, C.: A new variety of $LiMnO_2$ with a layered structure. *Solid State Ionics* **1996**, *89*, 197-202.

[79] Vitins, G.; West, K.: Lithium intercalation into layered $LiMnO_2$. *J. Electrochem. Soc.* **1997**, *144*, 2587-2592.

[80] Liu, Z. L.; Yu, A. S.; Lee, J. Y.: Synthesis and characterization of $LiNi_{1-x-y}Co_xMn_yO_2$ as the cathode materials of secondary lithium batteries. *J. Power Sources* **1999**, *81*, 416-419.

[81] Yoshio, M.; Noguchi, H.; Itoh, J.; Okada, M.; Mouri, T.: Preparation and properties of $LiCo_yMn_xNi_{1-x-y}O_2$ as a cathode for lithium ion batteries. *J. Power Sources* **2000**, *90*, 176-181.

[82] Ohzuku, T.; Makimura, Y.: Layered lithium insertion material of $LiCo_{1/3}Ni_{1/3}Mn_{1/3}O_2$ for lithium-ion batteries. *Chem. Lett.* **2001**, 642-643.

[83] Zhou, F.; Zhao, X. M.; Dahn, J. R.: Synthesis, Electrochemical Properties, and Thermal Stability of Al-Doped $LiNi_{1/3}Mn_{1/3}Co_{1/3-z}Al_zO_2$ Positive Electrode Materials. *J. Electrochem. Soc.* **2009**,

156, A343-A347.

[84] Luo, W. B.; Zhou, F.; Zhao, X. M.; Lu, Z. H.; Li, X. H.; Dahn, J. R.: Synthesis, Characterization, and Thermal Stability of $LiNi_{1/3}Mn_{1/3}Co_{1/3-z}Mg_zO_2$, $LiNi_{1/3-z}Mn_{1/3}Co_{1/3}Mg_zO_2$ and $LiNi_{1/3}Mn_{1/3-z}Co_{1/3}Mg_zO_2$. *Chem. Mater.* **2010**, *22*, 1164-1172.

[85] Thackeray, M. M.; David, W. I. F.; Bruce, P. G.; Goodenough, J. B.: Lithium insertion into manganese spinels. *Mater. Res. Bull.* **1983**, *18*, 461-472.

[86] Tarascon, J. M.; Wang, E.; Shokoohi, F. K.; McKinnon, W. R.; Colson, S.: The spinel phase of $LiMn_2O_4$ as a cathode in secondary lithium cells. *J. Electrochem. Soc.* **1991**, *138*, 2859-2864.

[87] Tarascon, J. M.; McKinnon, W. R.; Coowar, F.; Bowmer, T. N.; Amatucci, G.; Guyomard, D.: Synthesis conditions and oxygen stoichiometry effects on Li insertion into the spinel $LiMn_2O_4$. *J. Electrochem. Soc.* **1994**, *141*, 1421-1431.

[88] Guyomard, D.; Tarascon, J. M.: The carbon $Li_{1+X}Mn_2O_4$ system. *Solid State Ionics* **1994**, *69*, 222-237.

[89] Yonemura, M.; Yamada, A.; Kobayashi, H.; Tabuchi, M.; Kamiyama, T.; Kawamoto, Y.; Kanno, R.: Synthesis, structure, and phase relationship in lithium manganese oxide spinel. *J. Mater. Chem.* **2004**, *14*, 1948-1958.

[90] Thackeray, M. M.: Manganese oxides for lithium batteries. *Prog. Solid State Chem.* **1997**, *25*, 1-71.

[91] Cho, J.; Thackeray, M. M.: Structural changes of LiMn2O4 spinel electrodes during electrochemical cycling. *J. Electrochem. Soc.* **1999**, *146*, 3577-3581.

[92] Sun, Y. K.; Hong, K. J.; Prakash, J.: The effect of ZnO coating on electrochemical cycling behavior of spinel $LiMn_2O_4$ cathode materials at elevated temperature. *J. Electrochem. Soc.* **2003**,

150, A970-A972.

[93] Kim, J. S.; Johnson, C. S.; Vaughey, J. T.; Hackney, S. A.; Walz, K. A.; Zeltner, W. A.; Anderson, M. A.; Thackeray, M. M.: The electrochemical stability of spinel electrodes coated with ZrO_2, Al_2O_3, and SiO_2 from colloidal suspensions. *J. Electrochem. Soc.* **2004**, *151*, A1755-A1761.

[94] Hosono, E.; Kudo, T.; Honma, I.; Matsuda, H.; Zhou, H. S.: Synthesis of Single Crystalline Spinel $LiMn_2O_4$ Nanowires for a Lithium Ion Battery with High Power Density. *Nano Lett.* **2009**, *9*, 1045-1051.

[95] Kim, D. K.; Muralidharan, P.; Lee, H. W.; Ruffo, R.; Yang, Y.; Chan, C. K.; Peng, H.; Huggins, R. A.; Cui, Y.: Spinel $LiMn_2O_4$ Nanorods as Lithium Ion Battery Cathodes. *Nano Lett.* **2008**, *8*, 3948-3952.

[96] Ding, Y. L.; Xie, J. A.; Cao, G. S.; Zhu, T. J.; Yu, H. M.; Zhao, X. B.: Single-Crystalline $LiMn_2O_4$ Nanotubes Synthesized Via Template-Engaged Reaction as Cathodes for High-Power Lithium Ion Batteries. *Adv. Funct. Mater.* **2011**, *21*, 348-355.

[97] Jiao, F.; Bao, J. L.; Hill, A. H.; Bruce, P. G.: Synthesis of Ordered Mesoporous Li-Mn-O Spinel as a Positive Electrode for Rechargeable Lithium Batteries. *Angew. Chem. Int. Ed.* **2008**, *47*, 9711-9716.

[98] von Bulow, J. F.; Zhang, H. L.; Morse, D. E.: Hydrothermal realization of high-power nanocomposite cathodes for lithium ion batteries. *Adv. Energy Mater.* **2012**, *2*, 309-315.

[99] Ding, Y. H.; Li, J. X.; Zhao, Y.; Guan, L. H.: Direct growth of $LiMn_2O_4$ on carbon nanotubes as cathode materials for lithium ion batteries. *Mater. Lett.* **2012**, *68*, 197-200.

[100] Zhao, X.; Hayner, C. M.; Kung, H. H.: Self-assembled lithium manganese oxide nanoparticles on carbon nanotube or graphene as high-performance cathode material for lithium-ion batteries.

J. Mater. Chem. **2011**, *21*, 17297-17303.

[101] Padhi, A. K.; Nanjundaswamy, K. S.; Goodenough, J. B.: Phospho-olivines as positive-electrode materials for rechargeable lithium batteries. *J. Electrochem. Soc.* **1997**, *144*, 1188-1194.

[102] Zhang, W. J.: Structure and performance of $LiFePO_4$ cathode materials: A review. *J. Power Sources* **2011**, *196*, 2962-2970.

[103] Herle, P. S.; Ellis, B.; Coombs, N.; Nazar, L. F.: Nano-network electronic conduction in iron and nickel olivine phosphates. *Nat. Mater.* **2004**, *3*, 147-152.

[104] Zaghib, K.; Shim, J.; Guerfi, A.; Charest, P.; Striebel, K. A.: Effect of carbon source as additives in $LiFePO_4$ as positive electrode for lithium-ion batteries. *Electrochem. Solid State Lett.* **2005**, *8*, A207-A210.

[105] Wang, G. X.; Liu, H.; Liu, J.; Qiao, S. Z.; Lu, G. Q. M.; Munroe, P.; Ahn, H.: Mesoporous $LiFePO_4$/C Nanocomposite Cathode Materials for High Power Lithium Ion Batteries with Superior Performance. *Adv. Mater.* **2010**, *22*, 4944-4948.

[106] Ouyang, C. Y.; Shi, S. Q.; Wang, Z. X.; Huang, X. J.; Chen, L. Q.: First-principles study of Li ion diffusion in $LiFePO_4$. *Phys. Rev. B* **2004**, *69*.

[107] Yuan, L. X.; Wang, Z. H.; Zhang, W. X.; Hu, X. L.; Chen, J. T.; Huang, Y. H.; Goodenough, J. B.: Development and challenges of $LiFePO_4$ cathode material for lithium-ion batteries. *Energy Environ. Sci.* **2011**, *4*, 269-284.

[108] Chung, S. Y.; Bloking, J. T.; Chiang, Y. M.: Electronically conductive phospho-olivines as lithium storage electrodes. *Nat. Mater.* **2002**, *1*, 123-128.

[109] Wang, Y. G.; He, P.; Zhou, H. S.: Olivine $LiFePO_4$: development and future. *Energy Environ. Sci.* **2011**, *4*, 805-817.

[110] Delacourt, C.; Poizot, P.; Levasseur, S.; Masquelier, C.: Size effects on carbon-free $LiFePO_4$ powders. *Electrochem. Solid State Lett.* **2006**, *9*, A352-A355.

[111] Ravet, N.; Goodenough, J. B.; Besner, S.; Simoneau, M.; Hovington, P.; Armand, M.: The Electrochemical Society and The Electrochemical Society of Japan Meeting Abstracts. **1999**; Vol. 99-2.

[112] Huang, H.; Yin, S. C.; Nazar, L. F.: Approaching theoretical capacity of $LiFePO_4$ at room temperature at high rates. *Electrochem. Solid State Lett.* **2001**, *4*, A170-A172.

[113] Doeff, M. M.; Hu, Y. Q.; McLarnon, F.; Kostecki, R.: Effect of surface carbon structure on the electrochemical performance of $LiFePO_4$. *Electrochem. Solid State Lett.* **2003**, *6*, A207-A209.

[114] Wang, Y. G.; Wang, Y. R.; Hosono, E. J.; Wang, K. X.; Zhou, H. S.: The design of a $LiFePO_4$/carbon nanocomposite with a core-shell structure and its synthesis by an in situ polymerization restriction method. *Angew. Chem. Int. Ed.* **2008**, *47*, 7461-7465.

[115] Wang, G. X.; Yang, L.; Chen, Y.; Wang, J. Z.; Bewlay, S.; Liu, H. K.: An investigation of polypyrrole-$LiFePO_4$ composite cathode materials for lithium-ion batteries. *Electrochim. Acta* **2005**, *50*, 4649-4654.

[116] Huang, Y. H.; Goodenough, J. B.: High-Rate $LiFePO_4$ Lithium Rechargeable Battery Promoted by Electrochemically Active Polymers. *Chem. Mater.* **2008**, *20*, 7237-7241.

[117] Fedorkova, A.; Nacher-Alejos, A.; Gomez-Romero, P.; Orinakova, R.; Kaniansky, D.: Structural and electrochemical studies of PPy/PEG-$LiFePO_4$ cathode material for Li-ion batteries. *Electrochim. Acta* **2010**, *55*, 943-947.

[118] Xie, H. M.; Wang, R. S.; Ying, J. R.; Zhang, L. Y.; Jalbout, A. F.; Yu, H. Y.; Yang, G. L.; Pan, X. M.; Su, Z. M.: Optimized $LiFePO_4$-polyacene cathode material for lithium-ion batteries. *Adv.*

Mater. **2006**, *18*, 2609-+.

[119] Croce, F.; Epifanio, A. D.; Hassoun, J.; Deptula, A.; Olczac, T.; Scrosati, B.: A novel concept for the synthesis of an improved $LiFePO_4$ lithium battery cathode. *Electrochem. Solid State Lett.* **2002**, *5*, A47-A50.

[120] Park, K. S.; Son, J. T.; Chung, H. T.; Kim, S. J.; Lee, C. H.; Kang, K. T.; Kim, H. G.: Surface modification by silver coating for improving electrochemical properties of $LiFePO_4$. *Solid State Commun.* **2004**, *129*, 311-314.

[121] Liu, H.; Wang, G. X.; Wexler, D.; Wang, J. Z.; Liu, H. K.: Electrochemical performance of $LiFePO_4$ cathode material coated with ZrO_2 nanolayer. *Electrochem. Commun.* **2008**, *10*, 165-169.

[122] Hu, Y. S.; Guo, Y. G.; Dominko, R.; Gaberscek, M.; Jamnik, J.; Maier, J.: Improved electrode performance of porous $LiFePO_4$ using RuO_2 as an oxidic nanoscale interconnect. *Adv. Mater.* **2007**, *19*, 1963-+.

[123] Cui, Y.; Zhao, X. L.; Guo, R. S.: High rate electrochemical performances of nanosized ZnO and carbon co-coated $LiFePO_4$ cathode. *Mater. Res. Bull.* **2010**, *45*, 844-849.

[124] Cui, Y.; Zhao, X. L.; Guo, R. S.: Enhanced electrochemical properties of $LiFePO_4$ cathode material by CuO and carbon co-coating. *J. Alloys Compd.* **2010**, *490*, 236-240.

[125] Islam, M. S.; Driscoll, D. J.; Fisher, C. A. J.; Slater, P. R.: Atomic-scale investigation of defects, dopants, and lithium transport in the $LiFePO_4$ olivine-type battery material. *Chem. Mater.* **2005**, *17*, 5085-5092.

[126] Nishimura, S.; Kobayashi, G.; Ohoyama, K.; Kanno, R.; Yashima, M.; Yamada, A.: Experimental visualization of lithium diffusion in Li_xFePO_4. *Nat. Mater.* **2008**, *7*, 707-711.

[127] Nan, C. Y.; Lu, J.; Chen, C.; Peng, Q.; Li, Y. D.: Solvothermal synthesis of lithium iron phosphate nanoplates. *J. Mater. Chem.* **2011**, *21*, 9994-9996.

[128] Su, J.; Wei, B. Q.; Rong, J. P.; Yin, W. Y.; Ye, Z. X.; Tian, X. Q.; Ren, L.; Cao, M. H.; Hu, C. W.: A general solution-chemistry route to the synthesis $LiMPO_4$ (M=Mn, Fe, and Co) nanocrystals with [010] orientation for lithium ion batteries. *J. Solid State Chem.* **2011**, *184*, 2909-2919.

[129] Chen, Z. H.; Dahn, J. R.: Reducing carbon in $LiFePO_4$/C composite electrodes to maximize specific energy, volumetric energy, and tap density. *J. Electrochem. Soc.* **2002**, *149*, A1184-A1189.

[130] Zhao, J. Q.; He, J. P.; Zhou, J. H.; Guo, Y. X.; Wang, T.; Wu, S. C.; Ding, X. C.; Huang, R. M.; Xue, H. R.: Facile Synthesis for $LiFePO_4$ Nanospheres in Tridimensional Porous Carbon Framework for Lithium Ion Batteries. *J. Phys. Chem. C* **2011**, *115*, 2888-2894.

[131] Sun, C. W.; Rajasekhara, S.; Goodenough, J. B.; Zhou, F.: Monodisperse Porous $LiFePO_4$ Microspheres for a High Power Li-Ion Battery Cathode. *J. Am. Chem. Soc.* **2011**, *133*, 2132-2135.

[132] Lou, X. M.; Zhang, Y. X.: Synthesis of $LiFePO_4$/C cathode materials with both high-rate capability and high tap density for lithium-ion batteries. *J. Mater. Chem.* **2011**, *21*, 4156-4160.

[133] Su, D. S.; Schlogl, R.: Nanostructured Carbon and Carbon Nanocomposites for Electrochemical Energy Storage Applications. *Chemsuschem* **2010**, *3*, 136-168.

[134] Dai, H. J.: Carbon nanotubes: opportunities and challenges. *Surf. Sci.* **2002**, *500*, 218-241.

[135] Dai, H. J.: Carbon nanotubes: Synthesis, integration, and properties. *Acc. Chem. Res.* **2002**, *35*, 1035-1044.

[136] Withers, J. C.; Loutfy, R. O.; Lowe, T. P.: Fullerene commercial vision. *Fullerene Sci. Technol.*

1997, *5*, 1-31.

[137] Leroux, F.; Metenier, K.; Gautier, S.; Frackowiak, E.; Bonnamy, S.; Beguin, F.: Electrochemical insertion of lithium in catalytic multi-walled carbon nanotubes. *J. Power Sources* **1999**, *81*, 317-322.

[138] Claye, A. S.; Fischer, J. E.; Huffman, C. B.; Rinzler, A. G.; Smalley, R. E.: Solid-state electrochemistry of the Li single wall carbon nanotube system. *J. Electrochem. Soc.* **2000**, *147*, 2845-2852.

[139] Chew, S. Y.; Ng, S. H.; Wang, J. Z.; Novak, P.; Krumeich, F.; Chou, S. L.; Chen, J.; Liu, H. K.: Flexible free-standing carbon nanotube films for model lithium-ion batteries. *Carbon* **2009**, *47*, 2976-2983.

[140] Rong, J. P.; Masarapu, C.; Ni, J.; Zhang, Z. J.; Wei, B. Q.: Tandem structure of porous silicon film on single-walled carbon nanotube macrofilms for lithium-ion battery applications. *Acs Nano* **2010**, *4*, 4683-4690.

[141] Oberlin, A.; Endo, M.; Koyama, T.: Filamentous growth of carbon through benzene decomposition. *J. Cryst. Growth* **1976**, *32*, 335-349.

[142] Kim, C.; Yang, K. S.; Kojima, M.; Yoshida, K.; Kim, Y. J.; Kim, Y. A.; Endo, M.: Fabrication of electrospinning-derived carbon nanofiber webs for the anode material of lithium-ion secondary batteries. *Adv. Funct. Mater.* **2006**, *16*, 2393-2397.

[143] Kim, C.; Jeong, Y. I.; Ngoc, B. T. N.; Yang, K. S.; Kojima, M.; Kim, Y. A.; Endo, M.; Lee, J. W.: Synthesis and characterization of porous carbon nanofibers with hollow cores through the thermal treatment of electrospun copolymeric nanofiber webs. *Small* **2007**, *3*, 91-95.

[144] Yoon, S. H.; Park, C. W.; Yang, H. J.; Korai, Y.; Mochida, I.; Baker, R. T. K.; Rodriguez, N. M.:

Novel carbon nanofibers of high graphitization as anodic materials for lithium ion secondary batteries. *Carbon* **2004**, *42*, 21-32.

[145] Ji, L. W.; Zhang, X. W.: Fabrication of porous carbon nanofibers and their application as anode materials for rechargeable lithium-ion batteries. *Nanotechnology* **2009**, *20*.

[146] Zhou, H. S.; Zhu, S. M.; Hibino, M.; Honma, I.; Ichihara, M.: Lithium storage in ordered mesoporous carbon (CMK-3) with high reversible specific energy capacity and good cycling performance. *Adv. Mater.* **2003**, *15*, 2107-+.

[147] Geim, A. K.; Novoselov, K. S.: The rise of graphene. *Nat. Mater.* **2007**, *6*, 183-191.

[148] Wang, G. X.; Yang, J.; Park, J.; Gou, X. L.; Wang, B.; Liu, H.; Yao, J.: Facile synthesis and characterization of graphene nanosheets. *J. Phys. Chem. C* **2008**, *112*, 8192-8195.

[149] Wang, G. X.; Shen, X. P.; Yao, J.; Park, J.: Graphene nanosheets for enhanced lithium storage in lithium ion batteries. *Carbon* **2009**, *47*, 2049-2053.

[150] Yao, J.; Shen, X. P.; Wang, B.; Liu, H. K.; Wang, G. X.: In situ chemical synthesis of SnO_2-graphene nanocomposite as anode materials for lithium-ion batteries. *Electrochem. Commun.* **2009**, *11*, 1849-1852.

[151] Paek, S. M.; Yoo, E.; Honma, I.: Enhanced cyclic performance and lithium storage capacity of SnO_2/graphene nanoporous electrodes with three-dimensionally delaminated flexible structure. *Nano Lett.* **2009**, *9*, 72-75.

[152] Wang, G. X.; Wang, B.; Wang, X. L.; Park, J.; Dou, S. X.; Ahn, H.; Kim, K.: Sn/graphene nanocomposite with 3D architecture for enhanced reversible lithium storage in lithium ion batteries. *J. Mater. Chem.* **2009**, *19*, 8378-8384.

[153] Wu, Z. S.; Ren, W. C.; Wen, L.; Gao, L. B.; Zhao, J. P.; Chen, Z. P.; Zhou, G. M.; Li, F.; Cheng,

H. M.: Graphene anchored with Co_3O_4 nanoparticles as anode of lithium ion batteries with enhanced reversible capacity and cyclic performance. *Acs Nano* **2010**, *4*, 3187-3194.

[154] Chen, S. Q.; Wang, Y.: Microwave-assisted synthesis of a Co_3O_4-graphene sheet-on-sheet nanocomposite as a superior anode material for Li-ion batteries. *J. Mater. Chem.* **2010**, *20*, 9735-9739.

[155] Dey, A. N.: Electrochemical alloying of lithium in organic electrolytes. *J. Electrochem. Soc.* **1971**, *118*, 1547-&.

[156] Park, C. M.; Kim, J. H.; Kim, H.; Sohn, H. J.: Li-alloy based anode materials for Li secondary batteries. *Chem. Soc. Rev.* **2010**, *39*, 3115-3141.

[157] Wen, C. J.; Huggins, R. A.: Chemical diffusion in intermediate phases in the lithium-silicon system. *J. Solid State Chem.* **1981**, *37*, 271-278.

[158] Obrovac, M. N.; Christensen, L.: Structural changes in silicon anodes during lithium insertion/extraction. *Electrochem. Solid State Lett.* **2004**, *7*, A93-A96.

[159] Hatchard, T. D.; Dahn, J. R.: In situ XRD and electrochemical study of the reaction of lithium with amorphous silicon. *J. Electrochem. Soc.* **2004**, *151*, A838-A842.

[160] Li, H.; Huang, X. J.; Chen, L. Q.; Wu, Z. G.; Liang, Y.: A high capacity nano-Si composite anode material for lithium rechargeable batteries. *Electrochem. Solid State Lett.* **1999**, *2*, 547-549.

[161] Ng, S. H.; Wang, J. Z.; Wexler, D.; Konstantinov, K.; Guo, Z. P.; Liu, H. K.: Highly reversible lithium storage in spheroidal carbon-coated silicon nanocomposites as anodes for lithium-ion batteries. *Angew. Chem. Int. Ed.* **2006**, *45*, 6896-6899.

[162] Wang, G. X.; Ahn, J. H.; Yao, J.; Bewlay, S.; Liu, H. K.: Nanostructured Si-C composite anodes for lithium-ion batteries. *Electrochem. Commun.* **2004**, *6*, 689-692.

[163] Chew, S. Y.; Guo, Z. P.; Wang, J. Z.; Chen, J.; Munroe, P.; Ng, S. H.; Zhao, L.; Liu, H. K.: Novel nano-silicon/polypyrrole composites for lithium storage. *Electrochem. Commun.* **2007**, *9*, 941-946.

[164] Chan, C. K.; Peng, H. L.; Liu, G.; McIlwrath, K.; Zhang, X. F.; Huggins, R. A.; Cui, Y.: High-performance lithium battery anodes using silicon nanowires. *Nat. Nanotechnol.* **2008**, *3*, 31-35.

[165] Park, M. H.; Kim, M. G.; Joo, J.; Kim, K.; Kim, J.; Ahn, S.; Cui, Y.; Cho, J.: Silicon Nanotube Battery Anodes. *Nano Lett.* **2009**, *9*, 3844-3847.

[166] Tamura, N.; Ohshita, R.; Fujimoto, M.; Kamino, M.; Fujitani, S.: Advanced structures in electrodeposited tin base negative electrodes for lithium secondary batteries. *J. Electrochem. Soc.* **2003**, *150*, A679-A683.

[167] Goward, G. R.; Taylor, N. J.; Souza, D. C. S.; Nazar, L. F.: The true crystal structure of $Li_{17}M_4$ (M=Ge, Sn, Pb)-revised from $Li_{22}M_5$. *J. Alloys Compd.* **2001**, *329*, 82-91.

[168] Derrien, G.; Hassoun, J.; Panero, S.; Scrosati, B.: Nanostructured Sn-C composite as an advanced anode material in high-performance lithium-ion batteries. *Adv. Mater.* **2007**, *19*, 2336-+.

[169] Courtney, I. A.; Dahn, J. R.: Electrochemical and in situ x-ray diffraction studies of the reaction of lithium with tin oxide composites. *J. Electrochem. Soc.* **1997**, *144*, 2045-2052.

[170] Courtney, I. A.; Dahn, J. R.: Key factors controlling the reversibility of the reaction of lithium with SnO_2 and Sn_2BPO_6 glass. *J. Electrochem. Soc.* **1997**, *144*, 2943-2948.

[171] Park, M. S.; Wang, G. X.; Kang, Y. M.; Wexler, D.; Dou, S. X.; Liu, H. K.: Preparation and electrochemical properties of SnO_2 nanowires for application in lithium-ion batteries. *Angew.*

Chem. Int. Ed. **2007**, *46*, 750-753.

[172] Park, M. S.; Kang, Y. M.; Wang, G. X.; Dou, S. X.; Liu, H. K.: The effect of morphological modification on the electrochemical properties of SnO_2 nanomaterials. *Adv. Funct. Mater.* **2008**, *18*, 455-461.

[173] Poizot, P.; Laruelle, S.; Grugeon, S.; Dupont, L.; Tarascon, J. M.: Nano-sized transition-metaloxides as negative-electrode materials for lithium-ion batteries. *Nature* **2000**, *407*, 496-499.

[174] Amatucci, G. G.; Pereira, N.: Fluoride based electrode materials for advanced energy storage devices. *J. Fluorine Chem.* **2007**, *128*, 243-262.

[175] Liu, H.; Wexler, D.; Wang, G. X.: One-pot facile synthesis of iron oxide nanowires as high capacity anode materials for lithium ion batteries. *J. Alloys Compd.* **2009**, *487*, L24-L27.

[176] Liu, H.; Wang, G. X.; Park, J.; Wang, J.; Zhang, C.: Electrochemical performance of alpha-Fe_2O_3 nanorods as anode material for lithium-ion cells. *Electrochim. Acta* **2009**, *54*, 1733-1736.

[177] Chen, J.; Xu, L. N.; Li, W. Y.; Gou, X. L.: alpha-Fe_2O_3 nanotubes in gas sensor and lithium-ion battery applications. *Adv. Mater.* **2005**, *17*, 582-+.

[178] Li, W. Y.; Xu, L. N.; Chen, J.: Co_3O_4 nanomaterials in lithium-ion batteries and gas sensors. *Adv. Funct. Mater.* **2005**, *15*, 851-857.

[179] Cheng, F.; Tao, Z.; Liang, J.; Chen, J.: Template-directed materials for rechargeable lithium-ion batteries. *Chem. Mater.* **2008**, *20*, 667-681.

[180] Wang, G. X.; Liu, H.; Horvat, J.; Wang, B.; Qiao, S. Z.; Park, J.; Ahn, H.: Highly ordered mesoporous cobalt oxide nanostructures: synthesis, characterisation, magnetic Properties, and applications for electrochemical energy devices. *Chem. Eur. J.* **2010**, *16*, 11020-11027.

[181] Liu, H.; Wang, G. X.; Liu, J.; Qiao, S. Z.; Ahn, H. J.: Highly ordered mesoporous NiO anode material for lithium ion batteries with an excellent electrochemical performance. *J. Mater. Chem.* **2011**, *21*, 3046-3052.

[182] Liu, H.; Du, X. W.; Xing, X. R.; Wang, G. X.; Qiao, S. Z.: Highly ordered mesoporous Cr_2O_3 materials with enhanced performance for gas sensors and lithium ion batteries. *Electrochem. Commun.* **2012**, *48*, 865-867.

[183] Zhi, L. J.; Hu, Y. S.; El Hamaoui, B.; Wang, X.; Lieberwirth, I.; Kolb, U.; Maier, J.; Mullen, K.: Precursor-controlled formation of novel carbon/metal and carbon/metal oxide nanocomposites. *Adv. Mater.* **2008**, *20*, 1727-+.

[184] Liu, H.; Wang, G. X.; Wang, J. Z.; Wexler, D.: Magnetite/carbon core-shell nanorods as anode materials for lithium-ion batteries. *Electrochem. Commun.* **2008**, *10*, 1879-1882.

[185] Wang, G. X.; Shen, X. P.; Yao, J. N.; Wexler, D.; Ahn, J.: Hydrothermal synthesis of carbon nanotube/cobalt oxide core-shell one-dimensional nanocomposite and application as an anode material for lithium-ion batteries. *Electrochem. Commun.* **2009**, *11*, 546-549.

[186] Wang, H. L.; Cui, L. F.; Yang, Y. A.; Casalongue, H. S.; Robinson, J. T.; Liang, Y. Y.; Cui, Y.; Dai, H. J.: Mn_3O_4-Graphene Hybrid as a High-Capacity Anode Material for Lithium Ion Batteries. *J. Am. Chem. Soc.* **2010**, *132*, 13978-13980.

[187] Wang, J. Z.; Zhong, C.; Wexler, D.; Idris, N. H.; Wang, Z. X.; Chen, L. Q.; Liu, H. K.: Graphene-Encapsulated Fe_3O_4 Nanoparticles with 3D Laminated Structure as Superior Anode in Lithium Ion Batteries. *Chem. Eur. J.* **2011**, *17*, 661-667.

[188] Zhu, X. J.; Zhu, Y. W.; Murali, S.; Stollers, M. D.; Ruoff, R. S.: Nanostructured Reduced Graphene Oxide/Fe_2O_3 Composite As a High-Performance Anode Material for Lithium Ion

Batteries. *Acs Nano* **2011**, *5*, 3333-3338.

[189] Wang, B.; Wang, Y.; Park, J.; Ahn, H.; Wang, G. X.: In situ synthesis of Co_3O_4/graphene nanocomposite material for lithium-ion batteries and supercapacitors with high capacity and supercapacitance. *J. Alloys Compd.* **2011**, *509*, 7778-7783.

[190] Wagner, F. T.; Lakshmanan, B.; Mathias, M. F.: Electrochemistry and the Future of the Automobile. *J. Phys. Chem. Lett.* **2010**, *1*, 2204-2219.

[191] Debart, A.; Paterson, A. J.; Bao, J.; Bruce, P. G.: alpha-MnO_2 nanowires: A catalyst for the O_2 electrode in rechargeable lithium batteries. *Angew. Chem. Int. Ed.* **2008**, *47*, 4521-4524.

[192] Abraham, K. M.; Jiang, Z.: A polymer electrolyte-based rechargeable lithium/oxygen battery. *J. Electrochem. Soc.* **1996**, *143*, 1-5.

[193] Wang, Y. G.; Zhou, H. S.: A lithium-air battery with a potential to continuously reduce O_2 from air for delivering energy. *J. Power Sources* **2010**, *195*, 358-361.

[194] Beattie, S. D.; Manolescu, D. M.; Blair, S. L.: High-Capacity Lithium-Air Cathodes. *J. Electrochem. Soc.* **2009**, *156*, A44-A47.

[195] Albertus, P.; Girishkumar, G.; McCloskey, B.; Sanchez-Carrera, R. S.; Kozinsky, B.; Christensen, J.; Luntz, A. C.: Identifying Capacity Limitations in the Li/Oxygen Battery Using Experiments and Modeling. *J. Electrochem. Soc.* **2011**, *158*, A343-A351.

[196] Lee, J. S.; Kim, S. T.; Cao, R.; Choi, N. S.; Liu, M.; Lee, K. T.; Cho, J.: Metal-Air Batteries with High Energy Density: Li-Air versus Zn-Air. *Adv. Energy Mater.* **2011**, *1*, 34-50.

[197] Ogasawara, T.; Debart, A.; Holzapfel, M.; Novak, P.; Bruce, P. G.: Rechargeable Li_2O_2 electrode for lithium batteries. *J. Am. Chem. Soc.* **2006**, *128*, 1390-1393.

[198] Read, J.: Characterization of the lithium/oxygen organic electrolyte battery. *J. Electrochem. Soc.*

2002, *149*, A1190-A1195.

[199] Visco, S. J.; Katz, B. D.; Nimon, Y. S.; DeJonghe, L. C.: Protected active metal electrode and battery cell structures with nonaqueous interlayer architecture. *U. S. Patent #7282295* **2007**.

[200] Christensen, J.; Albertus, P.; Sanchez-Carrera, R. S.; Lohmann, T.; Kozinsky, B.; Liedtke, R.; Ahmed, J.; Kojic, A.: A Critical Review of Li/Air Batteries. *J. Electrochem. Soc.* **2012**, *159*, R1-R30.

[201] Peng, Z. Q.; Freunberger, S. A.; Hardwick, L. J.; Chen, Y. H.; Giordani, V.; Barde, F.; Novak, P.; Graham, D.; Tarascon, J. M.; Bruce, P. G.: Oxygen Reactions in a Non-Aqueous Li^+ Electrolyte. *Angew. Chem. Int. Ed.* **2011**, *50*, 6351-6355.

[202] Xu, W.; Xu, K.; Viswanathan, V. V.; Towne, S. A.; Hardy, J. S.; Xiao, J.; Hu, D. H.; Wang, D. Y.; Zhang, J. G.: Reaction mechanisms for the limited reversibility of Li-O_2 chemistry in organic carbonate electrolytes. *J.Power Sources* **2011**, *196*, 9631-9639.

[203] Christensen, J.; Albertus, P.; Sanchez-Carrera, R. S.; Lohmann, T.; Kozinsky, B.; Liedtke, R.; Ahmed, J.; Kojic, A.: A Critical Review of Li/Air Batteries. *Journal of the Electrochemical Society* **2012**, *159*, R1-R30.

[204] Xiao, J.; Hu, J. Z.; Wang, D. Y.; Hu, D. H.; Xu, W.; Graff, G. L.; Nie, Z. M.; Liu, J.; Zhang, J. G.: Investigation of the rechargeability of Li-O_2 batteries in non-aqueous electrolyte. *J. Power Sources* **2011**, *196*, 5674-5678.

[205] Laoire, C. O.; Mukerjee, S.; Abraham, K. M.; Plichta, E. J.; Hendrickson, M. A.: Influence of Nonaqueous Solvents on the Electrochemistry of Oxygen in the Rechargeable Lithium-Air Battery. *J. Phys. Chem. Lett.* **2010**, *114*, 9178-9186.

[206] Freunberger, S. A.; Chen, Y. H.; Peng, Z. Q.; Griffin, J. M.; Hardwick, L. J.; Barde, F.; Novak, P.;

Bruce, P. G.: Reactions in the Rechargeable Lithium-O_2 Battery with Alkyl Carbonate Electrolytes. *J. Am. Chem. Soc.* **2011**, *133*, 8040-8047.

[207] Freunberger, S. A.; Chen, Y. H.; Drewett, N. E.; Hardwick, L. J.; Barde, F.; Bruce, P. G.: The Lithium-Oxygen Battery with Ether-Based Electrolytes. *Angew. Chem. Int. Ed.* **2011**, *50*, 8609-8613.

[208] Eswaran, M.; Munichandraiah, N.; Scanlon, L. G.: High Capacity Li-O_2 Cell and Electrochemical Impedance Spectroscopy Study. *Electrochem. Solid State Lett.* **2010**, *13*, A121-A124.

[209] Zhang, D.; Fu, Z. H.; Wei, Z.; Huang, T.; Yu, A. S.: Polarization of Oxygen Electrode in Rechargeable Lithium Oxygen Batteries. *J. Electrochem. Soc.* **2010**, *157*, A362-A365.

[210] Mirzaeian, M.; Hall, P. J.: Characterizing capacity loss of lithium oxygen batteries by impedance spectroscopy. *J. Power Sources* **2010**, *195*, 6817-6824.

[211] Cheng, H.; Scott, K.: Carbon-supported manganese oxide nanocatalysts for rechargeable lithium-air batteries. *J. Power Sources* **2010**, *195*, 1370-1374.

[212] Xiao, J.; Wang, D. H.; Xu, W.; Wang, D. Y.; Williford, R. E.; Liu, J.; Zhang, J. G.: Optimization of Air Electrode for Li/Air Batteries. *J. Electrochem. Soc.* **2010**, *157*, A487-A492.

[213] Yang, X. H.; He, P.; Xia, Y. Y.: Preparation of mesocellular carbon foam and its application for lithium/oxygen battery. *Electrochem. Commun.* **2009**, *11*, 1127-1130.

[214] Sun, B.; Wang, B.; Su, D. W.; Xiao, L. D.; Ahn, H.; Wang, G. X.: Graphene nanosheets as cathode catalysts for lithium-air batteries with an enhanced electrochemical performance. *Carbon* **2012**, *50*, 727-733.

[215] Tran, C.; Yang, X. Q.; Qu, D. Y.: Investigation of the gas-diffusion-electrode used as lithium/air

cathode in non-aqueous electrolyte and the importance of carbon material porosity. *J. Power Sources* **2010**, *195*, 2057-2063.

[216] Xiao, J.; Mei, D. H.; Li, X. L.; Xu, W.; Wang, D. Y.; Graff, G. L.; Bennett, W. D.; Nie, Z. M.; Saraf, L. V.; Aksay, I. A.; Liu, J.; Zhang, J. G.: Hierarchically Porous Graphene as a Lithium-Air Battery Electrode. *Nano Lett.* **2011**, *11*, 5071-5078.

[217] Mitchell, R. R.; Gallant, B. M.; Thompson, C. V.; Shao-Horn, Y.: All-carbon-nanofiber electrodes for high-energy rechargeable Li-O_2batteries. *Energy Environ. Sci.* **2011**, *4*, 2952-2958.

[218] Mizuno, F.; Nakanishi, S.; Kotani, Y.; Yokoishi, S.; Iba, H.: Rechargeable Li-Air Batteries with Carbonate-Based Liquid Electrolytes. *Electrochemistry* **2010**, *78*, 403-405.

[219] Debart, A.; Bao, J.; Armstrong, G.; Bruce, P. G.: An O_2 cathode for rechargeable lithium batteries: The effect of a catalyst. *J. Power Sources* **2007**, *174*, 1177-1182.

[220] Lu, Y. C.; Gasteiger, H. A.; Parent, M. C.; Chiloyan, V.; Shao-Horn, Y.: The Influence of Catalysts on Discharge and Charge Voltages of Rechargeable Li-Oxygen Batteries. *Electrochem. Solid State Lett.* **2010**, *13*, A69-A72.

[221] Lu, Y. C.; Xu, Z. C.; Gasteiger, H. A.; Chen, S.; Hamad-Schifferli, K.; Shao-Horn, Y.: Platinum-Gold Nanoparticles: A Highly Active Bifunctional Electrocatalyst for Rechargeable Lithium-Air Batteries. *J. Am. Chem. Soc.* **2010**, *132*, 12170-12171.

[222] Lu, Y. C.; Gasteiger, H. A.; Crumlin, E.; McGuire, R.; Shao-Horn, Y.: Electrocatalytic Activity Studies of Select Metal Surfaces and Implications in Li-Air Batteries. *J. Electrochem. Soc.* **2010**, *157*, A1016-A1025.

[223] Lu, Y. C.; Gasteiger, H. A.; Shao-Horn, Y.: Method Development to Evaluate the Oxygen Reduction Activity of High-Surface-Area Catalysts for Li-Air Batteries. *Electrochem. Solid State*

Lett. **2011**, *14*, A70-A74.

[224] Lu, Y. C.; Kwabi, D. G.; Yao, K. P. C.; Harding, J. R.; Zhou, J. G.; Zuin, L.; Shao-Horn, Y.: The discharge rate capability of rechargeable Li-O_2 batteries. *Energy Environ. Sci.* **2011**, *4*, 2999-3007.

[225] Lu, Y. C.; Gasteiger, H. A.; Shao-Horn, Y.: Catalytic Activity Trends of Oxygen Reduction Reaction for Nonaqueous Li-Air Batteries. *J. Am. Chem. Soc.* **2011**, *133*, 19048-19051.

[226] Thapa, A. K.; Saimen, K.; Ishihara, T.: Pd/MnO_2 Air Electrode Catalyst for Rechargeable Lithium/Air Battery. *Electrochem. Solid State Lett.* **2010**, *13*, A165-A167.

[227] Thapa, A. K.; Ishihara, T.: Mesoporous alpha-MnO_2/Pd catalyst air electrode for rechargeable lithium-air battery. *J. Power Sources* **2011**, *196*, 7016-7020.

[228] Thapa, A. K.; Hidaka, Y.; Hagiwara, H.; Ida, S.; Ishihara, T.: Mesoporous beta-MnO_2 Air Electrode Modified with Pd for Rechargeability in Lithium-Air Battery. *J. Electrochem. Soc.* **2011**, *158*, A1483-A1489.

[229] Cui, Y. M.; Wen, Z. Y.; Liu, Y.: A free-standing-type design for cathodes of rechargeable Li-O_2 batteries. *Energy Environ. Sci.* **2011**, *4*, 4727-4734.

[230] Wan, Y.; Zhao, D. Y.: On the controllable soft-templating approach to mesoporous silicates. *Chem. Rev.* **2007**, *107*, 2821-2860.

[231] Lu, A. H.; Schuth, F.: Nanocasting: A versatile strategy for creating nanostructured porous materials. *Adv. Mater.* **2006**, *18*, 1793-1805.

[232] Gardiner, D. J.: *Practical Raman spectroscopy*; Springer-Verlag, **1989**.

[233] http://en.wikipedia.org/wiki/File:Raman_energy_levels.svg.

[234] Brunauer, S.; Emmett, P. H.; Teller, E.: Adsorption of gases in multimolecular layers. *J. Am.*

Chem. Soc. **1938**, *60*, 309-319.

[235] Bard, A. J.; Faulkner, L. R.: *Electrochemical Methods: Fundamentals and Applications (2nd ed.)*; Wiley, **2000**.

[236] Kang, B.; Ceder, G.: Battery materials for ultrafast charging and discharging. *Nature* **2009**, *458*, 190-193.

[237] Delmas, C.; Maccario, M.; Croguennec, L.; Le Cras, F.; Weill, F.: Lithium deintercalation in $LiFePO_4$ nanoparticles via a domino-cascade model. *Nat. Mater.* **2008**, *7*, 665-671.

[238] Lepage, D.; Michot, C.; Liang, G. X.; Gauthier, M.; Schougaard, S. B.: A Soft Chemistry Approach to Coating of $LiFePO_4$ with a Conducting Polymer. *Angew. Chem. Int. Ed.* **2011**, *50*, 6884-6887.

[239] Gibot, P.; Casas-Cabanas, M.; Laffont, L.; Levasseur, S.; Carlach, P.; Hamelet, S.; Tarascon, J. M.; Masquelier, C.: Room-temperature single-phase Li insertion/extraction in nanoscale Li_xFePO_4. *Nat. Mater.* **2008**, *7*, 741-747.

[240] Lim, S. Y.; Yoon, C. S.; Cho, J. P.: Synthesis of nanowire and hollow $LiFePO_4$ cathodes for high-performance lithium batteries. *Chem. Mater.* **2008**, *20*, 4560-4564.

[241] Zhu, C. B.; Yu, Y.; Gu, L.; Weichert, K.; Maier, J.: Electrospinning of Highly Electroactive Carbon-Coated Single-Crystalline $LiFePO_4$ Nanowires. *Angew. Chem. Int. Ed.* **2011**, *50*, 6278-6282.

[242] Qian, J. F.; Zhou, M.; Cao, Y. L.; Ai, X. P.; Yang, H. X.: Template-Free Hydrothermal Synthesis of Nanoembossed Mesoporous $LiFePO_4$ Microspheres for High-Performance Lithium-Ion Batteries. *J. Phys. Chem. C* **2010**, *114*, 3477-3482.

[243] Zhou, W. W.; Zhu, J. X.; Cheng, C. W.; Liu, J. P.; Yang, H. P.; Cong, C. X.; Guan, C.; Jia, X. T.;

Fan, H. J.; Yan, Q. Y.; Li, C. M.; Yu, T.: A general strategy toward graphene@metal oxide core-shell nanostructures for high-performance lithium storage. *Energy Environ. Sci.* **2011**, *4*, 4954-4961.

[244] Yang, S. B.; Feng, X. L.; Ivanovici, S.; Mullen, K.: Fabrication of Graphene-Encapsulated Oxide Nanoparticles: Towards High-Performance Anode Materials for Lithium Storage. *Angew. Chem. Int. Ed.* **2010**, *49*, 8408-8411.

[245] Ding, Y.; Jiang, Y.; Xu, F.; Yin, J.; Ren, H.; Zhuo, Q.; Long, Z.; Zhang, P.: Preparation of nano-structured $LiFePO_4$/graphene composites by co-precipitation method. *Electrochem. Commun.* **2010**, *12*, 10-13.

[246] Zhou, X. F.; Wang, F.; Zhu, Y. M.; Liu, Z. P.: Graphene modified $LiFePO_4$ cathode materials for high power lithium ion batteries. *J. Mater. Chem.* **2011**, *21*, 3353-3358.

[247] Stankovich, S.; Dikin, D. A.; Piner, R. D.; Kohlhaas, K. A.; Kleinhammes, A.; Jia, Y.; Wu, Y.; Nguyen, S. T.; Ruoff, R. S.: Synthesis of graphene-based nanosheets via chemical reduction of exfoliated graphite oxide. *Carbon* **2007**, *45*, 1558-1565.

[248] Belharouak, I.; Johnson, C.; Amine, K.: Synthesis and electrochemical analysis of vapor-deposited carbon-coated $LiFePO_4$. *Electrochem. Commun.* **2005**, *7*, 983-988.

[249] Liu, J.; Conry, T. E.; Song, X. Y.; Doeff, M. M.; Richardson, T. J.: Nanoporous spherical $LiFePO_4$ for high performance cathodes. *Energy Environ. Sci.* **2011**, *4*, 885-888.

[250] Yu, F.; Zhang, J. J.; Yang, Y. F.; Song, G. Z.: Porous micro-spherical aggregates of $LiFePO_4$/C nanocomposites: A novel and simple template-free concept and synthesis via sol-gel-spray drying method. *J. Power Sources* **2010**, *195*, 6873-6878.

[251] Wang, Q.; Zhang, W. X.; Yang, Z. H.; Weng, S. Y.; Jin, Z. J.: Solvothermal synthesis of

hierarchical $LiFePO_4$ microflowers as cathode materials for lithium ion batteries. *J. Power Sources* **2011**, *196*, 10176-10182.

[252] Yin, Y. H.; Gao, M. X.; Pan, H. G.; Shen, L. K.; Ye, X.; Liu, Y. F.; Fedkiw, P. S.; Zhang, X. W.: High-rate capability of $LiFePO_4$ cathode materials containing Fe_2P and trace carbon. *J. Power Sources* **2012**, *199*, 256-262.

[253] Allen, J. L.; Jow, T. R.; Wolfenstine, J.: Kinetic study of the electrochemical $FePO_4$ to $LiFePO_4$ phase transition. *Chem. Mater.* **2007**, *19*, 2108-2111.

[254] Yu, D. Y. W.; Fietzek, C.; Weydanz, W.; Donoue, K.; Inoue, T.; Kurokawa, H.; Fujitani, S.: Study of $LiFePO_4$ by cyclic voltammetry. *J. Electrochem. Soc.* **2007**, *154*, A253-A257.

[255] Liu, W. L.; Tu, J. P.; Qiao, Y. Q.; Zhou, J. P.; Shi, S. J.; Wang, X. L.; Gu, C. D.: Optimized performances of core-shell structured $LiFePO_4$/C nanocomposite. *J. Power Sources* **2011**, *196*, 7728-7735.

[256] Gao, F.; Tang, Z. Y.: Kinetic behavior of $LiFePO_4$/C cathode material for lithium-ion batteries. *Electrochim. Acta* **2008**, *53*, 5071-5075.

[257] Jain, G.; Balasubramanian, M.; Xu, J. J.: Structural studies of lithium intercalation in a nanocrystalline alpha-Fe_2O_3 compound. *Chem. Mater.* **2006**, *18*, 423-434.

[258] Wu, C. Z.; Yin, P.; Zhu, X.; OuYang, C. Z.; Xie, Y.: Synthesis of hematite (alpha-Fe_2O_3) nanorods: Diameter-size and shape effects on their applications in magnetism, lithium ion battery, and gas sensors. *J. Phys. Chem. B* **2006**, *110*, 17806-17812.

[259] Gou, X. L.; Wang, G. X.; Kong, X. Y.; Wexler, D.; Horvat, J.; Yang, J.; Park, J.: Flutelike porous hematite nanorods and branched nanostructures: Synthesis, characterisation and application for gas-sensing. *Chem. Eur. J.* **2008**, *14*, 5996-6002.

[260] Hermanek, M.; Zboril, R.; Medrik, N.; Pechousek, J.; Gregor, C.: Catalytic efficiency of iron(III) oxides in decomposition of hydrogen peroxide: Competition between the surface area and crystallinity of nanoparticles. *J. Am. Chem. Soc.* **2007**, *129*, 10929-10936.

[261] Feldmann, C.: Preparation of nanoscale pigment particles. *Adv. Mater.* **2001**, *13*, 1301-1303.

[262] Srivastava, D. N.; Perkas, N.; Gedanken, A.; Felner, I.: Sonochemical synthesis of mesoporous iron oxide and accounts of its magnetic and catalytic properties. *J. Phys. Chem. B* **2002**, *106*, 1878-1883.

[263] Larcher, D.; Bonnin, D.; Cortes, R.; Rivals, I.; Personnaz, L.; Tarascon, J. M.: Combined XRD, EXAFS, and Mossbauer studies of the reduction by lithium of alpha-Fe2O3 with various particle sizes. *J. Electrochem. Soc.* **2003**, *150*, A1643-A1650.

[264] Larcher, D.; Masquelier, C.; Bonnin, D.; Chabre, Y.; Masson, V.; Leriche, J. B.; Tarascon, J. M.: Effect of particle size on lithium intercalation into alpha-Fe2O3. *J. Electrochem. Soc.* **2003**, *150*, A133-A139.

[265] Wang, G. X.; Gou, X. L.; Horvat, J.; Park, J.: Facile synthesis and characterization of iron oxide semiconductor nanowires for gas sensing application. *J. Phys. Chem. C* **2008**, *112*, 15220-15225.

[266] Reddy, M. V.; Yu, T.; Sow, C. H.; Shen, Z. X.; Lim, C. T.; Rao, G. V. S.; Chowdari, B. V. R.: alpha-Fe_2O_3 nanoflakes as an anode material for Li-ion batteries. *Adv. Funct. Mater.* **2007**, *17*, 2792-2799.

[267] Tahir, A. A.; Wijayantha, K. G. U.; Saremi-Yarahmadi, S.; Mazhar, M.; McKee, V.: Nanostructured alpha-Fe_2O_3 Thin Films for Photoelectrochemical Hydrogen Generation. *Chem. Mater.* **2009**, *21*, 3763-3772.

[268] Wu, Z. C.; Yu, K.; Zhang, S. D.; Xie, Y.: Hematite hollow spheres with a mesoporous shell:

Controlled synthesis and applications in gas sensor and lithium ion batteries. *J. Phys. Chem. C* **2008**, *112*, 11307-11313.

[269] Woo, K.; Lee, H. J.; Ahn, J. P.; Park, Y. S.: Sol-gel mediated synthesis of Fe_2O_3 nanorods. *Adv. Mater.* **2003**, *15*, 1761-+.

[270] Dong, W. T.; Zhu, C. S.: Use of ethylene oxide in the sol-gel synthesis of alpha-Fe_2O_3 nanoparticles from Fe(III) salts. *J. Mater. Chem.* **2002**, *12*, 1676-1683.

[271] Wang, L.; Xu, H. W.; Chen, P. C.; Zhang, D. W.; Ding, C. X.; Chen, C. H.: Electrostatic spray deposition of porous Fe2O3 thin films as anode material with improved electrochemical performance for lithium-ion batteries. *J.Power Sources* **2009**, *193*, 846-850.

[272] Zeng, S. Y.; Tang, K. B.; Li, T. W.; Liang, Z. H.; Wang, D.; Wang, Y. K.; Qi, Y. X.; Zhou, W. W.: Facile route for the fabrication of porous hematite nanoflowers: Its synthesis, growth mechanism, application in the lithium ion battery, and magnetic and photocatalytic properties. *J. Phys. Chem. C* **2008**, *112*, 4836-4843.

[273] Lian, J. B.; Duan, X. C.; Ma, J. M.; Peng, P.; Kim, T. I.; Zheng, W. J.: Hematite (alpha-Fe_2O_3) with Various Morphologies: Ionic Liquid-Assisted Synthesis, Formation Mechanism, and Properties. *Acs Nano* **2009**, *3*, 3749-3761.

[274] Liu, J. P.; Li, Y. Y.; Fan, H. J.; Zhu, Z. H.; Jiang, J.; Ding, R. M.; Hu, Y. Y.; Huang, X. T.: Iron Oxide-Based Nanotube Arrays Derived from Sacrificial Template-Accelerated Hydrolysis: Large-Area Design and Reversible Lithium Storage. *Chem. Mater.* **2010**, *22*, 212-217.

[275] Kresge, C. T.; Leonowicz, M. E.; Roth, W. J.; Vartuli, J. C.; Beck, J. S.: Ordered mesoporous molecular-sieves synthesized by a liquid-crystal template mechanism. *Nature* **1992**, *359*, 710-712.

[276] He, X.; Antonelli, D.: Recent advances in synthesis and applications of transition metal containing mesoporous molecular sieves. *Angew. Chem. Int. Ed.* **2002**, *41*, 214-229.

[277] Jiao, F.; Harrison, A.; Hill, A. H.; Bruce, P. G.: Mesoporous Mn_2O_3 and Mn_3O_4 with crystalline walls. *Adv. Mater.* **2007**, *19*, 4063-+.

[278] Yu, C. C.; Dong, X. P.; Guo, L. M.; Li, J. T.; Qin, F.; Zhang, L. X.; Shi, J. L.; Yan, D. S.: Template-free preparation of mesoporous Fe_2O_3 and its application as absorbents. *J. Phys. Chem. C* **2008**, *112*, 13378-13382.

[279] Shaju, K. M.; Jiao, F.; Debart, A.; Bruce, P. G.: Mesoporous and nanowire Co_3O_4 as negative electrodes for rechargeable lithium batteries. *Phys. Chem. Chem. Phys.* **2007**, *9*, 1837-1842.

[280] Jiao, F.; Harrison, A.; Jumas, J. C.; Chadwick, A. V.; Kockelmann, W.; Bruce, P. G.: Ordered mesoporous Fe_2O_3 with crystalline walls. *J. Am. Chem. Soc.* **2006**, *128*, 5468-5474.

[281] Wang, K. X.; Wei, M. D.; Morris, M. A.; Zhou, H. S.; Holmes, J. D.: Mesoporous titania nanotubes: Their preparation and application as electrode materials for rechargeable lithium batteries. *Adv. Mater.* **2007**, *19*, 3016-+.

[282] Liu, P.; Lee, S. H.; Tracy, C. E.; Yan, Y. F.; Turner, J. A.: Preparation and lithium insertion properties of mesoporous vanadium oxide. *Adv. Mater.* **2002**, *14*, 27-30.

[283] Yang, P. D.; Zhao, D. Y.; Margolese, D. I.; Chmelka, B. F.; Stucky, G. D.: Generalized syntheses of large-pore mesoporous metal oxides with semicrystalline frameworks. *Nature* **1998**, *396*, 152-155.

[284] Yang, P. D.; Zhao, D. Y.; Margolese, D. I.; Chmelka, B. F.; Stucky, G. D.: Block copolymer templating syntheses of mesoporous metal oxides with large ordering lengths and semicrystalline framework. *Chem. Mater.* **1999**, *11*, 2813-2826.

[285] Laetsch, T.; Downs, R. T.: 19th General Meeting of the International Mineralogical Association. *Kobe*, *Japan*.

[286] Kim, C. H.; Chun, H. J.; Kim, D. S.; Kim, S. Y.; Park, J.; Moon, J. Y.; Lee, G.; Yoon, J.; Jo, Y.; Jung, M. H.; Jung, S. I.; Lee, C. J.: Magnetic anisotropy of vertically aligned alpha-Fe_2O_3 nanowire array. *Appl. Phys. Lett.* **2006**, *89*.

[287] Bersani, D.; Lottici, P. P.; Montenero, A.: Micro-Raman investigation of iron oxide films and powders produced by sol-gel syntheses. *J. Raman Spectrosc.* **1999**, *30*, 355-360.

[288] Akl, A. A.: Optical properties of crystalline and non-crystalline iron oxide thin films deposited by spray pyrolysis. *Appl. Surf. Sci.* **2004**, *233*, 307-319.

[289] Vayssieres, L.; Sathe, C.; Butorin, S. M.; Shuh, D. K.; Nordgren, J.; Guo, J. H.: One-dimensional quantum-confinement effect in alpha-Fe_2O_3 ultrafine nanorod arrays. *Adv. Mater.* **2005**, *17*, 2320-+.

[290] Corma, A.: From microporous to mesoporous molecular sieve materials and their use in catalysis. *Chem. Rev.* **1997**, *97*, 2373-2419.

[291] Morales, J.; Sanchez, L.; Martin, F.; Berry, F.; Ren, X. L.: Synthesis and characterization of nanometric iron and iron-titanium oxides by mechanical milling: Electrochemical properties as anodic materials in lithium cells. *J. Electrochem. Soc.* **2005**, *152*, A1748-A1754.

[292] Grugeon, S.; Laruelle, S.; Dupont, L.; Tarascon, J. M.: An update on the reactivity of nanoparticles Co-based compounds towards Li. *Solid State Sci.* **2003**, *5*, 895-904.

[293] Balaya, P.; Li, H.; Kienle, L.; Maier, J.: Fully reversible homogeneous and heterogeneous Li storage in RuO_2 with high capacity. *Adv. Funct. Mater.* **2003**, *13*, 621-625.

[294] Wu, X. L.; Guo, Y. G.; Wan, L. J.; Hu, C. W.: alpha-Fe_2O_3 Nanostructures: Inorganic

Salt-Controlled Synthesis and Their Electrochemical Performance toward Lithium Storage. *J. Phys. Chem. C* **2008**, *112*, 16824-16829.

[295] Jiao, F.; Bao, J. L.; Bruce, P. G.: Factors influencing the rate of Fe_2O_3 conversion reaction. *Electrochem. Solid State Lett.* **2007**, *10*, A264-A266.

[296] Hu, Y. S.; Kienle, L.; Guo, Y. G.; Maier, J.: High lithium electroactivity of nanometer-sized rutile TiO_2. *Adv. Mater.* **2006**, *18*, 1421-+.

[297] Ji, L. W.; Zhang, X. W.: Manganese oxide nanoparticle-loaded porous carbon nanofibers as anode materials for high-performance lithium-ion batteries. *Electrochem. Commun.* **2009**, *11*, 795-798.

[298] Zhang, W. M.; Wu, X. L.; Hu, J. S.; Guo, Y. G.; Wan, L. J.: Carbon Coated Fe3O4 Nanospindles as a Superior Anode Material for Lithium-Ion Batteries. *Adv. Funct. Mater.* **2008**, *18*, 3941-3946.

[299] Fang, X. P.; Lu, X.; Guo, X. W.; Mao, Y.; Hu, Y. S.; Wang, J. Z.; Wang, Z. X.; Wu, F.; Liu, H. K.; Chen, L. Q.: Electrode reactions of manganese oxides for secondary lithium batteries. *Electrochem. Commun.* **2010**, *12*, 1520-1523.

[300] Poizot, P.; Laruelle, S.; Grugeon, S.; Tarascon, J. M.: Rationalization of the low-potential reactivity of 3d-metal-based inorganic compounds toward Li. *J. Electrochem. Soc.* **2002**, *149*, A1212-A1217.

[301] Li, H.; Balaya, P.; Maier, J.: Li-storage via heterogeneous reaction in selected binary metal fluorides and oxides. *J. Electrochem. Soc.* **2004**, *151*, A1878-A1885.

[302] Gao, Y. Q.; Wang, Z. G.; Wan, J. X.; Zou, G. F.; Qian, Y. T.: A facile route to synthesize uniform single-crystalline alpha-MnO_2 nanowires. *J. Cryst. Growth* **2005**, *279*, 415-419.

[303] Wu, M. S.; Chiang, P. C. J.; Lee, J. T.; Lin, J. C.: Synthesis of manganese oxide electrodes with

interconnected nanowire structure as an anode material for rechargeable lithium ion batteries. *J. Phys. Chem. B* **2005**, *109*, 23279-23284.

[304] Laruelle, S.; Grugeon, S.; Poizot, P.; Dolle, M.; Dupont, L.; Tarascon, J. M.: On the origin of the extra electrochemical capacity displayed by MO/Li cells at low potential. *J. Electrochem. Soc.* **2002**, *149*, A627-A634.

[305] Zhong, K. F.; Xia, X.; Zhang, B.; Li, H.; Wang, Z. X.; Chen, L. Q.: MnO powder as anode active materials for lithium ion batteries. *J. Power Sources* **2010**, *195*, 3300-3308.

[306] Ominde, N.; Bartlett, N.; Yang, X. Q.; Qu, D. Y.: The effect of oxygen reduction on activated carbon electrodes loaded with manganese dioxide catalyst. *J. Power Sources* **2008**, *185*, 747-753.

[307] Zhang, T.; Imanishi, N.; Shimonishi, Y.; Hirano, A.; Takeda, Y.; Yamamoto, O.; Sammes, N.: A novel high energy density rechargeable lithium/air battery. *Chem. Commun.* **2010**, *46*, 1661-1663.

[308] Tran, C.; Kafle, J.; Yang, X. Q.; Qu, D. Y.: Increased discharge capacity of a Li-air activated carbon cathode produced by preventing carbon surface passivation. *Carbon* **2011**, *49*, 1266-1271.

[309] Wang, Y. G.; Zhou, H. S.: To draw an air electrode of a Li-air battery by pencil. *Energy Environ. Sci.* **2011**, *4*, 1704-1707.

[310] Yoo, E.; Zhou, H. S.: Li-Air Rechargeable Battery Based on Metal-free Graphene Nanosheet Catalysts. *Acs Nano* **2011**, *5*, 3020-3026.

[311] Campos-Delgado, J.; Romo-Herrera, J. M.; Jia, X. T.; Cullen, D. A.; Muramatsu, H.; Kim, Y. A.; Hayashi, T.; Ren, Z. F.; Smith, D. J.; Okuno, Y.; Ohba, T.; Kanoh, H.; Kaneko, K.; Endo, M.;

Terrones, H.; Dresselhaus, M. S.; Terrones, M.: Bulk production of a new form of sp^2 carbon: Crystalline graphene nanoribbons. *Nano Lett.* **2008**, *8*, 2773-2778.

[312] Park, S.; An, J.; Potts, J. R.; Velamakanni, A.; Murali, S.; Ruoff, R. S.: Hydrazine reduction of graphite and graphene oxide. *Carbon* **2011**, *49*, 3019-3023.

[313] Jiang, D. E.; Sumpter, B. G.; Dai, S.: Unique chemical reactivity of a graphene nanoribbon's zigzag edge. *J. Chem. Phys.* **2007**, *126*.

[314] Zhu, S. M.; Zhou, H. A.; Hibino, M.; Honma, I.; Ichihara, M.: Synthesis of MnO_2 nanoparticles confined in ordered mesoporous carbon using a sonochemical method. *Adv. Funct. Mater.* **2005**, *15*, 381-386.

[315] Cheng, M. Y.; Hwang, B. J.: Mesoporous carbon-encapsulated NiO nanocomposite negative electrode materials for high-rate Li-ion battery. *J. Power Sources* **2010**, *195*, 4977-4983.

[316] Zhang, H. J.; Tao, H. H.; Jiang, Y.; Jiao, Z.; Wu, M. H.; Zhao, B.: Ordered CoO/CMK-3 nanocomposites as the anode materials for lithium-ion batteries. *J. Power Sources* **2010**, *195*, 2950-2955.

[317] Taguchi, A.; Schuth, F.: Ordered mesoporous materials in catalysis. *Micropor. and Mesopor. Mater.* **2005**, *77*, 1-45.

[318] Su, F. B.; Zeng, J. H.; Bao, X. Y.; Yu, Y. S.; Lee, J. Y.; Zhao, X. S.: Preparation and characterization of highly ordered graphitic mesoporous carbon as a Pt catalyst support for direct methanol fuel cells. *Chem. Mater.* **2005**, *17*, 3960-3967.

[319] Zhou, H. S.; Zhu, S. M.; Hibino, M.; Honma, I.: Electrochemical capacitance of self-ordered mesoporous carbon. *J. Power Sources* **2003**, *122*, 219-223.

[320] Wang, Y. G.; Cheng, L.; Li, F.; Xiong, H. M.; Xia, Y. Y.: High electrocatalytic performance of

Mn_3O_4/mesoporous carbon composite for oxygen reduction in alkaline solutions. *Chem. Mater.* **2007**, *19*, 2095-2101.

[321] Zhao, D. Y.; Feng, J. L.; Huo, Q. S.; Melosh, N.; Fredrickson, G. H.; Chmelka, B. F.; Stucky, G. D.: Triblock copolymer syntheses of mesoporous silica with periodic 50 to 300 angstrom pores. *Science* **1998**, *279*, 548-552.

[322] Jun, S.; Joo, S. H.; Ryoo, R.; Kruk, M.; Jaroniec, M.; Liu, Z.; Ohsuna, T.; Terasaki, O.: Synthesis of new, nanoporous carbon with hexagonally ordered mesostructure. *J. Am. Chem. Soc.* **2000**, *122*, 10712-10713.

[323] Ryoo, R.; Joo, S. H.; Kruk, M.; Jaroniec, M.: Ordered mesoporous carbons. *Adv. Mater.* **2001**, *13*, 677-681.

[324] McCloskey, B. D.; Bethune, D. S.; Shelby, R. M.; Girishkumar, G.; Luntz, A. C.: Solvents' Critical Rope in Nonaqueous Lithium-Oxygen Battery Electrochemistry. *J. Phys. Chem. Lett.* **2011**, *2*, 1161-1166.

[325] Bryantsev, V. S.; Blanco, M.: Computational Study of the Mechanisms of Superoxide-Induced Decomposition of Organic Carbonate-Based Electrolytes. *J. Phys. Chem. Lett.* **2011**, *2*, 379-383.